



Self-assembled permanent micro-magnets for the isolation of Circulating Tumor Cells in a microfluidic device

Lucie Descamps

► To cite this version:

Lucie Descamps. Self-assembled permanent micro-magnets for the isolation of Circulating Tumor Cells in a microfluidic device. Physics [physics]. Université de Lyon, 2021. English. NNT : 2021LYSE1253 . tel-03592962

HAL Id: tel-03592962

<https://theses.hal.science/tel-03592962>

Submitted on 1 Mar 2022

HAL is a multi-disciplinary open access archive for the deposit and dissemination of scientific research documents, whether they are published or not. The documents may come from teaching and research institutions in France or abroad, or from public or private research centers.

L'archive ouverte pluridisciplinaire **HAL**, est destinée au dépôt et à la diffusion de documents scientifiques de niveau recherche, publiés ou non, émanant des établissements d'enseignement et de recherche français ou étrangers, des laboratoires publics ou privés.

N°d'ordre NNT :
2021LYSE1253



THESE de DOCTORAT DE L'UNIVERSITE DE LYON

opérée au sein de
l'Université Claude Bernard Lyon 1

Ecole Doctorale N° 160
Électronique, Électrotechnique, Automatique de Lyon (EEA)

Spécialité de doctorat : Ingénierie pour le vivant

Soutenue publiquement le 08/12/2021, par :
Lucie Descamps

Self-assembled permanent micro-magnets for the isolation of Circulating Tumor Cells in a microfluidic device

Devant le jury composé de :

Den Toonder, Jaap, Professeur, Université technique d'Eindhoven
Le Pioufle, Bruno, Professeur des universités, ENS Cachan
Ferrigno, Rosaria, Professeure des universités, Université Lyon 1
Raillon, Camille, Ingénieure de recherche, CEA Grenoble

Deman, Anne-Laure, Maître de conférence, INL
Le Roy, Damien, Maître de conférence, ILM

Payen, Léa, Professeure des Universités-Praticien Hospitalier,

Rapporteur
Rapporteur
Examinatrice
Examinatrice

Directrice de thèse
Co-directeur de thèse

Invitée

Acknowledgements

First, I would like to thank all the jury members for accepting to be part of it, the rich discussion we had, as well as the precious feedback. Their compliments helped me tackle my next adventure with confidence.

I will now express myself in my native language to fully embrace what I would like to share.

D'abord, je voudrais remercier Anne-Laure et Damien, mes superviseurs, pour votre soutien et votre bienveillance. On ne pouvait rêver mieux. Cela a été un vrai plaisir de travailler à vos côtés durant ces trois années de thèse, mais aussi de pouvoir échanger sur notre monde et partager les mêmes valeurs.

J'aimerais également remercier tous mes collègues de l'INL pour leurs bons conseils et leur bonne humeur au quotidien. Merci en particulier à Samir de m'avoir ouvert la voie, transmis ton savoir, et partagé ton esprit vif ; à Magalie pour ton expertise en microfluidique mais aussi ta gentillesse ; Marie-Charlotte pour nos moments MFM partagés et ton enthousiasme quotidien ; Jérôme pour sa disponibilité ; Caterina, bien que nos chemins se soient croisés, j'ai beaucoup apprécié de te connaître ; Patrick, grâce à qui il était possible de rester même à la tombée de la nuit ; et Laurent, notamment pour ton assistance le jour de la soutenance. Je n'oublierai pas également mes nombreuses pauses de midi passées en bonne compagnie, notamment aux côtés de Magalie, Marie-Charlotte, Jérôme et Josué !

Je voudrais également remercier toute l'équipe aux HCL pour leur accueil, cette collaboration a été une expérience très enrichissante. Merci au professeur Léa Payen pour avoir rendu cela possible, merci à Florence, Julie, Margaux et Gaëlle pour leur disponibilité. Merci tout particulièrement à Jessica et David pour leur aide considérable et leur bienveillance.

Je voudrais maintenant remercier mes amis. D'abord mes copines de Lyon, ma coloc Alizé pour avoir embelli cette expérience, aux côtés de Houdna, avec qui les mois de confinement toutes les trois ont été précieux ; également aux côtés d'Elise, Manon et Meriem. J'ai partagé avec vous de si nombreux moments mémorables, à découvrir la région, regarder nos émissions de télé favorites, ou encore concocter de si bons petits (gros) plats. Votre grain de folie a été si rafraichissant ! Je pense également à Jordyn, qui a partagé un petit bout de chemin avec moi et que je n'oublierai pas. J'aimerais également remercier mes copains d'école d'ingénieur, Emmanuelle, Kelly, Simon, Charlotte, Younesse, Alex, Nolwenn, Quentin, Céline, Mathieu et tous les autres, pour nos retrouvailles à chaque fois aux quatre coins de l'Europe : Bruxelles, Delft, Paris, Toulouse, et j'en passe. C'était toujours génial de se retrouver, comme si nous n'avions jamais quitté Strasbourg. Merci à toutes les autres personnes que j'ai pu croiser ces trois dernières années, cette expérience a été d'autant plus facile car j'ai été extrêmement bien entourée.

Enfin, j'aimerais remercier tout particulièrement ma famille, mes parents pour avoir toujours cru en moi et encouragé à faire ce qui me plaisait ; Florian, mon petit frère qui n'en est pas vraiment un, j'apprends tous les jours auprès de toi. Tous les quatre, le noyau dur, pour toujours.

Un merci tout particulier à Paul, pour ton soutien sans faille et pour avoir toujours réussi à trouver les bons mots pour me rassurer, même séparés dans des pays différents. Je t'aime.

In short, what I learned from this PhD is to focus on the journey, not the destination. I encountered happiness along the way by meeting new people, learning from their experiences, sharing about life, spending precious time with family and friends, and feeling supported the whole time. So thank you for being there along the way and contributing to this incredible journey.

Introduction

Cancer is one of the leading health issues, accounting for nearly 1 in 6 deaths worldwide. According to the Global Cancer Observatory, in 2020 there were an estimated 19.3 million new cancer cases and 9.96 million cancer deaths globally. By 2040, the disease burden is expected to reach 30.2 million new cancer cases and 16.3 million cancer deaths. Cancer burden can be reduced through early detection and appropriate treatment. To date, tissue biopsies are core components of cancer patient management to diagnose, assess disease stage and prescribe appropriate therapeutic regimens. However, biopsies not only are invasive and risky but also may not recapitulate intra-tumor heterogeneity. For all these reasons, tissue biopsies fail to provide a frequent insight of tumor evolution.

The study of circulating tumor cells (CTCs) may overcome these limitations and complement tissue biopsies. CTCs are released into the bloodstream from primary and metastatic tumors, and, besides playing an important role in cancer metastasis, they offer a promising clinical potential for cancer diagnosis and prognosis. The isolation of CTCs directly from a blood test, referring as “liquid biopsy”, has therefore raised strong interest in recent years. These samples can be collected non-invasively and frequently, providing real-time monitoring of tumor evolution and response to treatment. Liquid biopsy may lead to changes in the paradigm of cancer diagnosis and management by providing earlier diagnosis and more personalized treatment.

Nevertheless, until now, isolating CTCs has been a technical challenge limiting their wider use in research and clinical studies. The primary challenge has been the rarity of CTCs (1–1000 CTCs per mL) among a high background of blood cells (10^9 red blood cells (RBCs) and 10^7 white blood cells (WBCs) per mL). The other challenge has been their phenotypic heterogeneity since CTCs can undergo an epithelial-to-mesenchymal transition (EMT), which results in a decreased expression of epithelial markers and an increased phenotypic plasticity. Finally, the isolation of CTCs should be achieved while preserving their integrity for downstream characterizations.

The CellSearch™ system (Veridex, USA) was the first instrument available for CTC isolation and remains the only Food and Drug Administration (FDA)-approved assay for CTC enumeration used to predict cancer patient outcome. The method relies on the enrichment of CTCs expressing epithelial cell adhesion molecule (EpCAM) through the use of immunomagnetic particles. Although this system is considered a “gold standard” for CTC detection, the detection sensitivity highly depends on epithelial markers, consequently cells lacking these markers would be missed. In addition to relatively low recovery, low purity has been reported since CTCs are enriched with a high background of contaminating WBCs, limiting downstream characterization.

Over the past decade microfluidic devices have emerged as promising tools to address these limitations. Their micrometric dimensions and laminar flow nature enable precise cell manipulation and single-cell study, in a cost-effective and versatile manner. The handling of small quantities of volume also facilitates the analysis of such rare samples and speeds up processes. Several microfluidic technologies, awaiting FDA clearance, have been commercialized for CTC isolation, such as Parsortix® (ANGLE plc, UK), ClearCell® FX1 (Biolidics, Singapore), and VTX-1 (Vortex Biosciences, USA). These technologies are based on the difference in CTC size and deformability compared to blood cells. Other physical properties such as density and electrical charges, as well as biological properties, essentially surface marker expression, can also be exploited. Despite the tremendous work achieved in CTC isolation devices, there are still CTC-specific challenges which must be overcome. Indeed, CTC size and tumor marker heterogeneities account for the difficulty to reach high purity and perform subsequent analysis.

In this thesis, we tackled these issues by developing a magnetophoretic-based microfluidic device for CTC isolation. The developed magnetophoretic device was further combined to a size-based separation technology (ClearCell) to reach highly purified samples. The adopted strategy is based on magnetophoresis, which refers to the motion of magnetic particles or magnetically labelled cells when

subjected to a non-uniform magnetic field. In particular, the strategy relies on negative selection using immunomagnetic nanoparticles targeting WBC-specific markers to deplete WBCs. The separation is therefore size-independent and tumor marker-independent, therefore enabling the isolation of heterogeneous CTCs. Besides, over the past few years, researchers have shed the light on the potential of magnetophoresis to sort biological objects. It offers a contactless manipulation, making this technique nondestructive for biological samples; robustness, since this method is not sensitive to pH, temperature, etc.; and tunability, the magnetic force depends on the particle size, the magnetic properties of the target and surrounding medium, as well as the gradient of the magnetic field.

This work was devoted to the maximization of the sorting efficiency, which could be achieved by the generation of high magnetic forces. The integration of micro-scale magnetic sources into microfluidic devices has proven to be the most suitable strategy since micro-scale magnetic sources generate strong magnetic field gradients at their surface. However, some challenges remain regarding the complexity of microfabrication of these microscale magnetic sources, and their integration into polymer-based microfluidic systems. Here, we reported an approach breaking with standard microfabrication techniques, based on magnetic polymer composites, to integrate large density arrays of permanent micro-magnets into a microfluidic system. Permanent micro-magnets were obtained by mixing hard NdFeB magnetic particles with a PDMS matrix and further self-organized due to dipole-dipole interactions between magnetic particles. These self-assembled micrometric-sized magnets, which act as micro-traps, were then integrated into a microfluidic device, leading to autonomous and compact systems. In order to help the understanding of the different axes tackled in this thesis, the manuscript was articulated in five chapters, as follows:

The Chapter 1 (state of the art) gives a detailed study of CTC isolation, from its challenges to the promising reported microfluidic technologies to address the issues at stake. Then, the study focuses on magnetophoresis, its principle and implementation in microfluidics. Finally, the breakthrough of magnetic composites for the integration of microscale magnetic sources in microfluidic devices is highlighted.

In the Chapter 2 (materials and methods) is reported the fabrication process of the micro-magnets, relying on the composite approach, the characterization methods of the micro-magnet microstructure and magnetic properties, and their implementation in microfluidics for CTC isolation via depletion of magnetically labeled WBCs. Finally, we elaborated on the downstream biological studies performed after CTC recovery.

In the Chapter 3, we investigated several aspects of the fabrication process, such as the concentration of hard magnetic particles within the PDMS matrix, the application of a non-uniform magnetic field during magnetic particle self-assembly, and studied their influence on the micro-magnet structure and magnetic properties using a broad range of methods. From numerical calculations using Comsol finite element modeling to estimate magnetic fields and magnetic field gradients, to experimental measurements using colloidal probe atomic force microscopy (AFM) and hydrodynamic experiments to determine generated magnetic forces. These magnetic characterizations revealed the behavior of the micro-magnets, which generate high magnetic field gradients at their surface but with limited interaction reach. We overcame this limitation by adding an additional millimeter-scale permanent magnet to attract target objects towards the channel bottom where the micro-traps are located.

The Chapter 4 details the implementation strategy of the micro-magnet-integrated microfluidic device for CTC isolation. Cancer cell lines were used as CTC models. We presented the prior optimizations that were conducted on the device features and operation procedure before testing the compatibility of the chip with routine biological studies (cell culture, phenotypic and genotypic analyses) after CTC recovery. Finally, as part of a collaboration with biologists from Hospices Civils de Lyon, the magnetophoretic-based microfluidic chip was combined with a size-based separation technology (ClearCell FX1®) as a two-step separation process, to meet the needs of physicians for highly purified samples.

Finally, the last part (conclusion and future outlook) closes the thesis work by giving a summary of achieved results, highlighting the assets and limitations of the device, and opening the perspectives of the project in clinical studies aiming at determining tumor molecular characteristics and predicting response to treatment.

Contents

Acknowledgements	i
Introduction.....	iii
List of abbreviations	ix
Chapter I Immunomagnetic-based isolation of CTC in microfluidic devices.....	1
1. CTC isolation in microfluidics	1
1.1. Context and challenges of circulating tumor cell study	1
1.2. CTC enrichment in microfluidic devices	3
1.2.1. Physical-based separation methods	3
1.2.2. Biological-based separation methods	17
2. Magnetophoresis-based microfluidics.....	24
2.1. Theory and phenomenon	24
2.1.1. Magnetism fundamentals for magnetophoresis	24
2.1.2. Governing forces in magnetic-based microfluidic device	26
2.2. Interest of micro-scale magnetic sources	29
2.2.1. Maximizing the magnetic force	29
2.2.2. Conventional microfabrication techniques of micro-scale magnetic sources	30
2.3. Implementation of magnetophoresis for CTC isolation	31
2.3.1. From macroscale to microscale magnetic sources	31
2.3.2. Diverse immunomagnetic separation approaches	33
2.3.3. Combination of immunomagnetic separation with physical-based separation methods..	37
2.3.4. Summary	39
3. Magnetic composites for microscale patterning in microfluidic separation systems	43
3.1. Breakthrough of the composite polymers	43
3.2. Magnetic PDMS composites in microfluidics	43
4. Aim and scope of the thesis	48
References.....	49
Chapter II Materials and Methods.....	61
1. Fabrication and characterization of self-assembled micro-magnets	62
1.1. Composite preparation and structuration.....	62
1.1.1. Preparation	62
1.1.2. Shaping process	62
1.2. Structural characterization	64
1.2.1. X-ray tomography	64

1.2.2.	Optical microscopy	65
1.3.	Magnetic characterization	65
1.3.1.	SQUID magnetometry	65
1.3.2.	Colloidal probe atomic force microscopy	65
1.4.	Finite element simulation	66
2.	Integration of micro-magnets into a microfluidic device and operation	68
2.1.	Device assembly.....	68
2.2.	Device sterilization	69
2.3.	Microfluidic experimental set-up	70
2.3.1.	Manipulated magnetic objects.....	70
2.3.2.	Experimental set-up	71
2.3.3.	Injection procedure	71
2.3.4.	Addition of an external permanent magnet	72
3.	Biological sample preparation	72
3.1.	Cell culture	72
3.1.1.	Cell lines	72
3.1.2.	Routine culture protocol.....	73
3.2.	Blood sample preparation	73
3.2.1.	RBC Lysis protocol.....	73
3.2.2.	Magnetic labeling of white blood cells	73
4.	Downstream analysis performed after purification	74
4.1.	Estimation of cell capture and recovery efficiencies	74
4.2.	Cell culture in well-plate format.....	75
4.3.	Live/Dead assay	76
4.4.	Immunofluorescence assay	76
4.4.1.	Protocol.....	76
4.4.2.	Fluorescent image analysis	77
4.5.	Fluorescence In-Situ Hybridization	79
4.5.1.	Principle and objective.....	79
4.5.2.	Protocol.....	79
5.	Integrated workflow: size-based pre-enrichment separation followed by magnetic purification. 80	
5.1.	Context: a need to take into account CTC heterogeneity and improve sample purity	80
5.2.	ClearCell FX1 system instructions.....	80
5.3.	Workflow protocol	80
	References.....	83

Chapter III PDMS membrane integrating self-organized micro-magnet arrays: Structure, magnetism, and magnetophoretic trapping in microfluidics	85
1. Previous work of the group on anisotropic magnetic composites	86
2. Influence of the magnetic field on the micro-magnet array formation.....	88
2.1. Study of two experimental set-ups.....	88
2.2. Micro-magnet microstructure	89
2.3. Micro-magnet organization within the array	92
2.4. Magnetic properties of micro-magnets.....	94
2.5. Summary.....	95
3. Micro-magnet finite element analysis.....	96
3.1. Isolated microstructure	96
3.2. Demagnetizing effect of the array	97
3.3. Effect of an external permanent magnet.....	100
3.4. Calculation of the magnetic force exerted on a model bead	102
4. Magnetic force determination by colloidal probe AFM.....	103
4.1. Effect of the micro-magnet microstructure	104
4.2. Effect of an external permanent magnet.....	106
5. Microfluidic experiments	107
5.1. Magnetic particle capture efficiency	107
5.1.1. Effect of the micro-magnet microstructure	109
5.1.2. Influence of the external permanent magnet.....	109
5.1.3. Summary	110
5.2. Hydrodynamic determination of the holding magnetic force	110
5.2.1. Effect of the micro-magnet network	112
5.2.2. Influence of the external permanent magnet.....	112
6. Comparison with magnetic performances in the literature.....	113
7. Conclusion.....	116
References.....	117
Chapter IV Negative selection of cancer cells via white blood cell depletion for downstream analysis.....	121
1. Introduction.....	122
2. Immuno-magneto-capture of white blood cells and cancer cell recovery.....	125
2.1. Optimization of the magnetic labeling	125
2.2. Optimization of the magnetic chip.....	128
2.2.1. Enhancement of micro-magnet properties	128
2.2.2. Conception of a microfluidic chamber with high trapping capacity	128

2.2.3.	Determination of the operating flow rate	130
3.	Downstream analysis after magnetic-based separation.....	132
3.1.	Study of cancer cell viability	132
3.2.	Study of cancer cell integrity.....	133
3.3.	Long-term 2D cell culturing	135
3.4.	Spheroid formation	136
3.5.	Analysis of cancer cell genotype.....	138
3.6.	Summary.....	140
4.	Test of the complete workflow for blood sample processing.....	140
4.1.	Sample purification	140
4.2.	Study of long-term cell viability	143
4.3.	Analysis of cancer cell phenotype	144
5.	Conclusion.....	147
	References.....	148
	Conclusion and future outlook.....	153
1.	Summary	153
2.	Assets and limitations of the developed device	155
3.	Future outlook	156
3.1.	Improvements to the device.....	156
3.2.	Clinical applications.....	156
	List of publications	159
	List of communications	159
	Résumé en français	161
	Abstracts	186

List of abbreviations

Abbreviation	Meaning
ALDH1	Aldehyde dehydrogenase 1
ALK	Anaplastic lymphoma kinase
AFM	Atomic force microscopy
CK	Cytokeratin
Cm	Magnetic coefficient
CTC	Circulating tumor cell
EDTA	Ethylene diamine tetra-acetic acid
EGFR	Epidermal growth factor receptor
EML4	Echinoderm microtubule-associated protein like-4
EMT	Epithelial-to-mesenchymal transition
EpCAM	Epithelial cell adhesion molecule
EthD-1	Ethidium homodimer-1
DEP	Dielectrophoresis
DFF	Dean flow fractionation
DLD	Deterministic lateral displacement
FDA	Food drug administration
FISH	Fluorescence in situ hybridization
Her2	Epidermal growth factor receptor 2
HG	High gradient
IF	Immunofluorescence
I-PDMS	Iron carbonyl-PDMS
LG	Low gradient
MCA	Microcavity array
mCTC	Mimicking CTC
mRNA	Messenger RNA
NP	Nanoparticle
NSCLC	Non-small cell lung cancer
PBS	Phosphate buffer saline
PCR	Polymerase chain reaction
PD-L1	Programmed death–ligand 1
PDMS	Polydimethylsiloxane
qPCR	Quantitative PCR
RBC	Red blood cell
RNA	Ribonucleic acid
SCLC	Small cell lung cancer
SEM	Scanning electron microscopy
SPMB	Superparamagnetic bead
SQUID	Superconducting quantum interference device
WBC	White blood cell

Chapter I

Immunomagnetic-based isolation of CTC in microfluidic devices

1. CTC isolation in microfluidics

1.1. Context and challenges of circulating tumor cell study

Early cancer diagnosis and personalized cancer medicine are target objectives in cancer research. In the early stage of the disease, the small size of the primary tumor, as well as the lack of symptoms, are stumbling blocks for early screening. But when identified early, cancer is more likely to respond to therapy, and therefore leading to a greater survival probability. In addition, early diagnosis could prevent the formation of metastasis, a multistep process responsible for cancer spread and high morbidity rates [1]. The metastatic process occurs when cancer cells detach from the primary tumor and invade the blood circulation. Then, these circulating tumor cells (CTCs) can extravasate and colonize distant sites, leading to secondary tumor(s) (Figure 1.1).

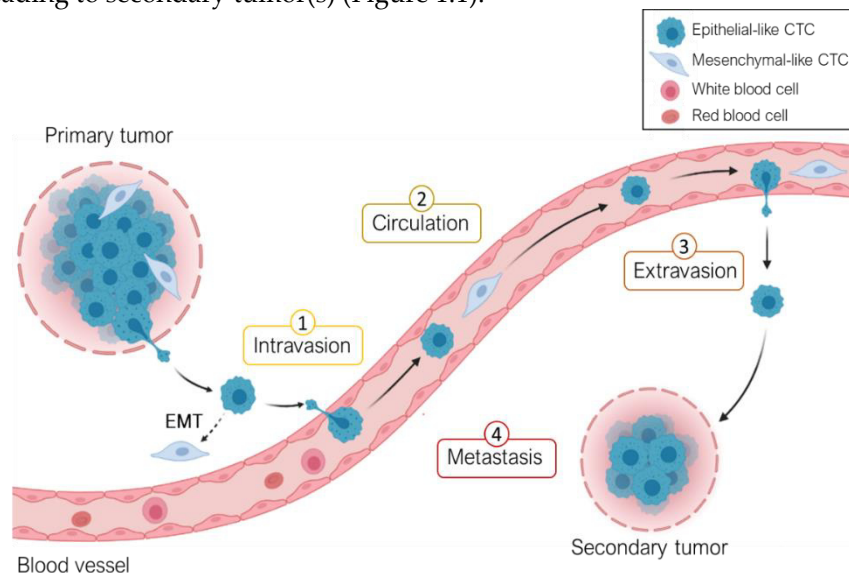


Figure 1.1: The metastatic cascade involving: the detachment of CTCs from the primary tumor and their (1) invasion into the blood circulation, (2) survival in the circulation, (3) extravasation, and (4) colonization of distant sites (secondary tumor). CTC may undergo epithelial-to-mesenchymal transition (EMT) which enables them to become more invasive. Adapted from “Circulating Tumor Cells” by BioRender.com.

Evidence of this progression through the blood circulation was first discovered in 1869 by Thomas Ashworth during an autopsy of a metastatic cancer patient. He observed that cancer cells from a distant site were morphologically consistent with primary tumor cells and concluded that cancer cells were transported through the blood to reach the distant site [2]. On one hand, the detection of CTCs can

provide clinical information on the tumor stage and can be used in early cancer diagnosis and disease prognosis [3–6]. On the other hand, CTCs are good surrogate biomarkers for treatment efficacy monitoring, enabling a personalized therapeutic approach [7,8]. Indeed, it became clear over time that “one drug fits all” treatment model was limited, and is being replaced by personalized medicine where treatment selection for each cancer patient is becoming individualized or customized. Being easily accessible in the bloodstream, the detection, enumeration, and characterization of CTCs, have highlighted their potential clinical significance in early detection of aggressive cancers [9,10], selection of therapies [11], identification of drug resistance [12], and discovery of novel therapeutic targets [13].

The selection of CTCs directly from blood, which is referred as a “liquid biopsy”, has therefore raised strong interest in recent years. First, liquid biopsy, in comparison with the traditional tissue biopsy consisting in removing a piece of the tumor, is noninvasive. It can therefore provide a frequent insight of the tumor evolution, and a real-time information on treatment efficacy and potential drug resistance. Second, liquid biopsy could be beneficial for monitoring cancers that are anatomically inaccessible or have high risks of post-biopsy complications, such as pancreatic ductal adenocarcinoma (PDAC) and lung cancer. Third, contrary to a tissue biopsy which gives a “snapshot” of the tumor, liquid biopsy permits to investigate intratumor heterogeneity, which reduces therapy effectiveness [14]. Finally, the molecular and genetic profiling of CTCs can provide extensive information to identify drug resistance and discover new therapeutic targets. For all these reasons, CTCs obtained by liquid biopsy represent promising biomarkers for early diagnosis, prognosis, and therapeutic monitoring, and will lead to a paradigm shift towards personalized cancer medicine (Figure 1.2).

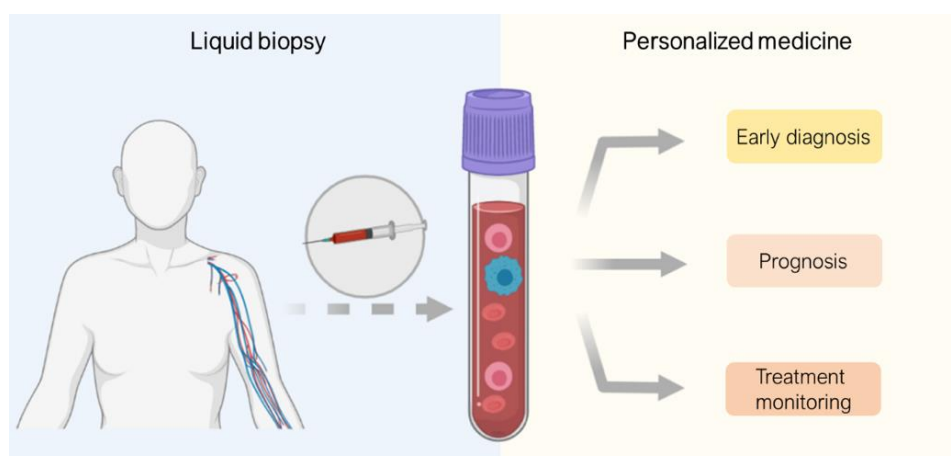


Figure 1.2: The isolation of CTCs directly from blood (liquid biopsy) opens new perspectives in personalized cancer medicine. Created with BioRender.com.

However, CTC study is a great challenge due to their rarity and phenotypical heterogeneity. There are approximatively 1 to 1000 CTCs among 10^7 white blood cells (WBCs) and 10^9 red blood cells (RBCs) in 1 mL of blood. Regarding their phenotypical heterogeneity, it is a result of the epithelial-mesenchymal transition (EMT) that CTCs can undergo. It leads to a diminution of epithelial markers (EpCAM, CK) and the appearance of a mesenchymal phenotype, which is associated with an increase of the capacity of invasiveness, immune escape, and metastasis [15]. Finally, CTC isolation should result in viable cells to perform downstream analysis such as cell culture, phenotype and genotype investigations, as well as chemoresistance studies.

Until now, Cellsearch™ is the only device approved by the US Food and Drug Administration (FDA) for CTC detection and enumeration for clinical use. The device uses ferrofluid particles coated with antibodies targeting epithelial cell adhesion molecule (EpCAM) for the enrichment of CTCs from the patient’s blood. Isolated cells are subsequently immunostained with fluorescently labeled antibodies and then counted using automated cell image capture and analysis. Since its introduction in 2004, the CellSearch™ system has been used as a diagnostic and prognostic tool in patients with metastatic breast, colorectal, and prostate cancer [16]. Although this system is considered a “gold standard” for CTC

detection, it has several drawbacks. The detection sensitivity of this approach highly depends on epithelial markers, which results in a low purity for cells that underwent EMT. CellSearch demonstrates a recovery rate of only 2% for mesenchymal breast cancer cell lines [17]. In addition, the system enriches CTCs with a high background of contaminating WBCs leading to low purity (0.01–0.1%) [18] and limiting further analyses. As a negative enrichment approach, the RosetteSep™ technology is based on bispecific antibodies that can crosslink RBCs and WBCs to form clusters (cell rosettes), which can be subsequently removed through density gradient centrifugation [19]. However, besides requiring different kits depending on the cancer type, the isolation of CTCs from the plasma and density gradient interface is extremely challenging and may further compromise their biological integrity. Another approach based on their size, the ISET (Isolation by Size of Epithelial Tumor cells) kit is used to isolate CTCs [20], but similarly to CellSearch™, this method only monitors epithelial cells. As CTC count corresponds to the patient's prognosis, CTC isolation techniques should be urgently developed with high efficiency and sensitivity in order to contribute to downstream CTC characterization.

1.2. CTC enrichment in microfluidic devices

Over the past decade, microfluidics has emerged for CTC isolation and characterization (Figure 1.3). Microfluidic devices possess unique advantages over conventional approaches, among which we can cite: (i) their micrometric dimensions and laminar flow nature, enabling precise object manipulation and single-cell study; (ii) the handling of small quantities of volume, which facilitates the analysis of rare or expensive samples and speeds up processes, leading to cost-effective devices; (iii) the integration of various functions (mixing, focusing, sorting, trapping, detection...) into a single device, leading to compact and portable systems, and therefore opening the way for the implementation of point-of-care devices. All these merits demonstrate that microfluidic devices offer new prospects in CTC study, in particular in terms of viability, recovery efficiency, sensitivity, purity and throughput [21].

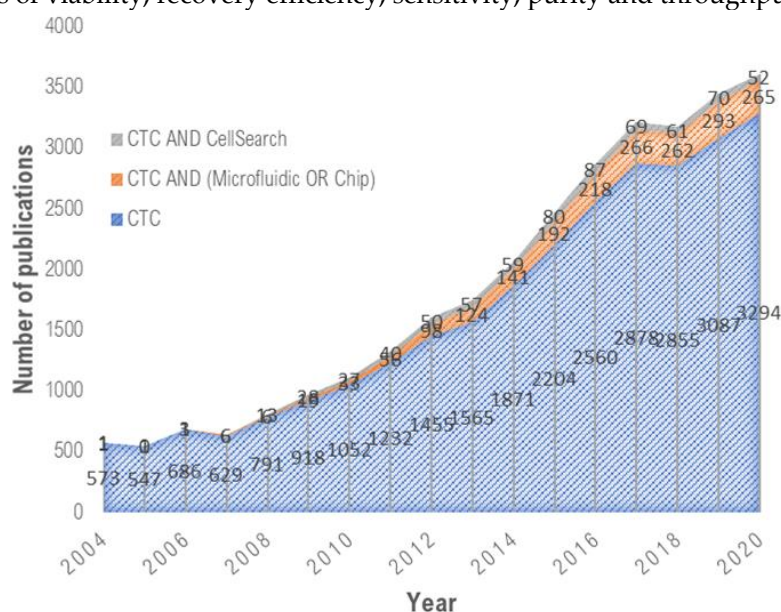


Figure 1.3: Emerging microfluidic technologies for CTC isolation. Data collected from Web of Science advanced search using specific keywords (“CTC”, “CellSearch”, “Microfluidic”, “Chip”).

1.2.1. Physical-based separation methods

Numerous studies (morphological, mechanical, electrical) have highlighted physical and biomechanical properties of CTCs, enabling their distinction from other blood cells [22]. Indeed, most of CTCs have a bigger size (17 to 52 μm) than RBCs (6 to 8 μm) and WBCs (7 to 15 μm for the majority, 20 μm for monocytes), a higher nuclear-cytoplasmic ratio, as well as an intricately folded membrane. Besides, their mechanical properties allow them to deform when passing through blood vessels [23]. This low stiffness of the cytoplasm plays a part in the metastatic process: it facilitates CTC migration towards secondary sites and increases their resistance to shear stress involved in the vascular system [24]. Finally, cytoskeletal remodelling has an impact on membrane structure conservation which leads to a

modification of the electrical surface charges and therefore of the electrical properties of CTCs. This is why separation methods based on physical criterion (size, deformability, electrical properties) were developed to isolate CTCs from blood.

Some of the most widespread separation techniques based on CTC physical properties are illustrated in Figure 1.4. Biological-based separation methods will be discussed in the next part.

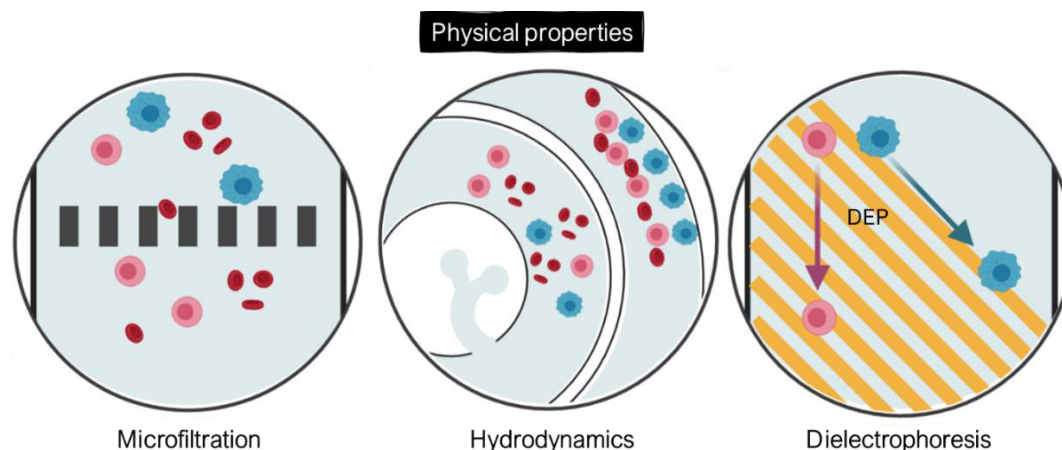


Figure 1.4: CTC enrichment technologies based on their physical properties through integrated microposts (microfiltration), specific microchannel designs (hydrodynamics), or application of electric fields (dielectrophoresis). Created with BioRender.com.

A- Microfiltration separation methods

Microfiltration techniques in microfluidics were implemented for CTC isolation [10–25], which consist in flowing a blood sample through micrometric constrictions to capture CTCs while other blood cells pass through. This separation method relies on cell size property, as well as on a combination of size and deformability criterion. Several strategies were studied for CTC isolation: microstructure post filters [26,31,37–39], microporous membranes [25,28,32,36,40], or microfluidic constrictions [30,33–35].

The first approach consists in integrating an array of micrometric-sized posts that will act like filters to capture CTCs. To this end, several microstructure post shapes were imagined: from micro-ellipse [37] to micro-pillars [38,39] and funnel constrictions [26]. Chen et al. integrated an array of micro-ellipse filters which consists of microfluidic slits in series gradually narrowed [37]. Ellipse-shaped filters reduce friction and shear stress, therefore preserving tumor cell viability. They achieved a capture efficiency of 90% of cancer cells at 1 mL/h with a viability of 96%. Then, they processed blood samples from four metastatic breast cancer patients and nine non-small cell lung cancer (NSCLC) patients to evaluate micro-ellipse clinical performances. CTCs were detected positive for the 2–3 mL blood samples of all the patients, with 4 patients having more than 20 CTCs. Nevertheless, additional concerns include the low sample capacity resulting from cell clogging as the usual blood volume processed in clinical experiments is 7.5 mL. In addition, in this developed device, CTCs cannot be recovered to conduct downstream analysis.

Strategies were investigated by other researchers to tackle these issues. Park et al. developed deformability-based device to enrich viable CTCs directly from whole blood by integrating funnel-shaped constrictions with openings smaller than the diameter of the cell [26]. The device takes advantage from the microfluidic ratchet mechanism which relies on the distinct deformability (or more precisely, squeezability) of CTCs relative to hematological cells. They fabricated a 2D array of funnel constrictions where the size of the funnel opening is gradually reduced from the bottom row to the top row (from 18 to 2 μm). Using continuous oscillatory flow, whole blood is infused from the bottom-left corner of the funnel array and cells proceed to travel in a zigzag diagonal path until reaching a blocking funnel row, where they proceed horizontally toward the outlet reservoirs (Figure 1.5-A). The combination of oscillatory flow and asymmetrical deformation enables to process whole blood

continuously and eliminate clogging issues. They achieved a capture efficiency comprised between 77% to 90% in spike samples, with an enrichment factor varying from 5000 to 14,000. The device was validated with 20 clinical samples from patients with metastatic prostate cancer and results were compared with the CellSearch™ system. The microfluidic ratchets present a high sensitivity and allowed the detection of a median 178 CTCs/7.5 mL compared to a median 7 CTCs/7.5 mL with the CellSearch™ system. CTC counts were obtained from 2 mL of patient blood using the microfluidic ratchet device and were therefore scaled to 7.5 mL to compare with results obtained using the CellSearch system. As the throughput of microfluidic ratchets is relatively low, about 1 mL/h, two devices were run in parallel to process the 2 mL of blood (1 mL/device). However, this device hasn't been able yet to process 7.5 mL of blood (standard volume for protocols), which could increase the probability of recovering CTCs.

The second filtration approach consists of microporous membranes which leads to higher throughput (> 3 mL/h). Hosokawa et al. developed a microfluidic device equipped with a nickel-based microcavity array (MCA) filter to enrich CTCs from blood samples (Figure 1.5-B). The first fabricated device consisted of 10 000 circular cavities, with diameters of 8-11 μm , and a distance of 60 μm between each of them [41]. The MCA filter was sandwiched between an upper substrate, which consists of a microchamber, sample inlet, and an outlet; and a vacuum line in the lower substrate, to produce a negative pressure and enable cell entrapment. The device showed very high capture efficiency in non-small cell lung cancer (NSCLC) cells, with a separation efficiency as high as 97% in 1-mL of blood spiked with 10-100 cells, processed within 15 min. However, once single cells are trapped on the circular microcavities, other cells are driven towards unoccupied microcavities and pass through under a higher pressure. This excessive flow resistance causes cell deformation and leads to the escape of small tumor cells such as small-cell lung cancer (SCLC) cells from the circular microcavities, therefore reducing the capture efficiency. The researchers further optimized the structure of the MCA to successfully separate small-sized tumor cells, like those found in SCLC. They fabricated rectangular-shaped microcavities, with a width of 5-9 μm and a length of 30 μm [42]. With this optimized rectangular MCA, they reached higher recovery and purity rates than those obtained with the circular MCA for small tumor cells. They conducted a clinical study on a newly automated MCA system and demonstrated the superiority of the system in comparison with CellSearch™ for the detection of CTCs in patients with NSCLC [36]. Nevertheless, for patients with SCLC, the CellSearch™ system showed better performances. This can be explained by the dependence of the MCA system on the difference in cell size between tumor cells and normal blood cells, which inevitably results in a loss for tumor cells of smaller size such as SCLC cells. Further development should therefore be made to achieve better sensitivity.

Recently, another MCA structure was imagined by Yin et al. since vertical entrances (presented above) keep blood cells from entering and escaping the microcavities and thus decrease the efficiency and purity of separation [43]. They integrated a MCA filter with pyramidal microstructures into a microfluidic device for CTC enrichment from raw blood samples [28] (Figure 1.5-C). The silicon-based microcavity array was fabricated by lithography and induced couple plasma reactive ion etching (ICPRIE) technologies to obtain 10 000 microcavities in a 14 x 14 mm filter. Microcavities have a length of 30 μm and a width of 8 μm and are spaced of 60 μm between each other. The device is fabricated by adhering the top and bottom polydimethylsiloxane (PDMS) layers on the pyramidal MCA. In this device, the slope at the entrance of the cavity, combined with a gradual increase of the channel size from top to bottom, facilitates the deformation and escape of blood cells. Approximately 80% of spiked tumor cells were separated from 1 mL of whole blood at a flow rate of 6 mL/h and less than 0.003% of unwanted WBCs were captured. Furthermore, the microfluidic chip successfully identified CTCs in 5 out of 6 blood samples from cancer patients, with a range of 5-86 CTCs per mL. Further clinical sample processing should be performed to assess the clinical readiness of the device. However, due to the heterogeneity of CTCs, smaller CTCs couldn't be captured by microcavities. The same team later used functionalized microspheres to increase the size of CTCs and to enable better discrimination against WBCs [44], but therefore undoing the benefit of the label-free separation method.

Finally, the last filtration approach consists in narrowing the dimensions of the fluidic path through which cells flow to entrap CTCs. Hovich et al. developed a semi-automated separation system, the Parsortix™ (Figure 1.5-D), which might be the first microfluidic technology approved by the FDA. The system is currently awaiting FDA clearance for its use in metastatic breast cancer patients. The system achieved an average capture efficiency of 64% at high throughput (10 mL/h), with high purity (200–6000 leukocytes left) and high viability (99%) [35]. The performance of the system was compared to CellSearch™ in 26 clinical samples. The ranges of CTC counts were 0–6.5/mL for Parsortix™ and 0–33/mL for CellSearch™, respectively. Despite a lower sensitivity, the major advantage of Parsortix™ is the recovery of viable tumor cells to perform molecular and functional downstream analysis. For personalized treatment, it is also crucial to understand the biological processes coming into play in drug susceptibilities, which can be established by proteomic profiling of CTCs. Recently, Armbrecht et al. developed a microfluidic device integrating a bead-based assay for the direct quantification of proteins secreted by both single CTCs and CTC clusters [45]. These clusters, although rare, are the most aggressive subset of CTCs and could affect clinical decisions [46,47]. The device consists of two layers, the top one containing a channel network with trapping units, and the bottom one containing pneumatic donut-shaped valves. The trapping units, 1152 in total, are arranged in four parallel segments to reduce processing times of 6.5 mL whole blood samples. The integrated device could achieve capture, isolation, and subsequent analysis within a single trapping unit. CTCs and CTC clusters are first captured through a reduction of channel heights from 25 to 7.5 μm and retained by two micropillars forming a 2D constriction. CTCs are then co-captured with beads and the valves are actuated to form the analysis chamber in which a sandwich immunoassay will be performed. They achieved capture efficiencies superior to 95% for various cell lines at a flow rate of approximately 1 mL/h, with <5% of co-captured WBCs. Using this system, the secretion level of granulocyte colony stimulating factor (G-CSF), which indicates acute inflammation [48], was directly quantified. The device enabled the processing of full blood samples without pretreatment within 5–6 h. Further improvement could be made to reduce the processing time, as well as to achieve a fully automated protocol.

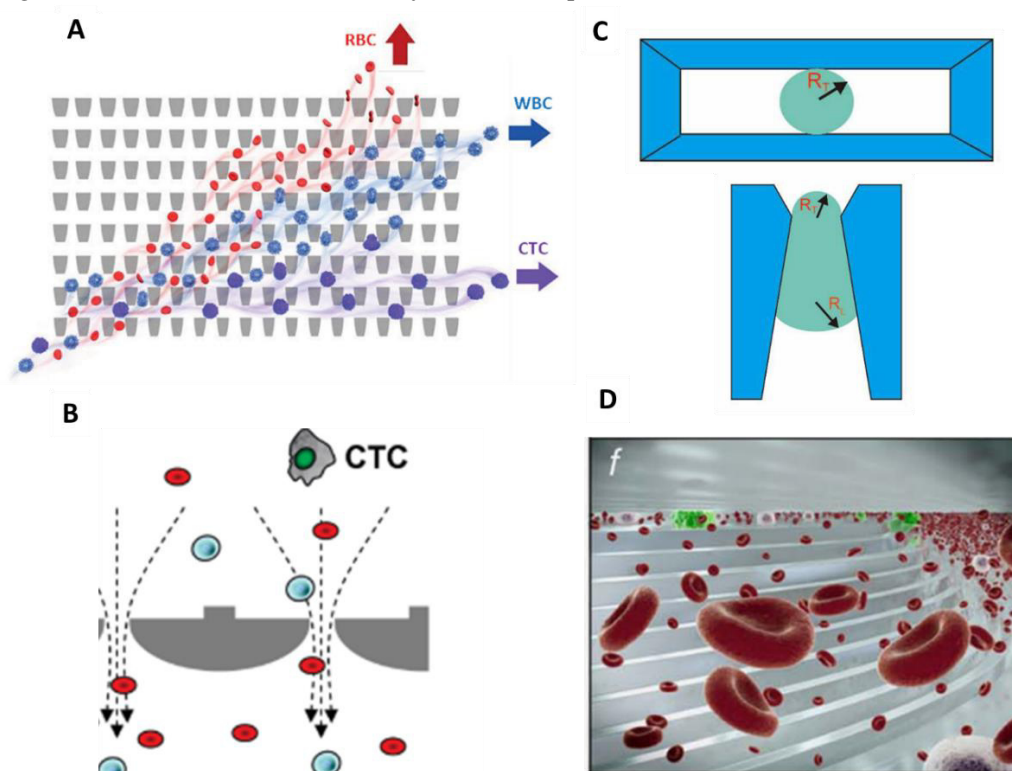


Figure 1.5: Microfiltration separation technologies. (A) Microfluidic ratchets for continuous CTC separation. Whole blood is infused from the bottom-left corner of the funnel array and cells travel in a zigzag diagonal path until reaching a blocking funnel row, where they proceed horizontally toward the outlet reservoirs. Reprinted from [26]. (B) Circular MCA filter. The size of the microcavities was optimized in order to trap CTCs on the microcavities while letting blood cells flow through the filter. Reprinted from [41]. (C) Pyramidal MCA filter. Top view and

vertical section of cell retention in a pyramidal MCA. R_T and R_L are respectively the radius of the curvature of the trailing and leading edges of the cell. Reprinted from [28]. **(D)** The Parsortix™ system. Blood is forced along a series of channels with a cross-sectional gap that gradually decreases the dimension of the fluid path and retains CTCs based on their deformable nature and size. Reprinted from [35].

Several filtration technologies were presented in microfluidic for CTC capture. Overall, these techniques offer a label-free isolation method of CTCs but raise additional concerns regarding the low sample capacity resulting from cell clogging, cell viability, and intermediate throughput. Hydrodynamic microfluidic devices can overcome obstacles associated with filtration methods.

A- Hydrodynamic separation methods

Further label-free separation methods using hydrodynamic forces were developed. Compared to microfiltration techniques, hydrodynamic isolation exerts a low fluid stress on cancer cells as they do not pass through physical obstacles. Besides, samples are processed at high flow rates to ensure the generation of relevant hydrodynamic forces, which leads to high-throughput sorting, while cancer cells can be retrieved for subsequent analysis. Some of the most promising hydrodynamic isolation strategies can be classified into: size-dependent deterministic flow pathways in pillar arrays (so-called deterministic lateral displacement), inertial migration of cells in a multi-flow straight microchannel, inertial focusing in spiral microfluidic channels (so-called dean flow fractionation), and microfluidic vortices generated in micro-reservoirs aside the channel.

Deterministic lateral displacement

The deterministic lateral displacement (DLD) utilizes an array of posts within micro-channels, where each post is laterally shifted at a set distance from the previous post. By optimizing the gap distance and post size, one can determine a critical size. Cells smaller than the critical size flow between the post gaps, while larger cells constantly collide with posts and are forced to move laterally following the post arrangement, achieving continuous CTC sorting. When DLD was firstly reported, circular shape of post was used, with a gap distance of 10 μm [49,50]. However, isolation of CTCs from cancer patient's bloods by the DLD method easily results in clogging. Thus, Louterback et al. replaced circular posts with triangular ones and increased the gap distance to 42 μm (Figure 1.6-A). They achieved >85% capture efficiency of spiked breast cancer cell lines from whole blood at high flow rate (600 mL/h) [51]. Recently, Au et al. fabricated a two-stage DLD device to isolate intact CTC clusters [52]. The first stage is a "standard" DLD step, designed as an array of 50 μm diameter micropillars with 63 μm gaps between each one to extract large clusters (>30 μm) from whole blood without clogging. Remaining clusters, cancer cells and blood are shuttled into the inlet of the second device stage, which uses asymmetrical pillars and height restrictions to extract smaller clusters based on the inherent asymmetric nature of multicellular aggregates. The novelty of this two-stage capture strategy rests on the enrichment of small and large clusters (100 cells) in two distinct outputs. These size enriched outputs may be useful to further investigate the influence of cluster size on the function, composition and potency of clusters. In comparison with small clusters, large clusters appear to harbor heterogeneous cells (e.g., fibroblasts, endothelial or tumor-infiltrated myeloid cells), increasing tumor cells viability within CTC clusters, and facilitating metastases formation [53].

Inertial focusing

Another hydrodynamic size separation technology utilizes inertial focusing to order cells based on their size into distinct equilibrium positions within a microchannel. This phenomenon relies on the balance of lift forces arising from the curvature of the velocity profile (the shear-gradient lift) and the interaction between cell and the channel wall (the wall-effect lift) for Reynold number of order of 1 or greater [54]. It results in a lateral ordering of cells according to their size: larger cells migrate to the channel centerline. Zhou et al. implemented a inertial-based separation in a simple straight channel for CTC isolation, from untreated whole blood in the first developed device [55], or from RBC-lysed blood in their more recent device [56]. Indeed, the considerable contamination from RBCs compromises its outcome. The device is designed as a multi-flow configuration in a straight microchannel of 150 μm in width and 50 μm in height, with two inputs and two outputs (Figure 1.6-B). Buffer (PBS) and sample are injected at the inner

inlet and outer inlet, respectively, forming three flow streams in the main channel. The buffer flow is sandwiched between the two sample flows in the middle of the channel, and, under the influence of inertial forces, larger target cells migrate laterally away from the sample streams into the buffer stream. The authors set 15 μm as the cut-off size to differentiate CTCs from WBCs, this threshold is largely determined by the channel length, fixed to 20 mm from previous work estimations [57]. With this cut-off size, this device is not suitable for the recovery of CTCs smaller than 15 μm . The performances of the device were first studied using spiked cancer cells at clinically relevant concentrations (10 cells per 5 mL and above) and a recovery rate superior to 93% was achieved, with high purity (> 87%). The clinical potential of the device was also demonstrated after successful CTC detection from 6 out of 8 NSCLC patients. Further applications were conducted with this device, including CTC cluster isolation and molecular characterization [58], as well as on-chip cell culture [59].

Other channel geometries are reported in inertial microfluidics for CTC separation and can generate secondary flows that create additional hydrodynamic effects beyond shear-gradient and wall-effect lift forces for improved separation. In a spiral microchannel, the channel curvature introduces two symmetrical counter-rotating flows, called Dean vortices, within the transverse plane of the channel. This Dean flow fractionation (DFF) separation method causes large cells (CTCs) to move toward the inner wall, because of the balance of inertial lift force and Dean drag force, while small cells (RBCs and WBCs) flow toward the outer wall. Cells with different size thus can be collected in two separate outlets. Spiral microchannels can provide inertial focusing but in a much smaller footprint [60]. The group of Lim has done a lot of work on the DFF isolation approach for CTC enrichment in recent years [61–65]. In 2013, they reported a single spiral microfluidics and achieved a cell line recovery rate of 85% at a flow rate of 3 mL/h [61] (Figure 1.6-C). Clinical validation was demonstrated with 100% sensitivity in samples from patients with metastatic lung cancer with a purity of 0.1–10%. They further improved the separation throughput to 12 mL/h while preserving purity by fabricating a multiplexed spiral chip which consists of a three-stack spiral chip and including an RBC lysis step [64]. This RBC lysis pretreatment step substantially removes blood contaminants and reduces the overall cell concentration, therefore limiting the undesired cell dispersion due to cell-cell interaction [65]. The clinical use of this new chip was demonstrated by detecting CTCs from 100% (10/10) of blood samples collected from patients with advanced-stage metastatic breast and lung cancers. With this device, ~10s to 10,000s of WBCs per ml of blood (median from 30 samples = 3,109 WBCs per ml) remain after spiral chip processing, this purity was sufficient for downstream sequencing or fluorescence in situ hybridization (FISH) analysis [62]. They had to compromise for either high CTC recovery or high WBC removal. This separation technique has been commercialized as ClearCell FX1® (Biolidics) and has recently been recognized through its ISO certifications (Europe: CE-marked for In Vitro Diagnostic, US FDA and China NMPA (National Medical Products Administration) Class I Medical Device registered).

Recently, Lin et al. created the Labyrinth device to address the challenge of focusing of smaller cells, such as WBCs, which remain unfocused in most DFF technologies. It was achieved by incorporating numerous sharp corners placed across the flow pattern to enhance Dean forces for the migration of smaller cells to their equilibrium positions [66]. It resulted in a high recovery rate of >90% with cell lines from breast, pancreatic, prostate, and lung cancers, with high purity (600 WBCs/mL) and at an extremely high flow rate of 150 mL/h. The combination of long loops and sharp corners lead to separated focusing of both large (CTCs) and small (WBCs) cells, while most spiral devices have to compromise for either low CTC recovery or low WBC removal. The device was successfully clinically validated in pancreatic and breast cancer samples with a sensitivity of 95% (72 out of 76).

Vortices

Finally, similarly to DFF, contraction-expansion arrays, whose cross-sections periodically widen and narrow, utilize Dean drag forces to differentiate the focusing positions of particles depending on their sizes. When cells flow through a series of expansion-contraction reservoirs within a microchannel, they experience multiple micro-vortices because of the shear gradient lift force in expansion reservoirs. Cells larger than a critical size are collected in the center of the vortices, therefore CTCs can be separated from other blood cells using this method. This Vortex technology was developed by the group of Di Carlo

and has been well described for CTC enrichment over the years [67–70] (Figure 1.6-D). Sollier et al. first developed and optimized the Vortex chip by varying several parameters such as channel dimensions and flow rates to achieve maximum trapping efficiency and purity [67]. Trapped CTCs in the vortices are released on-demand by lowering the washing buffer (PBS) flow rate. High blood volumes (10 mL volume samples of 20× diluted blood) were processed at high throughput (22.5 mL/h) and spiked cancer cells were concentrated to a small final volume of 300 μ L. They obtained a capture efficiency of 21% and a purity as high as 89%. They further optimized the platform into an advanced Vortex HT chip by replacing the long straight upstream focusing channel with serial 1000 μ m-spaced reservoirs to improve cell capture and increasing parallelization from 8 to 16 channels. They achieved improved capture efficiency (up to 83%), high purity (28.8 ± 23.6 WBCs/mL) and ultrahigh throughput (480 mL/h of whole blood) [68]. The Vortex HT chip enabled the coupling of in-flow label-free cell enumeration on bright field images with various standard assays downstream, such as cytology and cytogenetics [71]. They assessed the feasibility of characterizing the anaplastic lymphoma receptor tyrosine kinase (ALK) gene rearrangement by FISH in CTCs isolated from patients with NSCLC. Recent studies have demonstrated that detecting ALK rearrangements can be of clinical value for physicians to select more effective therapies [72]. Finally, they highlighted the phenotypical heterogeneity of CTCs from 22 patients with advanced prostate cancers [70]. A fraction of the collected cells (10.4%) did not express epithelial prostate markers while some instead expressed markers of epithelial–mesenchymal transition, revealing the importance of specific marker surface establishment. This Vortex technology has been commercialized as the VTX-1 Liquid Biopsy System by Vortex Biosciences.

Inertial-based sorting methods have therefore numerous advantages: high throughput, high recovery, and CTC retrieval for subsequent analysis. However, the main drawback of this method is the risk of CTC loss during the process, leading to a false-negative result. Reducing the cut-off size can help to minimize this loss with the tradeoff of the increased contamination of white blood cells, reducing purity. Hence, despite the straightforward and label-free separation methods based on CTC size, the non-specificity of the size criteria limits their efficacies. Indeed, the separation methods were optimized on cancer cell lines, but studies have shown the morphological heterogeneity of CTCs found in patient bloods, from round to oval shapes and with diameters varying from 4 to 30 μ m [73]. Besides, some WBCs have shown diameters as big as CTCs', leading to low purity. For all this reasons, other physical-based strategies were investigated to perform CTC isolation.

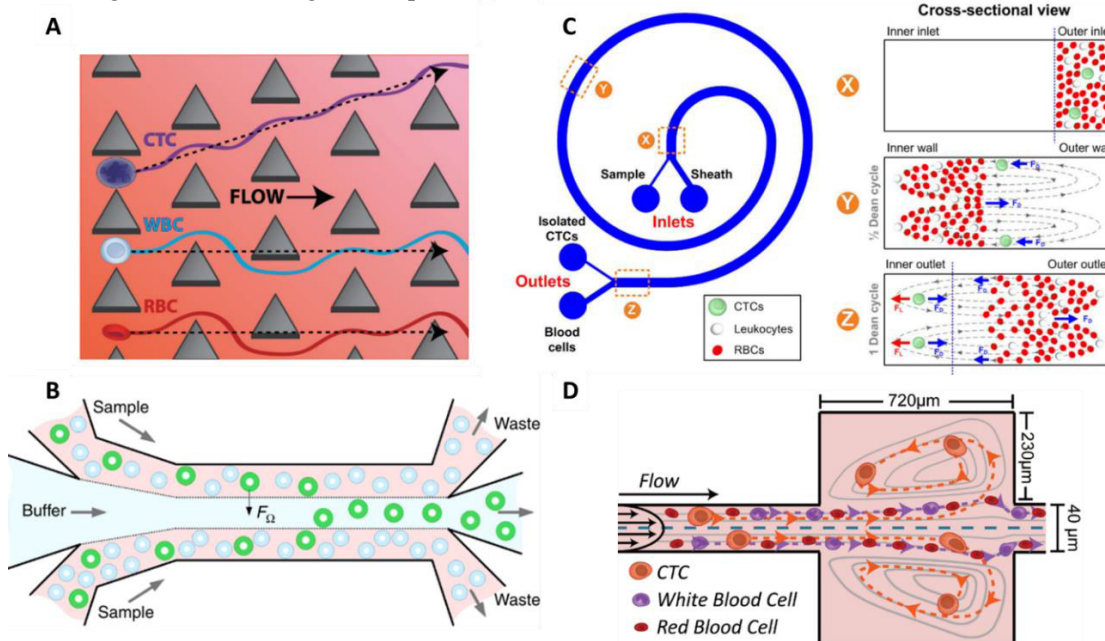


Figure 1.6: Hydrodynamic separation technologies. (A) Deterministic lateral displacement. An array of triangular posts with a gap distance of 42 μ m was integrated into a microfluidic channel for continuous CTC sorting. CTCs constantly collide with posts and are forced to move laterally following the post arrangement. Reprinted from [51]. (B) Inertial focusing in a straight channel. The multi-flow configuration leads to the lateral migration of CTCs from

the sample streams into the buffer stream due to the predominancy of the rotation-induced lift force ($F\Omega$). Reprinted from [56]. **(C)** Dean flow fractionation. CTCs move toward the inner wall of the spiral microchannel, because of the balance of inertial lift force and Dean drag force, while small cells (RBCs and WBCs) flow toward the outer wall. Reprinted from [61]. **(D)** Micro-vortices. Cells flowing through a series of expansion-contraction reservoirs experience multiple micro-vortices because of the shear gradient lift force in expansion reservoirs. CTCs are collected in the center of the vortices. Reprinted from [68].

A- Dielectrophoretic separation methods

Besides size-based and deformability-based separation methods, dielectrophoresis (DEP) utilizes electrophysical properties of CTCs to isolate them under a nonuniform electric field. When applying an AC voltage across two electrodes of different sizes, the non-uniform distribution of the charges generates a net DEP force will move the cell either towards the higher electric field gradient region (so called “positive DEP”), or in the opposite direction, towards the lower electric field gradient region (negative DEP). At a given electric field frequency (so-called crossover frequency) and depending on the electrical conductivity of the cells and its suspending medium, cell may experience either positive DEP (higher cell conductivity) or negative DEP (higher medium conductivity). Generally, viable cells express negative DEP at low frequencies and positive DEP at high frequencies. In particular, cells with different membrane surface area exhibit distinct DEP frequency responses. As previously mentioned, CTCs are larger, but they also present a 60% greater surface area than a WBC of the same size [74], which gives them larger capacitance per unit area and enables their controlled motion in a DEP-based device.

Two DEP-based devices were commercialized ten years ago for CTC isolation, the DEPArray™ (Silicon Biosystems) for single CTC DEP trapping [75], and the ApoStream™ (Precision for Medicine, Inc.) for continuous CTC enrichment [76]. The DEPArray™ device consists of an array of individually controllable micro-electrodes which, when the electric field created above a subset of electrodes is in counter-phase with the electric field of adjacent electrodes, generate up to tens of thousands “DEP cages”. Each DEP cage is able to capture a CTC in stable levitation, avoiding contacts between the cells and the surface. DEPArray™ is frequently used as a downstream single-CTC isolation technique using the recovered CTC samples from CellSearch™ system to perform subsequent molecular characterizations [77]. The Apostream™ system integrates interdigitated electrodes located on the floor of the chamber above which cells are flowing (Figure 1.7-A). The sample is injected at a low flow rate into the bottom of the flow chamber to minimize cell levitation and to ensure cells stay within the effective DEP field [78]. By applying an AC voltage signal at a frequency in between the crossover frequency of cancer cells and WBCs, cancer cells are attracted by positive DEP forces towards the electrode plane and collected in the bottom collection output, while WBCs are repelled by negative DEP and levitate towards the top waste output. They achieved a >70% recovery efficiency for both epithelial and mesenchymal cell lines, with a purity of approximatively 0.3% (~ 10 000 WBCs/mL) at a flow rate of 1 mL/h. The device has been successfully employed in clinical samples for the isolation of CTCs from epithelial and non-epithelial cancer types [79–81].

Other DEP strategies were reported for CTC isolation, including DEP field flow fractionation (DEP-FFF) and optically-induced-dielectrophoresis (ODEP) but they suffer from relatively low throughput in the range of 0.01–1.0 mL/h [82–84]. Recently, Li et al. fabricated arrays of wireless bipolar electrodes (BPE) generating AC field across channel walls and attracting CTCs towards micropockets located along the microchannel walls [85]. These micropockets aligned to the BPE tips provide discrete capture sites with defined volume, thus enabling single-cell capture (Figure 1.7-B). They showed that over 80% of pockets captured individual MDA cells at a flow rate of 0.1 mL/h. In addition, they demonstrated the processing of 7.5 mL standard blood volume within their parallel-channel device and removed the need for wires. Further developments are investigated to improve the throughput, by increasing the device footprint and reducing DEP buffer volume.

Thus, DEP-based separation methods provide high recovery rates, but their implementation can be challenging. Indeed, they require specific electrode geometries and controlled microfabrication. In addition, DEP separation systems rely on cells polarization differences, therefore any cell exhibiting

damaged membrane may influence isolation efficiencies. The use of specific buffers such as sucrose can induce osmotic stress and cause leakage of cytosolic ions over time [74]. Finally, the high conductivity of blood can modify the separation performances and therefore limiting efficacy and purity.

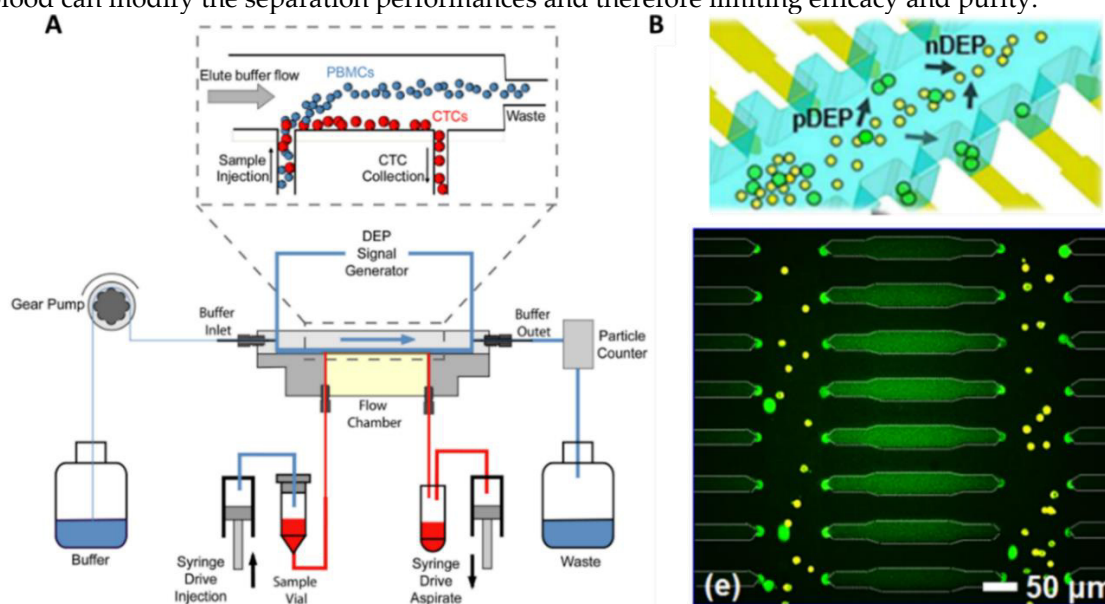


Figure 1.7: Dielectrophoretic separation technologies. **(A)** The ApoStream™ system. The flow chamber applies an AC electric field to the sample at a frequency in between the crossover frequency of CTCs and WBCs to pull the former towards the chamber floor (positive DEP) and repel the latter (negative DEP). Reprinted from [76]. **(B)** Wireless bipolar electrode (BPE) array. Capacitive charging of the electrical double layer at the BPE tips transmits an AC field across the device and provides sufficient electric field gradients to exert DEP trapping force. Cancer cells (in green) experience positive DEP and are trapped at the electric field maxima around the BPE tips (single-cell capture), while other cells (in yellow) undergo negative DEP and remain in fluid flow. Reprinted from [85].

B- Summary of physical-based separation methods

The advantages and limitations of each presented separation method can be found in Table 1-1. The performances of reported technologies are then summarized in Table 1-2 and Table 1-3, for cell line studies and clinical studies, respectively.

Table 1-1: Advantages and limitations of physical-based separation methods for CTC isolation.

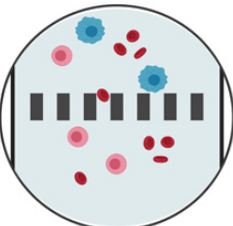
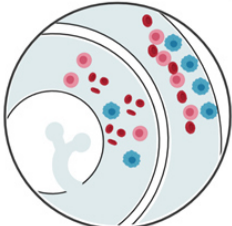
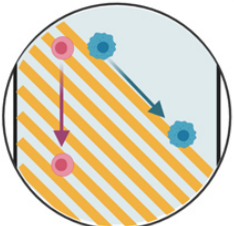
Separation method	 <p data-bbox="571 427 708 454">Microfiltration</p>	 <p data-bbox="815 427 984 454">Hydrodynamics</p>	 <p data-bbox="1070 427 1240 454">Dielectrophoresis</p>
Separation criteria	Size, deformability	Size	Size and dielectric properties
Pros	Easy approach, high throughput, label free	High throughput, label free, CTC recovery	Label free, CTC recovery
Cons	Risk of clogging, low purity, challenging downstream analysis	Low purity	Low throughput, separation is limited over time, specific cell type, electric field frequency and buffers are required

Table 1-2: Performances of physical-based separation methods in cell line studies.

Separation method	Technology	Selection criteria	Throughput	Sample composition	Recovery	Viability	Purity	WBC Depletion	Enrichment factor	Ref
Microfiltration	Micro-ellipse filters	Size (5-18 μm)	1 mL/h	MCF-7, HepG2, and Hela cells in 1 mL PBS supplemented w/ 1% BSA and 0.05% tween-20	>90%	90%	--	--	--	[37]
Microfiltration	Microfluidic ratchets	Size (6 μm), deformability	1 mL/h	UM-UC13 cells in 5 mL whole blood	77-90% (various cell lines)	99%	--	--	8500	[26]
Microfiltration	Rectangular MCA	Size (8 μm)	12 mL/h	NCI-H358, NCI-H69, and NCI-H82 cells in 1mL whole blood	80-90%	98%	76-78%	--	7000	[42]
Microfiltration	Pyramidal MCA	Size (8 μm)	6 mL/h	MCF-7, SW620, and Hela cells in 1 mL whole blood	76-84%	--	--	99.9985%	--	[43]
Microfiltration	Parsortix™	Size (10 μm)	10 mL/h	PANC-1, PC3, A375, A549 and T24 cells in 2 mL whole blood	42-70%*	99%	~60%	~99.96%	--	[35]
Hydrodynamics (DLD)	Triangular posts	Size (7 μm)	600 mL/h	MDAMB231, PC3, and MCF10A cells in 1 mL diluted blood	>85%	$\geq 95\%$	--	--	--	[51]
Hydrodynamics (DLD)	Asymmetric pillars	Size (>30 μm , CTC clusters)	0.5 mL/h	<i>Ex-vivo</i> cultured breast cancer	$98.7 \pm 2.4\%$ (large clusters)	$91.7 \pm 2.5\%$	--	1.58 ± 0.13 log (stage 1) and 2.48	--	[52]

				clusters in whole blood	$65.5 \pm 6.5\%$ (small clusters)			$\pm 0.22 \log$ (stage 2)		
Hydrodynamics (Inertial migration)	Multi-flow straight channel	Size (15 μm)	1.2 mL/h	HCC827 and H460 in 5 mL diluted blood	>93%	--	88.7%	--	--	[56]
Hydrodynamics (DFF)	ClearCell	Size (14 μm), deformability	36 mL/h	T24, MCF-7, and MDA-MB-231 cells in lysed and 2 \times concentrated blood in PBS	$80.3 \pm 7.9\%$	87.5%	--	$\sim 99.99\%$ 4 log	--	[64], [65]
Hydrodynamics (DFF)	Labyrinth (spiral channel w/ sharp corners)	Size, deformability	150 mL/h	MCF-7, PANC-1, PC-3, and H1650 cells in buffer or whole blood	>90%	High	--	>4 log	--	[66]
Hydrodynamics (Microvortices)	Vortex HT	Size (13 μm), deformability	480 mL/h (10 \times diluted blood) or 48 mL/h (whole blood)	MCF-7 cells in 4 mL 10 \times diluted blood	84%	$83.9 \pm 4.0\%$	>80%	4-5 log	--	[68]
Dielectrophoresis	Apostream™ (DEP-FFF)	Size and dielectric properties	~ 1 mL/h	SKOV3 and MDA-MB-231 cells in 1 mL buffer	$68.3 \pm 10.4\%$	97.6%	0.3%	$99.33 \pm 0.56\%$	--	[76]
Dielectrophoresis	ODEP	Size and dielectric properties	24 $\mu\text{L/h}$	PC-3 cells in sucrose solution	$54 \pm 7\%$	--	$94.9 \pm 0.3\%$	--	--	[83]

*With the Parsortix™, captured cancer cells could be harvested from the device for further downstream analyses. Harvest efficiency ranged from 27% to 40%.

Table 1-3: Performances of physical-based separation methods in clinical studies.

Separation method	Technology	Blood sample volume	Cancer type	Number of CTCs	Detection sensitivity	Remaining WBCs/mL	Downstream analysis	Ref
Microfiltration	Micro-ellipse filters	2-3 mL	Metastatic (M)-breast cancer (n=4), Colon (n=1), NSCLC (n=12)	1-10/2-3 mL, 6-10/2-3 mL, 1->20/2-3 mL	100% (17/17)	--	Immunofluorescence staining and enumeration	[37]
Microfiltration	Microfluidic ratchets	2 mL	M-castrate-resistant prostate cancer (n=20)	Median 178/7.5 mL	95% (19/20)	--	Immunofluorescence staining and enumeration	[26]
Microfiltration	Rectangular MCA	2-4 mL	SCLC (n=16)	1-73/mL (Median 2/mL)	100% (16/16)	854 ± 306 (Median)	Immunofluorescence staining and enumeration	[42]
Microfiltration	Pyramidal MCA	1-3 mL	Breast (n=3), Lung (n=3)	23-86/mL, 0-48/mL	83% (5/6)	396-3,845	Immunofluorescence staining and enumeration	[43]
Microfiltration	Parsortix™	4 mL	Breast (n=10), Colon (n=10), Lung (n=6)	0-3/mL, 0-1/mL, 0-7/mL	38% (10/26)	--	Immunofluorescence staining and enumeration, molecular characterization (RT-PCR and array-based comparative genomic hybridization)	[35]

Hydrodynamics (Inertial focusing)	Multi-flow straight channel	2 mL	M-NSCLC (n=8)	Median 12/mL	75% (6/8)	--	Immunofluorescence staining and enumeration	[56]
Hydrodynamics (DFF)	ClearCell	7.5 mL	Lung (n=15), Breast (n=15)	12-549/mL (Median 97), 12-322/mL (Median 44)	100% (30/30)	9-29,824 (Median 3,109)	Immunofluorescence staining and enumeration, FISH, ICE-COLD PCR, Sanger sequencing, Cell culture	[65]
Hydrodynamics (DFF)	Labyrinth (spiral channel w/ sharp corners)	7.5 mL	Pancreatic (n=20), M-Breast (n=56)	0-63/mL (Mean 51.6 ± 25.5), 0-21.7/mL (Mean 5.4 ± 4.6)	95% (72/76)	663 ± 647	Immunofluorescence staining and enumeration, Single-cell multiplex gene profiling (multiplex qRT- PCR)	[66]
Hydrodynamics (Microvortices)	Vortex HT	~8 mL	M-Breast (n=22), M-Lung (n=15)	0.75-23.25/mL (Mean 5.4), 0.5-24.2/mL (Mean 5.3)	84% (31/37)	187 ± 164	Immunofluorescence staining and enumeration, Single-cell RT-PCR, Cell culture, Pharmacological studies, Single-cell Western blotting	[68]
Dielectrophoresis	Apostream™	7.5 mL	M-NSCLC adenocarcinoma (n = 14), Breast (n = 20), M-ovarian (n = 6), Squamous lung (n=6)	47-216/7.5 mL (Mean 89), 0-36/7.5 mL (Mean 9), 0-5/7.5 mL (Mean 2), 0-4/7.5 mL (Mean 1)	87% (40/46)	--	Immunofluorescence staining and enumeration, Phenotypic analysis by laser scanning cytometry	[79]

1.2.2. Biological-based separation methods

The isolation of CTCs from other blood cells can also be achieved by exploiting biological properties of CTCs, such as their surface marker expression. These methods rely on the high specificity of the bonding between antibodies and expressed antigens in targeted cells. CTC isolation can be performed either by positive selection, where CTCs are collected as the target cell population, or negative selection, with WBCs as targeted cells. Biological-based separation methods can be categorized into either surface affinity approach through microchannel functionalization or immunomagnetic approach using functionalized magnetic particles (Figure 1.8).

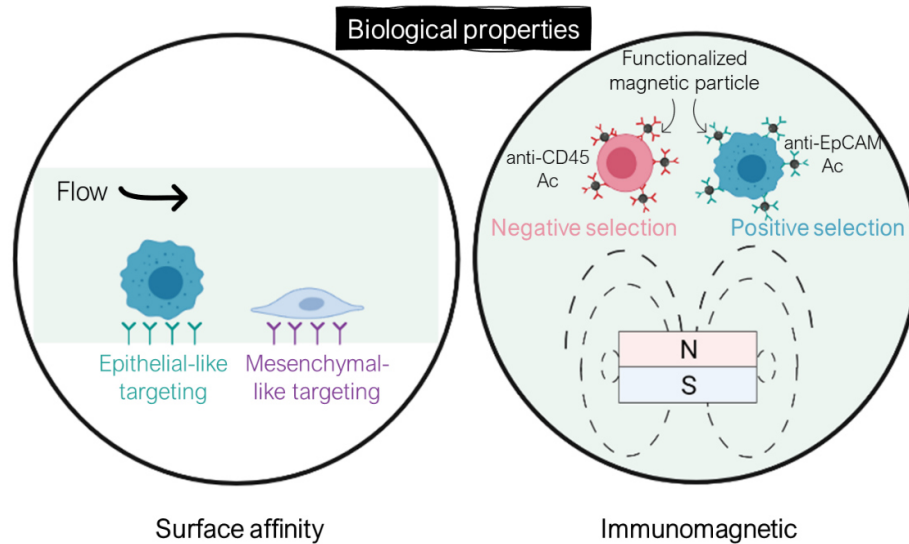


Figure 1.8: CTC enrichment technologies based on their biological properties via antigen-antibody recognition through either surface functionalization or immunomagnetic separation using magnetic particles. Created with BioRender.com.

A- Surface affinity separation

The most notable geometrically patterned microfluidic device with antibody-coated surfaces is the CTC-Chip, reported by Toner's group in 2007 [86]. The device consists of an array of 78 000 anti-EpCAM-coated micropillars (100 μm in diameter, spaced by 50 μm) (Figure 1.9-A). The array was arranged such that every three rows form an equilateral triangular to favor collisions between CTCs and functionalized micropillar surfaces. They obtained recovery efficiencies comprised between 74% and 80% for various cancer lines at a flow rate of 1 mL/h. The CTC-chip was successfully tested for clinical samples with 99% sensitivity (115 out of 116) in the blood of patients with metastatic lung, prostate, pancreatic, breast and colon cancer, with a purity of 50%. In addition, the chip enabled CTC isolation in 7/7 patients with early-stage prostate cancer. Toner's group later reported an enhanced CTC isolation platform, the herringbone-chip (or ^{HB}CTC-Chip), integrating herringbone grooves on the roof of the anti-EpCAM-coated microchannel [87]. These structures generate micro-vortices which enhance CTC capture through chaotic mixing and increased contact time between flowing cells and the antibody-functionalized surface. In comparison with the CTC-Chip, the ^{HB}CTC-Chip allowed for higher sample throughput and increased CTC capture efficiency and purity. A capture efficiency of 92% on spiked cancer cells was achieved at 1 mL/h, with a 5% better purity. Clinical use of ^{HB}CTC-Chip was further established and enabled the determination of CTC signaling pathways by RNA sequencing [88], identification of dynamic changes in CTC phenotypes [89], and investigation of the metastatic role of CTC clusters [46].

The use of nanostructured substrates, such as silicon nanopillars (NanoVelcro Chip) [90] (Figure 1.9-B) or graphene nanosheets (GO Chip) [91] (Figure 1.9-C), was also reported in microsystems to enhance CTC isolation sensitivity as nanomaterials offer high surface area-to-volume ratio and similar size to cellular surface components (e.g., microvilli and filopodia) [92]. However, the irreversible capture of

CTCs on these nanostructures significantly limits downstream analyses and subsequent cell culture. Various approaches have been investigated to release CTCs after their isolation, using either thermosensitive polymers [93–95] or enzymatic degradation [96]. Nevertheless, thermoresponsive substrates require additional equipment to precisely control the temperature while the use of enzymes such as alginate lyase may compromise the viability of CTCs due to the over exposure to the degraded film itself and the enzymatic solution. Recently, Stott's group engineered the surface of the ^{HB}CTC-Chip with a gold nanoparticle coating and utilized a thiolated ligand-exchange reaction to isolate and release CTCs from whole blood [97]. Indeed, metal–thiol interactions can be disrupted in the presence of excess thiol molecules (i.e., glutathione), leading to an exchange between the original ligands with immobilized antibodies and the thiol molecules, resulting in the release of cancer cells from the surface (Figure 1.9-D). This strategy takes also advantage from the nanoroughened surface of the nanoparticle (NP) assemblies to increase contact between CTCs and immobilized antibodies, therefore enhancing capture efficiency. This new NP-functionalized chip achieved a capture efficiency as high as 99% for epithelial cancer lines with a lower nonspecific binding compared to their previous ^{HB}CTC-Chip (35% decrease). For non-epithelial cancer lines, a cocktail of antibodies had to be used within the chip to increase capture efficiency, from 16% to >90%. In addition, the chip successfully released 90% of the captured cells that were further cultured for 5 days with a preserved viability (78-87%).

Similarly, Tseng's group reported the tuning of their NanoVelcro Chip with a phenylboronic acid (PBA)-grafted PEDOT nanosubstrate to release captured CTCs upon exposure to a glycan molecule (i.e., sorbitol) [98], which has a stronger affinity to PBA. CTCs were isolated from the blood with patients with prostate cancer (PCa) and purified by this PEDOT NanoVelcro chip. The chip provided well-preserved RNA transcripts for the analysis of the expression level of several PCa-specific RNA biomarkers which may provide clinical insights into the disease.

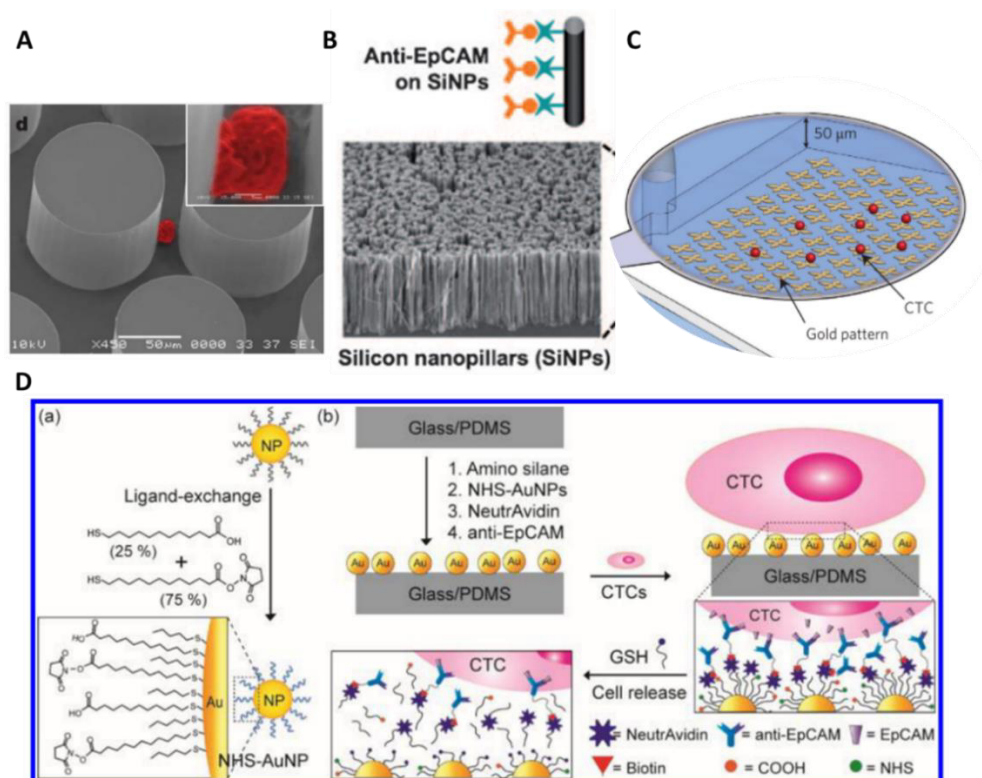


Figure 1.9: Surface affinity-based separation technologies. **(A)** CTC-Chip. CTCs are trapped on micropillars functionalized with anti-EpCAM antibodies. Reprinted from [86]. **(B)** NanoVelcro Chip. Silicon nanopillars are coated with anti-EpCAM antibodies. This strategy takes advantage from the nanoroughened surface of the NP assemblies to increase contact between CTCs and immobilized antibodies. Reprinted from [90]. **(C)** GO Chip. Graphene oxide nanosheets are adsorbed onto the gold pattern and functionalized with anti-EpCAM antibodies. Reprinted from [91]. **(D)** Tuned ^{HB}CTC-Chip for CTC release. The chip surface was coated with thiol-functionalized gold nanoparticles (AuNPs). In the presence of excess thiol molecules (GSH), the original thiol ligands with

immobilized antibodies on the surface of the AuNPs can be exchanged with GSH molecules. Based on this thiol exchange reactions, captured CTCs can be detached from the chip surface. Reprinted from [97].

The main advantage of this method based on antibody-antigen reaction within functionalized microfluidic systems is the high sensitivity for a given cellular type with a preserved viability. Nonetheless, lower throughput is achieved compared to physical-based separation approaches. In addition, special attention should be paid to enable the collection of captured CTCs. The main drawback of this method remains that, most of the time, a unique antigen is targeted (usually EpCAM), therefore limiting the recovery of heterogeneous CTCs.

The performances of reported surface affinity-based separation technologies are summarized in Table 1-4 and Table 1-5, for cell line studies and clinical studies, respectively.

Table 1-4: Performances of surface affinity-based separation methods in cell line studies.

Separation method	Technology	Selection criteria	Throughput	Sample composition	Recovery	Viability	Purity	WBC Depletion	Enrichment factor	Ref
Surface affinity	^{HB} CTC-Chip	EpCAM	1.2 mL/h	PC-3 cells in whole blood	91.8 ± 5.2%	95% ± 0.6%	14.0 ± 0.1%	--	--	[87]
Surface affinity	NanoVelcro Chip	EpCAM	1 mL/h	MCF-7, PC-3, and T24 cells in 1 mL whole blood	>95%	--	--	--	--	[90]
Surface affinity	NP- ^{HB} CTC-Chip	EpCAM/HER2/EGFR	1 mL/h	PC3 and MDA-MB-231 cells in 3 mL whole blood	>90%	Mean 82.5%	Non-specific binding: ~3,000 WBCs/3 mL	--	--	[97]
Surface affinity	PEDOT NanoVelcro Chip	EpCAM	130 min incubation (capture + release time)	LNCaP, PC3, and 22Rv1 cells in whole blood	72.5 ± 3.0%* 75.2 ± 3.2%, 67.8 ± 1.7%	95% after release	46% after release	99.98% after release	4300	[98]

*With the PEDOT NanoVelcro Chip, captured LNCaP cells could be released with 71% efficiency.

Table 1-5: Performances of surface affinity-based separation methods in clinical studies.

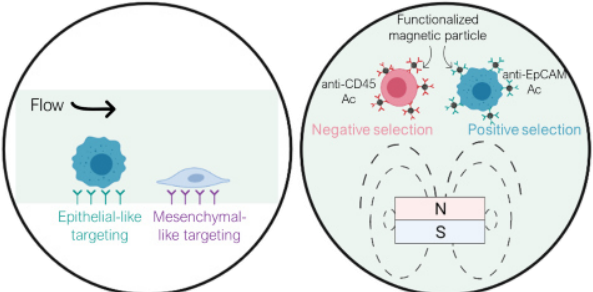
Separation method	Technology	Blood sample volume	Cancer type	Number of CTCs	Detection sensitivity	Remaining WBCs/mL	Downstream analysis	Ref
Surface affinity	^{HB} CTC-Chip	4 mL	M-prostate (n=15) M-pancreatic (n=15)	12-3,167/mL (Median 63) 1-57/mL (Median 11)	93% (14/15) --	-- 165-11190	Immunofluorescence staining and enumeration, molecular characterization (RT-PCR, single-molecule RNA sequencing)	[87], [88]
Surface affinity	NanoVelcro Chip	1 mL	Prostate (n=26)	0-33/mL	81% (21/26)	--	Immunofluorescence staining and enumeration	[90]
Surface affinity	NP- ^{HB} CTC-Chip	3-4 mL	M-breast (n=4)	6-12/mL (Median 7.4)	100% (4/4)	--	Immunofluorescence staining and enumeration, Next generation RNA sequencing	[97]
Surface affinity	PEDOT NanoVelcro Chip	--	Prostate (n=17)	1-7/mL	100% (17/17)	--	Immunofluorescence staining and enumeration, RT-qPCR	[98]

A- Immunomagnetic separation

The immunomagnetic separation relies on the conjugation of magnetic particles to cells via antigen-antibody recognition in order to confer them magnetic properties. The magnetic particles can either target CTCs (positive selection) or WBCs (negative selection). The benefit of the negative selection over the positive one is the ability to collect all CTCs regardless their surface marker expression. Nonetheless, given the high concentration of WBCs in blood, their depletion is more challenging.

The immunomagnetic separation requires therefore a labeling step to achieve high sensitivity and specificity, due to the antigen-antibody reaction and magnetic contrast supplied by conjugated magnetic particles, respectively. Besides, in comparison with the surface affinity approach, the immunomagnetic separation provides higher throughput and is compatible with downstream analysis. The advantages and limitations of each separation method can be found in Table 1-6. The immunomagnetic separation relies on magnetophoresis, which refers to the motion of magnetic particles or magnetically labelled cells when subjected to a non-uniform magnetic field. This thesis is part of the magnetophoresis-based separation and this strategy which will be further described in the next part (theory, CTC isolation examples, etc.).

Table 1-6: Advantages and limitations of biological-based separation methods for CTC isolation.

Separation method		
	Surface affinity	Immunomagnetic
Separation criteria	Surface marker expression of CTCs	Magnetic properties of nano/micro-particles and surface marker expression of WBCs or CTCs
Pros	High sensitivity, specificity, and purity	High sensitivity, specificity, and purity, high throughput, CTC recovery
Cons	Low throughput and challenging downstream analysis	Labeling step is required

In a nutshell, biological-based separation methods (surface affinity and immunomagnetic separation), which are dependent on surface marker expression, lead to high sensitivity and specificity, and therefore higher purity in comparison with physical-based separation methods. Physical-based separation methods have the advantage of being label-free and providing significantly high throughput, but their low purity limits downstream analysis. Thus, the immunomagnetic separation approach presents a good compromise between throughput, purity, sensitivity and downstream analysis.

2. Magnetophoresis-based microfluidics

2.1. Theory and phenomenon

2.1.1. Magnetism fundamentals for magnetophoresis

As mentioned above, the manipulation of cells requires external forces, such as acoustic [99], electrical [100], or optical [101] actuations. The suitability of magnetic forces for this purpose has been well established [102–107]. Magnetic force-based manipulation relies on magnetophoresis, which refers to the motion of magnetic particles or magnetically labelled cells when subjected to a non-uniform magnetic field. Magnetophoresis [106,108–110] has been demonstrated as an efficient way to trap and separate biological entities, such as DNA [111–113], proteins [114–116], beads [117], and cells [107,118–121], including deoxygenated RBCs [122–124]. This strategy benefits from several advantages compared to its alternatives: (i) the contactless manipulation, which makes this technique nondestructive for biological samples and preserves cell viability/integrity; (ii) the specificity, since magnetic fields increase the magnetic contrast of non-magnetic objects, either using magnetic labels or with the aid of magnetic fluids [125], (iii) the low sensitivity to medium parameters, such as surface charges, ionic concentration, pH and temperature; and (iv) the tunability, as the magnetic force depends on the particle size, the magnetic properties of the target and surrounding medium, as well as the gradient of the magnetic field. The magnetic force can be attractive (positive magnetophoresis) or repulsive (negative magnetophoresis) whether its orientation is parallel or in the opposite direction to the magnetic field gradient, respectively; which depends on the apparent magnetic susceptibility of the target particle in its medium. Positive magnetophoresis is the most widespread manipulation method and occurs when magnetic objects (particles or labeled cells) are suspended in a diamagnetic fluid. On the contrary, negative magnetophoresis is a label-free technique, where diamagnetic objects are suspended in a magnetic fluid (paramagnetic salt solution or ferrofluid). However, the lesser visualization and viability of cells in ferrofluids can be a limitation to the widespread use of this approach in biomedical applications [106]. Both methods rely on the generation of high magnetic field gradients which can be controlled by various types of magnetic field sources.

The magnetic response of materials, including the manipulated object, its surrounding medium, and the magnetic field source, can be classified based on their magnetic susceptibility χ as being diamagnetics ($\chi < 0$), paramagnetics ($\chi > 0$), ferromagnetics ($\chi \gg 0$), or superparamagnetics [109]. The magnetic susceptibility establishes the relationship between the magnetic field H and the magnetization M , as $M = \chi H$. The magnetic response of these materials to an applied field is given Figure 1.10.

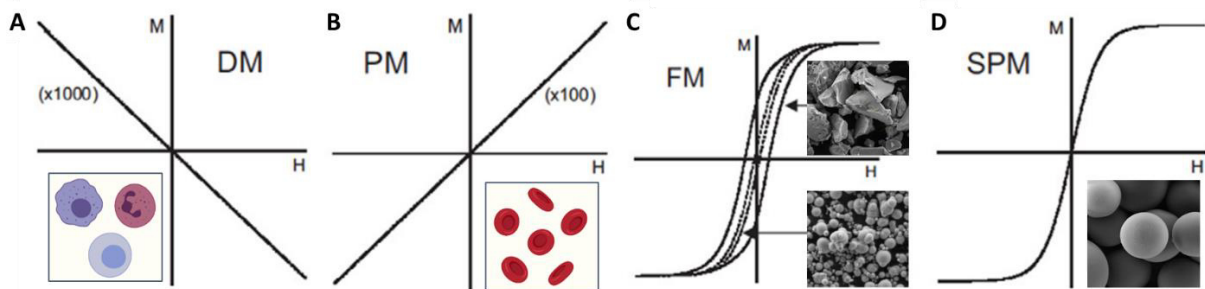


Figure 1.10: M-H curves of different types of magnetic materials with inset of material examples. (A) Diamagnetics with inset of various cell types, (B) paramagnetics with inset of deoxygenated red blood cells, (C) ferromagnetics with insets SEM images of NdFeB (top) and Fe-C (bottom) particles used in thesis, and (D) superparamagnetics with inset SEM images of superparamagnetic beads used in this thesis. Adapted from [126].

Diamagnetics

Diamagnetic materials are composed of atoms that do not have permanent net magnetic moment. It is the case for atoms having all their electrons paired, creating a closed electronic shell configuration within the atoms comprising the material. When subjected to an applied magnetic field, the diamagnetic substance develops a negative moment, proportional to the field. The susceptibility of diamagnetic materials is negative and very weak, on the order of -10^{-5} to -10^{-6} [110]. Diamagnetism is an important

consideration as most biological objects are usually formed from organic compounds or structures with closed-shell electronic configurations.

Paramagnetics

Paramagnetic materials are composed of atoms exhibiting a net magnetic moment as they contain unpaired electrons in their electronic structure. These unpaired electrons hold electronic magnetic moments or 'spins' that do not interact with each other. In the absence of external magnetic field, the atomic magnetic moments point in random directions leading to no net magnetic moment. When a magnetic field is applied, the moments tend to align along the direction of the external magnetic field. The paramagnetic effect is reversible when the magnetic field is removed. The susceptibility of paramagnetic materials is positive and small, on the order of 10^{-4} to 10^{-5} [110]. Examples of paramagnetic materials are oxygen, deoxygenated RBCs, magnetotactic bacteria, and manganese (II) chloride (MnCl_2).

Ferromagnetics

Ferromagnetic materials are characterized by the capacity to exhibit a spontaneous magnetic moment in the absence of a magnetic field. In particular, the magnetic moments held by unpaired electrons provide interatomic magnetic coupling: two adjacent magnetic moments are coupled parallel, and accounts for the volume magnetization of the material. Unlike paramagnetic materials, spins remain aligned in the absence of a magnetic field to produce ferromagnetism. Ferromagnetism is temperature-dependent, the material's magnetic moment decreases with increasing temperature, and the ferromagnetic order vanishes at the Curie temperature [126].

Ferromagnetic materials can be characterized by their magnetic anisotropy which is the directional dependence of the material's magnetic moment [110]. Such anisotropy confers preferred orientations of the atomic moments in space (referred to as easy magnetization axes). Magnetic anisotropy originates from various sources, including magnetocrystalline anisotropy and shape anisotropy [127]. Ferromagnetics can therefore be divided in two types: soft ferromagnetics and hard ferromagnetics.

Soft ferromagnetics (Ni, Fe, Fe-Ni alloys...), characterized by a small magnetic anisotropy, exhibit the properties of high magnetic susceptibility, low coercive field (the applied field needed to bring the net magnetization to zero, H_c), and reversible magnetization (no hysteresis). Through their high magnetic susceptibility, soft ferromagnets concentrate the magnetic field lines from an external field, resulting in high magnetic field gradients. In the absence of external fields, the material magnetization is null. Magnetically soft materials are particularly suitable for guiding or screening magnetic fields.

Hard ferromagnetics ($\text{L}_{10}\text{-FePt}$, $\text{Nd}_2\text{Fe}_{14}\text{B}$...), in contrast, present a high uniaxial magnetic anisotropy, their magnetization can significantly remain when the applied field is removed. This net magnetization when the field is brought to zero is called the remanent magnetization (M_R). Thus, in the absence of external fields, magnetically hard materials can generate a magnetic field, which make them suitable for the fabrication of permanent magnets.

Characteristic magnetization curves for hard and soft ferromagnets are illustrated in Figure 1.11.

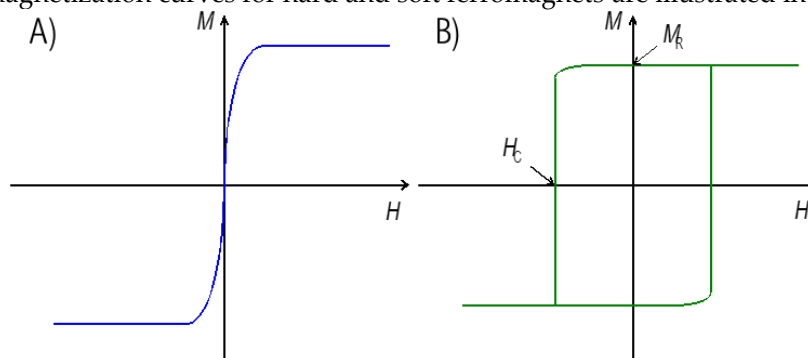


Figure 1.11: Magnetization curves of soft vs hard ferromagnetic materials. From [110].

Superparamagnetics

Superparamagnetic materials refer to nano-sized ferromagnetic materials (diameters of 3-50 nm, depending on the materials) which are single domain, i.e., composed of a single magnetic domain. Their net magnetization can randomly flip direction under the influence of temperature [126]. Superparamagnetic materials present a paramagnetic-like behavior, but with a giant magnetic moment, hence the denomination “superparamagnetism”. The magnetization increases linearly in response to a moderate applied magnetic field and saturates at high fields. They exhibit a large ferromagnetic response in the presence of a magnetic field, but unlike ferromagnetic materials, do not retain any net magnetization once the external field has been removed. This property can be very useful in cell sorting applications requiring a magnetic labeling as superparamagnetic particle magnetic behavior can be ‘turned on and off’ by a magnetic field.

The nature of the magnetic materials permits to establish their magnetophoretic behavior under the application of an external magnetic field. The study of the governing forces should also be studied in order to predict their motion in a microfluidic system.

2.1.2. Governing forces in magnetic-based microfluidic device

Magnetophoresis, which, as introduced earlier, is the motion of an object under the influence of an external magnetic field, and coupled with microfluidic technology, can be used for sorting applications, in particular for trapping of magnetic particles or magnetically labeled cells. When the latter flow in a microfluidic channel, various forces govern their transport within the magnetophoretic system, including: (i) the magnetic force, (ii) the fluidic drag force, (iii) the gravitational force, (iv) the buoyancy force, as well as (v) thermal kinetic energy, and finally (vi) forces resulting from interparticle interactions, particle-channel wall interactions and particle-fluid interactions. The main competitive forces are illustrated in Figure 1.12. Each of these forces will be further detailed below.

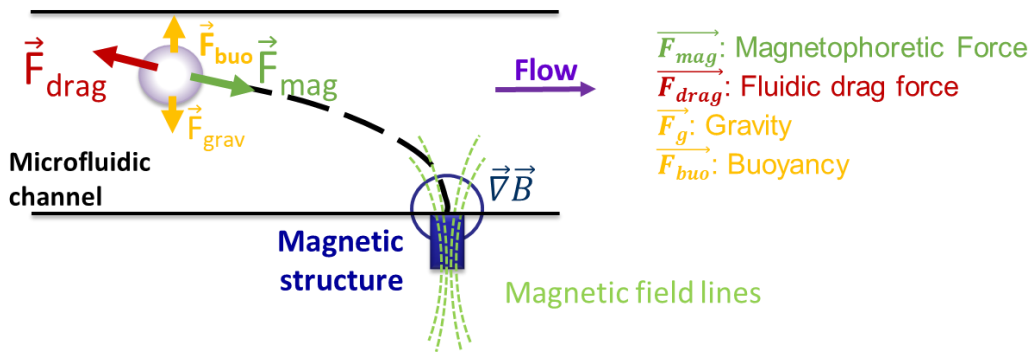


Figure 1.12: Governing forces in a microfluidic system integrating magnetic structures.

Magnetic force

The magnetic force (\vec{F}_m) acting on a magnetic dipole of magnetic moment \vec{m} , under a magnetic field \vec{B} , is given by:

$$\vec{F}_m = (\vec{m} \cdot \vec{\nabla}) \vec{B} \quad (1)$$

Considering a particle of volume V_p and magnetization M_p , its magnetic moment is $\vec{m} = V_p \vec{M}_p$, the magnetic force can therefore be described as:

$$\vec{F}_m = V_p (\vec{M}_p \cdot \vec{\nabla}) \vec{B} \quad (2)$$

The magnetization expression varies as a function of the field intensity H up to saturation:

$$\vec{M}_p = f(H) \vec{H} \quad (3)$$

At low magnetic fields, the particle is not saturated, its magnetization is a linear function of the applied magnetic field and is expressed as:

$$\vec{M}_p = \Delta\chi\vec{H} \quad (4)$$

Where $\Delta\chi$ represents the difference in magnetic susceptibility between the particle (χ_p) and the surrounding fluid (χ_f). In free space $\vec{B} = \mu_0\vec{H}$, μ_0 being the vacuum permeability, the magnetic force can be written from Eq. 2 and Eq. 4 as follows:

$$\vec{F}_m = \frac{V_p\Delta\chi}{\mu_0}(\vec{B} \cdot \vec{\nabla})\vec{B} = \frac{V_p\Delta\chi}{2\mu_0}\vec{\nabla}B^2 \quad (5)$$

For large magnetic fields, the particle magnetization is saturated (all atomic moments being aligned along the magnetic field) and $\vec{M}_p = M_s$, M_s being the magnetization at saturation. The magnetic force can therefore be expressed as:

$$\vec{F}_m = \frac{V_p\Delta\chi M_s}{\mu_0}\vec{\nabla}B \quad (6)$$

Whether the particle is saturated or not, the magnetophoretic force can be positive or negative depending on difference in magnetic susceptibilities. Positive magnetophoresis happens when $\chi_p > \chi_f$, in which case the particle will be drawn towards the maxima of the non-uniform magnetic field. Examples include magnetic oxide particles ($\chi_p = 0.1 - 1$) suspended in a diamagnetic fluid, such as phosphate buffer saline solution ($\chi_f = 10^{-7}$) or blood ($\chi_f = 10^{-6}$) [126]. On the other hand, negative magnetophoresis occurs when diamagnetic particles ($\chi_p < 0$) are dispersed in a magnetic medium (paramagnetic solutions or ferrofluids). The particle will be drawn towards the minima of the non-uniform magnetic field.

Eventually, the magnetic force acting on a nanoparticle-labeled cell is given by multiplying the magnetic force on an individual nanoparticle by the average number of nanoparticles per cell (N_p):

$$\vec{F}_{m,cell} = \frac{N_p V_p \Delta\chi}{2\mu_0} \vec{\nabla}B^2 \quad (7)$$

Most of works utilize this simplified approach of the magnetic force acting on a magnetically labeled cells, but some might also consider a cell-particle complex which modifies the resulting volume and magnetic susceptibility [110].

In a nutshell, the magnetophoretic force depends on the size of the object, its magnetic properties, as well as the magnetic field and its gradient. Magnetophoretic forces can therefore be tailored and enhanced based on the manipulated objects and the designed magnetic system. Typical force values reported in the literature range from few pN to several nN.

Fluidic drag force

In a microfluidic channel, particles that are moved by the magnetophoretic force will be submitted to the Stokes' drag force (\vec{F}_d), which acts in the opposite direction to particle motion. In low Reynolds numbers, the drag force is expressed using Stokes' law, as follows:

$$\vec{F}_d = -6\pi\eta R_p(\vec{v}_p - \vec{v}_f)C_w \quad (8)$$

Where η is the suspension medium viscosity, R_p the particle radius, v_p the particle relative velocity in the direction of the magnetophoretic force versus v_f the carrier fluid velocity. C_w is a constant that accounts for the influence of channel wall on the drag force of the particle [110]. This value varies from 1, when the particle is far from the wall, to 3 when the distance d the two is zero. Its expression can be given by:

$$C_w = \left[1 - \frac{9}{16} \left(\frac{R_p}{R_p + d} \right) + \frac{1}{8} \left(\frac{R_p}{R_p + d} \right)^3 - \frac{45}{256} \left(\frac{R_p}{R_p + d} \right)^4 - \frac{1}{16} \left(\frac{R_p}{R_p + d} \right)^5 \right]^{-1} \quad (9)$$

For small particle radius compared to the dimensions of the microfluidic channel, this coefficient can be ignored.

In most microfluidic applications, the fluid flow profile is not uniform but varies along the channel section (laminar flow regime). However, particle diameter being usually smaller than microfluidic channel dimensions, the fluid velocity is considered relatively constant across the particle [128]. The drag force is then estimated at a time t , with particle velocity at t and fluid flow velocity at the position of the particle at t . Several studies were conducted to consider the fluid velocity profile depending on the position of the particle in channel of various section shapes (i.e. rectangular, triangular, cylindrical, etc.) [110].

The drag force is the main force competing with the magnetic force, with values typically in the order of few to few tens of pN in microfluidic devices.

Gravitational and buoyancy forces

The gravitational force (\vec{F}_g) and the buoyant force (\vec{F}_b) are expressed as follows:

$$\vec{F}_g = \rho_p V_p \vec{g} \quad (10)$$

$$\vec{F}_b = -\rho_f V_p \vec{g} \quad (11)$$

with ρ_p and ρ_f , the density of the particle and the solution, respectively, and \vec{g} the acceleration due to gravity. Gravitational force and buoyancy forces are neglected for sub-micrometer or nanoscale particles [129]. Indeed, they are much lower than magnetic forces. As an example, 1-micron Fe_3O_4 particles ($\rho_p = 5000 \text{ kg/m}^3$), flowing in water ($\rho_f = 1000 \text{ kg/m}^3$), experience $F_g = 2.56 \cdot 10^{-2} \text{ pN}$ and $F_b = 0.51 \cdot 10^{-2} \text{ pN}$, several orders of magnitude smaller than the magnetic force. However, for a particle diameter higher than $10 \mu\text{m}$, these forces cannot be neglected [126].

Other forces

Other forces can contribute to the overall trajectory of magnetic particles in a magnetophoretic microfluidic device. Thermal kinetic energy resulting from Brownian motion can be neglected for particles having a diameter greater than 40 nm [130].

Interactions between the particles and their environment (other particles, channel wall, fluid...) result from magnetic and electrostatic forces. Interparticle interactions, which includes magnetic dipole-dipole interactions and electric-double layer repulsion forces, as well as particle/fluid interactions, are usually ignored for particles relatively spaced from each other and for particle suspension at low volume concentration [131].

Interactions between the particle and microchannel wall, being electrostatic and van der Waals forces [132], result from their respective surface charges when residing in an electrolytic solution (e.g. buffers, cell culture media, blood...). Both forces can generate unwanted particle adhesion to the micro-channel walls. This can be avoided by modifying the pH and the ionic strength of the solution or by coating micro-channel wall or particle surfaces with proteins (Bovine Serum Albumin, BSA for example) or non-ionic surfactants (such as Pluronic). These forces are negligible at distances greater than tens of nanometers between the particle and the channel wall [126].

Overall force balance

Finally, the balance of forces on a moving particle according to Newton's second law determines its motion in microfluidic devices:

$$m_p \frac{d\vec{v}_p}{dt} = \sum \text{Forces} = \vec{F}_m + \vec{F}_a + \vec{F}_g + \vec{F}_b + \dots \quad (12)$$

For a submicrometer-sized particle, the inertial force contribution to the total force balance ($m_p \frac{d\vec{v}_p}{dt}$) can be negligible in comparison with the other forces acting on the particle, due to its small mass [128]. Additionally, the magnetophoretic force is mainly in competition with the drag force, which gives the following expression:

$$V_p(\vec{M}_p \cdot \vec{\nabla})\vec{B} = 6\pi\eta R_p(\vec{v}_p - \vec{v}_f) \quad (13)$$

The magnetophoretic separation performances can therefore be optimized by judicious selection of particle properties (R_p, M_s, χ_p), fluid characteristics (η, χ_f), cell magnetic loading (N_p), and flow rates (v_f). In particular, tuning the magnetic source (B) can help in reaching high magnetic field gradients so as to overcome fluidic drag force.

2.2. Interest of micro-scale magnetic sources

2.2.1. Maximizing the magnetic force

From Eq. 5 and Eq. 6, it is apparent that it is crucial to generate high magnetic field gradients ($\vec{\nabla}\vec{B}$). The first, and the simplest approach for gradient generation, involves employing centimeter-sized permanent magnets. NdFeB is the material of choice for macro-scale magnets as it offers the highest values of remanent induction (Br) at room temperature among other hard magnetic materials. However, this approach suffers from the relatively low magnetic field gradient (few hundreds of T/m) and the large distance between the macro-magnet positioned nearby the device and the microchannel.

Scaling down the size of magnetic field source scales up the magnetic field gradients [133]. Indeed, the magnetic field generated by a uniformly magnetized object depends on its magnetization and shape, but magnetization is an inherent property. Both large and small magnets, with the same magnetization, will produce similar magnetic fields. On the other hand, the size of the object has an impact on the decreasing distance of the magnetic stray field: the distance on which the magnetic stray field decays scales with the size of the object (Figure 1.13). By decreasing the size of the magnetic by a factor k , the generated volume force can be increased by the same factor [133]. It is therefore beneficial to integrate micro-scale magnetic sources in microfluidic systems.

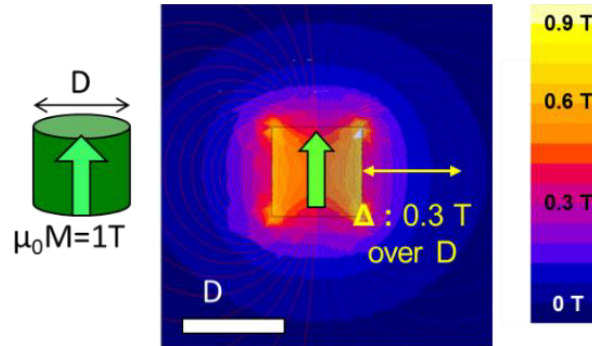


Figure 1.13: Influence of the size of a magnet on the pattern of magnetic stray field around the magnet. The magnet is of diameter D and has a magnetization of 1 T directed upwards.

Three main approaches are used to generate localized micro-magnetic field gradients: (i) micro-coils, (ii) micro-concentrators, and (iii) micro-magnets (Figure 1.14). Micro-coils, or microscale electromagnets, consist of tiny wires of electrical conductor in which an electric current pass through to generate a magnetic field. The advantage of this approach is the tunability: the magnetic field can be easily switched on/off to facilitate cell capture and release, as well as its intensity can be altered by controlling the input electric current. Plouffe et al. implemented this strategy in a microfluidic device by integrating two single current-carrying wires, run in the antiparallel direction, on both sides of a microfluidic straight channel [134]. Interestingly, depending on the desired end results, either high current should be used for high efficiency or low current for high purity. However, this strategy suffers from bulkiness, as micro-coils require an external power, and Joule heating, limiting the magnetic field

to a few tens of mT when operating in static conditions [135]. In contrast, micro-concentrators and micro-magnets can produce relatively strong magnetic fields (of a fraction of a Tesla) and are thus preferred for microfluidic applications. Micro-concentrators are made of soft ferromagnets (mainly Ni and Fe-Ni alloys) and, because of their high magnetic susceptibility, they are used to concentrate an external magnetic flux. In the absence of an external magnetic field, their magnetization is null. On the contrary, micro-magnets are made of hard ferromagnetic materials (usually NdFeB), that once magnetized, can permanently generate a magnetic field in their vicinity. In the literature, the term “micro-magnets” can also be found to refer to soft ferromagnetic structures.

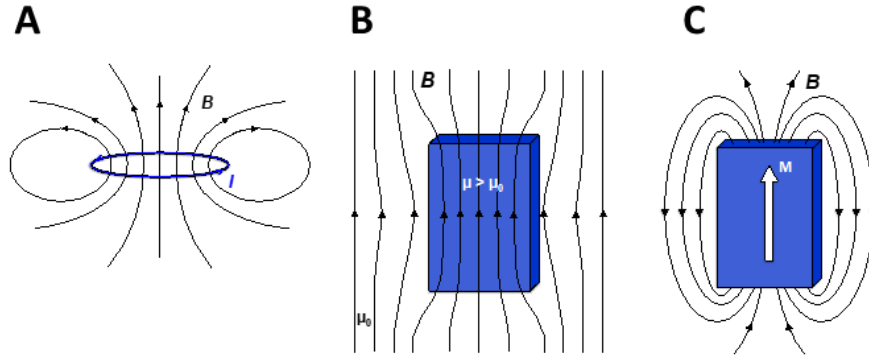


Figure 1.14: The main microscale magnetic sources. (A) Current carrying micro-coils made of conducting materials. (B) Micro-concentrators made of soft ferromagnetic materials and magnetized by an external magnetic field. (C) Permanently magnetized micro-magnets made of hard ferromagnetic materials. Reprinted from [110].

2.2.2. Conventional microfabrication techniques of micro-scale magnetic sources

Conventional fabrication of microscale magnetic sources, such as micro-magnets or micro-concentrators, relies on the microfluidic chip technology based on photolithography followed by etching techniques in silicon or glass substrates to pattern the shapes. Magnetic films are then obtained using physical vapor deposition or electrochemical deposition methods. Physical vapor deposition techniques include thermal evaporation [136], pulsed-laser deposition [137], and sputtering [138] (Figure 1.15). The simplest preparation method is thermal evaporation, but this method is restricted to materials with moderately low melting points (such as Ni). For more refractory materials (i.e. resistant to high temperature, like Fe), electron-beam evaporation is required [139]. Pulsed laser deposition (PLD), in which the material is ablated from the target by a focused intense laser pulse, is simple of use and enables the growing of complex materials such as transition metal oxides. However, PLD suffers from relatively low deposition rate, of order of 1 nm/s [140], and relatively small deposition areas. Sputtering, which is the most widely used method for magnetic thin film preparation, can overcome these issues. This method consists in ejecting atoms or molecules from any surface by bombardment of the surface with energetic ions, which are usually Ar^+ .

Among chemical methods to produce magnetic films, electrodeposition is a method widely used. By the action of an electric current, metallic films can be plated on a conductive surface immersed in a solution containing metal ions. Given the high deposition rate, of about 50 nm/s [140], electrodeposition has been found as an efficient way to deposit and pattern thick films (LIGA process) of Ni and alloys, such as permalloys ($\text{Ni}_{78}\text{Fe}_{22}$). However, this method is not suitable for rare-earths which are too electronegative.

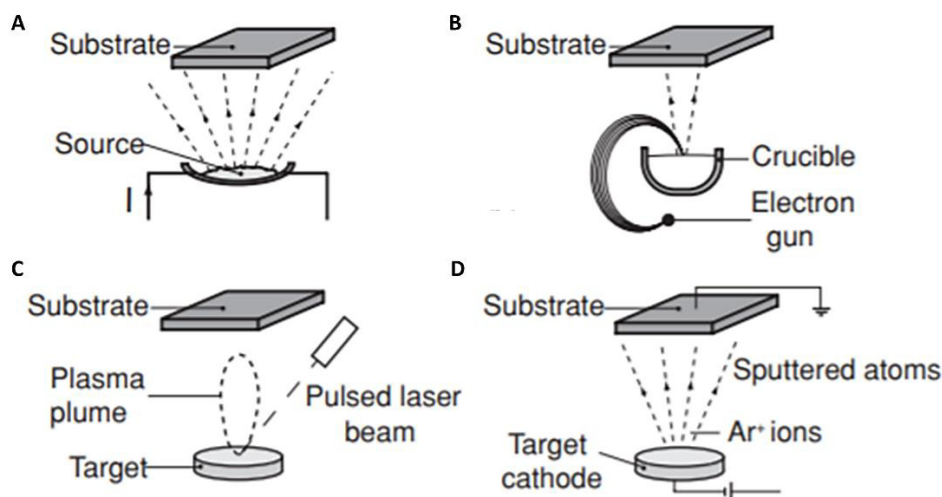


Figure 1.15: Magnetic film preparation methods: (a) thermal evaporation, (b) e-beam evaporation, (c) pulsed-laser deposition, and (d) sputtering. Adapted from [140].

All these film-based fabrication methods are easy to implement for micro-concentrators but require additional steps for micro-magnets. Indeed, contrary to micro-concentrators which present a low degree of chemical ordering and a poor crystallinity, micro-magnets possess a large magneto-crystalline anisotropy. Additional preparation constraints are therefore required to reach chemical order, such as thermal treatments at 500°C, which limit the choice of substrate and resins/polymers in microfabrication routes. In addition, once prepared, the application of external magnetic fields of several Teslas is necessary to reach micro-magnet full remanence.

One can notice, that besides standard micro-patterning techniques (lithography and etching), other microfabrication routes were investigated to obtain multi-pole magnetization of NdFeB films, including electrical pulses (pulse magnetization) [141] and thermo-magnetic patterning (TMP) [142].

2.3. Implementation of magnetophoresis for CTC isolation

2.3.1. From macroscale to microscale magnetic sources

Hoshino's group and Kelley's group provided tremendous work on CTC isolation over the past ten years. In particular, they demonstrated the advantage of downscaling the size of the magnetic source. Historically, Hoshino et al. implemented a CTC sorting device using an array of three NdFeB block magnets ($19 \times 13 \times 5.6 \text{ mm}^3$) located at the bottom of the microfluidic channel. CTCs in blood were labelled with EpCAM-functionalized Fe_3O_4 magnetic nanoparticles and captured by the magnetic field as the blood flows through the micro-channel [143] (Figure 1.16-A). Similarly, Kelley's group developed a more complex device integrating X-shaped microstructures as capture spots [144]. These capture structures generate regions of locally low flow velocity (Figure 1.16-B), termed velocity valleys, so that the magnetic force, resulting from an external millimeter-sized magnet, is sufficient to overcome the lowered drag force. Cancer cells, which are labelled with anti-EpCAM magnetic nanoparticles, entering the valley will get captured. Furthermore, they devised successive zones with increasing channel cross-section to decrease the average linear velocity and thus the drag force. Doing so, they managed to capture cancer cells as a function of EpCAM expression by studying their trapping location.

Later, both groups highlighted the benefit of working with micrometer-sized magnets. Hoshino's group integrated nickel (Ni) microstructures within the microfluidic channel which act like micro-traps [145] (Figure 1.16-C). Arrayed Ni microstructures were first defined by standard photolithography and next, a thin-film of nickel layer (250 nm thick) was deposited by thermal deposition (on top of a 15 nm-thick chromium adhesion layer). These nickel microstructures with the dimensions of $20 \mu\text{m} \times 20 \mu\text{m}$ were designed so as to be compatible with CTC diameter. In total, about 8750 magnetic traps were integrated on the chip, i.e. 25 traps/ mm^2 [146]. They are magnetized upon application of a magnetic field which is generated by the same configuration as their previous chip, i.e. three NdFeB block magnets. With this new design, they achieved an average 18.4% increase in capture rate in comparison with their previous

configuration where the magnetic field was generated by external magnets only. In addition, they observed an improved working stability with the nickel micro-concentrators as capture rate variability was lowered. The average capture rate with nickel-patterned microstructures was 97.3% at a flow rate of 2.5 mL/h. Subsequent immunofluorescence staining and FISH analysis were performed by fixing captured cancer cells on the channel substrate. Furthermore, they studied the trapping distribution within the chip according to the position of the permanent magnets and nickel micro-traps. The median capture position was located on the front edge of the permanent magnets array, indicating that the permanent magnets provide the major attractive forces. Besides, the total ranges of cell distribution area increased which demonstrates the additional magnetic trapping sites of the nickel microstructures, therefore preventing cell aggregation issues. Finally, they clinically verified the trapping ability of the device by screening blood samples from patients with metastatic cancers (colorectal, lung, prostate, and breast cancers) and found between 1 and 215 CTCs in screened patient samples (blood volume ranging from 5 to 10 mL).

Regarding Kelley's group work, they upgraded their "velocity valley" design by integrating round nickel microstructures centered on their X-shaped capture spots [147]. These microstructures were first patterned using standard lithography processes, and then covered with a 1.5 μm -thick Ni layer by sputtering. These Ni microstructures increase in radius along the length of the channel, from 136 to 235 μm , generating 100 discrete zones. Each of the 100 zones has two rows of X-structures with the same Ni structure diameter. This gradual increase of the magnetic capture sites exposes the magnetically labeled cancer cells to enhanced magnetic field gradients at the edges of the Ni traps, enabling their magnetically ranking regarding their surface marker expression (magnetic ranking cytometry device, MagRC) (Figure 1.16-D). The capture of low-expression cells requires the action of larger nickel structures, therefore occurring in the later zones of the chip. This combination of low flow and high magnetic field gradients lead to a >90% capture efficiency for cell lines with various EpCAM expression, at a flow rate of 0.5 mL/h. In comparison, their previous velocity valley chip reached similar performances but by tuning the flow rate for each cell type. At a flow rate of 0.5 mL/h, 40% of SKBR3 cells were captured. They later achieved successful profiling of CTC phenotypes in clinical samples [148]. They observed that patients with localized prostate cancers presented a greater phenotype diversity than patients with metastatic prostate cancer. Recently, Kelley's group implemented their MagRC device for the tracking of the expression of therapeutic protein targets in CTCs [149]. This was achieved using magnetic cell-labelling reagents that can target intracellular proteins, and therefore enable magnetic ranking of CTCs according to the expression levels of intracellular proteins. By measuring these protein levels within isolated CTCs and analyzing these protein markers at the single-cell-level, they could identify drug targets or predict therapeutic response.

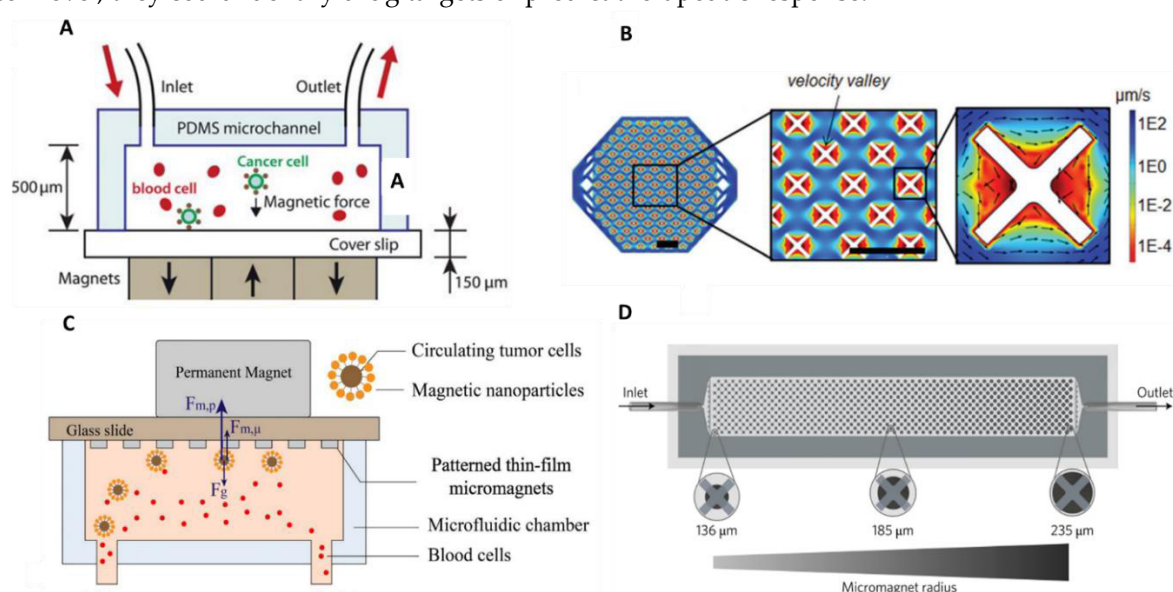


Figure 1.16: From macroscale to microscale magnetic sources for CTC isolation. (A,C) From the use of an external permanent magnet to the integration of nickel microstructures within the microfluidic channel. These

microstructures, acting like microtraps, achieved an average 18.4% increase in capture rate of magnetically labeled CTCs in comparison with the previous design. Reprinted from [143] and [145]. **(B,D)** Toward the combination of X-shaped velocity valleys as low flow velocity regions with circular nickel microstructures as capture spots. This configuration achieved a >90% capture efficiency for cancer cell lines with various EpCAM expression levels and enabled their magnetically ranking thanks to the gradual increase of nickel microstructure size. The capture of low-expression cells requires the action of larger nickel structures, therefore occurring in the later zones of the chip. Reprinted from [144] and [147].

2.3.2. Diverse immunomagnetic separation approaches

Various strategies were implemented for the immunomagnetic separation of CTCs, either by directly isolating CTCs from blood using specific antibodies (positive selection), usually targeting the epithelial surface marker EpCAM; or by depleting WBCs (negative selection) for downstream CTC collection.

Positive selection

Viovy's group reported the Ephesia technology which consists of self-assembled anti-EpCAM functionalized magnetic beads forming columnar arrays along the microchannel height and acting as a trap for target cells (Figure 1.17-A). They first proposed to use a permanent magnetic pattern with the desired organization, deposited at the bottom of the microchannel, to direct bead self-assembly [150]. This method is based on the microcontact printing of a water-based ferrofluid onto glass, to localize and organize the functionalized beads columns in the channel. They demonstrated a capture efficiency as high as 94%, and the possibility to cultivate in situ the captured cells. Further characterizations were conducted within the chip on isolated cancer cells from patient blood samples, including phenotype and morphology analyses, as well as intranuclear high resolution imaging. Magnetic columns must be tightly anchored to the bottom layer of the chip to stand firm against hydrodynamic flow during the whole capture and analysis. They later proposed a capillary assembly technique [151], using a microstructured PDMS template with micron-sized well patterns, to improve the stability of the bead columns [152]. Similarly, Zhang's group reported the use of micrometric nickel squares as a magnetic pattern to control the arrangement of anti-EpCAM-coated magnetic nanospheres (MNs) within the microchannel [153]. 9- μm -thick nickel microstructures were obtained by electroplating and encapsulated in a 2- μm -thick PDMS film [154]. When nickel patterns are magnetized through the presence of external permanent magnets, they generate a high magnetic field gradient around them, resulting in the capture of magnetic beads at their edges. Interestingly, captured CTCs could be recovered after removal of the permanent magnets. This magnetically controlled microfluidic device was further implemented for a liquid biopsy-guided drug release system to capture CTCs and accordingly release an appropriate amount of anti-cancer drug [155]. This system consisted of two areas loaded with two functionalized MNs: recognition MNs for CTC capture, and drug-loaded MNs for drug release (Figure 1.17-B). Cancer cells are recognized and captured by EpCAM aptamers on recognition MNs which then triggers the release of complementary strands inducing a subsequent drug release. Thus, drugs were released according to the number of captured CTCs, and different levels of treatment could be implemented according to the malignant progression of cancers. The novelty of this device is the combination of cancer diagnosis and therapeutic functions and may help in the development of personalized cancer medicine.

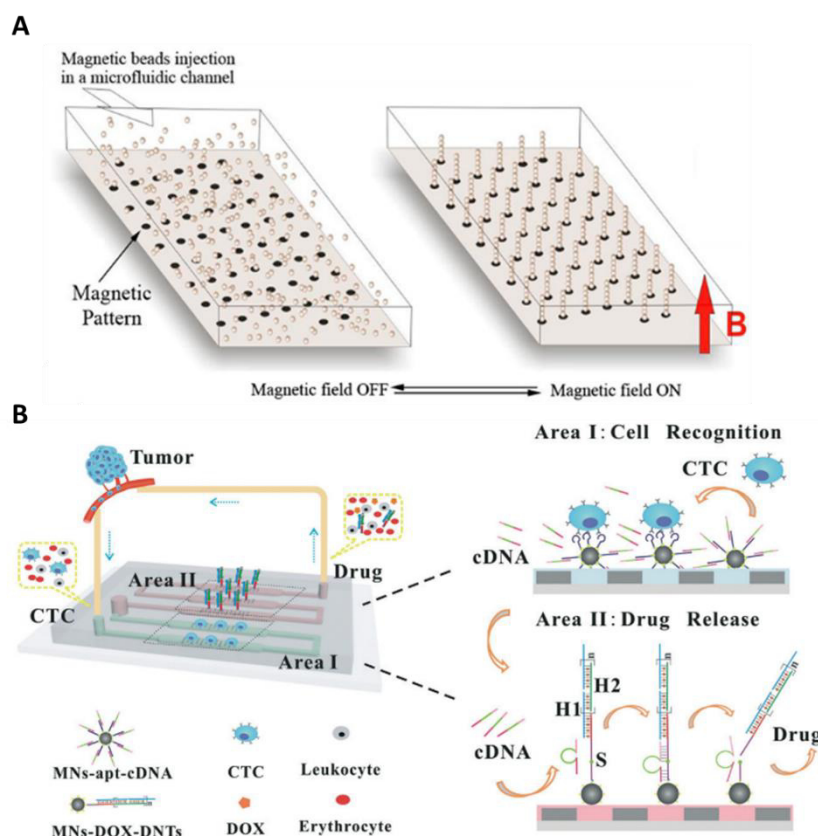


Figure 1.17: Ephesia technology for CTC isolation. **(A)** Self-assembly of anti-EpCAM functionalized magnetic beads along the microchannel height which act as traps for CTCs. Columnar bead arrays were localized by microcontact printing of a magnetic pattern made of ferrofluid. Captured CTCs can be released by removing the external permanent magnet. Reprinted from [150]. **(B)** Arrangement of functionalized magnetic nanospheres within the microchannel through the use of a nickel patterns. The liquid biopsy-guided drug release system (LBDR system) consists of two areas loaded with two types of functionalized magnetic nanospheres (MNs). Tumor cells are first recognized and captured by EpCAM aptamer-functionalized MNs (Area I) which leads to the release of corresponding complementary strands (cDNAs), due to the conformational change of the aptamers. cDNAs present cleaving capability which could trigger a subsequent doxorubicin (DOX) drug release process (Area II). Reprinted from [155].

Nevertheless, the approaches cited above do not take into account the surface marker expression heterogeneity in CTCs. Special designs were imagined to track this heterogeneity in immunomagnetic separation-based systems for CTC sorting. Kwak et al. reported the fabrication of a spiral shape channel capable of capturing magnetically labeled CTCs by magnetophoresis regarding their EpCAM expression level [156]. This was achieved thanks to the spiral shape design that can gradually decrease the distance to the center circular shape permanent magnet (external to the microsystem), resulting in specific positioning of heterogeneous CTCs depending on the number of anti-EpCAM-conjugated magnetic nanoparticles on their surface (Figure 1.18-A). CTCs with high EpCAM expression will be captured in cell trapping segments located along the first channel loop while CTCs with low EpCAM expression will travel along successive channel loops to finally get trapped where the distance between the circular channel and magnet is small. Aldridge et al. reported the Prism Chip, a more complex design using variably angled ferromagnetic guides (magnetized by an external neodymium magnet) to induce prismatic deflection of magnetically labeled CTCs and separate them distinct subpopulations corresponding to their EpCAM expression levels [157] (Figure 1.18-B). Analogously to the functioning of an optical prism dispersing light into its component wavelengths, this approach separates a flowing stream of cells into discrete fractions. They achieved a recovery efficiency of 88% at a flow rate of 30 mL/h, and improved purity by performing a first prismatic deflection of WBCs using magnetic nanoparticles conjugated to anti-CD45 and anti-CD15 antibodies. They integrated a graphene Hall sensor array to enumerate the isolated cell subpopulations, including cell clusters. The Hall sensor array

consists of patterned graphene crosses on which titanium (10 nm) and gold (50 nm) contacts were deposited using electron beam evaporation. Magnetically labeled cells flowing over the sensor array induce a change in magnetism, proportional to the cell's magnetic loading, which is converted into a voltage difference. Heterogeneous cells, such as single CTCs or CTC clusters (with more surface biomarkers due to the larger surface area), can therefore be differentiated without requiring the whole equipment needed for fluorescence microscopy, offering low-footprint solutions for cancer diagnosis.

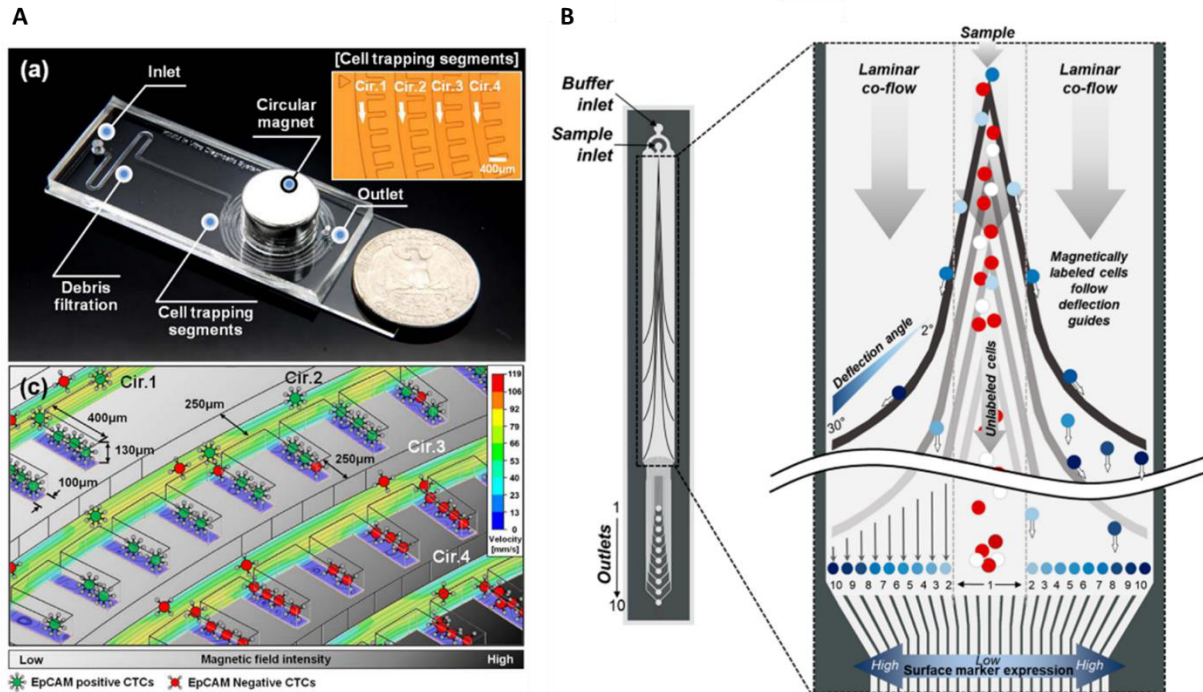


Figure 1.18: Heterogeneity tracking in immunomagnetic-based separation systems. **(A)** Spiral shape design can gradually decrease the distance to the center circular shape permanent magnet. Heterogeneous CTCs specifically position in trapping segments regarding the number of anti-EpCAM-conjugated magnetic nanoparticles on their surface. Low-expression cells will get captured in the center of the spiral channel where the distance to the external permanent magnet is small. Reprinted from [156]. **(B)** Prismatic deflection separates a continuous CTC sample stream into discrete subpopulations based on CTC surface marker expression level. Co-based ferromagnetic guides are made up of distinct segments having angles ranging from 2 to 30° and, in the presence of an external magnetic field, induce a lateral deflection of a magnetically-labeled target. The angle of the deflection guides relative to the direction of flow dictates the direction of the magnetic force while the amount of magnetic loading on the surface of the cell dictates its magnitude. Reprinted from [157].

Negative selection

Tumor-antigen independent immunomagnetic separation methods were also investigated to overcome marker expression variability among CTCs by specifically removing WBC, typically using anti-CD45 antibodies. These approaches offer an opportunity to isolate CTCs regardless of their phenotype and ensure that CTC viability is maintained. Hyun et al. fabricated a two-stage microfluidic chip (μ -MixMACS chip) for negative selection of CTCs [158,159]. The microfluidic chamber, with a height of 930 μ m and total volume of 1 mL, was sandwiched between two magnet array cartridges. The magnet array, which consisted of millimeter rectangular NdFeB block magnets arrayed in a laser-cut plastic cartridge, generated magnetic fields parallel to the flow direction for WBC depletion, with strong magnetic field gradients located between two adjacent magnets.

In the first stage, WBCs labeled with CD45 antibody-conjugated magnetic nanoparticles were depleted inside the chip by magnetophoresis while CTCs exited through the outlet. Cells are then focused in the center of the channel by inertial forces and entered the second stage in which CTCs were specifically captured on the antibody-coated (e.g. EpCAM or HER2) channels (Figure 1.19-A). They isolated tumor cells based on their surface marker expression levels on the anti-EpCAM antibody-coated chip and anti-HER2 antibody-coated chip and respectively achieved capture efficiencies of 98.91% for EpCAM+ cells

and 86.51% for HER2+ cells, with 22% purity, at a high throughput (24 mL/h). Nonetheless, a limitation of this approach is the risk of channel clogging for high-capacity isolation.

Large volumes of blood have to be processed to ensure the collection of a sufficient number of CTCs, which might cause clogging due to the large number of WBCs per 1 mL of blood (about 10^6). Recently, Mishra et al. reported an ultrahigh-throughput magnetic sorting chip, the ^{LP}CTC-iChip, which processed very large blood volumes (65 mL) for negative selection of CTCs [160]. By combining soft iron-filled channels to intensify the field gradient within sorting channels, with inertially focused streams of cells, they achieved massive depletion of magnetically labeled WBCs. CTCs and WBCs were collected in two separated outputs. They obtained an 86% recovery efficiency with 99.97% of depleted, resulting in an average purity of 0.3% at a remarkable flow rate of 168 mL/h. This magnetic device was used after a previous non-equilibrium inertial separation array [161] which removes RBCs and platelets based on their small physical size, compared with nucleated cells (Figure 1.19-B). From this prior physical-based isolation step, they depleted >99.999% RBCs and >99.999% platelets.

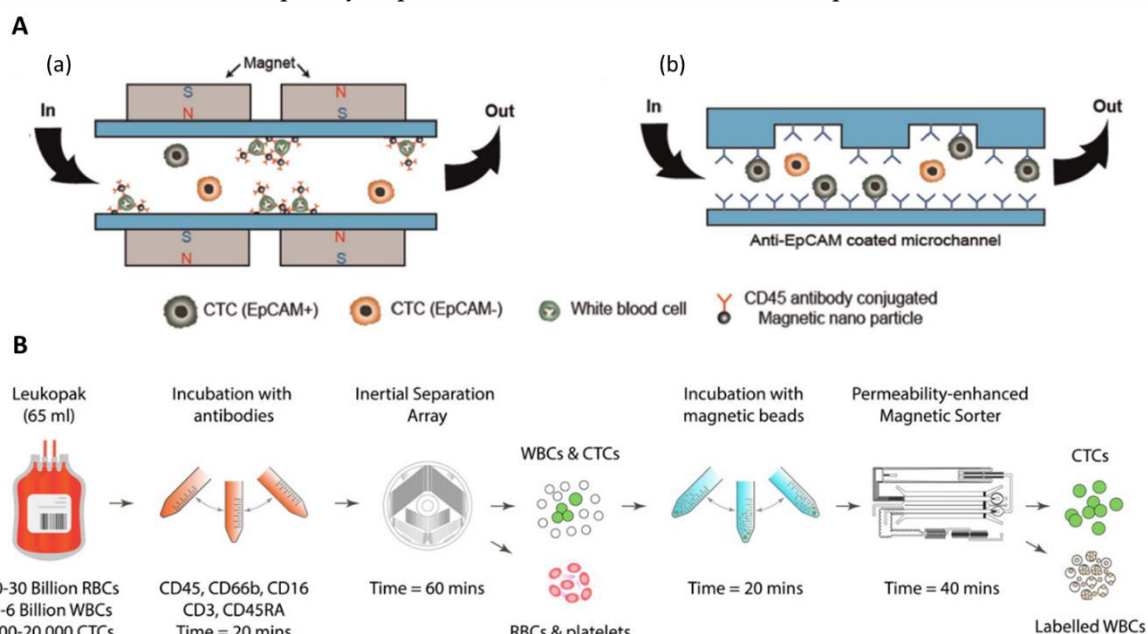


Figure 1.19: Tumor marker-independent selection. **(A)** Two-stage microfluidic chip for negative selection of CTCs. (a) Magnetically labeled WBCs are first eliminated in the first immunomagnetic stage and (b) CTCs are then selectively isolated based on their surface marker expression in the anti-EpCAM coated chip region. Reprinted from [158]. **(B)** Whole workflow for high-throughput CTC separation from full (65 mL) leukapheresis samples. RBCs and platelets are first removed from leukapheresis products using size-based inertial separation, followed by immunomagnetic removal of WBCs which were priorly labeled with a mixture of biotinylated antibodies targeting the pan-leukocyte cell surface antigens. CTCs were recovered without relying on antigen markers. Reprinted from [161].

2.3.3. Combination of immunomagnetic separation with physical-based separation methods

It can be of first interest to combine immunomagnetic separation with other physical-based approaches. The combination of the two approaches can compensate inherent drawback from each technique, enabling the detection of a wider range of tumor cells exhibiting different properties among them. Most multi-step isolation methods can be divided into pre-enrichment and isolation steps. The pre-enrichment part is usually based on a label-free method that allows for continuous CTC enrichment.

Nagrath's group reported a two-step isolation method: the first pre-enrichment stage consists of Dean flow fractionation in a spiral channel to remove RBCs and most of WBCs, and the second isolation step is performed by magnetophoresis on magnetically labeled CTCs [162]. Contrary to most separation devices, CTC labeling is conducted on-chip in a passive mixer where EpCAM coated magnetic beads and CTCs are infused at 100 $\mu\text{L}/\text{min}$, following a 5 min on-chip incubation in reservoirs to promote antibody-antigen interactions (Figure 1.20-A). The magnetic sorter module enables the distinct isolation of CTCs according to their EpCAM expression levels by adjusting on the micron scale the distance of the external magnet from magnetic particles flowing in the sorter. The magnetic field strength experienced by the labeled cancer cells could thereby be tuned, and as cell magnetic loading depends on their surface marker expression, cells could be specifically separated. The device achieved a 90% recovery efficiency on a spiked cell line, with 82 to 801 contaminating WBCs/mL, resulting in purities of up to 75%. The clinical utility of the device was demonstrated by processing pancreatic ductal adenocarcinoma blood samples from 6 patients and characterizing the isolated CTCs from these samples. Tumor cells were isolated based on low, moderate and high EpCAM levels. This platform enables the comparison of tumor cell subpopulations and further investigation should help identifying the impact of cell heterogeneity on patient outcomes and tailoring therapeutic targets for virulent cell subpopulations. Besides, the ultra-pure isolation of CTCs from patient blood samples enabled highly specific molecular profiling of patient CTCs [163].

Toner's group first reported the CTC-iChip which combines three different antigen-independent principles for CTC isolation: deterministic lateral displacement, inertial focusing, and magnetophoresis [164] (Figure 1.20-B). The individual components previously manufactured using deep reactive ion silicon etching and PDMS soft lithography [165] were integrated on a single mass-produced plastic chip, improving the accessibility of the CTC-iChip technology. Whole blood is injected within the monolithic chip and pass through a first DLD separation step after which RBCs and platelets are removed. The remaining CTCs and magnetically labeled WBCs then enter two successive inertial focusing and magnetic sorting stages for WBC depletion. Magnetic field gradients were generated by four magnets arranged in a quadrupole configuration and housed in a custom aluminum manifold. The sensitivity of the first stage enables the removal of labeled WBCs with more than 6 magnetic beads on their surface. The remaining cells enter the second stage which removes cells that are labeled with at least 1 magnetic bead. The performances of the chip were characterized across 11 different cell lines, and the chip achieved a remarkable median recovery of 99.5%, with a high purity (445 WBCs/mL). In particular, they highlighted the importance of performing negative depletion of blood cells as they found that neither CTC size nor EpCAM expression can maximize isolation efficiency as many CTCs found were small and expressed lower levels of EpCAM. In addition, they found that both parameters were significantly dependent on the individual patient and widely variable within a single patient. These results will help guide the design of future CTC isolation and diagnostic strategies based on negative depletion of blood cells.

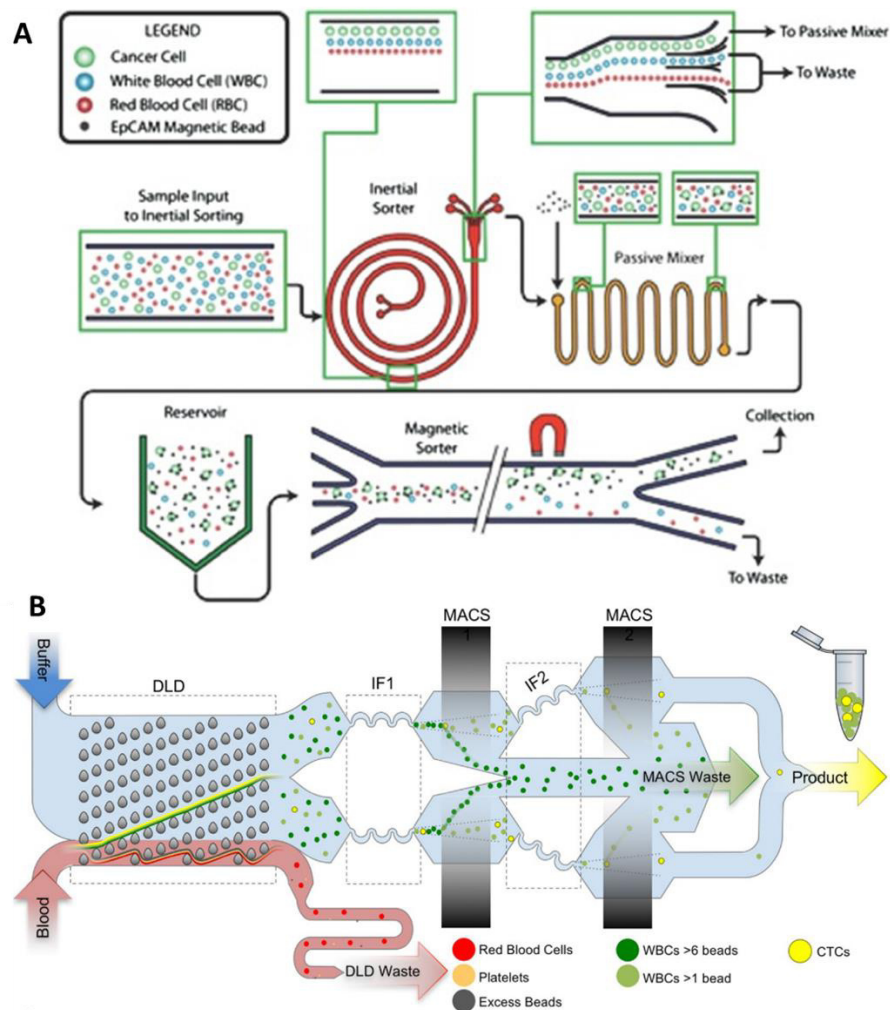


Figure 1.20: Integrated separation devices combining a size-based pre-enrichment step and an immunomagnetic-based purification step. **(A)** Integration of inertial sorter and magnetic sorter modules. Complete RBCs removal and partial WBC depletion through an inertial separation step in a spiral shape microchannel, followed by immunomagnetic separation of magnetically labeled CTC. The labeling step of CTCs with anti-EpCAM coated magnetic beads is performed on-chip. The magnetic sorting step enabled the distinct isolation of CTCs according to their EpCAM expression levels by adjusting the distance of the external magnet from magnetic particles flowing in the sorter. Reprinted from [158]. **(B)** CTC-iChip technology. RBCs and platelets are first removed by deterministic lateral displacement and remaining CTCs and magnetically labeled WBCs then enter two successive inertial focusing/magnetic sorting stages for WBC depletion. Reprinted from [161].

Recent microfluidic devices have mainly been reported in this introduction for CTC isolation, but several reviews can be studied to broaden this subject [21,74,166–171].

In summary, these studies highlighted the importance to achieve both high recovery of CTCs and high purity in microfluidic sorting systems, which can be challenging due to the low abundance, morphological and phenotypical heterogeneities of CTCs. Integrated microfluidic systems, combining magnetophoresis with other size-based separation methods, have therefore emerged as next-generation CTC isolation systems and can offer: (i) effective recovery of CTCs and CTCs clusters simultaneously, (ii) ultra-pure samples with minimal contamination of normal blood cells, and (iii) high-throughput sorting with preserved viability. Besides, the system should enable the selection of heterogenous CTCs with various surface marker expressions. Such microfluidic systems will represent a paradigm shift for cancer clinical care.

2.3.4. Summary

The performances of the reported magnetophoretic technologies are summarized in Table 1-7 and Table 1-8, for cell lines and clinical studies, respectively.

In a nutshell, the immunomagnetic approach is widely implemented for CTC isolation. It is of interest to reduce the size of the magnetic field source in order to maximize magnetic field gradients as highlighted in section 2.2.1. The above-mentioned microfabrication techniques of such micro-scale magnetic sources (section 2.2.2.), based on film-based approaches, led to unrivalled control over the reproducibility, shape, and microstructuration of the magnetic films. However, these approaches suffer from poor adhesion with polymer substrates, difficulty to achieve large aspect ratio microstructures, and require expensive and tedious fabrication processes. Other strategies have been explored to implement microstructured magnetic sources in microfluidic devices, such as the introduction of ferromagnetic wires (Ni, Fe-Ni) in microchannel [172,173], or the coating of 3D hot-embossed thermoplastic microstructures with a thin layer of nickel [174].

Recently, the magnetic composite polymer strategy has emerged as a real breakthrough for compatible and cost-effective integration of magnetic materials into polymer-based microfluidic devices. This original approach will be further described in the next section.

Table 1-7. Performances of immunomagnetic-based separation methods in cell line studies.

Separation method	Technology	Selection criteria	Throughput	Sample composition	Recovery	Viability	Purity	WBC Depletion	Enrichment factor	Ref
Magnetophoresis	Integrated Ni microstructures	EpCAM	2.5 mL/h	MCF-7, PC3, SK-BR-3, and COLO 205 cells in whole blood	97.3%	--	--	--	--	[145]
Magnetophoresis	MagRC	EpCAM	500 μ L/h	MCF-7, SKBR3, PC-3 and MDA-MB-231 in 1 mL whole blood	93.3%	98%	--	99.98%	--	[148]
Magnetophoresis	Immuno-magnetic nanosphere patterns	EpCAM	60 μ L/h	MCF-7 cells, Hep G2 cells and Cal 27 cells in PBS w/ 1% hydroxyl propyl methyl cellulose	~90%	93.1 \pm 2.6%	--	--	--	[153]
Magnetophoresis	Spiral channel w/ trapping segments and centered magnet	EpCAM	9 mL/h	MCF-7 and MDA-MB-231 cells	96.3 \pm 1.5% and 81.2 \pm 3.5%	--	--	--	--	[156]
Magnetophoresis	Prism Chip	EpCAM	30 mL/h	PC-3M, LNCaP, VCaP, and 22Rv1 in Hanks' balanced salt solution w/ 2% BSA and 5 mM EDTA	88 \pm 6%	91 \pm 4%	--	<3 log	--	[157]
Magnetophoresis	μ -MixMACS Chip	CD45 (negative selection)	24 mL/h	MCF-7 cells in whole blood resuspended in	90.97%		22.91%	>99%	763.14	[158]

				3 mL of PBS with 2% FBS						
Magnetophoresis	^{LP} CTC-iChip (Permeability-enhanced magnetic sorter)	CD45, CD16, CD3, CD45RA, and CD66b (negative selection)	168 mL/h	MGH-BRx-142 cells in 65 mL whole blood**	$86.1 \pm 0.6\%$	--	0.3%	3.55 ± 0.26 log 99.97%	--	[160]
DFF and Magnetophoresis	Integrated spiral module, passive mixer, and magnetic sorter	Size (15 μ m) and EpCAM	3 mL/h to 24 mL/h (8 parallel sorters)	PANC-1 cells in 1 mL whole blood	~90%	--	75%	6 log	--	[163]
DLD and Magnetophoresis	CTC-iChip	Size (3.8 μ m) and CD45, CD16 and CD66b (negative selection)	9.6 mL/h	11 different cell lines in 1x PBS with 1% Pluronic-F68	98%	--	7.8%	~ 5 log	--	[164]

*Once the field was removed, 92% of captured cancer cells were recovered from the MagRC device for further offline analysis.

**Cancer cells and WBCs were sorted through a magnetic sorter. RBCs were priorly removed using a size-based inertial separation.

Table 1-8. Performances of immunomagnetic-based separation methods in clinical studies.

Separation method	Technology	Blood sample volume	Cancer type	Number of CTCs	Detection sensitivity	Remaining WBCs/mL	Downstream analysis	Ref
Magnetophoresis	Integrated Ni microstructures	5-10 mL	M-colon (n=1) M-lung (n=1) M-prostate (n=1) M-breast (n=10)	1/5 mL 1/10 mL 13/7.5 mL 0.1-43/mL	100% (13/13)	--	Immunofluorescence staining and enumeration, FISH	[145]
Magnetophoresis	MagRC	10 mL	M-castration-resistant prostate (n=10) Prostate (n=14)	9-48/10 mL 16-95/10 mL	100% (24/24)	2000	Immunofluorescence staining and enumeration, Phenotypic profiling	[148]
Magnetophoresis	Immuno-magnetic nanosphere patterns	0.6-0.8 mL	M-Lung (n=6) M-Gastric (n=1) M-Gastric antrum (n=1) Lymphatic metastasis (n=1) M-Liver (n=1)	2-12/0.8 mL 6/0.8 mL 9/0.8 mL 4/0.6 mL 9/0.8 mL	100% (10/10)	--	Immunofluorescence staining and enumeration	[153]
DFF and Magnetophoresis	Integrated spiral module, passive mixer, and magnetic sorter	1.4 mL (6.5 mL for miRNA analysis)	Pancreatic (n=14)	14-938/mL (Mean 146 ± 231)	100% (14/14)	0-389 (Mean 42.4 ± 101)	Immunofluorescence staining and enumeration, MicroRNA and mRNA profiling (qRT-PCR)	[163]
DLD and Magnetophoresis	CTC-iChip	5-10 mL	Melanoma (n=2) Lung (n=9) M-Prostate (n=2) Breast (n=26)	1.2/mL 7.9/mL -- 9.6/mL	100% (39/39)	445	Immunofluorescence staining and enumeration, Size and phenotypic profiling using imaging flow cytometry	[164]

3. Magnetic composites for microscale patterning in microfluidic separation systems

3.1. Breakthrough of the composite polymers

Whether for CTC isolation or, more generally, bead and cell manipulation by magnetophoresis, researchers have provided hard work on the optimization of magnetic field gradient sources. Challenges remain regarding the complexity of microfabrication of microscale magnetic sources, and their integration with polymer-based microfluidic systems. The powder-based approach presents an alternative to the limitations of film-based approaches for the integration in polymer-based devices. It consists in doping the polymer matrix with magnetic particles or filaments, conferring magnetic properties to composite polymers. Magnetic polymers have recently emerged as a real breakthrough for compatible and cost-effective integration of magnetic materials into polymer-based MEMS and microfluidic devices [175,176]. In general, the composite approach allows conferring new properties to the polymers and finds many applications in the field of smart devices [177]. Concerning magnetic composite polymers dedicated to microfluidic systems, this approach enables the tailoring of the magnetic function depending on the properties of the magnetic powder, the nature of the polymer matrix, and the microfabrication method. Various polymer materials have been investigated for microfluidic applications: elastomers such as polydimethylsiloxane (PDMS), photosensitive resists such as SU-8 [178,179], or thermoplastics such as polymethylmethacrylate (PMMA) [41]. A large panel of microfluidic functionalities for fluid sample handling has thus emerged employing magnetic polymers such as: micro-valves, micro-pumps, or micro-mixers for microfluidic flow control [36,40,42–47]; dynamic artificial cilia [41,48–50]; and reversible microchannel bonding [51].

In particular, PDMS composite is the most commonly encountered due to the microfabrication properties of PDMS by soft lithography and the massive use of the latter for the realization of microfluidic systems. Magnetic PDMS composites have been used in microsystems to manipulate magnetic entities such as labeled cells or magnetic micro-beads by magnetophoresis [180]. Trapping and sorting applications using magnetic PDMS composites will be further described in the next section.

3.2. Magnetic PDMS composites in microfluidics

PDMS composites are excellent candidates for the integration of active functions into PDMS microsystems. There are many examples in the literature of dielectrophoretic functions based on conductive PDMS [181,182] and magnetic functions based on magnetic PDMS. Magnetic PDMS composites are mainly obtained by mixing soft (Fe, Ni, and Ni-Fe alloys) or hard (NdFeB, ferrites) magnetic powders with PDMS mixture (base polymer and curing agent). By modifying the nature, shape, concentration, and organization of the doping particles, it is possible to modulate the magnetic properties of the composite materials. One of the major advantages of these composites is that they preserve fabrication properties of PDMS such as micropatterning by soft lithography and surface activation by O₂ for plasma bonding with glass and PDMS substrates. This approach enables the microstructuration of magnetic composites of several micrometers in thickness and with aspect ratios that are hardly obtained with conventional microfabrication techniques. In addition, the composite microstructure can be directly integrated into the microchannels, in a one-step soft-lithography process, avoiding tedious alignment procedures. This very versatile approach allows localizing the magnetic structures inside the channel or in its close vicinity, underneath or on the sides. Moreover, as the magnetic structures are integrated into PDMS microsystems, the polymer matrix being the same for the whole system, the magnetic function is tightly integrated and does not raise heterogeneous integration issues.

Table 1-9 summarizes examples of magnetic PDMS composites in microsystems for sorting applications, revealing the broad range of magnetic composites depending on the nature, size, and concentration of magnetic particles, as well as their arrangement within microsystems. In particular, the effect of the magnetic particle concentration will be further studied.

Table 1-9: Examples of magnetic PDMS composites in microfluidic devices for magnetophoretic applications.

Nature	Doping agent		Application	Implementation in microsystem	Ref
	Particle diameter	Concentration (wt%)			
Carbonyl iron	7 μm	50-83	Micro-bead sorting and cell trapping	Pillars inside the channel	[183]
Nickel	50 nm	N/A	Magnetic bead and cell trapping	Pillars inside the channel	[184]
Carbonyl iron	1-3 μm	N/A	Nano-bead trapping	Pillar inside the channel	[185]
Neodymium oxide	5 μm	N/A	Immuno-magnetic sorting of beads	Pillars inside the channel	[186]
Carbonyl iron	N/A	N/A	Magnetic bead conveyor belt	Mushroom-shaped structures buried under the channel	[187]
Carbonyl iron	N/A	75	Cell trapping and sorting	Composites stripes under the channel	[188]
NdFeB	5 μm	66	Cell trapping and sorting	Composites stripes under the channel	[188]
Fe_3O_4	50-100 nm	38	Trapping of magnetically labeled Vorticella	Composite blocks in the channel walls	[189]
Iron	1-6 μm	44, 60, 70	Manipulation of functionalized magnetic particles	Integrated magnetic structure in the channel wall	[190]
Carbonyl iron	N/A	50, 66.7	Magnetic particle separation	Microstructured composite next to the channel	[191]
NdFeB	N/A	66.7	Magnetic particle separation, Microfluidic Mixer	Microstructured composite next to the channel	[192]
Carbonyl iron	7 μm	83	Micro-bead trapping and magnetic force measurement	Self-ordered composite block in the channel wall	[193]
NdFeB	N/A	N/A	Cell sorting	Self-ordered composite at the channel bottom	[194]
Carbonyl iron	0.5-7 μm	1-5	Micro-bead trapping	Columnar agglomerates under the channel	[195]

As mentioned, it is possible to tune magnetic composite properties, in particular its microstructure, by selecting an appropriate magnetic particle concentration. Highly concentrated PDMS composites (concentrations greater than 30 wt%) are favored for the integration of dense magnetic microstructures such as pillars [184–186,196] (Figure 1.21-A), mushroom-like structures [187], or stripes [188,197] (Figure 1.21-B) located at the channel bottom; as well for the fabrication of composite blocks located on or near the channel wall [189–192] (Figure 1.21-C). Furthermore, it is possible to control the organization of the magnetic particles within the PDMS matrix by submitting the composite to a magnetic field during the polymer cross-linking step. It results in a composite magnetic anisotropy that is no longer solely related to the shape of the magnetic field micro-source but can be explained by the anisotropic mechanisms of field-induced structures such as agglomeration and self-organization [198,199]. Deman et al. demonstrated the self-alignment of highly concentrated magnetic particles (83%) in chains along the field lines of an external magnetic field during the cross-linking step [200]. It resulted in a multiplication by two of the magnetic force exerted on superparamagnetic beads (12 μm in diameter), which was attributed to the 16% increase of the composite magnetization and to the local magnetic field gradients originating from the fine alternation of magnetic and non-magnetic regions. This anisotropic approach will be further detailed in Chapter 3 (part 1).

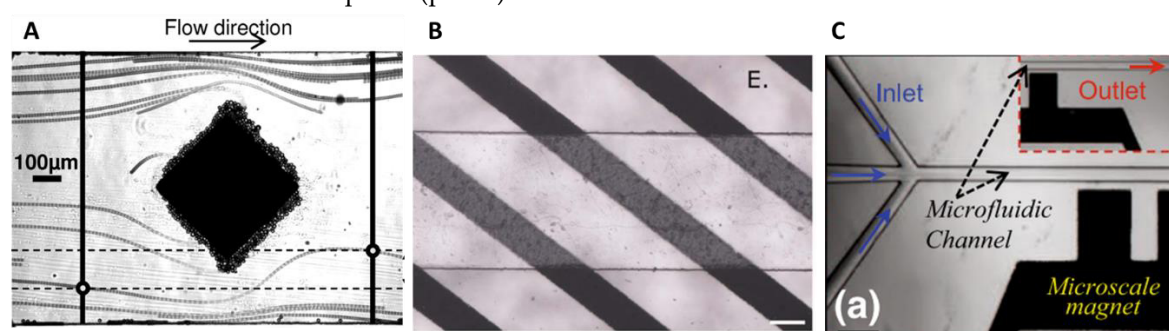


Figure 1.21: High concentrated magnetic PDMS composites. **(A)** Carbonyl iron pillar microstructures as magnetic traps located at the channel bottom. Flow patterns of superparamagnetic particles flowing at the vicinity of an i-PDMS microstructure in presence of an external magnetic field are highlighted. Beads can be detached and collected by rinsing after removal of the magnets. Reprinted from [196]. **(B)** Integrated magnetic stripes at the bottom of the microfluidic chip. The composite mixture was composed either of soft (FeC) or hard (NdFeB) ferromagnetic particles. Reprinted from [188]. **(C)** NdFeB-PDMS composite blocks located near the channel wall. The composite was magnetized to form microscale permanent magnet for particle separation via vertical deflection. Reprinted from [192].

In contrast, when the volume fraction of the magnetic entities is reduced to few volume percents, typically less than 10%, individual micrometer-sized magnetic flux sources can be formed and organized in regular patterns at the micrometer scale within the non-magnetic polymer matrix (low concentrated magnetic composites). In a same way, low concentrated composites are submitted to a magnetic field during the polymer cross-linking step to obtain regular micrometric-sized magnetic patterns with large aspect ratio. Mekkaoui et al. fabricated PDMS composites composed of carbonyl iron particles (I-PDMS) and demonstrated a chain-like organization of the soft magnetic particles when submitted to a uniform magnetic field during PDMS curing (Figure 1.22-A) [195]. The auto-organized I-PDMS composite constitutes the channel's floor and exhibits high densities of magnetic traps, of 1500 traps/ mm^2 and 5000 traps/ mm^2 , for carbonyl iron fraction of 1 and 5 wt%, respectively. They measured magnetic forces as high as several nN, from both numerical and experimental analysis. Finally, they demonstrated a high bead trapping throughput of 7100 trapped beads/min at a flow rate of 0.83 $\mu\text{L/s}$ and a remarkable trapping efficiency of 99.94%. This approach is relatively simple to implement and is well suited for magnetic trapping of individual bio-entities, including cells that have typical sizes comparable with the trap sizes. In turn, it restricts the shape of agglomerates to 1D structures and does not allow to independently tune the lateral size and the density of traps. To form other geometries of micro-patterns, strategies of replication were developed with non-uniform magnetic field templates [135,201] (Figure 1.22-B). This approach will also be detailed in Chapter 3.

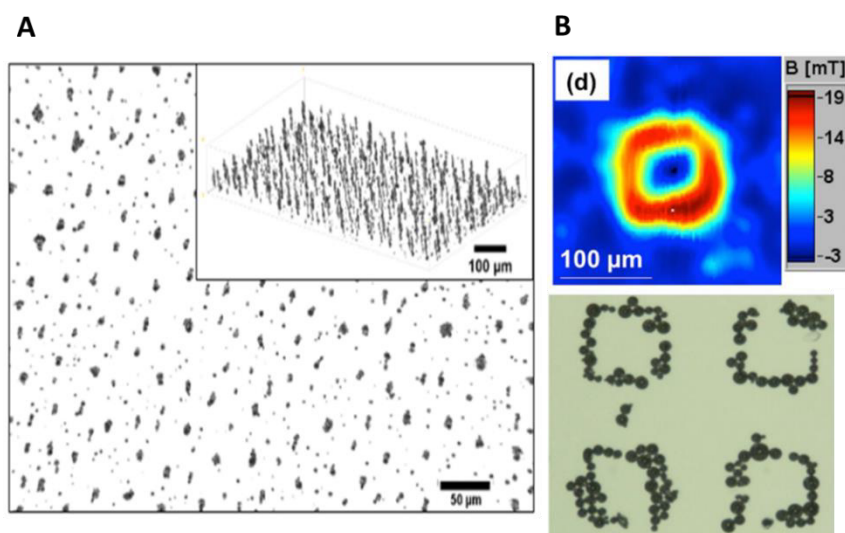


Figure 1.22: Low concentrated magnetic PDMS composites. **(A)** Chain-like auto-organization of carbonyl iron particles under the application of magnetic field during the polymer cross-linking step. Top view of the 5 wt% I-PDMS array of microtraps obtained by X-ray tomography, with a 3D reconstruction in the inset. The auto-organized I-PDMS composite exhibits a long-to-short axis ratio of more than 10 and a magnetic trap density as high as 5000/mm². This approach enabled magnetic trapping of individual bio-entities, including cells that have typical sizes comparable with the trap sizes (<10 μm). Reprinted from [195]. **(B)** Micro-magnetic imprinting (μMI) of NdFeB micro-flux sources. The stray magnetic fields produced by a thermomagnetically patterned (TMP) square magnetic film are used to imprint micron-scaled patterns of magnetic particles in a PDMS matrix. Top image: Scanning Hall Probe measurements of the stray magnetic field B_z measured at a height of 20 μm. Bottom image: Optical images of μMI structures made with spherical NdFeB particles. Reprinted from [135].

In relation to CTC sorting, Chung et al. reported on the self-organization of priorly magnetized NdFeB particles in a PDMS matrix in a chessboard-like multipoles pattern [194]. The alternation of up and down magnetization leads to a regular modulation of the generated stray field and high field gradients. The self-ordered NdFeB-PDMS composite layer constitutes a magnetic filter. The authors reported an original chip design, the hybrid magnetic/size-sorting (HMSS) chip (Figure 1.23-A), integrating multiple functions for CTC isolation and profiling, including: the magnetic filter for WBC depletion through immunomagnetic capture, a size-selective sorter for individual CTC capture at predefined locations, followed by an on-chip molecular staining. In addition, they integrated a chaotic mixer by microstructuring the top of the channel in a herringbone shape in order to deflect WBCs to the magnetic layer at the bottom of the channel and enhance trapping efficiency. The enrichment ratio was enhanced by more than 30-fold with the chaotic mixture. Recently, Toner's group reported a two-stage microfluidic system [160] which consists of a first stage integrating a series of asymmetric serpentine channels to focus cells in a single line through inertial focusing, and a second stage composed of soft iron-filled channels to act as magnetic micro-concentrators to intensify the field gradient (Figure 1.23-B). After a prior size-based inertial separation to remove RBCs and platelets, CTCs are isolated from magnetically labeled WBCs within their two-stage device.

It should be underlined that both implemented magnetic polymers for magnetophoretic CTC separation were combined with a prior size-based enrichment step to improve purity.

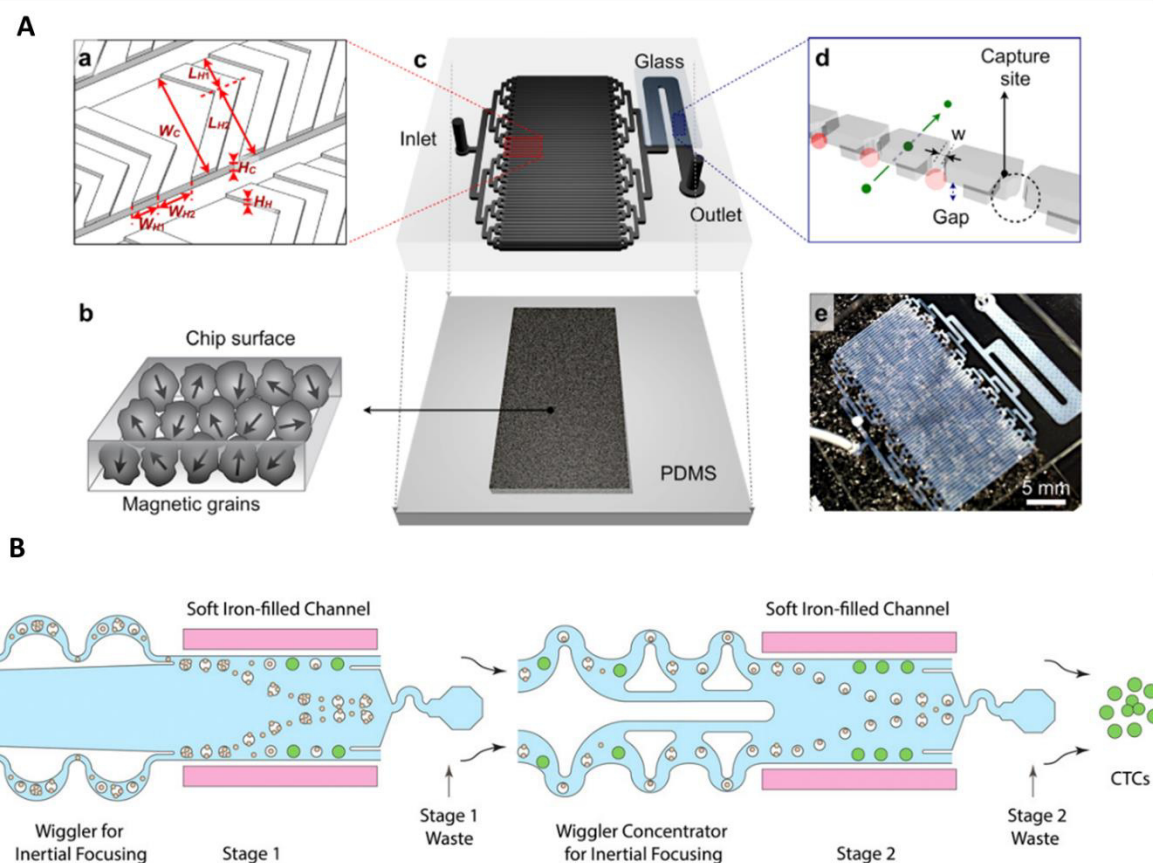


Figure 1.23: Magnetic composites for CTC isolation in microfluidic devices. **(A)** Hybrid magnetic/size-sorting (HMSS) chip. The magnetic sorter consists of self-assembled NdFeB particles in a PDMS matrix located on the bottom surface of the channel, leading to a chessboard-like multipoles pattern with high magnetic field gradients for WBC depletion. The bottom magnetic sorter was bonded to a top size-based sorter. The size-based sorter consists of 900 capture sites (15 μm in diameter) with a low size cut-off ($\sim 5 \mu\text{m}$). Cells (red) larger than the underpass gap (6 μm width, 5 μm height) are captured while smaller cells (green) pass through the gap. A herringbone pattern was integrated on the channel top to deflect WBCs towards the magnetic layer. Reprinted from [194]. **(B)** Two-stage magnetic sorter composed of two adjacent channels, one on each side of the sorting channels, which are compactly packed with soft magnetic iron particles. This was achieved by dispersing particles in 50% ethanol and retaining them through the use of filters while the fluid could escape. A series of asymmetric serpentine channels was positioned upstream of the sorting channels to focus cells into a single line through inertial focusing. Reprinted from [160].

In summary, magnetic polymers break with conventional microfabrication techniques and offer a promising alternative in terms of cost and simplicity of manufacture, as well as for flexible integration of magnetic functions in microsystems. Magnetic polymers haven't been fully explored for CTC sorting but the versatility of this approach should open new prospects in CTC study.

4. Aim and scope of the thesis

CTCs have sparked great interest within recent years for their potential clinical significance since they give an insight of the tumor. Detecting, enumerating, and characterizing these cells may help for guiding treatment decisions before the detection of overt metastases, and for developing novel therapeutics, all in a personalized way. Over the past decade, deep research has been achieved in the development of microfluidic devices for the isolation of CTCs, based on either their physical or biological properties. Size-based approaches provide label-free and high-throughput separation but are limited by low purity. On the contrary, immunoaffinity-based approaches offer high purity but are dependent on surface marker expression and show lower throughput. In particular, the immunomagnetic approach present appealing features such as selectivity, specificity, and CTC collection. There is deep research work going on for the fabrication of magnetic sources generating high magnetic forces, while preserving compatibility and easy implementation with polymer-based microfluidic devices. This could be achieved by the composite approach. Finally, the target device should provide high CTC recovery, purity, and throughput, therefore combining size-based and immunomagnetic-based separation approaches could meet this objective.

The thesis has for aim to develop a microfluidic device for CTC isolation through WBC depletion by magnetophoresis. The microfluidic device will integrate arrays of micro-magnets, acting like micro-traps, obtained by the composite approach. This project results from a multi-disciplinary collaboration, with actors from microfluidics (INL-Lyon 1), magnetism (Institut Lumière Matière, ILM), chemistry (INL-Centrale), and biology (Hospices Civils de Lyon, HCL) fields. The developed magnetic chip will be used after a pre-enrichment step in the ClearCell FX1® (Biolidics), which is a system well established at the HCL in a clinical context. The immunomagnetic separation will have for aim to improve purity of this size-selective sorting method, by depleting remaining WBCs, and therefore facilitate downstream analysis. The device should therefore present high recovery and good throughput, as well as suitability for downstream analysis. The advantage of this negative selection approach relies on the size-independent and tumor marker-independent separation, which enables the recovery of heterogeneous cancer cells (Figure 1.24).

The thesis work could be divided in several steps:

- Fabrication of the micro-magnet with the composite approach and characterization of their magnetic performances
- Integration into a microfluidic device for cell sorting and optimization of the trapping performances
- Study of the magnetic chip compatibility with biological analysis
- Application for cancer cell isolation from whole blood and downstream analysis

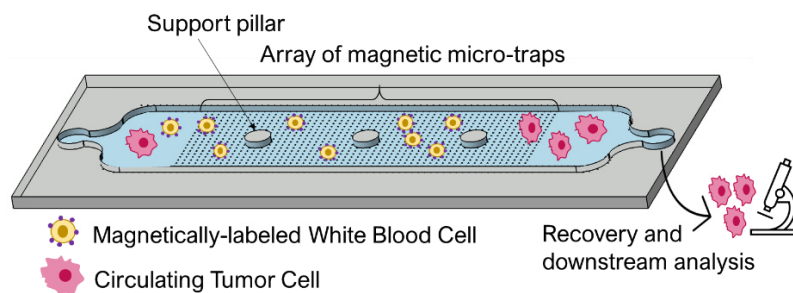


Figure 1.24: CTC enrichment after trapping of magnetically labeled WBCs on integrated micro-magnets obtained by the composite approach.

References

1. Mehlen, P.; Puisieux, A. Metastasis: a question of life or death. *Nat. Rev. Cancer* **2006**, *6*, 449–458, doi:10.1038/nrc1886.
2. Ashworth, T.R. A Case of Cancer in Which Cells Similar to Those in the Tumours Were Seen in the Blood after Death. *Med. J. Aust.* **1869**, *14*, 146–147.
3. Tanaka, F.; Yoneda, K.; Kondo, N.; Hashimoto, M.; Takuwa, T.; Matsumoto, S.; Okumura, Y.; Rahman, S.; Tsubota, N.; Tsujimura, T.; et al. Circulating tumor cell as a diagnostic marker in primary lung cancer. *Clin. Cancer Res.* **2009**, *15*, 6980–6986, doi:10.1158/1078-0432.CCR-09-1095.
4. Thiele, J.A.; Bethel, K.; Králíčková, M.; Kuhn, P. Circulating Tumor Cells: Fluid Surrogates of Solid Tumors. *Annu. Rev. Pathol. Mech. Dis.* **2017**, *12*, 419–447.
5. Moreno, J.G.; Miller, M.C.; Gross, S.; Allard, W.J.; Gomella, L.G.; Terstappen, L.W.M.M. Circulating tumor cells predict survival in patients with metastatic prostate cancer. *Urology* **2005**, *65*, 713–718, doi:10.1016/j.urology.2004.11.006.
6. Cristofanilli, M.; Hayes, D.F.; Budd, G.T.; Ellis, M.J.; Stopeck, A.; Reuben, J.M.; Doyle, G. V.; Matera, J.; Allard, W.J.; Miller, M.C.; et al. Circulating tumor cells: A novel prognostic factor for newly diagnosed metastatic breast cancer. *J. Clin. Oncol.* **2005**, *23*, 1420–1430, doi:10.1200/JCO.2005.08.140.
7. La Thangue, N.B.; Kerr, D.J. Predictive biomarkers: a paradigm shift towards personalized cancer medicine. *Nat. Rev. Clin. Oncol.* **2011**, *8*, 587–596, doi:10.1038/nrclinonc.2011.121.
8. Den Toonder, J. Circulating tumor cells: The Grand Challenge. *Lab Chip* **2011**, *11*, 375–377, doi:10.1039/c0lc90100h.
9. Cristofanilli, M. Circulating Tumor Cells, Disease Progression, and Survival in Metastatic Breast Cancer. *Semin. Oncol.* **2006**, *33*, 9–14, doi:10.1053/j.seminoncol.2006.03.016.
10. Jin, X.R.; Zhu, L.Y.; Qian, K.; Feng, Y.G.; Zhou, J.H.; Wang, R.W.; Bai, L.; Deng, B.; Liang, N.; Tan, Q.Y. Circulating tumor cells in early stage lung adenocarcinoma: A case series report and literature review. *Oncotarget* **2017**, *8*, 23130–23141, doi:10.18632/oncotarget.15506.
11. Chami, F.; Mohan, S.; Guevara, T.; Clipson, A.; Rothwell, D.G.; Dive, C. Early Dissemination of Circulating Tumor Cells: Biological and Clinical Insights. *Front. Oncol.* **2021**, *11*.
12. Alix-Panabières, C.; Pantel, K. Clinical applications of circulating tumor cells and circulating tumor DNA as liquid biopsy. *Cancer Discov.* **2016**, *6*, 479–491, doi:10.1158/2159-8290.CD-15-1483.
13. Quandt, D.; Zucht, H.D.; Amann, A.; Wulf-Goldenberg, A.; Borrebaeck, C.; Cannarile, M.; Lambrechts, D.; Oberacher, H.; Garrett, J.; Nayak, T.; et al. Implementing liquid biopsies into clinical decision making for cancer immunotherapy. *Oncotarget* **2017**, *8*, 48507–48520.
14. Hölzel, M.; Bovier, A.; Tüting, T. Plasticity of tumour and immune cells: a source of heterogeneity and a cause for therapy resistance? *Nat. Rev. Cancer* **2013**, *13*, 365–376.
15. Francart, M.E.; Lambert, J.; Vanwynsberghe, A.M.; Thompson, E.W.; Bourcy, M.; Polette, M.; Gilles, C. Epithelial–mesenchymal plasticity and circulating tumor cells: Travel companions to metastases. *Dev. Dyn.* **2018**, *247*, 432–450, doi:10.1002/dvdy.24506.
16. Riethdorf, S.; O’Flaherty, L.; Hille, C.; Pantel, K. Clinical applications of the CellSearch platform in cancer patients. *Adv. Drug Deliv. Rev.* **2018**, *125*, 102–121, doi:10.1016/j.addr.2018.01.011.
17. Mostert, B.; Kraan, J.; Bolt-de Vries, J.; van der Spoel, P.; Sieuwerts, A.M.; Schutte, M.; Timmermans, A.M.; Foekens, R.; Martens, J.W.M.; Gratama, J.-W.; et al. Detection of circulating tumor cells in breast cancer may improve through enrichment with anti-CD146. *Breast Cancer Res. Treat.* **2011**, *127*, 33–41, doi:10.1007/s10549-010-0879-y.
18. Smirnov, D.A.; Zweitzig, D.R.; Foulk, B.W.; Miller, M.C.; Doyle, G. V.; Pienta, K.J.; Meropol, N.J.; Weiner, L.M.; Cohen, S.J.; Moreno, J.G.; et al. Global gene expression profiling of circulating tumor cells. *Cancer Res.* **2005**, *65*, 4993–4997, doi:10.1158/0008-5472.CAN-04-4330.
19. Naume, B.; Borgen, E.; Tøssvik, S.; Pavlak, N.; Oates, D.; Nesland, J.M. Detection of isolated tumor cells in peripheral blood and in BM: evaluation of a new enrichment method. *Cytotherapy* **2004**, *6*, 244–252,

doi:10.1080/14653240410006086.

20. Vona, G.; Sabile, A.; Louha, M.; Sitruk, V.; Romana, S.; Schütze, K.; Capron, F.; Franco, D.; Pazzagli, M.; Vekemans, M.; et al. Isolation by size of epithelial tumor cells : a new method for the immunomorphological and molecular characterization of circulating tumor cells. *Am. J. Pathol.* **2000**, *156*, 57–63, doi:10.1016/S0002-9440(10)64706-2.
21. Lin, E.; Cao, T.; Nagrath, S.; King, M.R. Circulating Tumor Cells: Diagnostic and Therapeutic Applications. *Annu. Rev. Biomed. Eng.* **2018**, *20*, 329–352, doi:10.1146/annurev-bioeng-062117-120947.
22. Low, W.S.; Wan Abas, W.A.B. Benchtop technologies for circulating tumor cells separation based on biophysical properties. *Biomed Res. Int.* **2015**, *2015*, 239362, doi:10.1155/2015/239362.
23. Yamauchi, K.; Yang, M.; Jiang, P.; Yamamoto, N.; Xu, M.; Amoh, Y.; Tsuji, K.; Bouvet, M.; Tsuchiya, H.; Tomita, K.; et al. Real-time in vivo dual-color imaging of intracapillary cancer cell and nucleus deformation and migration. *Cancer Res.* **2005**, *65*, 4246–4252, doi:10.1158/0008-5472.CAN-05-0069.
24. Wirtz, D.; Konstantopoulos, K.; Searson, P.C. The physics of cancer: The role of physical interactions and mechanical forces in metastasis. *Nat. Rev. Cancer* **2011**, *11*, 512–522, doi:10.1038/nrc3080.
25. Zhou, M. Da; Hao, S.; Williams, A.J.; Harouaka, R.A.; Schrand, B.; Rawal, S.; Ao, Z.; Brennaman, R.; Gilboa, E.; Lu, B.; et al. Separable bilayer microfiltration device for viable label-free enrichment of circulating tumour cells. *Sci. Rep.* **2014**, *4*, 1–11, doi:10.1038/srep07392.
26. Park, E.S.; Jin, C.; Guo, Q.; Ang, R.R.; Duffy, S.P.; Matthews, K.; Azad, A.; Abdi, H.; Todenhöfer, T.; Bazov, J.; et al. Continuous Flow Deformability-Based Separation of Circulating Tumor Cells Using Microfluidic Ratchets. *Small* **2016**, *12*, 1909–1919, doi:10.1002/sml.201503639.
27. Chen, Y.H.; Pulikkathodi, A.K.; Ma, Y.D.; Wang, Y.L.; Lee, G. Bin A microfluidic platform integrated with field-effect transistors for enumeration of circulating tumor cells. *Lab Chip* **2019**, *19*, 618–625, doi:10.1039/c8lc01072b.
28. Yin, J.; Mou, L.; Yang, M.; Zou, W.; Du, C.; Zhang, W.; Jiang, X. Highly efficient capture of circulating tumor cells with low background signals by using pyramidal microcavity array. *Anal. Chim. Acta* **2019**, *1060*, 133–141, doi:10.1016/j.aca.2019.01.054.
29. Wang, K.; Zhou, L.; Zhao, S.; Cheng, Z.; Qiu, S.; Lu, Y.; Wu, Z.; Wahab, A.H.A.A.; Mao, H.; Zhao, J. A microfluidic platform for high-purity separating circulating tumor cells at the single-cell level. *Talanta* **2019**, *200*, 169–176, doi:10.1016/j.talanta.2019.03.035.
30. Armbrecht, L.; Rutschmann, O.; Szczerba, B.M.; Nikoloff, J.; Aceto, N.; Dittrich, P.S. Quantification of Protein Secretion from Circulating Tumor Cells in Microfluidic Chambers. *Adv. Sci.* **2020**, *1903237*, 1–10, doi:10.1002/advs.201903237.
31. Zhang, X.; Lu, X.; Gao, W.; Wang, Y.; Jia, C.; Cong, H. A label-free microfluidic chip for the highly selective isolation of single and cluster CTCs from breast cancer patients. *Transl. Oncol.* **2021**, *14*, doi:10.1016/j.tranon.2020.100959.
32. Fan, X.; Jia, C.; Yang, J.; Li, G.; Mao, H.; Jin, Q.; Zhao, J. A microfluidic chip integrated with a high-density PDMS-based microfiltration membrane for rapid isolation and detection of circulating tumor cells. *Biosens. Bioelectron.* **2015**, *71*, 380–386, doi:10.1016/j.bios.2015.04.080.
33. Xu, L.; Mao, X.; Imrali, A.; Syed, F.; Mutsvangwa, K.; Berney, D.; Cathcart, P.; Hines, J.; Shamash, J.; Lu, Y.J. Optimization and evaluation of a novel size based circulating tumor cell isolation system. *PLoS One* **2015**, *10*, 1–23, doi:10.1371/journal.pone.0138032.
34. Gogoi, P.; Sepehri, S.; Zhou, Y.; Gorin, M.A.; Paolillo, C.; Capoluongo, E.; Gleason, K.; Payne, A.; Boniface, B.; Cristofanilli, M.; et al. Development of an Automated and Sensitive Microfluidic Device for Capturing and Characterizing Circulating Tumor Cells (CTCs) from Clinical Blood Samples. *PLoS One* **2016**, *11*, e0147400, doi:10.1371/journal.pone.0147400.
35. Hvichia, G.E.; Parveen, Z.; Wagner, C.; Janning, M.; Quidde, J.; Stein, A.; Müller, V.; Loges, S.; Neves, R.P.L.; Stoecklein, N.H.; et al. A novel microfluidic platform for size and deformability based separation and the subsequent molecular characterization of viable circulating tumor cells. *Int. J. Cancer* **2016**, *138*, 2894–2904, doi:10.1002/ijc.30007.

36. Yagi, S.; Koh, Y.; Akamatsu, H.; Kanai, K.; Hayata, A.; Tokudome, N.; Akamatsu, K.; Endo, K.; Nakamura, S.; Higuchi, M.; et al. Development of an automated size-based filtration system for isolation of circulating tumor cells in lung cancer patients. *PLoS One* **2017**, *12*, 1–12, doi:10.1371/journal.pone.0179744.
37. Chen, H.; Cao, B.; Sun, B.; Cao, Y.; Yang, K.; Lin, Y.S.; Chen, H. Highly-sensitive capture of circulating tumor cells using micro-ellipse filters. *Sci. Rep.* **2017**, *7*, 1–10, doi:10.1038/s41598-017-00232-6.
38. Masuda, T.; Song, W.; Nakanishi, H.; Lei, W.; Noor, A.M.; Arai, F. Rare cell isolation and recovery on open-channel microfluidic chip. *PLoS One* **2017**, *12*, 1–14, doi:10.1371/journal.pone.0174937.
39. Ribeiro-Samy, S.; Oliveira, M.I.; Pereira-Veiga, T.; Muinelo-Romay, L.; Carvalho, S.; Gaspar, J.; Freitas, P.P.; López-López, R.; Costa, C.; Diéguez, L. Fast and efficient microfluidic cell filter for isolation of circulating tumor cells from unprocessed whole blood of colorectal cancer patients. *Sci. Rep.* **2019**, *9*, 1–12, doi:10.1038/s41598-019-44401-1.
40. Liu, Y.; Li, T.; Xu, M.; Zhang, W.; Xiong, Y.; Nie, L.; Wang, Q.; Li, H.; Wang, W. A high-throughput liquid biopsy for rapid rare cell separation from large-volume samples. *Lab Chip* **2019**, doi:10.1039/C8LC01048J.
41. Hosokawa, M.; Hayata, T.; Fukuda, Y.; Arakaki, A.; Yoshino, T.; Tanaka, T.; Matsunaga, T. Size-selective microcavity array for rapid and efficient detection of circulating tumor cells. *Anal. Chem.* **2010**, *82*, 6629–6635, doi:10.1021/ac101222x.
42. Hosokawa, M.; Yoshikawa, T.; Negishi, R.; Yoshino, T.; Koh, Y.; Kenmotsu, H.; Naito, T.; Takahashi, T.; Yamamoto, N.; Kikuhara, Y.; et al. Microcavity array system for size-based enrichment of circulating tumor cells from the blood of patients with small-cell lung cancer. *Anal. Chem.* **2013**, *85*, 5692–5698, doi:10.1021/ac400167x.
43. Yin, J.; Deng, J.; Du, C.; Zhang, W.; Jiang, X. Microfluidics-based approaches for separation and analysis of circulating tumor cells. *TrAC Trends Anal. Chem.* **2019**, *117*, 84–100, doi:https://doi.org/10.1016/j.trac.2019.07.018.
44. Yin, J.; Deng, J.; Wang, L.; Du, C.; Zhang, W.; Jiang, X. Detection of Circulating Tumor Cells by Fluorescence Microspheres-Mediated Amplification. *Anal. Chem.* **2020**, *92*, 6968–6976, doi:10.1021/acs.analchem.9b05844.
45. Armbrecht, L.; Rutschmann, O.; Szczerba, B.M.; Nikoloff, J.; Aceto, N.; Dittrich, P.S. Quantification of Protein Secretion from Circulating Tumor Cells in Microfluidic Chambers. *Adv. Sci.* **2020**, *1903237*, 1–10, doi:10.1002/advs.201903237.
46. Aceto, N.; Bardia, A.; Miyamoto, D.T.; Donaldson, M.C.; Wittner, B.S.; Spencer, J.A.; Yu, M.; Pely, A.; Engstrom, A.; Zhu, H.; et al. Circulating tumor cell clusters are oligoclonal precursors of breast cancer metastasis. *Cell* **2014**, *158*, 1110–1122, doi:10.1016/j.cell.2014.07.013.
47. Szczerba, B.M.; Castro-Giner, F.; Vetter, M.; Krol, I.; Gkoutela, S.; Landin, J.; Scheidmann, M.C.; Donato, C.; Scherrer, R.; Singer, J.; et al. Neutrophils escort circulating tumour cells to enable cell cycle progression. *Nature* **2019**, *566*, 553–557, doi:10.1038/s41586-019-0915-y.
48. Mouchemore, K.A.; Anderson, R.L.; Hamilton, J.A. Neutrophils, G-CSF and their contribution to breast cancer metastasis. *FEBS J.* **2018**, *285*, 665–679, doi:https://doi.org/10.1111/febs.14206.
49. Huang, L.R.; Cox, E.C.; Austin, R.H.; Sturm, J.C. Continuous Particle Separation Through Deterministic Lateral Displacement. *Science (80-.)*. **2004**, *304*, 987–990, doi:10.1126/science.1094567.
50. Inglis, D.W.; Davis, J.A.; Austin, R.H.; Sturm, J.C. Critical particle size for fractionation by deterministic lateral displacement. *Lab Chip* **2006**, *6*, 655–658, doi:10.1039/b515371a.
51. Louterback, K.; D'Silva, J.; Liu, L.; Wu, A.; Austin, R.H.; Sturm, J.C. Deterministic separation of cancer cells from blood at 10 mL/min. *AIP Adv.* **2012**, *2*, doi:10.1063/1.4758131.
52. Au, S.H.; Edd, J.; Stoddard, A.E.; Wong, K.H.K.; Fachin, F.; Maheswaran, S.; Haber, D.A.; Stott, S.L.; Kapur, R.; Toner, M. Microfluidic isolation of circulating tumor cell clusters by size and asymmetry. *Sci. Rep.* **2017**, *7*, 1–10, doi:10.1038/s41598-017-01150-3.
53. Duda, D.G.; Duyverman, A.M.M.J.; Kohno, M.; Snuderl, M.; Steller, E.J.A.; Fukumura, D.; Jain, R.K. Malignant cells facilitate lung metastasis by bringing their own soil. *Proc. Natl. Acad. Sci. U. S. A.* **2010**, *107*, 21677–21682, doi:10.1073/pnas.1016234107.

54. Kalyan, S.; Torabi, C.; Khoo, H.; Sung, H.W.; Choi, S.E.; Wang, W.; Treutler, B.; Kim, D.; Hur, S.C. Inertial microfluidics enabling clinical research. *Micromachines* **2021**, *12*, 1–43, doi:10.3390/mi12030257.
55. Zhou, J.; Tu, C.; Liang, Y.; Huang, B.; Fang, Y.; Liang, X.; Papautsky, I.; Ye, X. Isolation of cells from whole blood using shear-induced diffusion. *Sci. Rep.* **2018**, *8*, 1–13, doi:10.1038/s41598-018-27779-2.
56. Zhou, J.; Kulasinghe, A.; Bogseth, A.; O'Byrne, K.; Punyadeera, C.; Papautsky, I. Isolation of circulating tumor cells in non-small-cell-lung-cancer patients using a multi-flow microfluidic channel. *Microsystems Nanoeng.* **2019**, *5*, doi:10.1038/s41378-019-0045-6.
57. Zhou, J.; Papautsky, I. Fundamentals of inertial focusing in microchannels. *Lab Chip* **2013**, *13*, 1121–1132, doi:10.1039/c2lc41248a.
58. Kulasinghe, A.; Zhou, J.; Kenny, L.; Papautsky, I.; Punyadeera, C. Capture of circulating tumour cell clusters using straight microfluidic chips. *Cancers (Basel)*. **2019**, *11*, 1–11, doi:10.3390/cancers11010089.
59. Zhou, J.; Tu, C.; Liang, Y.; Huang, B.; Fang, Y.; Liang, X.; Ye, X. The label-free separation and culture of tumor cells in a microfluidic biochip. *Analyst* **2020**, *145*, 1706–1715, doi:10.1039/c9an02092f.
60. Kuntaegowdanahalli, S.S.; Bhagat, A.A.S.; Kumar, G.; Papautsky, I. Inertial microfluidics for continuous particle separation in spiral microchannels. *Lab Chip* **2009**, *9*, 2973–2980, doi:10.1039/b908271a.
61. Hou, H.W.; Warkiani, M.E.; Khoo, B.L.; Li, Z.R.; Soo, R.A.; Tan, D.S.W.; Lim, W.T.; Han, J.; Bhagat, A.A.S.; Lim, C.T. Isolation and retrieval of circulating tumor cells using centrifugal forces. *Sci. Rep.* **2013**, *3*, 1–8, doi:10.1038/srep01259.
62. Khoo, B.L.; Warkiani, M.E.; Tan, D.S.-W.; Bhagat, A.A.S.; Irwin, D.; Lau, D.P.; Lim, A.S.T.; Lim, K.H.; Krisna, S.S.; Lim, W.-T.; et al. Clinical Validation of an Ultra High-Throughput Spiral Microfluidics for the Detection and Enrichment of Viable Circulating Tumor Cells. *PLoS One* **2014**, *9*, e99409, doi:10.1371/journal.pone.0099409.
63. Warkiani, M.E.; Khoo, B.L.; Tan, D.S.W.; Bhagat, A.A.S.; Lim, W.T.; Yap, Y.S.; Lee, S.C.; Soo, R.A.; Han, J.; Lim, C.T. An ultra-high-throughput spiral microfluidic biochip for the enrichment of circulating tumor cells. *Analyst* **2014**, *139*, 3245–3255, doi:10.1039/c4an00355a.
64. Warkiani, M.E.; Guan, G.; Luan, K.B.; Lee, W.C.; Bhagat, A.A.S.; Kant Chaudhuri, P.; Tan, D.S.W.; Lim, W.T.; Lee, S.C.; Chen, P.C.Y.; et al. Slanted spiral microfluidics for the ultra-fast, label-free isolation of circulating tumor cells. *Lab Chip* **2014**, *14*, 128–137, doi:10.1039/c3lc50617g.
65. Warkiani, M.E. brahim.; Khoo, B.L. ua.; Wu, L.; Tay, A.K. a. P.; Bhagat, A.A. sga. S.; Han, J.; Lim, C.T. ec. Ultra-fast, label-free isolation of circulating tumor cells from blood using spiral microfluidics. *Nat. Protoc.* **2016**, *11*, 134–148, doi:10.1038/nprot.2016.003.
66. Lin, E.; Rivera-Báez, L.; Fouladdel, S.; Yoon, H.J.; Guthrie, S.; Wieger, J.; Deol, Y.; Keller, E.; Sahai, V.; Simeone, D.M.; et al. High-Throughput Microfluidic Labyrinth for the Label-free Isolation of Circulating Tumor Cells. *Cell Syst.* **2017**, *5*, 295–304.e4, doi:10.1016/j.cels.2017.08.012.
67. Sollier, E.; Go, D.E.; Che, J.; Gossett, D.R.; O'Byrne, S.; Weaver, W.M.; Kummer, N.; Rettig, M.; Goldman, J.; Nickols, N.; et al. Size-selective collection of circulating tumor cells using Vortex technology. *Lab Chip* **2014**, *14*, 63–77, doi:10.1039/c3lc50689d.
68. Che, J.; Yu, V.; Dhar, M.; Renier, C.; Matsumoto, M.; Heirich, K.; Garon, E.B.; Goldman, J.; Rao, J.; Sledge, G.W.; et al. Classification of large circulating tumor cells isolated with ultra-high throughput microfluidic Vortex technology. *Oncotarget* **2016**, *7*, doi:10.18632/oncotarget.7220.
69. Dhar, M.; Pao, E.; Renier, C.; Go, D.E.; Che, J.; Montoya, R.; Conrad, R.; Matsumoto, M.; Heirich, K.; Triboulet, M.; et al. Label-free enumeration, collection and downstream cytological and cytogenetic analysis of circulating tumor cells. *Sci. Rep.* **2016**, *6*, 1–12, doi:10.1038/srep35474.
70. Renier, C.; Pao, E.; Che, J.; Liu, H.E.; Lemaire, C.A.; Matsumoto, M.; Triboulet, M.; Srivinas, S.; Jeffrey, S.S.; Rettig, M.; et al. Label-free isolation of prostate circulating tumor cells using Vortex microfluidic technology. *npj Precis. Oncol.* **2017**, *1*, 15, doi:10.1038/s41698-017-0015-0.
71. Dhar, M.; Pao, E.; Renier, C.; Go, D.E.; Che, J.; Montoya, R.; Conrad, R.; Matsumoto, M.; Heirich, K.; Triboulet, M.; et al. Label-free enumeration, collection and downstream cytological and cytogenetic analysis of circulating tumor cells. *Sci. Rep.* **2016**, *6*, 1–12, doi:10.1038/srep35474.

72. Shaw, A.T.; Yeap, B.Y.; Solomon, B.J.; Riely, G.J.; Gainor, J.; Engelman, J.A.; Shapiro, G.I.; Costa, D.B.; Ou, S.H.I.; Butaney, M.; et al. Effect of crizotinib on overall survival in patients with advanced non-small-cell lung cancer harbouring ALK gene rearrangement: A retrospective analysis. *Lancet Oncol.* **2011**, *12*, 1004–1012, doi:10.1016/S1470-2045(11)70232-7.
73. Allard, W.J.; Matera, J.; Miller, M.C.; Repollet, M.; Connelly, M.C.; Rao, C.; Tibbe, A.G.J.; Uhr, J.W.; Terstappen, L.W.M.M. Tumor Cells Circulate in the Peripheral Blood of All Major Carcinomas but not in Healthy Subjects or Patients With Nonmalignant Diseases. *Clin. Cancer Res.* **2004**, *10*, 6897–6904.
74. Jackson, J.M.; Witek, M.A.; Kamande, J.W.; Soper, S.A. Materials and Microfluidics: Enabling the Efficient Isolation and Analysis of Circulating Tumour Cells. *Chem. Soc. Rev.* **2017**, *46*, 4245–4280, doi:10.1039/c7cs00016b.
75. Di Trapani, M.; Manaresi, N.; Medoro, G. DEPArray™ system: An automatic image-based sorter for isolation of pure circulating tumor cells. *Cytom. Part A* **2018**, *93*, 1260–1266, doi:10.1002/cyto.a.23687.
76. Gupta, V.; Jafferji, I.; Garza, M.; Melnikova, V.O.; Hasegawa, D.K.; Pethig, R.; Davis, D.W. ApoStream™, a new dielectrophoretic device for antibody independent isolation and recovery of viable cancer cells from blood. *Biomicrofluidics* **2012**, *6*, doi:10.1063/1.4731647.
77. Peeters, D.J.E.; De Laere, B.; Van Den Eynden, G.G.; Van Laere, S.J.; Rothé, F.; Ignatiadis, M.; Sieuwerts, A.M.; Lambrechts, D.; Rutten, A.; Van Dam, P.A.; et al. Semiautomated isolation and molecular characterisation of single or highly purified tumour cells from CellSearch enriched blood samples using dielectrophoretic cell sorting. *Br. J. Cancer* **2013**, *108*, 1358–1367, doi:10.1038/bjc.2013.92.
78. Hughes, M.P.; Pethig, R.; Wang, X.B. Dielectrophoretic forces on particles in travelling electric fields. *J. Phys. D. Appl. Phys.* **1996**, *29*, 474–482, doi:10.1088/0022-3727/29/2/029.
79. O'Shannessy, D.J.; Davis, D.W.; Anderes, K.; Somers, E.B. Isolation of Circulating Tumor Cells from Multiple Epithelial Cancers with ApoStream® for Detecting (or Monitoring) the Expression of Folate Receptor Alpha. *Biomark. Insights* **2016**, *11*, 7–18, doi:10.4137/BMI.S35075.
80. Balasubramanian, P.; Kinders, R.J.; Kummar, S.; Gupta, V.; Hasegawa, D.; Menachery, A.; Lawrence, S.M.; Wang, L.; Ferry-Galow, K.; Davis, D.; et al. Antibody-independent capture of circulating tumor cells of non-epithelial origin with the ApoStream® system. *PLoS One* **2017**, *12*, 1–15, doi:10.1371/journal.pone.0175414.
81. Le Du, F.; Fujii, T.; Kida, K.; Davis, D.W.; Park, M.; Liu, D.D.; Wu, W.; Chavez-MacGregor, M.; Barcenas, C.H.; Valero, V.; et al. EpCAM-independent isolation of circulating tumor cells with epithelial-to-mesenchymal transition and cancer stem cell phenotypes using ApoStream® in patients with breast cancer treated with primary systemic therapy. *PLoS One* **2020**, *15*, 1–13, doi:10.1371/journal.pone.0229903.
82. Shim, S.; Stemke-Hale, K.; Tsimberidou, A.M.; Noshari, J.; Anderson, T.E.; Gascoyne, P.R.C. Antibody-independent isolation of circulating tumor cells by continuous-flow dielectrophoresis. *Biomicrofluidics* **2013**, *7*, 1–12, doi:10.1063/1.4774304.
83. Chou, W.P.; Wang, H.M.; Chang, J.H.; Chiu, T.K.; Hsieh, C.H.; Liao, C.J.; Wu, M.H. The utilization of optically-induced-dielectrophoresis (ODEP)-based virtual cell filters in a microfluidic system for continuous isolation and purification of circulating tumour cells (CTCs) based on their size characteristics. *Sensors Actuators, B Chem.* **2017**, *241*, 245–254, doi:10.1016/j.snb.2016.10.075.
84. Liao, C.J.; Hsieh, C.H.; Chiu, T.K.; Zhu, Y.X.; Wang, H.M.; Hung, F.C.; Chou, W.P.; Wu, M.H. An optically induced dielectrophoresis (ODEP)-based microfluidic system for the isolation of high-purity CD45neg/EpCAMneg cells from the blood samples of cancer patients-demonstration and initial exploration of the clinical significance of these cells. *Micromachines* **2018**, *9*, doi:10.3390/mi9110563.
85. Li, M.; Anand, R.K. High-Throughput Selective Capture of Single Circulating Tumor Cells by Dielectrophoresis at a Wireless Electrode Array. *J. Am. Chem. Soc.* **2017**, *139*, 8950–8959, doi:10.1021/jacs.7b03288.
86. Nagrath, S.; Sequist, L. V.; Maheswaran, S.; Bell, D.W.; Irimia, D.; Ulkus, L.; Smith, M.R.; Kwak, E.L.; Digumarthy, S.; Muzikansky, A.; et al. Isolation of rare circulating tumour cells in cancer patients by microchip technology. *Nature* **2007**, *450*, 1235–1239, doi:10.1038/nature06385.
87. Stott, S.L.; Hsu, C.; Tsukrov, D.I.; Yu, M.; Miyamoto, D.T.; Waltman, B.A.; Rothenberg, S.M.; Shah, A.M.;

- Smas, M.E.; Korir, G.K.; et al. Isolation of circulating tumor cells using a microvortex-generating herringbone-chip. *Proc. Natl. Acad. Sci. U. S. A.* **2010**, doi:10.1073/pnas.1012539107/-/DCSupplemental.www.pnas.org/cgi/doi/10.1073/pnas.1012539107.
88. Yu, M.; Ting, D.T.; Stott, S.L.; Wittner, B.S.; Ozsolak, F.; Paul, S.; Ciciliano, J.C.; Smas, M.E.; Winokur, D.; Gilman, A.J.; et al. RNA sequencing of pancreatic circulating tumour cells implicates WNT signalling in metastasis. *Nature* **2012**, *487*, 510–513, doi:10.1038/nature11217.
 89. Yu, M.; Bardia, A.; Wittner, B.S.; Stott, S.L.; Smas, M.E.; Ting, D.T.; Isakoff, S.J.; Ciciliano, J.C.; Wells, M.N.; Shah, A.M.; et al. Circulating breast tumor cells exhibit dynamic changes in epithelial and mesenchymal composition. *Science* (80-.). **2013**, *339*, 580–584, doi:10.1126/science.1228522.
 90. Wang, S.; Liu, K.; Liu, J.; Yu, Z.T.-F.; Xu, X.; Zhao, L.; Lee, T.; Lee, E.K.; Reiss, J.; Lee, Y.-K.; et al. Highly efficient capture of circulating tumor cells by using nanostructured silicon substrates with integrated chaotic micromixers. *Angew. Chem. Int. Ed. Engl.* **2011**, *50*, 3084–3088, doi:10.1002/anie.201005853.
 91. Yoon, H.J.; Kim, T.H.; Zhang, Z.; Azizi, E.; Pham, T.M.; Paoletti, C.; Lin, J.; Ramnath, N.; Wicha, M.S.; Hayes, D.F.; et al. Sensitive capture of circulating tumour cells by functionalized graphene oxide nanosheets. *Nat. Nanotechnol.* **2013**, *8*, 735–741, doi:10.1038/nnano.2013.194.
 92. Navya, P.N.; Daima, H.K. Rational engineering of physicochemical properties of nanomaterials for biomedical applications with nanotoxicological perspectives. *Nano Conver.* **2016**, *3*, 1–14, doi:10.1186/s40580-016-0064-z.
 93. Lin, M.; Chen, J.-F.; Lu, Y.-T.; Zhang, Y.; Song, J.; Hou, S.; Ke, Z.; Tseng, H.-R. Nanostructure embedded microchips for detection, isolation, and characterization of circulating tumor cells. *Acc. Chem. Res.* **2014**, *47*, 2941–2950, doi:10.1021/ar5001617.
 94. Reategui, E.; Aceto, N.; Lim, E.J.; Sullivan, J.P.; Jensen, A.E.; Zeinali, M.; Martel, J.M.; Aranyosi, A.J.; Li, W.; Castleberry, S.; et al. Tunable nanostructured coating for the capture and selective release of viable circulating tumor cells. *Adv. Mater.* **2015**, *27*, 1593–1599, doi:10.1002/adma.201404677.
 95. Yoon, H.J.; Shanker, A.; Wang, Y.; Kozminsky, M.; Jin, Q.; Palanisamy, N.; Burness, M.L.; Azizi, E.; Simeone, D.M.; Wicha, M.S.; et al. Tunable Thermal-Sensitive Polymer-Graphene Oxide Composite for Efficient Capture and Release of Viable Circulating Tumor Cells. *Adv. Mater.* **2016**, *28*, 4891–4897, doi:10.1002/adma.201600658.
 96. Li, W.; Reategui, E.; Park, M.H.; Castleberry, S.; Deng, J.Z.; Hsu, B.; Mayner, S.; Jensen, A.E.; Sequist, L. V; Maheswaran, S.; et al. Biodegradable nano-films for capture and non-invasive release of circulating tumor cells. *Biomaterials* **2015**, *65*, 93–102, doi:10.1016/j.biomaterials.2015.06.036.
 97. Park, M.H.; Reategui, E.; Li, W.; Tessier, S.N.; Wong, K.H.K.; Jensen, A.E.; Thapar, V.; Ting, D.; Toner, M.; Stott, S.L.; et al. Enhanced Isolation and Release of Circulating Tumor Cells Using Nanoparticle Binding and Ligand Exchange in a Microfluidic Chip. *J. Am. Chem. Soc.* **2017**, *139*, 2741–2749, doi:10.1021/jacs.6b12236.
 98. Shen, M.Y.; Chen, J.F.; Luo, C.H.; Lee, S.; Li, C.H.; Yang, Y.L.; Tsai, Y.H.; Ho, B.C.; Bao, L.R.; Lee, T.J.; et al. Glycan Stimulation Enables Purification of Prostate Cancer Circulating Tumor Cells on PEDOT NanoVelcro Chips for RNA Biomarker Detection. *Adv. Healthc. Mater.* **2018**, *7*, 1–9, doi:10.1002/adhm.201700701.
 99. Dao, M.; Suresh, S.; Huang, T.J.; Li, P.; Mao, Z.; Peng, Z.; Zhou, L.; Chen, Y.; Huang, P.H.; Truica, C.I.; et al. Acoustic separation of circulating tumor cells. *Proc. Natl. Acad. Sci. U. S. A.* **2015**, *112*, 4970–4975, doi:10.1073/pnas.1504484112.
 100. Song, Y.; Li, M.; Pan, X.; Wang, Q.; Li, D. Size-based cell sorting with a resistive pulse sensor and an electromagnetic pump in a microfluidic chip. *Electrophoresis* **2015**, *36*, 398–404, doi:10.1002/elps.201400292.
 101. Li, Y.; Guo, Z.; Qu, S. Living cell manipulation in a microfluidic device by femtosecond optical tweezers. *Opt. Lasers Eng.* **2014**, *55*, 150–154, doi:https://doi.org/10.1016/j.optlaseng.2013.11.001.
 102. Plouffe, B.D.; Murthy, S.K.; Lewis, L.H. Fundamentals and application of magnetic particles in cell isolation and enrichment: a review. *Reports Prog. Phys.* **2015**, *78*, 16601.
 103. Munaz, A.; Shiddiky, M.J.A.; Nguyen, N.T. Recent advances and current challenges in magnetophoresis

- based micro magnetofluidics. *Biomicrofluidics* **2018**, *12*, doi:10.1063/1.5035388.
104. Alnaimat, F.; Dagher, S.; Mathew, B.; Hilal-Alnqbi, A.; Khashan, S. Microfluidics Based Magnetophoresis: A Review. *Chem. Rec.* **2018**, *18*, 1596–1612, doi:10.1002/tcr.201800018.
 105. Alnaimat, F.; Karam, S.; Mathew, B.; Mathew, B. Magnetophoresis and Microfluidics: A Great Union. *IEEE Nanotechnol. Mag.* **2020**, *14*, 24–41, doi:10.1109/MNANO.2020.2966029.
 106. Cao, Q.; Fan, Q.; Chen, Q.; Liu, C.; Han, X.; Li, L. Recent advances in manipulation of micro- and nano-objects with magnetic fields at small scales. *Mater. Horizons* **2020**, *7*, 638–666, doi:10.1039/c9mh00714h.
 107. Luo, L.; He, Y. Magnetically driven microfluidics for isolation of circulating tumor cells. *Cancer Med.* **2020**, *9*, 4207–4231, doi:10.1002/cam4.3077.
 108. McCloskey, K.E.; Chalmers, J.J.; Zborowski, M. Magnetic Cell Separation: Characterization of Magnetophoretic Mobility. *Anal. Chem.* **2003**, *75*, 6868–6874, doi:10.1021/ac034315j.
 109. Pamme, N. Magnetism and microfluidics. *Lab Chip* **2006**, *6*, 24–38, doi:10.1039/b513005k.
 110. Deman, A.-L.; Le Roy, D. Magnetophoresis in Bio-Devices. In *Engineering of Micro/Nano Biosystems*; Springer, Singapore, 2020; pp. 309–361.
 111. Hung, P.Y.; Jiang, P.S.; Lee, E.F.; Fan, S.K.; Lu, Y.W. Genomic DNA extraction from whole blood using a digital microfluidic (DMF) platform with magnetic beads. *Microsyst. Technol.* **2015**, *23*, 313–320, doi:10.1007/s00542-015-2512-9.
 112. Dias, T.M.; Cardoso, F.A.; Martins, S.A.M.; Martins, V.C.; Cardoso, S.; Gaspar, J.F.; Monteiro, G.; Freitas, P.P. Implementing a strategy for on-chip detection of cell-free DNA fragments using GMR sensors: A translational application in cancer diagnostics using ALU elements. *Anal. Methods* **2016**, *8*, 119–128, doi:10.1039/c5ay01587a.
 113. Garbarino, F.; Minero, G.A.S.; Rizzi, G.; Fock, J.; Hansen, M.F. Integration of rolling circle amplification and optomagnetic detection on a polymer chip. *Biosens. Bioelectron.* **2019**, *142*, 111485, doi:10.1016/j.bios.2019.111485.
 114. Bejhed, R.S.; Tian, B.; Eriksson, K.; Brucas, R.; Oscarsson, S.; Strömberg, M.; Svedlindh, P.; Gunnarsson, K. Magnetophoretic Transport Line System for Rapid On-Chip Attomole Protein Detection. *Langmuir* **2015**, *31*, 10296–10302, doi:10.1021/acs.langmuir.5b01947.
 115. Zirath, H.; Schnetz, G.; Glatz, A.; Spittler, A.; Redl, H.; Peham, J.R. Bedside Immune Monitoring: An Automated Immunoassay Platform for Quantification of Blood Biomarkers in Patient Serum within 20 Minutes. *Anal. Chem.* **2017**, *89*, 4817–4823, doi:10.1021/acs.analchem.6b03624.
 116. Gao, Y.; Huo, W.; Zhang, L.; Lian, J.; Tao, W.; Song, C.; Tang, J.; Shi, S.; Gao, Y. Multiplex measurement of twelve tumor markers using a GMR multi-biomarker immunoassay biosensor. *Biosens. Bioelectron.* **2019**, *123*, 204–210, doi:10.1016/j.bios.2018.08.060.
 117. Gijs, M.A.M.; Lacharme, F.; Lehmann, U. Microfluidic applications of magnetic particles for biological analysis and catalysis. *Chem. Rev.* **2010**, *110*, 1518–1563, doi:10.1021/cr9001929.
 118. Lin, S.; Zhi, X.; Chen, D.; Xia, F.; Shen, Y.; Niu, J.; Huang, S.; Song, J.; Miao, J.; Cui, D.; et al. A flyover style microfluidic chip for highly purified magnetic cell separation. *Biosens. Bioelectron.* **2019**, *129*, 175–181, doi:10.1016/j.bios.2018.12.058.
 119. Zhi, S.; Sun, X.; Feng, Z.; Lei, C.; Zhou, Y. An innovative micro magnetic separator based on 3D micro-copper-coil exciting soft magnetic tips and FeNi wires for bio-target sorting. *Microfluid. Nanofluidics* **2019**, *23*, 0, doi:10.1007/s10404-019-2215-0.
 120. Kye, H.G.; Park, B.S.; Lee, J.M.; Song, M.G.; Song, H.G.; Ahrberg, C.D.; Chung, B.G. Dual-neodymium magnet-based microfluidic separation device. *Sci. Rep.* **2019**, *9*, 1–10, doi:10.1038/s41598-019-45929-y.
 121. Bongaerts, M.; Aizel, K.; Secret, E.; Jan, A.; Nahar, T.; Raudzus, F.; Neumann, S.; Telling, N.; Heumann, R.; Siaugue, J.-M.; et al. Parallelized Manipulation of Adherent Living Cells by Magnetic Nanoparticles-Mediated Forces. *Int. J. Mol. Sci.* **2020**, *21*, 6560, doi:10.3390/ijms21186560.
 122. Nam, J.; Huang, H.; Lim, H.; Lim, C.; Shin, S. Magnetic Separation of Malaria-Infected Red Blood Cells in Various Developmental Stages. *Anal. Chem.* **2013**, *85*, 7316–7323, doi:10.1021/ac4012057.

123. Blue Martin, A.; Wu, W.-T.; Kameneva, M. V.; Antaki, J.F. Development of a High-Throughput Magnetic Separation Device for Malaria-Infected Erythrocytes. *Ann. Biomed. Eng.* **2017**, *45*, 2888–2898, doi:10.1007/s10439-017-1925-2.
124. Moore, L.R.; Mizutani, D.; Tanaka, T.; Buck, A.; Yazer, M.; Zborowski, M.; Chalmers, J.J. Continuous, intrinsic magnetic depletion of erythrocytes from whole blood with a quadrupole magnet and annular flow channel; pilot scale study. *Biotechnol. Bioeng.* **2018**, *115*, 1521–1530, doi:10.1002/bit.26581.
125. Xuan, X. Recent advances in continuous-flow particle manipulations using magnetic fluids. *Micromachines* **2019**, *10*, doi:10.3390/mi10110744.
126. Plouffe, B.D.; Murthy, S.K.; Lewis, L.H. Fundamentals and application of magnetic particles in cell isolation and enrichment: A review. *Reports Prog. Phys.* **2015**, *78*, doi:10.1088/0034-4885/78/1/016601.
127. Gruszecki, P.; Banerjee, C.; Mruczkiewicz, M.; Hellwig, O.; Barman, A.; Krawczyk, M. Chapter Two - The influence of the internal domain wall structure on spin wave band structure in periodic magnetic stripe domain patterns. In *Recent Advances in Topological Ferroics and their Dynamics*; Stamps, R.L., Schultheiß, H., Eds.; Solid State Physics; Academic Press, 2019; Vol. 70, pp. 79–132.
128. Sinha, A.; Ganguly, R.; Puri, I.K. Magnetic separation from superparamagnetic particle suspensions. *J. Magn. Magn. Mater.* **2009**, *321*, 2251–2256, doi:10.1016/j.jmmm.2009.01.034.
129. Furlani, E.P. Analysis of particle transport in a magnetophoretic microsystem. *J. Appl. Phys.* **2006**, *99*, 024912, doi:10.1063/1.2164531.
130. Gerber, R.; Takayasu, M.; Friedlaender, F. Generalization of HGMS theory: The capture of ultra-fine particles. *IEEE Trans. Magn.* **1983**, *19*, 2115–2117, doi:10.1109/TMAG.1983.1062795.
131. Gerber, R. Magnetic filtration of ultra-fine particles. *IEEE Trans. Magn.* **1984**, *20*, 1159–1164, doi:10.1109/TMAG.1984.1063234.
132. Han, X.; Feng, Y.; Cao, Q.; Li, L. Three-dimensional analysis and enhancement of continuous magnetic separation of particles in microfluidics. *Microfluid. Nanofluidics* **2015**, *18*, 1209–1220, doi:10.1007/s10404-014-1516-6.
133. Cugat, O.; Delamare, J.; Reyne, G. Magnetic micro-actuators and systems (MAGMAS). *IEEE Trans. Magn.* **2003**, *39*, 3607–3612, doi:10.1109/TMAG.2003.816763.
134. Plouffe, B.D.; Mahalanabis, M.; Lewis, L.H.; Klapperich, C.M.; Murthy, S.K. Clinically relevant microfluidic magnetophoretic isolation of rare-cell populations for diagnostic and therapeutic monitoring applications. *Anal. Chem.* **2012**, *84*, 1336–1344, doi:10.1021/ac2022844.
135. Dempsey, N.M.; Le Roy, D.; Marelli-Mathevon, H.; Shaw, G.; Dias, A.; Kramer, R.B.G.; Viet Cuong, L.; Kustov, M.; Zanini, L.F.; Villard, C.; et al. Micro-magnetic imprinting of high field gradient magnetic flux sources. *Appl. Phys. Lett.* **2014**, *104*, 262401, doi:10.1063/1.4886375.
136. De Los Santos Valladares, L.; Ionescu, A.; Holmes, S.; Barnes, C.H.W.; Bustamante Domínguez, A.; Avalos Quispe, O.; González, J.C.; Milana, S.; Barbone, M.; Ferrari, A.C.; et al. Characterization of Ni thin films following thermal oxidation in air. *J. Vac. Sci. Technol. B, Nanotechnol. Microelectron. Mater. Process. Meas. Phenom.* **2014**, *32*, 051808, doi:10.1116/1.4895846.
137. Nakano, M.; Oshima, S.; Yanai, T.; Fukunaga, H. Magnetic properties of pulsed laser deposition-fabricated isotropic Pr-Fe-B thick-films magnets for magnetic micro-machines. *J. Appl. Phys.* **2014**, *115*, 1–4, doi:10.1063/1.4867130.
138. Castillo-Torres, K.Y.; Arnold, D.P.; McLamore, E.S. Rapid isolation of *Escherichia coli* from water samples using magnetic microdiscs. *Sensors Actuators, B Chem.* **2019**, *291*, 58–66, doi:10.1016/j.snb.2019.04.043.
139. Keavney, D.; Falco, C. Deposition Techniques for Magnetic Thin Films and Multilayers. In *Magnetic Interactions and Spin Transport*; Springer US, 2003; pp. 413–447.
140. Coey, J.M.D. Experimental methods. In *Magnetism and Magnetic Materials*; Cambridge University Press, 2010; pp. 333–373.
141. Töpfer, J.; Christopher, V. Multi-pole magnetization of NdFeB sintered magnets and thick films for magnetic micro-actuators. *Sensors Actuators, A Phys.* **2004**, *113*, 257–263, doi:10.1016/j.sna.2004.04.011.

142. Dumas-Bouchiat, F.; Zanini, L.F.; Kustov, M.; Dempsey, N.M.; Grechishkin, R.; Hasselbach, K.; Orlianges, J.C.; Champeaux, C.; Catherinot, A.; Givord, D. Thermomagnetically patterned micromagnets. *Appl. Phys. Lett* **2010**, *96*, 102511, doi:10.1063/1.3341190.
143. Hoshino, K.; Huang, Y.; Lane, N.; Huebschman, M.; Uhr, J.W. Microchip-based immunomagnetic detection of circulating tumor cells. *Lab Chip* **2011**, *11*, 3449–3457, doi:10.1039/c1lc20270g.
144. Besant, J.D.; Mohamadi, R.M.; Aldridge, P.M.; Li, Y.; Sargent, E.H.; Kelley, S.O. Velocity valleys enable efficient capture and spatial sorting of nanoparticle-bound cancer cells. *Nanoscale* **2015**, *7*, 6278–6285, doi:10.1039/c5nr00797f.
145. Huang, Y.Y.; Chen, P.; Wu, C.H.; Hoshino, K.; Sokolov, K.; Lane, N.; Liu, H.; Huebschman, M.; Frenkel, E.; Zhang, J.X.J. Screening and Molecular Analysis of Single Circulating Tumor Cells Using Micromagnet Array. *Sci. Rep.* **2015**, *5*, 1–11, doi:10.1038/srep16047.
146. Chen, P.; Huang, Y.Y.; Hoshino, K.; Zhang, J.X.J. Microscale magnetic field modulation for enhanced capture and distribution of rare circulating tumor cells. *Sci. Rep.* **2015**, *5*, 1–9, doi:10.1038/srep08745.
147. Poudineh, M.; Sargent, E.H.; Kelley, S.O. Amplified Micromagnetic Field Gradients Enable High-Resolution Profiling of Rare Cell Subpopulations. *ACS Appl. Mater. Interfaces* **2017**, *9*, 25683–25690, doi:10.1021/acsami.7b04677.
148. Poudineh, M.; Aldridge, P.M.; Ahmed, S.; Green, B.J.; Kermanshah, L.; Nguyen, V.; Tu, C.; Mohamadi, R.M.; Nam, R.K.; Hansen, A.; et al. Tracking the dynamics of circulating tumour cell phenotypes using nanoparticle-mediated magnetic ranking. *Nat. Nanotechnol.* **2017**, *12*, 274–281, doi:10.1038/nnano.2016.239.
149. Labib, M.; Wang, Z.; Ahmed, S.U.; Mohamadi, R.M.; Duong, B.; Green, B.; Sargent, E.H.; Kelley, S.O. Tracking the expression of therapeutic protein targets in rare cells by antibody-mediated nanoparticle labelling and magnetic sorting. *Nat. Biomed. Eng.* **2021**, *5*, 41–52, doi:10.1038/s41551-020-0590-1.
150. Saliba, A.-E.; Saias, L.; Psychari, E.; Minc, N.; Simon, D.; Bidard, F.-C.; Mathiot, C.; Pierga, J.-Y.; Fraissier, V.; Salamero, J.; et al. Microfluidic sorting and multimodal typing of cancer cells in self-assembled magnetic arrays. *Proc. Natl. Acad. Sci.* **2010**, *107*, 14524–14529, doi:10.1073/pnas.1001515107.
151. Malaquin, L.; Kraus, T.; Schmid, H.; Delamarche, E.; Wolf, H. Controlled particle placement through convective and capillary assembly. *Langmuir* **2007**, *23*, 11513–11521, doi:10.1021/la700852c.
152. Autebert, J.; Coudert, B.; Champ, J.; Saias, L.; Guneri, E.T.; Lebofsky, R.; Bidard, F.C.; Pierga, J.Y.; Farace, F.; Descroix, S.; et al. High purity microfluidic sorting and analysis of circulating tumor cells: Towards routine mutation detection. *Lab Chip* **2015**, *15*, 2090–2101, doi:10.1039/c5lc00104h.
153. Tang, M.; Wen, C.-Y.; Wu, L.-L.; Hong, S.-L.; Hu, J.; Xu, C.-M.; Pang, D.-W.; Zhang, Z.-L. A chip assisted immunomagnetic separation system for the efficient capture and in situ identification of circulating tumor cells. *Lab Chip* **2016**, *16*, 1214–1223, doi:10.1039/c5lc01555c.
154. Yu, X.; Feng, X.; Hu, J.; Zhang, Z.-L.; Pang, D.-W. Controlling the Magnetic Field Distribution on the Micrometer Scale and Generation of Magnetic Bead Patterns for Microfluidic Applications. *Langmuir* **2011**, *27*, 5147–5156, doi:10.1021/la104400m.
155. Xu, C.M.; Tang, M.; Feng, J.; Xia, H.F.; Wu, L.L.; Pang, D.W.; Chen, G.; Zhang, Z.L. A liquid biopsy-guided drug release system for cancer theranostics: integrating rapid circulating tumor cell detection and precision tumor therapy. *Lab Chip* **2020**, *20*, 1418–1425, doi:10.1039/d0lc00149j.
156. Kwak, B.; Lee, J.; Lee, J.; Kim, H.S.; Kang, S.; Lee, Y. Spiral shape microfluidic channel for selective isolating of heterogenic circulating tumor cells. *Biosens. Bioelectron.* **2018**, *101*, 311–316, doi:10.1016/j.bios.2017.10.036.
157. Aldridge, P.M.; Mukhopadhyay, M.; Ahmed, S.U.; Zhou, W.; Christinck, E.; Makonnen, R.; Sargent, E.H.; Kelley, S.O. Prismatic Deflection of Live Tumor Cells and Cell Clusters. *ACS Nano* **2018**, *12*, 12692–12700, doi:10.1021/acsnano.8b07616.
158. Hyun, K.-A.; Lee, T.Y.; Lee, S.H.; Jung, H.-I. Two-stage microfluidic chip for selective isolation of circulating tumor cells (CTCs). *Biosens. Bioelectron.* **2015**, *67*, 86–92, doi:10.1016/j.bios.2014.07.019.
159. Lee, T.Y.; Hyun, K.A.; Kim, S. Il; Jung, H. Il An integrated microfluidic chip for one-step isolation of circulating tumor cells. *Sensors Actuators, B Chem.* **2017**, *238*, 1144–1150, doi:10.1016/j.snb.2016.05.163.

160. Mishra, A.; Dubash, T.D.; Edd, J.F.; Jewett, M.K.; Garre, S.G.; Karabacak, N.M.; Rabe, D.C.; Mutlu, B.R.; Walsh, J.R.; Kapur, R.; et al. Ultrahigh-throughput magnetic sorting of large blood volumes for epitope-agnostic isolation of circulating tumor cells. *Proc. Natl. Acad. Sci. U. S. A.* **2020**, *117*, 16839–16847, doi:10.1073/pnas.2006388117.
161. Mutlu, B.R.; Smith, K.C.; Edd, J.F.; Nadar, P.; Dlamini, M.; Kapur, R.; Toner, M. Non-equilibrium Inertial Separation Array for High-throughput, Large-volume Blood Fractionation. *Sci. Rep.* **2017**, *7*, 1–9, doi:10.1038/s41598-017-10295-0.
162. Jack, R.; Hussain, K.; Rodrigues, D.; Zeinali, M.; Azizi, E.; Wicha, M.; Simeone, D.M.; Nagrath, S. Microfluidic continuum sorting of sub-populations of tumor cells via surface antibody expression levels. *Lab Chip* **2017**, *17*, 1349–1358, doi:10.1039/C6LC01496H.
163. Jack, R.M.; Grafton, M.M.G.; Rodrigues, D.; Giraldez, M.D.; Griffith, C.; Cieslak, R.; Zeinali, M.; Kumar Sinha, C.; Azizi, E.; Wicha, M.; et al. Ultra-Specific Isolation of Circulating Tumor Cells Enables Rare-Cell RNA Profiling. *Adv. Sci.* **2016**, *3*, 1–8, doi:10.1002/advs.201600063.
164. Fachin, F.; Spuhler, P.; Martel-Foley, J.M.; Edd, J.F.; Barber, T.A.; Walsh, J.; Karabacak, M.; Pai, V.; Yu, M.; Smith, K.; et al. Monolithic Chip for High-throughput Blood Cell Depletion to Sort Rare Circulating Tumor Cells. *Sci. Rep.* **2017**, *7*, 1–11, doi:10.1038/s41598-017-11119-x.
165. Ozkumur, E.; Shah, A.M.; Ciciliano, J.C.; Emmink, B.L.; Miyamoto, D.T.; Brachtel, E.; Yu, M.; Chen, P.; Morgan, B.; Trautwein, J.; et al. Inertial Focusing for Tumor Antigen – Dependent and – Independent Sorting of Rare Circulating Tumor Cells. *Sci. Transl. Med.* **2013**, *5*.
166. Shen, Z.; Wu, A.; Chen, X. Current detection technologies for circulating tumor cells. *Chem. Soc. Rev.* **2017**, *46*, 2038–2056, doi:10.1039/c6cs00803h.
167. Cho, H.; Kim, J.; Song, H.; Sohn, K.Y.; Jeon, M.; Han, K.H. Microfluidic technologies for circulating tumor cell isolation. *Analyst* **2018**, *143*, 2936–2970, doi:10.1039/c7an01979c.
168. Gwak, H.; Kim, J.; Kashefi-Kheyraadi, L.; Kwak, B.; Hyun, K.-A.; Jung, H.-I. Progress in Circulating Tumor Cell Research Using Microfluidic Devices. *Micromachines* **2018**, *9*, doi:10.3390/mi9070353.
169. Liang, W.; Liu, J.; Yang, X.; Zhang, Q.; Yang, W.; Zhang, H.; Liu, L. Microfluidic-based cancer cell separation using active and passive mechanisms. *Microfluid. Nanofluidics* **2020**, *24*, doi:10.1007/s10404-020-2331-x.
170. Yu, X.; Wu, N.; Chen, F.; Wei, J.; Zhao, Y. Engineering Microfluidic chip for Circulating Tumor Cells: From Enrichment, Release to Single Cell Analysis. *Trends Anal. Chem.* **2019**, doi:10.1016/j.trac.2019.03.027.
171. Tian, C.; Xu, X.; Wang, Y.; Li, D.; Lu, H.; Yang, Z. Development and clinical prospects of techniques to separate circulating tumor cells from peripheral blood. *Cancer Manag. Res.* **2020**, *12*, 7263–7275, doi:10.2147/CMAR.S248380.
172. Cho, H.; Kim, J.; Jeon, C.W.; Han, K.H. A disposable microfluidic device with a reusable magnetophoretic functional substrate for isolation of circulating tumor cells. *Lab Chip* **2017**, *17*, 4113–4123, doi:10.1039/c7lc00925a.
173. Guo, P.L.; Tang, M.; Hong, S.L.; Yu, X.; Pang, D.W.; Zhang, Z.L. Combination of dynamic magnetophoretic separation and stationary magnetic trap for highly sensitive and selective detection of *Salmonella typhimurium* in complex matrix. *Biosens. Bioelectron.* **2015**, *74*, 628–636, doi:10.1016/j.bios.2015.07.019.
174. Malic, L.; Zhang, X.; Brassard, D.; Clime, L.; Daoud, J.; Luebbert, C.; Barrere, V.; Boutin, A.; Bidawid, S.; Farber, J.; et al. Polymer-based microfluidic chip for rapid and efficient immunomagnetic capture and release of *Listeria monocytogenes*. *Lab Chip* **2015**, *15*, 3994–4007, doi:10.1039/C5LC00852B.
175. Gray, B.L. A Review of Magnetic Composite Polymers Applied to Microfluidic Devices. *J. Electrochem. Soc.* **2014**, *161*, B3173–B3183, doi:10.1149/2.023402jes.
176. Yunas, J.; Mulyanti, B.; Hamidah, I.; Said, M.M.; Pawinanto, R.E.; Wan Ali, W.A.F.; Subandi, A.; Hamzah, A.A.; Latif, R.; Majlis, B.Y. Polymer-Based MEMS electromagnetic actuator for biomedical application: A review. *Polymers (Basel)*. **2020**, *12*, doi:10.3390/POLYM12051184.
177. Thévenot, J.; Oliveira, H.; Sandre, O.; Lecommandoux, S. Magnetic responsive polymer composite

- materials. *Chem. Soc. Rev.* **2013**, 42, 7099–7116, doi:10.1039/c3cs60058k.
178. Nakahara, T.; Suzuki, J.; Hosokawa, Y.; Shimokawa, F.; Kotera, H.; Suzuki, T. Fabrication of Magnetically Driven Microvalve Arrays Using a Photosensitive Composite. *Magnetochemistry* **2018**, 4, 7, doi:10.3390/magnetochemistry4010007.
 179. Nakahara, T.; Ueda, Y.; Miyagawa, H.; Kotera, H.; Suzuki, T. Self-aligned fabrication process for active membrane in magnetically driven micropump using photosensitive composite. *J. Micromechanics Microengineering* **2020**, 30, doi:10.1088/1361-6439/ab6302.
 180. Descamps, L.; Le Roy, D.; Tomba, C.; Deman, A. Magnetic Polymers for Magnetophoretic Separation in Microfluidic Devices. *Magnetochemistry* **2021**, 7, doi:10.3390/magnetochemistry7070100.
 181. Niu, X.; Peng, S.; Liu, L.; Wen, W.; Sheng, P. Characterizing and patterning of PDMS-based conducting composites. *Adv. Mater.* **2007**, 19, 2682–2686, doi:10.1002/adma.200602515.
 182. Deman, A.L.; Brun, M.; Quatresous, M.; Chateaux, J.F.; Frenea-Robin, M.; Haddour, N.; Semet, V.; Ferrigno, R. Characterization of C-PDMS electrodes for electrokinetic applications in microfluidic systems. *J. Micromechanics Microengineering* **2011**, 21, 095013, doi:10.1088/0960-1317/21/9/095013.
 183. Faivre, M.; Gelszinnis, R.; Degouttes, J.; Terrier, N.; Rivière, C.; Ferrigno, R.; Deman, A.-L. Magnetophoretic manipulation in microsystem using carbonyl iron-polydimethylsiloxane microstructures. *Biomicrofluidics* **2014**, 8, 054103, doi:10.1063/1.4894497.
 184. Yu, X.; Wen, C.Y.; Zhang, Z.L.; Pang, D.W. Control of magnetic field distribution by using nickel powder@PDMS pillars in microchannels. *RSC Adv.* **2014**, 4, 17660–17666, doi:10.1039/c3ra47902a.
 185. Ezzaier, H.; Marins, J.A.; Claudet, C.; Hemery, G.; Sandre, O.; Kuzhir, P. Kinetics of aggregation and magnetic separation of multicore iron oxide nanoparticles: Effect of the grafted layer thickness. *Nanomaterials* **2018**, 8, doi:10.3390/nano8080623.
 186. Bae, Y.M.; Jeong, B.; Kim, J. Il; Kang, D.G.; Shin, K.Y.; Yoo, D.W. Array of 3D permanent micromagnet for immunomagnetic separation. *J. Micromechanics Microengineering* **2019**, 29, doi:10.1088/1361-6439/ab259f.
 187. Van Pelt, S.; Frijns, A.; Den Toonder, J. Microfluidic magnetic bead conveyor belt. *Lab Chip* **2017**, 17, 3826–3840, doi:10.1039/c7lc00718c.
 188. Royet, D.; Hériveaux, Y.; Marchalot, J.; Scorretti, R.; Dias, A.; Dempsey, N.M.; Bonfim, M.; Simonet, P.; Frénéa-Robin, M. Using injection molding and reversible bonding for easy fabrication of magnetic cell trapping and sorting devices. *J. Magn. Magn. Mater.* **2017**, 427, 306–313, doi:10.1016/j.jmmm.2016.10.102.
 189. Nagai, M.; Tanizaki, K.; Shibata, T. Batch Assembly of SU-8 Movable Components in Channel Under Mild Conditions for Dynamic Microsystems: Application to Biohybrid Systems. *J. Microelectromechanical Syst.* **2019**, 28, 419–428, doi:10.1109/JMEMS.2019.2907285.
 190. Serra, M.; Gontran, E.; Hajji, I.; Malaquin, L.; Viovy, J.-L.; Descroix, S.; Ferraro, D.; Hajji, I.; Serra, M.; Gotran, E.; et al. Development of a droplet microfluidics device based on integrated soft magnets and fluidic capacitor for passive extraction and redispersion of functionalized magnetic particles. *Adv. Mater. Technol.* **2020**.
 191. Zhou, R.; Wang, C. Microfluidic separation of magnetic particles with soft magnetic microstructures. *Microfluid. Nanofluidics* **2016**, 20, 1–11, doi:10.1007/s10404-016-1714-5.
 192. Zhou, R.; Yang, Q.; Bai, F.; Werner, J.A.; Shi, H.; Ma, Y.; Wang, C. Fabrication and integration of microscale permanent magnets for particle separation in microfluidics. *Microfluid. Nanofluidics* **2016**, 20, 1–12, doi:10.1007/s10404-016-1774-6.
 193. Deman, A.-L.; Mekkaoui, S.; Dhungana, D.; Chateaux, J.-F.; Tamion, A.; Degouttes, J.; Dupuis, V.; Le Roy, D. Anisotropic composite polymer for high magnetic force in microfluidic systems. *Microfluid. Nanofluidics* **2017**, 21, 170, doi:10.1007/s10404-017-2008-2.
 194. Chung, J.; Issadore, D.; Ullal, A.; Lee, K.; Weissleder, R.; Lee, H. Rare cell isolation and profiling on a hybrid magnetic/size-sorting chip. *Biomicrofluidics* **2013**, 7, 1–9, doi:10.1063/1.4821923.
 195. Mekkaoui, S.; Descamps, L.; Audry, M.C.; Deman, A.L.; Le Roy, D. Nanonewton Magnetophoretic Microtrap Array for Microsystems. *Langmuir* **2020**, 36, 14546–14553, doi:10.1021/acs.langmuir.0c02254.

196. Faivre, M.; Gelszinnis, R.; Terrier, N.; Ferrigno, R.; Deman, A. Magnetophoretic manipulation in microsystem using carbonyl iron-polydimethylsiloxane microstructures. *Biomicrofluidics* **2014**, *054103*, doi:10.1063/1.4894497.
197. Zhou, R.; Surendran, A.N. Study on micromagnets induced local wavy mixing in a microfluidic channel. *Appl. Phys. Lett.* **2020**, *117*, doi:10.1063/5.0024011.
198. Martin, J.E.; Venturini, E.; Odinek, J.; Anderson, R.A. Anisotropic magnetism in field-structured composites. *Phys. Rev. E - Stat. Physics, Plasmas, Fluids, Relat. Interdiscip. Top.* **2000**, *61*, 2818–2830, doi:10.1103/PhysRevE.61.2818.
199. Wang, M.; He, L.; Yin, Y. Magnetic field guided colloidal assembly. *Mater. Today* **2013**, *16*, 110–116, doi:10.1016/j.mattod.2013.04.008.
200. Deman, A.L.; Mekkaoui, S.; Dhungana, D.; Chateaux, J.F.; Tamion, A.; Degouttes, J.; Dupuis, V.; Le Roy, D. Anisotropic composite polymer for high magnetic force in microfluidic systems. *Microfluid. Nanofluidics* **2017**, *21*, 1–8, doi:10.1007/s10404-017-2008-2.
201. Bidan, C.M.; Fratzl, M.; Coullomb, A.; Moreau, P.; Lombard, A.H.; Wang, I.; Balland, M.; Boudou, T.; Dempsey, N.M.; Devillers, T.; et al. Magneto-active substrates for local mechanical stimulation of living cells. *Sci. Rep.* **2018**, *8*, 1–13, doi:10.1038/s41598-018-19804-1.

Chapter II

Materials and Methods

In this chapter will first be described the fabrication process of micro-magnets obtained from NdFeB@PDMS composite, as well as the characterization methods, based on experimental and numerical approaches, which were implemented to study their structure and magnetic properties. Then, the integration step of these micro-magnets, acting as micro-traps, into a microfluidic device is reported. The experimental procedure for the capture of target magnetic objects in microfluidics will also be detailed, the latter being either superparamagnetic beads or magnetically labeled white blood cells. Furthermore, in the context of circulating tumor cell (CTC) isolation, several downstream analyses (from cell culture to immunofluorescence and fluorescence in situ hybridization assays), performed on recovered CTCs, will be described. Finally, the final workflow, integrating a size-based enrichment step (using ClearCell FX1 system) and the developed magnetic-based purification step, will be detailed.

1. Fabrication and characterization of self-assembled micro-magnets

1.1. Composite preparation and structuration

1.1.1. Preparation

Hard ferromagnetic composites were fabricated by mixing NdFeB particles with polydimethylsiloxane (PDMS). The composite will be referred to as NdFeB@PDMS composite. NdFeB is a material of choice to produce permanent magnets with high magnetic performances [1] (i.e. high remanence and high coercivity). NdFeB micro-particles were purchased from Magnequench (ref MQFP-B) and are irregularly shaped flakes obtained from crushed melt spun ribbons with a size comprised between 0.5 and 7 μm . Scanning Electron Microscopy (SEM) image of the NdFeB micro-particles can be found in Figure 2.1. According to the supplier's datasheet, the magnetic properties of the particles are a remanent magnetic flux, B_r , of 0.9 T and a coercive field, H_c , of 740 kA/m. The Sylard silicon elastomer (PDMS) was purchased from Samaro and consists of two components: a base and a curing agent (10:1 mixing ratio). NdFeB micro-particles and PDMS were thoroughly mixed for a few minutes in a mortar. NdFeB@PDMS composites were prepared with concentration ranging from 1 to 4 wt% of NdFeB.

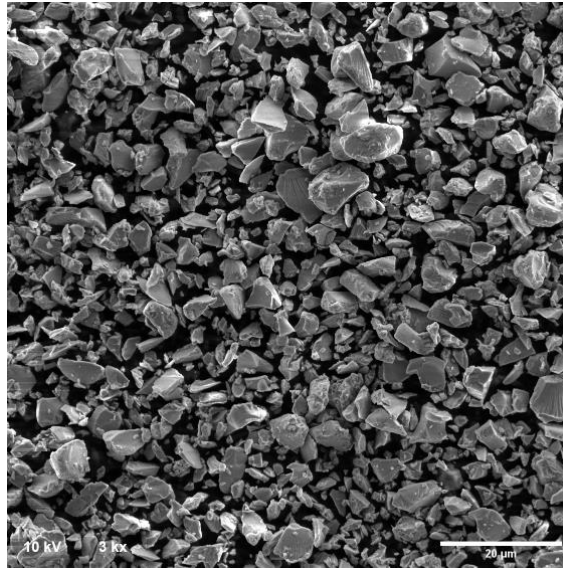


Figure 2.1: SEM images of irregularly shaped NdFeB flakes purchased from Magnequench.

1.1.2. Shaping process

The NdFeB@PDMS membrane is molded in a 100- μm -thick Kapton adhesive film, cut by Xurography [2], and stuck to a substrate. Two Kapton molds were used regarding the needed trapping area, one with dimensions of 15x0.5 mm², and the other with a larger area of 40x20mm². The composite was poured onto the mold and the excess was removed with a scraper. The Kapton mold was then removed, leaving a 100- μm -thick composite layer, which was cured at 70°C for 2h in a magnetic field of 300 mT supplied by a bulk NdFeB magnet (60 x 30 x 15 mm³, magnetization along the shortest dimension). During curing, NdFeB particles are free to move in the liquid polymer and self-organize driven by magnetic dipolar interactions. After curing, NdFeB particles are immobilized in the polymer matrix. Next, pure PDMS is poured on the composite membrane to increase its thickness up to 2 mm. The membrane is then cured at 70°C for 2 hours and peeled off from the substrate. The obtained micro-magnets will act as magnetic micro-traps. Finally, NdFeB@PDMS microstructures were magnetized. All the fabrication steps are summarized in Figure 2.2.

We used two different substrates to prepare the composite, either a silanized glass slide or a FeC@PDMS magnetic pattern, and studied their impact on NdFeB composite microstructure. The FeC@PDMS magnetic pattern consists of a soft ferromagnetic composite membrane made of self-organized carbonyl iron micro-particles (Fe dry powder, 0.5–7 μm diameter, 97% Fe basis, Sigma-Aldrich) in PDMS (5 to 10 wt%) [3]. Using the glass slide, the composite membrane is only submitted to the magnetic field gradient

generated by the external magnet during the crosslinking step, estimated at 20 T/m from numerical simulations (Comsol Multiphysics®). In the presence of the soft magnetic membrane, which contains chain-like agglomerates of Fe micro-particles oriented in the direction perpendicular to the substrate's surface, strong magnetic field gradients are generated locally, of about 10^5 T/m at the chain positions according to the results of Comsol® simulations.

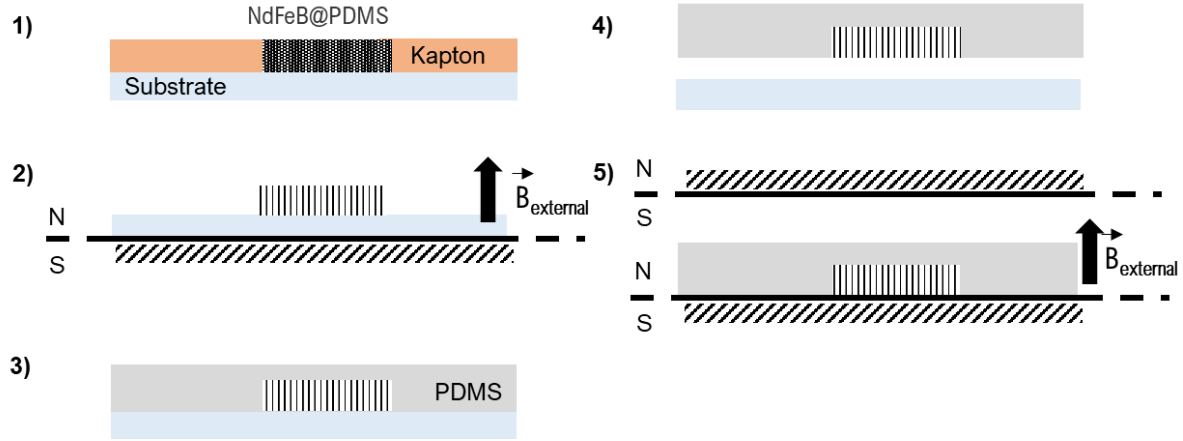


Figure 2.2: Flow-chart of the fabrication steps of NdFeB@PDMS composite. The composite is molded in a Kapton film bonded to a substrate (step 1). The substrate is either a silanized glass slide or a FeC@PDMS template. The composite is then placed in a 300 mT magnetic field for NdFeB particles self-organization in chains (step 2). Pure PDMS is then poured on the membrane (step 3). Finally, after curing at 70°C for 2h, the composite membrane is peeled off (step 4) and magnetized under a magnetic field of ~ 1 T (step 5).

For the magnetizing step, two magnetizing systems were designed. The first one, already existing in the laboratory, consists of two blocks of two NdFeB magnets spaced by 2 mm, each magnet of dimensions $20 \times 20 \times 10 \text{ mm}^3$, and, producing a relatively homogeneous field of 1 T. A second magnetizing system was then fabricated to increase the magnetizing volume. The system was made of two NdFeB magnets of dimensions $50.8 \times 50.8 \times 25.4 \text{ mm}^3$ and spaced by 2 mm, generating a field of 1.2 T. The generated magnetic field was enhanced thanks to the adding of a flux guide. Magnetic fields were measured using a gauss meter (PCE-MFM 3500) equipped with a flat Hall effect sensor, allowing for measurements in even small openings in the order millimeters. Magnetic field measurement profile can be found in Figure 2.3 before the adding of the flux guide, at both edges and center of the magnetizing system.

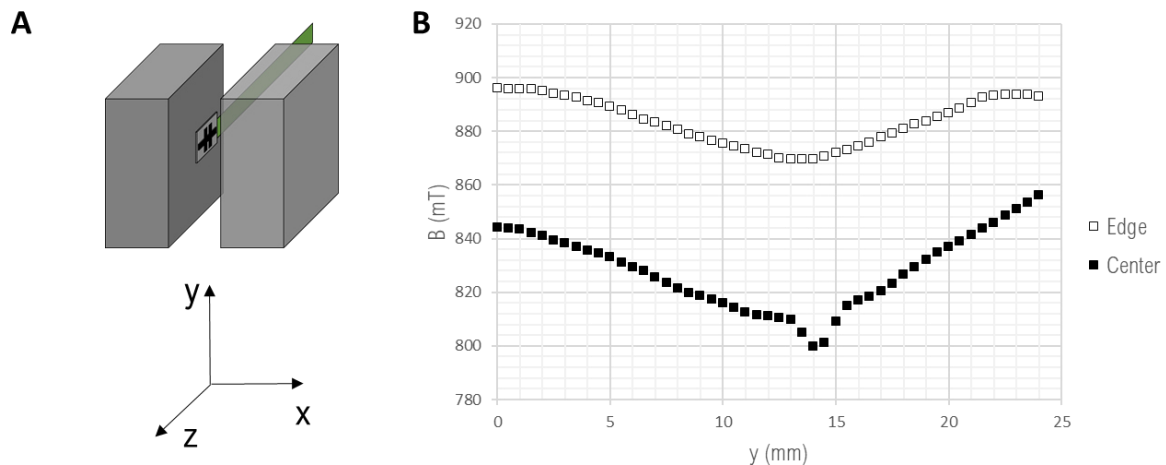


Figure 2.3: Measurements of the magnetic field generated by the new magnetizing system composed of two NdFeB magnets ($50.8 \times 50.8 \times 25.4 \text{ mm}^3$). (A) Schematics of the magnetizing system. The flat Hall effect probe was positioned between the two magnets, either at the edges or at the center. (B) Profile of the measured magnetic field. The probe position was varied by a 0.5-mm step along the height of the magnetizing system using a metric micrometer. The magnitude of the magnetic field was later enhanced to 1.2 T by adding a magnetic flux guide.

1.2. Structural characterization

The characterization of the microstructure was carried out in the volume of the composite by X-ray tomography and on the surface by optical microscopy.

1.2.1. X-ray tomography

X-ray tomography is a powerful technique to provide a three-dimensional map of macroscopic sample inner structure with sub-micrometer resolution and without destroying the specimen. It consists in directing an X-ray beam at the specimen to be imaged from multiple angular positions (typically between 0 and 180°) and recording the transmitted beam on a detector (a CCD or CMOS camera). Part of the X-rays is absorbed and, according to Beer-Lambert law, the ratio of the number of transmitted to incident photons is related to the integral of the absorption coefficient of the material along the path that the photons follow through the sample. This absorption coefficient depends on the density and atomic number of the material, and the energy of the X-rays. Three-dimensional microstructure representations are then calculated numerically from the recorded (2D) projection images by a tomographic reconstruction algorithm [4]. Figure 2.4 illustrates the principle of X-ray tomography.

The inner structure of a 1 mm³ NdFeB@PDMS membrane was characterized using the EasyTomNano μ CT tomograph (RX Solutions) at MATEIS laboratory. The X-ray source is a LaB₆ cathode with a diamond window leading to higher flux (20 μ A). Its focal spot measures 0.25 μ m and a tension of 90 kV was applied. Scans were acquired by a CCD detector, whose matrix measures 2000 x 1312 pixels, with a resolution of 0.3 μ m. 3D images were reconstructed from projections at 1400 different angular positions. Final images of 1700 x 1700 x 400 voxel, i.e 510 x 510 x 120 μ m³, were obtained and processed with ImageJ to characterize NdFeB particles' spatial organization in the volume of the composite membrane. In particular, the *Volume Viewer* plugin was used to perform 3D reconstruction from tomography scans.

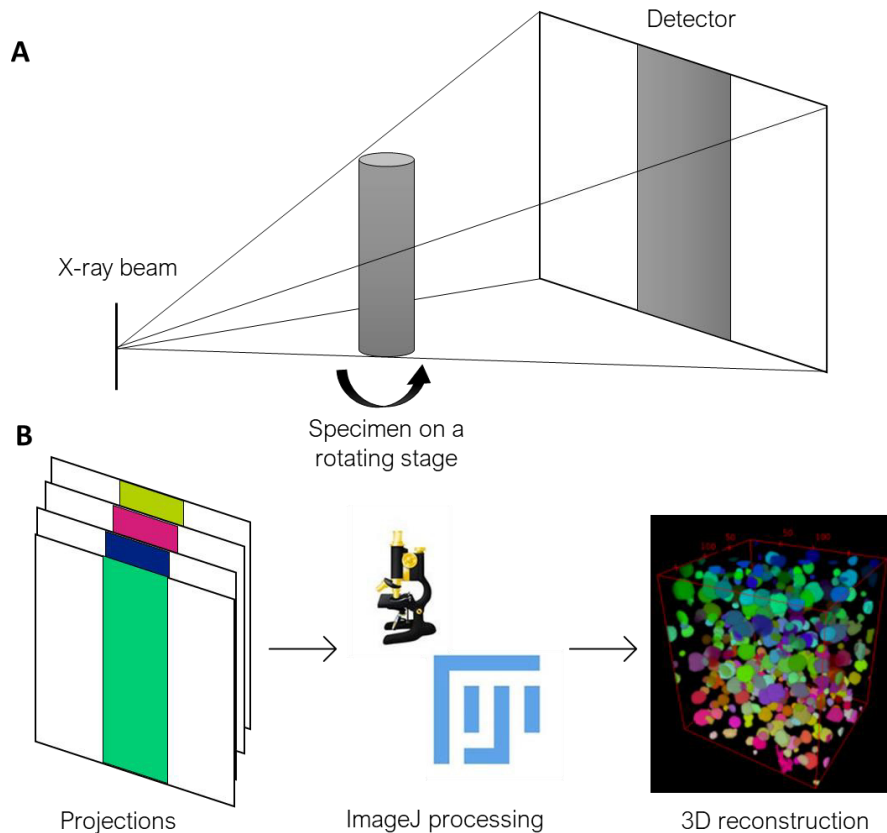


Figure 2.4. Principle of X-ray tomography. (A) X-ray imaging followed by (B) ImageJ processing.

1.2.2. Optical microscopy

Optical microscopy characterizations using an Olympus BX51M microscope coupled to a camera (Moticam2000, Motic) were also carried out with ImageJ to study the in-plane organization of the NdFeB agglomerates. Top view images of the micro-magnets were converted into binary contrast images and processed using ImageJ tools to perform a quantitative study on micro-magnet diameter, nearest neighbor distance and density within the membrane surface.

1.3. Magnetic characterization

The characterization of the magnetic properties of the micro-magnets was performed in a SQUID magnetometer for the global magnetic properties of the array and by colloidal probe AFM for magnetic properties of individual microtraps.

1.3.1. SQUID magnetometry

SQUID (Superconducting QUantum Interference Device) magnetometry enables ultrasensitive and fully automated measurements of the magnetization of a specimen as a function of magnetic field and/or temperature.

Typically, a SQUID consists of two Josephson junctions connected in parallel on a superconducting loop and uses Josephson effect phenomena to measure extremely small variations in magnetic flux [5]. When an external magnetic flux is coupled into the Josephson loop, the voltage drop across the Josephson junction will change (Figure 2.5). Monitoring the change in voltage allows the determination of the magnetic flux that has been coupled into the SQUID loop. A SQUID constitutes therefore a flux-to-voltage transducer, providing an output voltage that is periodic in the applied flux with a period of one flux quantum ($\phi_0 \cong 2.07 \cdot 10^{-15} \text{ T/m}^2$) [6].

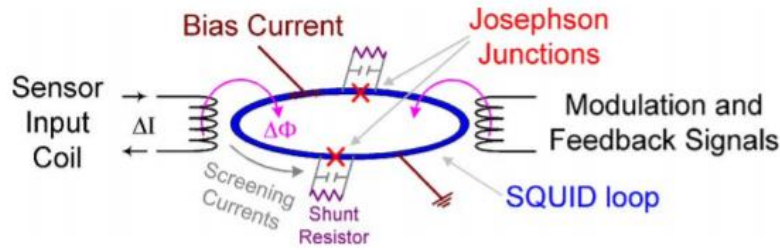


Figure 2.5. Voltage drop across dual junction SQUID loop [5].

Room temperature M-H magnetization curves of NdFeB@PDMS composite were measured in a SQUID magnetometer (Quantum design MPMS XL) at ILM-Tech. The characterized sample is a 5 mm-side square piece of composite fixed in a holding straw using Kapton tape. Magnetization curves were measured either parallel or perpendicular to the long axis of the agglomerates referred to as out-of-plane and in-plane, respectively.

1.3.2. Colloidal probe atomic force microscopy

Magnetic forces generated by the micro-magnets were measured by colloidal probe AFM. Colloidal probe AFM is a near-field microscopy technique enabling the monitoring of interaction forces between the sample surface and the cantilever tip, which is covered with a magnetic material to measure magnetic forces. The cantilever, on which a laser beam is focused, scans the sample surface and the presence of magnetic field gradients will cause its deflection. This deflection modifies the reflection angle of the beam which is detected by a photoelectric diode. The magnetic force can therefore be directly correlated to the measured phase angle (14).

$$\Delta\varphi = \frac{Q}{k} \frac{dF_{mag}}{dz} \quad (14)$$

With Q the resonance quality factor of the cantilever and k its stiffness.

Furthermore, the magnetic scan on the composite surface was performed in *two-pass* or *nap* mode which consists of a first scan to probe the sample surface (topography measurement), and a second one above the priorly scanned topography but vertically shifted in order to cancel surface interactions such as van der Waals and measure only magnetic forces (Figure 2.6) [7].

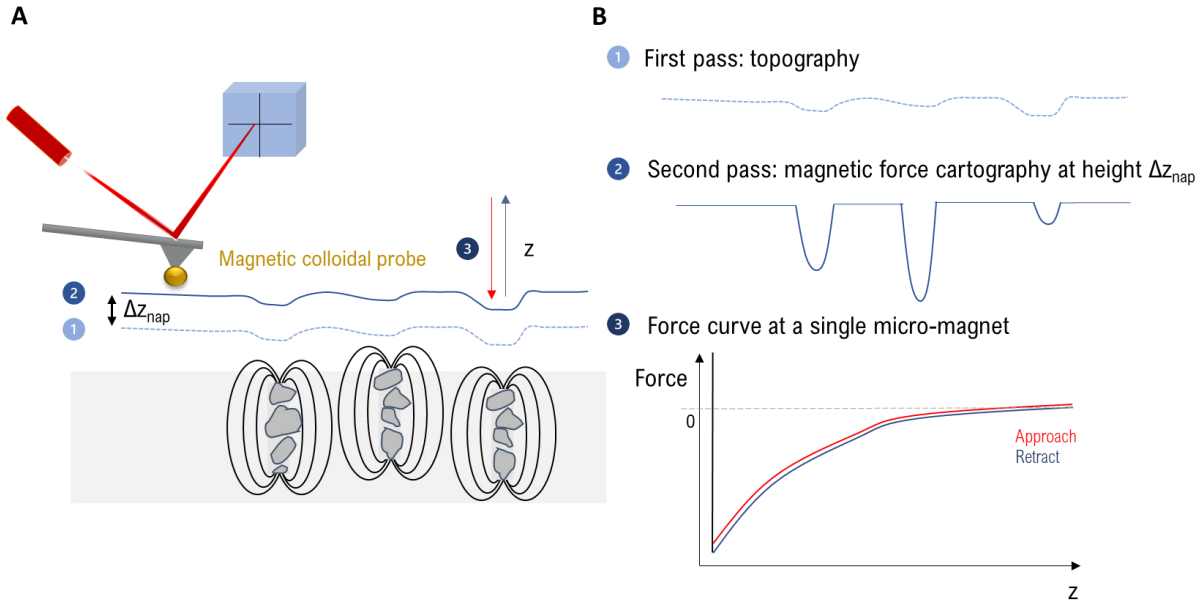


Figure 2.6: Principle of the colloidal probe AFM operating in two-pass mode.

Magnetic force measurements of the magnetic composites were performed at ILM-Tech on the AFM MFP-3D (Asylum Research, Oxford Instrument) using a 15- μm superparamagnetic colloidal probe glued to a silicon nitride cantilever (PNP-TR-TL, NanoAndMore, stiffness measured with thermal noise method: 43 pN/nm). The procedure to measure the magnetic force generated by a micro-magnet is described as follows: a first scan was performed at contact to locate the micro-magnets, then the probe height was shifted of a few hundred of nanometers (mode nap) and a second scan was performed to record the cantilever's deflection above the sample surface and therefore probe magnetic forces. Finally, the probe was positioned at the exact micro-magnet position where the magnetic force intensity is the highest. This way, the acting force between the colloidal probe and the sample was recorded as the probe approached and withdrew from the sample surface (approach/retract curves), at a 1 $\mu\text{m/s}$ constant velocity. Measurements were performed in a PBS-BSA 2% solution to avoid non-specific adsorption of the colloidal probe on the sample surface. For each sample, 20 micro-magnets were characterized using this method.

1.4. Finite element simulation

Simulations of the micro-magnet magnetic performances were performed on Comsol® software (version 5.2a) using the AC/DC module and the Magnetic Fields (mf) interface. It allowed the stationary study of magnetic materials and the computing of magnetic field.

Geometry and magnetic properties of NdFeB micro-magnet were set regarding observations from X-ray tomography and SQUID measurements. The microfluidic set-up with integrated micro-magnet to be modeled is schematized in Figure 2.7. The NdFeB micro-magnet was modeled as a chain-like agglomerate of NdFeB particles. The influence of an external permanent micro-magnet on the generated magnetic field was studied.

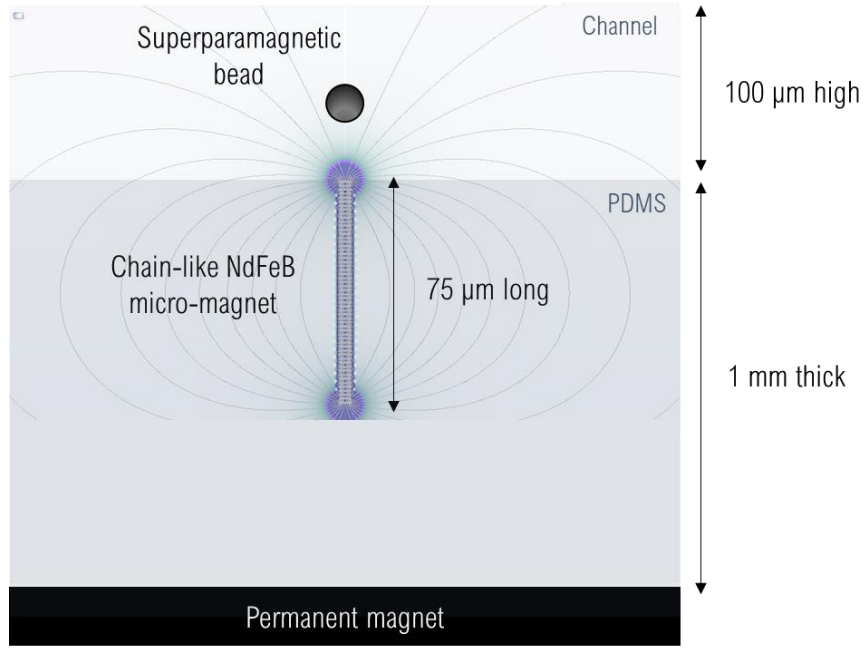


Figure 2.7: Schematics of the Comsol® model geometry. The micro-magnet is modeled as a chain of NdFeB particles. The chain length and interparticle distance were varied. The effect of a permanent magnet, positioned at 1 mm below the micro-magnet, was also studied.

2D and 2D axisymmetric modeling were performed (Figure 2.8), the former was used to describe collective effects in a periodic array of micro-magnets while the latter was used to describe the geometry of a unique micro-magnet. 2D geometry (Cartesian coordinates) is mathematically extended to infinity in both directions along the z-axis assuming no variation along this axis. However, to better describe the 3D geometry of a micro-magnet, 2D axisymmetric geometry (cylindrical coordinates) was used as a NdFeB particle can be constructed by revolving a cross section about an axis (axial symmetry). 2D axisymmetric modeling allows computing time to be reduced in comparison with 3D modeling but doesn't allow modeling of a micro-magnet network. Otherwise, it would lead to concentric cylinders

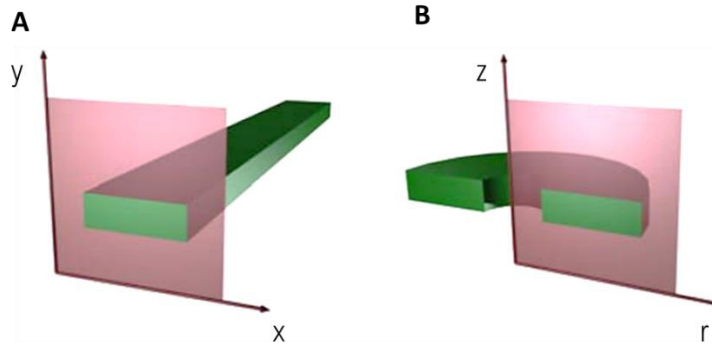


Figure 2.8: Cross sections and actual geometry for (A) Cartesian coordinates (2D) and (B) cylindrical coordinates (axial symmetry, 2D axisymmetric). Adapter from [8].

Two principal magnetic measures were calculated: the magnetic field and the magnetic field gradient, which are the two values coming into play in the expression of the magnetic force. In particular, the magnetic field gradient was depicted by a magnetic coefficient (C_m) [3], which was obtained from the expression of the magnetic force in cylindrical coordinates:

$$\vec{F}_m = V_p (\vec{M}_p \cdot \vec{\nabla}) \vec{B}$$

$$\vec{F}_m = V_p M_p \left(\frac{\vec{B}}{\|\vec{B}\|} \cdot \vec{\nabla} \right) \vec{B}$$

$$\vec{F}_m = \frac{V_p M_p}{\|\vec{B}\|} \begin{pmatrix} B_r \\ B_z \end{pmatrix} \cdot \begin{pmatrix} \frac{\partial}{\partial r} \\ \frac{\partial}{\partial z} \end{pmatrix} \begin{pmatrix} B_r \\ B_z \end{pmatrix}$$

$$\vec{F}_m = \frac{V_p M_p}{\|\vec{B}\|} \left(B_r \frac{\partial}{\partial r} + B_z \frac{\partial}{\partial z} \right) \begin{pmatrix} B_r \\ B_z \end{pmatrix}$$

$$\vec{F}_m = \frac{V_p M_p}{\sqrt{B_r^2 + B_z^2}} \begin{pmatrix} B_r \frac{\partial B_r}{\partial r} + B_z \frac{\partial B_r}{\partial z} \\ B_r \frac{\partial B_z}{\partial r} + B_z \frac{\partial B_z}{\partial z} \end{pmatrix} \begin{pmatrix} \vec{e}_r \\ \vec{e}_z \end{pmatrix}$$

The vertical component of the magnetic force is of interest when studying flowing magnetic object in a microfluidic channel located on top of micro-magnet. A vertical magnetic coefficient ($C_{m,z}$) can thus be expressed as:

$$C_{m,z} = \frac{1}{\sqrt{B_r^2 + B_z^2}} \left(B_r \frac{\partial B_z}{\partial r} + B_z \frac{\partial B_z}{\partial z} \right) \quad (15)$$

Several studies were conducted on Comsol: (i) modeling of a micro-magnet as a chain-like agglomerate of NdFeB particles and study of the effect of geometry parameters (chain length, interparticle distance, etc.) on the generated magnetic field and gradient (2D axisymmetric); (ii) study of the influence of an external millimeter-sized permanent magnet on the magnetic field and gradient (2D and 2D axisymmetric); (iii) study of the neighboring effect in a network of micro-magnets (2D); and finally (iv) calculation of the generated magnetic force on a model superparamagnetic bead.

2. Integration of micro-magnets into a microfluidic device and operation

2.1. Device assembly

The micro-magnets array was integrated into a microfluidic system where channel mold was obtained by soft-lithography. Two designs were in particular fabricated regarding the desired application: a first straight channel for micro-trap performance characterization experiments using superparamagnetic beads as targets (Figure 2.9-A) and a second more complex design for final cell experiments (Figure 2.9-B). For this second design, several requirements had to be fulfilled: (i) develop a large trapping chamber to integrate a larger number of micro-traps; (ii) optimize the liquid filling within the chamber and prevent the air bubble formation; and (iii) integrate support pillars to avoid the collapse of the chamber roof due to the large ratio between the chamber width (20 mm) and height (100 μ m). Both channel heights are 100 μ m and were obtained using two sheets of a 50- μ m dry-film photoresist (Etertec®).

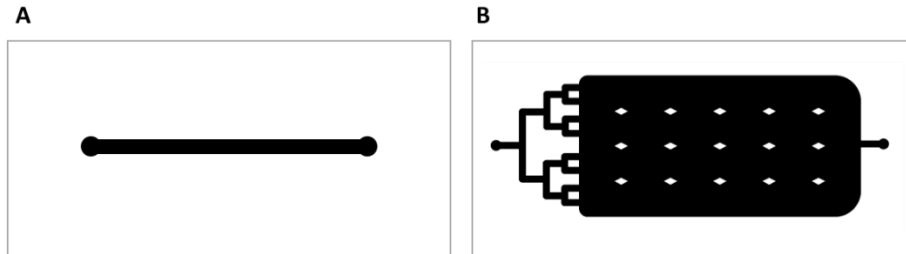


Figure 2.9: Channel mold designs. **(A)** Straight channel (45x0.5x0.1 mm³) for superparamagnetic bead trapping experiments. **(B)** Capture chamber (45x20x0.1 mm³) for CTC negative selection. Input and output channels are 970 μ m wide. Diamond shaped support pillars are 1-mm wide (short diagonal) and 2-mm high (large diagonal).

The first channel mold (40x0.5x0.1 mm³) was obtained by laser lithography (μ PG 101, Heidelberg Instruments) which is a maskless technique (i.e. no prefabricated masks are required) and consists in directly writing the desired pattern on the photoresist with a submicron laser spot. It gives access to high precision patterns, the critical dimension resolution being 3 μ m, in a simple manner. The resist was exposed at 22 mW. The second chamber mold (40x20x0.1 mm³) was obtained by UV lithography (UV-KUB 2, Kloe) using plastic masks. This approach allowed us to test several chamber geometries (about twenty) in a faster way and with lower costs than laser lithography. Despite the lower resolution (30 μ m), it is sufficient for the pattern size needed (minimal size of 970 μ m for the channel width). The resist, on top of which is the plastic mask with the channel design, is insulated by a UV light (14 mW, 8 s).

For both lithography methods, channel patterns are then cured at 70°C for 2 min and revealed in a developer bath of sodium carbonate at 10 g/L for 8 min with agitation. The fabricated mold was then silanized with trichloro(1H,1H,2H,2H-perfluorooctyl)silane (REF 448931, Sigma-Aldrich) in a desiccator for at least 3h at room temperature to prevent undesired bonding of PDMS to the mold. PDMS prepolymer (Sylgard 184, Samaro) with 1: 10 (v/v) curing agent to base ratio was poured on the mold and cured at 70 °C for 2h. After curing, the interconnection holes were punched using a biopsy punch with a diameter of 1.25mm (Elveflow, France). Finally, the channel mold was irreversibly bonded to the composite membrane using O₂ plasma surface treatment (Plasma Cleaner PDC-002-HPCE, Harrick Plasma).

2.2. Device sterilization

The manipulation of biological samples requires sterilized material, including the microfluidic device. Several sterilization conditions were investigated for the chip, whose efficiencies were determined by monitoring potential bacteria growth on agar plates (Columbia blood agar pharm, Merck Millipore).

To test the sterilization procedure, a straight microfluidic channel was used in which 1 mL cell culture medium was injected and collected to monitor bacterial growth on agar plates. Three chip sterilization conditions were studied: (i) UV exposure for 30min, power 50%; (ii) Ethanol 70% flushing; and (iii) UV exposure followed by Ethanol 70% flushing. A control group (no additional procedure after chip fabrication) was also studied. Each condition was performed in triplicate (total of 12 channels).

Bacterial growth was conducted following streak-plate method [9], which is designed to isolate single bacterial colonies, if there are any. The procedure is as follows: injected medium was collected using a sterile inoculating loop and then spread across one-quarter of the agar surface by gently streaking the loop in straight lines. This action was repeated twice for the second and third quadrants, to finally obtain the pattern illustrated in Figure 2.10-A. Finally, following inoculation, agar plates were incubated at 37°C, upside down, and plate reading was conducted after 48h and 72h. Bacteria growth, if any, is visible to the naked eye.

After 72h, three of the four conditions (ethanol flushing, UV+ethanol, and control) had no sign of bacteria growth while UV exposure condition presented one bacterial colony growth in the first quadrant on one of the three replicas (in Figure 2.10-B). Interestingly, the control group did not show a bacterial contamination (in Figure 2.10-B), which could be attributed to O₂ plasma surface treatment applied during the device assembly step. According to these results, the chosen sterilization method is Ethanol 70% flushing since it is the most convenient method and can be performed at the HCL before cell sample injection. For the transportation from INL (device fabrication place) to HCL (biological experiment place), chips were stored in a sterile plastic pouch (autoclavable self seal pouches, Amcor) to protect the chip against bacterial contamination from the time of fabrication until its use.

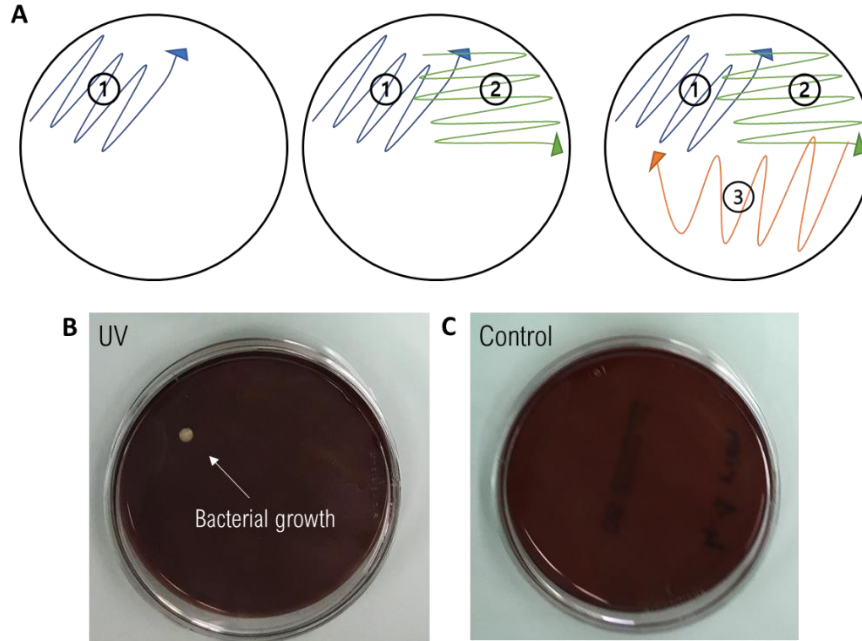


Figure 2.10: Bacterial growth monitoring in agar plates. **(A)** Streak-plate method to isolate single bacterial colonies. **(B)** One of the three replica of UV sterilization condition presented a bacterial growth, visible to the naked eye. **(C)** No contamination was observed for the control group (no sterilization).

2.3. Microfluidic experimental set-up

2.3.1. Manipulated magnetic objects

Target magnetic objects manipulated during the thesis were either superparamagnetic beads (SPMBs), used for fluidic characterization experiments, or magnetically labeled white blood cells, for the final purpose which is CTC isolation.

SPMBs were purchased from Kisker Biotech (average diameter: 12 μm , density: 1.1 g/cm^3 , magnetization: 0.66 kA/m , material: magnetite nano-inclusions in a polystyrene matrix, 1 vol % Fe_3O_4). SEM image of SPMBs is reported in Figure 2.11. SPMBs were suspended in a filtered PBS solution with 1% Pluronic F-108 at a concentration of 50 SPMBs/ μL . As the total number of traps was estimated at 7500 in the trapping area of the device dedicated to test the trapping performance area length of 1.5 cm, channel width of 500 μm , average trap density of 1000/ mm^2), 130 μL of the bead solution was therefore injected, corresponding to 6500 magnetic beads. These experiments were conducted at INL.

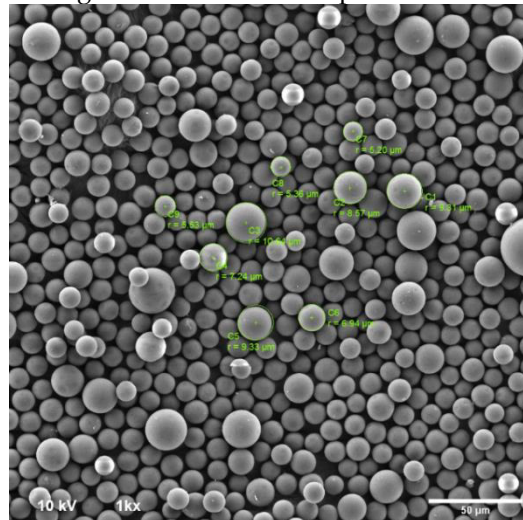


Figure 2.11 : SEM image of SPMBs. Bead radius varies from 4 to 10 μm .

Besides, in the context of CTC negative selection, samples containing magnetically labeled white blood cells (WBCs) and cancer cells were injected. These experiments were conducted at the Hospices Civils de Lyon. The preparation of biological samples will be described in the next section.

2.3.2. Experimental set-up

Fluid was injected using a pressure controller (FLOW EZ™, Fluigent). Two types of tubing were used with a consistent external diameter (1/16" OD i.e., 1.58 μm), but differing internal diameters (ID): 254 and 500 μm , for bead and cell trapping experiments, respectively. The input tubing was connected to the FLOW EZ™ pressure controller (Fluigent, France) while the output tubing was secured with tape into a clean 1.5 mL Eppendorf tube for sample collection. The airtightness was ensured thanks to Fluigent® connectors (P-CAP 2 mL kit).

The microfluidic device was placed under an optical microscope for injection and trapping monitoring. For SPMB trapping experiments, the system was monitored by an Olympus BX51M microscope and images were captured using a Guppy camera with AVT imaging software. For cell capture experiments, a Zeiss fluorescent microscope (Zeiss Imager D1) and Zeiss software (ZEN blue) were used. A picture of the experimental set-up is given in Figure 2.12.

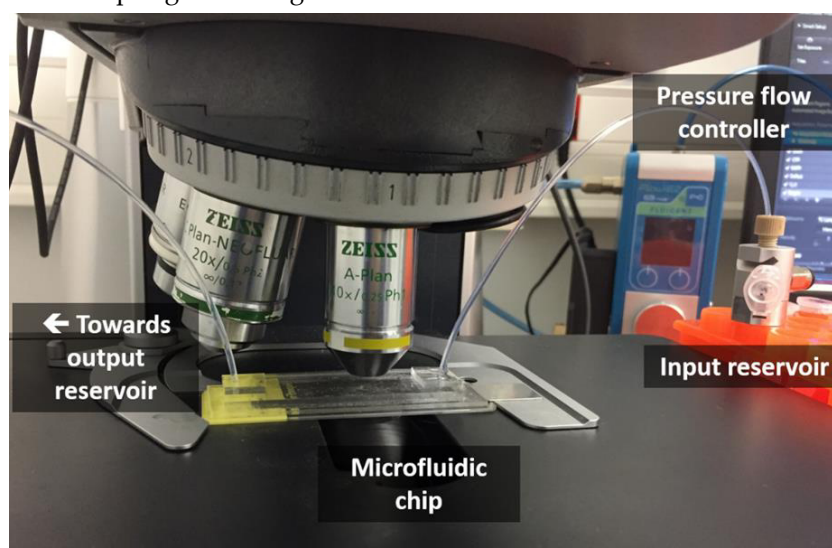


Figure 2.12: Picture of the experimental set up. The microfluidic system is placed under the microscope. The input reservoir is connected to Flow EZ™ pressure controller (Fluigent®) for pressure driven injection and to the channel input through FEP tubing. The processed sample is collected in a dedicated output reservoir. Reservoirs, tubing, and connectors were purchased from Fluigent®.

2.3.3. Injection procedure

Since the injection is controlled in pressure, the corresponding pressure (in mbar) for the desired flow rate (e.g. in mL/h) was first estimated by calculation, then experimentally assessed by measuring the collected liquid volume after a certain injection time.

Before bead/cell injection, the channel is flushed with filtered phosphate buffer saline (PBS, Sigma) solution with 1% Pluronic F-108 (Sigma) for at least 15 min to prevent bead/cell adsorption. Indeed, PDMS is prone to protein absorption and cell adhesion so the use of triblock polymer (Pluronic™ F-108), containing nonadhesive poly(ethylene oxide) (PEO)-based domains and poly(propylene oxide) (PPO) hydrophobic blocks. The triblock (PEO/PPO/PEO) Pluronic™ F108 will spontaneously adhere to the hydrophobic PDMS surface via the hydrophobic PPO domain while the PEO-terminated domain inhibit protein adsorption and cell adhesion through its hydrophilicity, flexibility, chain mobility, and high steric exclusion volume in water [10].

Furthermore, as aforementioned, an additional first step of sterilization is performed for cell experiments. The microfluidic device was sterilized with 70% ethanol for 10 min at 20 mbar. Then, the 1% Pluronic F-108 was flushed for 20 min at 10 mbar to remove ethanol and coat the channel walls.

Bead sample (130 μL volume) and cell sample (300 μL volume) were put in a 1.5 mL Eppendorf safe-lock tube® input reservoir and injected in the magnetic chip. Bead trapping experiments were performed at flow rates ranging from 0.5 to 4 mL/h (pressure range of 16-69 mbar, 254- μm ID tubing), corresponding to a speed ranging from 2.8 to 22 mm/s (straight channel design, 0.1x0.5 mm² cross-section). For cell trapping experiments, samples were injected at flow rates ranging from 1.5 to 5.5 mL/h (4-9 mbar, 500- μm ID tubing), corresponding to a speed range of 0.21 to 0.76 mm/s (chamber design, 0.1x20 mm² cross-section). A larger tubing internal diameter was chosen for cell experiments to avoid clogging since cancer cells can form clusters with sizes reaching 350 μm [11]. The exact flow rate was determined after each experiment by measuring the output volume (collected within the experiment time). When less than 10 μL of the sample remains in the input reservoir, the injection is paused and a volume of 1% Pluronic F-108 diluted in PBS is added to the tube carefully. The injection can then start again, the Pluronic will push remaining beads or cells in tubings and channel towards the output reservoir. Tubing and channel volumes were estimated at 30 μL for bead experiments, while tubing and chamber volumes for cell experiments were estimated at 180 μL , therefore 50 μL or 300 μL of 1% Pluronic was injected, respectively.

After injection, the collected target objects were counted using 10-chambered slides with a hemocytometer-type grid (KOVA® slides). To do so, the output was centrifuged to concentrate target objects in a smaller volume to get a more accurate counting.

2.3.4. Addition of an external permanent magnet

The influence of an external millimeter-sized permanent magnet (25x8x2 mm³, remanent magnetization BR \sim 1.4 T, Supermagnete) was also studied. For micro-bead trapping experiments, the magnet was placed centered under the trapping area of the channel. For cell trapping experiments, as the channel width is bigger, two permanent magnets (housed in a homemade plastic holder), spaced by 4 mm and positioned at 2 cm from the chamber input, were placed below the trapping chamber, as illustrated in Figure 2.13.

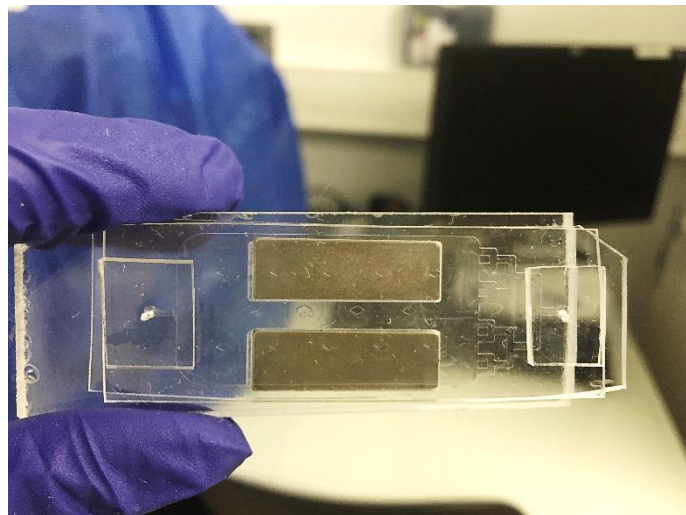


Figure 2.13: Position of the two permanent magnets (25x8x2 mm³ each) below the trapping chamber.

3. Biological sample preparation

3.1. Cell culture

3.1.1. Cell lines

A549 and MCF-7 cell lines were obtained from American Type Culture Collection (ATCC). A549 cells (CCL-185TM), which originate from a lung adenocarcinoma, were cultivated in F12-K medium (ATCC), while MCF-7 cells (HTB-22TM), originating from a breast cancer, were cultivated in Dulbecco's modified eagle medium (DMEM, Life Technologies). Both media were supplemented with 10% fetal bovine serum (FBS) and 1% penicillin–streptomycin. Cells were cultured at 37 °C under a humidified atmosphere of 5% CO₂. Cells were grown in T25 flasks to pre-confluence and detached from flasks for experiments using 1 mL of 0.25% Trypsin-ethylene diamine tetra acetic acid (EDTA) solution at 37 °C.

3.1.2. Routine culture protocol

The complete culture protocol to collect cancer cells is described as follows: the culture medium is first removed from the T25 flask and cells are washed twice with Dulbecco PBS (DPBS, 1X, GibcoTM) to remove all traces of serum that contains trypsin inhibitor. One mL of Trypsin-EDTA solution is added to the flask and put in the CO₂ incubator for 3-5 min until cell layer is dispersed. Cells that are difficult to detach may be agitated by hitting or shaking the flask. Finally, 4 mL of medium is added to the flask to inhibit trypsin effect. The final cell suspension is put in a FalconTM 15 mL tube and 10 µL is taken to perform cell counting in a KOVA® slide.

For experiments requiring fluorescent imaging, cancer cells were labeled with CellTrackerTM Green (Life Technologies) in 0.2% Pluronic (1 µL per 100 000 cells) and incubated for 45 min in the CO₂ incubator.

A549 (lung cancer) and MCF-7 (breast cancer) cells lines were then spiked in a blood sample to mimic CTCs, they can therefore be referred to as mCTCs.

3.2. Blood sample preparation

The capture experiments were performed with mimicking patient blood samples. Those samples were obtained from blood tests, from which red blood cells and platelets were first removed. Then, cancer cells were spiked in the WBC-containing sample, in concentration mimicking the ClearCell output, the first separation system used routinely by the biologists at the HCL. More information about this system can be found in section 5.

Added cancer cells within the injection sample should be in a sufficient number to study recovery efficiency and perform compatibilities studies of the magnetic chip with downstream analyses, while taking into account the rarity of CTCs.

3.2.1. RBC Lysis protocol

A volume of 0.5 mL of whole blood was incubated with 1.5 mL of lysis buffer (Biolidics limited®, CBB-F016003) for 10 min at room temperature (RT) and then centrifuged at 500xg for 10 min. After centrifugation, the supernatant, containing lysed red blood cells, is discarded and the pellet, containing WBCs, is resuspended in 1 mL of DPBS. Finally, WBCs were enumerated using a Türk's solution which destroys RBCs and platelets, and stains the nuclei of WBCs in blue, therefore facilitating their counting. A volume of 45 µL of Türk's solution was added to 5 µL of WBC solution to be counted in a KOVA slide (10 µL volume).

Finally, mCTCs were spiked to the WBC solution and a final mimicking sample composed of 300 000 WBCs and 20 000 mCTCs is obtained.

3.2.2. Magnetic labeling of white blood cells

(i) Magnetic nanoparticle functionalization

Superparamagnetic nanoparticles (NPs), with a diameter of 500 nm and composed of a magnetic core (approximately 70% iron oxide) encapsulated by a hydrophilic polymer shell with carboxyl groups on its surface, were purchased from Ademtech SA (ref 0215). Activation Buffer (AB) and Storage Buffer (SB) solutions were also provided by Ademtech SA. 1-ethyl-3-(3-dimethylamino propyl) carbodiimide hydrochloride (EDC), N-hydroxysuccinimide (NHS) and PBS were purchased from Sigma-Aldrich.

Human-anti-CD45-DL650 and human-anti-CD15-AlexaFluo647 fluorescent antibodies were purchased from R&D Systems.

Covalent attachment of anti-CD45 and anti-CD15 fluorescent antibodies to the nanoparticles' surface was performed following the manufacturer's protocol (Figure 2.14-A). First, nanoparticles were washed three times (using a permanent magnet) and resuspended at 1% in the AB solution. Then, carboxyl groups on the nanoparticles' surface were activated with a 4 mg/mL EDC/NHS solution. Next, anti-CD45 and anti-CD15 fluorescent antibodies were added to the surface-activated nanoparticles and incubated for 2h at 37°C under shaking. The quantity of antibodies to add was determined following a ratio of 4000 antibodies per carboxyl groups (COOH density of 313 $\mu\text{mol/g}$ according to the manufacturer's product information). Finally, antibody-conjugated nanoparticles were washed twice with PBS and resuspended in SB solution. In particular, two NP solutions were prepared: (i) 50 μL of NP solution to which 40 μL of EDC/NHS and 6.08 μL of anti-CD45 antibody were added and (ii) 15 μL of NP solution in which 12 μL of EDC/NHS and 8.58 μL of anti-CD15 antibody were added. Reaction schemes can be found in Figure 2.14-B.

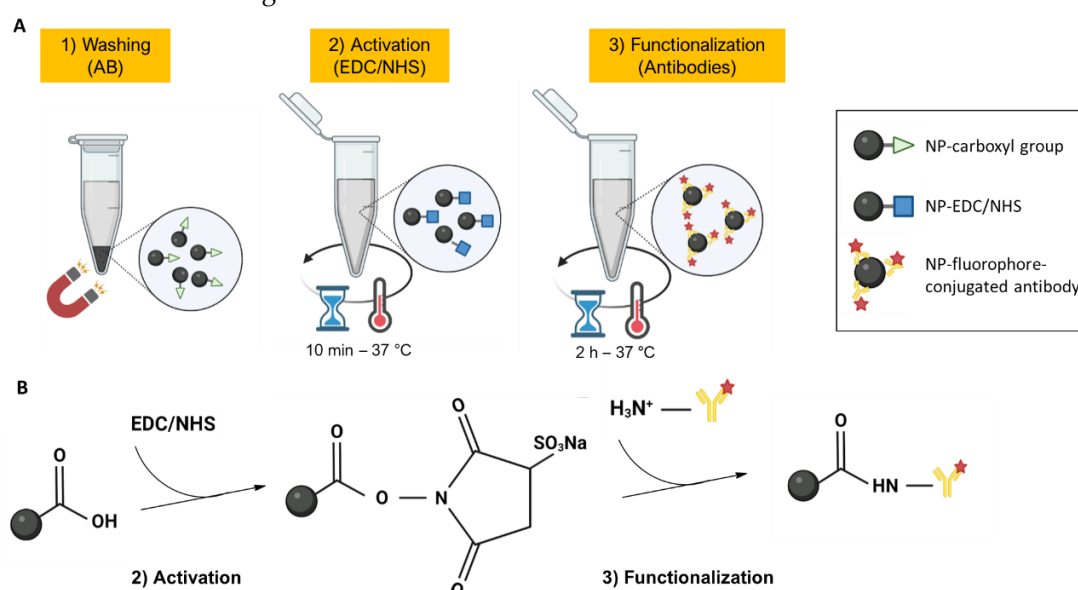


Figure 2.14: (A) Functionalization steps of superparamagnetic nanoparticles according to manufacturer's protocol. (B) Reaction schemes to functionalize superparamagnetic NP with fluorophore-conjugated antibodies. Created with BioRender.com.

(ii) White blood cell labeling

After RBC lysis, WBCs were labeled with antibody-conjugated magnetic nanoparticles at a concentration of 400 NP/WBC and 100 NP/WBC for anti-CD45 and anti-CD15 antibodies, respectively. WBCs were suspended at an appropriate concentration in PBS supplemented with 2 mM EDTA and 2% BSA in a final volume of 300 μL . WBCs and functionalized nanoparticles were incubated in a 24-well plate (CytoOne®) at 37°C for 30 min under a gentle vortex agitation of 200 rpm (MS-100 Thermoshaker Incubator, Labgene).

For experiments requiring a fluorescent imaging, WBC nuclei were marked with Hoechst (Ready Flow Reagent™, Invitrogen) by adding one drop of the marker solution to the solution of WBCs and NPs within the well, before the incubation.

4. Downstream analysis performed after purification

4.1. Estimation of cell capture and recovery efficiencies

To facilitate the visualization and discrimination of WBCs and mCTCs, the former was marked with Hoechst (nucleus staining), while the latter was marked with CellTracker™ Green (cytoplasm staining).

Cells were counted by the standardized procedure using 10-chambered slide with a hemocytometer-type grid (KOVA slide). When all the liquid was injected, the injection was stopped, and the output was centrifuged for 5 min at 300 g. The aim is to concentrate the cells in a smaller volume to get a more precise cell counting. After centrifugation, half of the supernatant is removed, and the cell pellet is resuspended in the remaining volume until getting a homogenized suspension. Cell loss caused by centrifugation was limited by selecting appropriate centrifugal acceleration values and keeping some of the supernatant as the resuspension volume.

Finally, to estimate WBC capture and mCTC recovery efficiencies, 2 to 3 counts were performed in KOVA slides using Zeiss (Imager D1) fluorescent microscope with DAPI and GFP channels. Capture and recovery efficiencies can then be calculated as follows:

$$\text{Capture efficiency (\%)} = \frac{\text{Initial number of WBCs} - \text{Final number of WBCs}}{\text{Initial number of WBCs}} \times 100 \quad (16)$$

$$\text{Recovery efficiency (\%)} = \frac{\text{Final number of mCTCs}}{\text{Initial number of mCTCs}} \times 100 \quad (17)$$

The reproducibility of capture and recovery was studied by performing each experiment at a fixed flow rate at least five times.

4.2. Cell culture in well-plate format

After purification within the magnetic chip, collected cells were cultured in (i) Falcon® 96-well flat bottom microplate to study the ability of recovered mCTCs to the re-adhere and proliferate (Figure 2.15-A); and in (ii) Corning® 96-well round bottom microplate to study their ability to form spheroids (Figure 2.15-B). Corning® round bottom microplates are ultra-low adherent (ULA) plates which favors spherical three-dimensional aggregation of mCTCs composed of proliferating cancer cells and therefore better mimics cellular organization in human tumors.

For both culture conditions, 3000 to 5000 of recovered mCTCs were spiked in a well with 150 µL of filtered medium and incubated at 37°C with 5% CO₂. Medium was renewed every two days: (i) it was completely removed for 2D cell culture as mCTCs are adhering to the well bottom so there is no risk of cell detachment (discarding remaining WBCs at the same time); and (ii) half of it was removed and replaced by a fresh medium for 3D cell culture since mCTCs are in suspension within the well. Cell growth was monitored with an automated microscope equipped with a microplate reader (LionHeart™, BioTek).

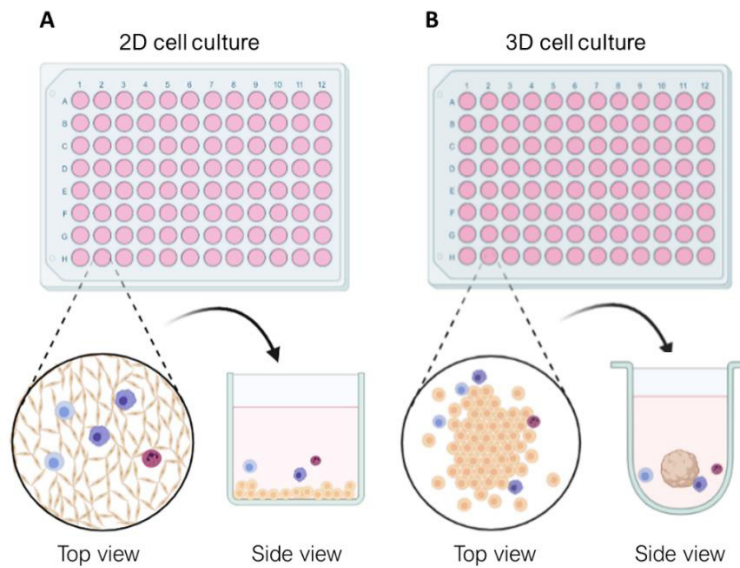


Figure 2.15: Cell culture in well plate formats. **(A)** 2D cell culture in 96-well microplate format. Collected mCTCs re-adhere to the microwell flat bottom while remaining WBCs (neutrophils, lymphocytes, macrophages, etc.) stay in the medium suspension. The latter can then be removed by discarding the medium. **(B)** 3D cell culture in ULA 96-well microplate format. After microplate centrifugation, collected mCTCs aggregate to each other to form a spheroid. A spheroid better mimics the cellular organization in human tumors. mCTCs appear in light color. Other cells represent different leucocytes: neutrophils, lymphocytes, and macrophages, which appear in red, light blue, and dark blue, respectively. Created with BioRender.com.

4.3. Live/Dead assay

It is crucial to study cell viability after injection within the magnetic chip. After magnetic purification, recovered cells were grown to pre-confluence (2 to 3 days of culture) in 2D and their viability was then studied using a LIVE/DEAD® Viability/Cytotoxicity Kit (Invitrogen™, L3224) which provides a two-color fluorescence cell viability assay with two molecular probes: calcein AM and ethidium homodimer-1 (EthD-1). Cell viability can be determined by biochemical and physical properties of cells such as ubiquitous intracellular esterase activity and plasma membrane integrity, which can be simultaneously measured with the two probes.

First, cells were stained by adding a 10x-diluted Hoechst solution (Invitrogen™ H3570) to the culture medium and incubated for 30 min at 37°C. Then, the culture medium was removed and replaced by 100 µL of a 2 µM Calcein AM and 4 µM EthD-1 solution. Cells were incubated for 30-45 min again in the CO₂ incubator. Finally, fluorescent imaging of live and dead cells was performed using LionHeart microscope (BioTek).

Live cells are distinguished by an intense uniform green fluorescence (ex/em ~495 nm/~515 nm) emitted by the polyanionic dye calcein, which results from the enzymatic conversion of the virtually nonfluorescent cell-permeant calcein AM (present within live cells) to the intensely fluorescent calcein. On the contrary, dead cells are distinguished by a bright red fluorescent signal (ex/em ~495 nm/~635 nm) which results from the binding of EthD-1 to nucleic acids within damaged membranes. EthD-1 is excluded by the intact plasma membrane of live cells. In particular, the exposition parameters for EthD-1 signal were first assessed within a dead control well containing cells that were exposed to a 10% Triton-PBS solution which permeabilizes cells.

4.4. Immunofluorescence assay

Immunofluorescence (IF) staining has remained the universal gold standard to distinguish recovered CTCs among background cells. In particular, it allows morphological and phenotypical studies by targeting specific molecules within cells. IF assay was therefore performed to assess CTC integrity and heterogeneity.

4.4.1. Protocol

IF assay was performed directly after magnetic purification. The output tube containing enriched mCTCs (A549 cells) and remaining WBCs was centrifuged at 300xg for 5 min. The supernatant was then carefully removed until leaving a final volume of 100-200 µL for cell resuspension. After coating the pipet tip with 0.2% Pluronic to prevent cell loss within the tip, the cell sample was mounted on a poly-L-lysine coated glass slide (Sigma-Aldrich) and transferred into a cytospin chamber (Shandon™ EZ Single Cytofunnel™, ThermoFisher) in which. The cytospin chamber was centrifuged during 4 min at 400 rpm with a medium acceleration (Cytospin® 4, ThermoFisher) to spread the enriched sample (mCTC+WBC) on the glass slide. After centrifugation, the cytospin chamber was discarded and the coated glass slide was dried under a laminar flow hood for 5 min. The deposition area was then bordered with a silicon isolator.

Cells were first fixed with 200 µL of paraformaldehyde fixative solution (PAF, 4%) for 10 min at RT. The fixative solution was then removed and the cytospot was washed three times with PBS for 2 min at RT. Next, cells were permeabilized with 0.1% Triton-PBS solution during 15 min at RT. The cytospot was washed 3 times for 2 min with PBS at RT. Thereafter, cells were incubated with 200 µL of an in-house

saturation solution mix (5% fetal bovine serum, 1% bovine serum albumin, and 5% Fc receptor blocking reagent from Miltenyi Biotec in sterile PBS) for 30 min at RT in dark. Finally, 200 μ L of primary antibody solution was added to the cells for incubation overnight in a humidity chamber at 4°C in dark. The following primary antibodies were used: (i) anti-CD45 antibody (rat anti-human, MA5-17687, ThermoFisher), AlexaFluor (AF) 647-conjugated anti-CD15 antibody (mouse anti-human, 562369, BD Bioscience), and AF647-conjugated anti-CD41 antibody (mouse anti-human, 303726, BioLegend) for white blood cell staining, diluted in the saturation mix at 1:500, 1:250, and 1:40, respectively; (ii) anti-ALDH1 antibody (rabbit anti-human, 702728, ThermoFisher) for mCTC (A549) staining, diluted at 1:100. ALDH1 (aldehyde dehydrogenase 1) is a marker of cancer stem-like cells, and its expression is associated with an aggressive phenotype and an augmented epithelial-mesenchymal transition [12,13].

The day after, the primary antibody solution was removed, and the sample was washed 3 times for 2 min with PBS at RT. Next, 200 μ L of secondary antibody solution was added to the cells for a 1h-incubation at RT in dark. The secondary antibody solution contained DAPI (4',6-diamidino-2-phenylindole, 62248, ThermoFisher), AF488 Phalloidin (A12379, ThermoFisher) for F-actin filament staining, and secondary antibodies which were AF647-conjugated anti-rat antibody (A-21247, ThermoFisher) (targeting rat anti-human CD45) and AF488-conjugated anti-rabbit antibody (11800074, ThermoFisher) (targeting rabbit anti-human ALDH1). After incubation, the cytospot was washed 4 times for 2 min with PBS at RT and let drying for 5 min. Finally, 15 μ L of FluoroMount™ solution (F4680, Sigma®) was added to the cytospot, preventing photobleaching and preserving the fluorescent-labeled molecules for long-term storage, and mounted with a coverslip. The slide was scanned using the Lionheart X/Y motorized fluorescent microscope equipped with 4X and 20X objectives. In particular, three filters were used to detect the fluorescent signal: DAPI for nucleus staining, CY5 for CD45, CD15, and CD41, and GFP for ALDH1 or Phalloidin. Parametric settings including exposure time, LED intensity, gain and focus were adjusted with the associated software (Gen5™ version 3.09, Biotek).

4.4.2. Fluorescent image analysis

After slide scanning, cell characterizations were performed by analyzing their fluorescent signal using Gen5™ software tools (version 3.09, Biotek). First, the potentially hazardous effect of the magnetic purification on cell integrity was studied by analyzing Phalloidin fluorescent signal. Phalloidin stains F-actin filament which is a major component of the cytoskeleton and is involved in fundamental cellular processes, such as cell division, morphogenesis, and migration [14]. Cell cytoskeletal and morphological integrity can therefore be studied. The following steps were performed on the software: a primary mask cellular analysis criterion was applied to automatically detect cell nuclei from DAPI signal. Then, a secondary mask was also applied to distinguish cell cytoplasm with Phalloidin signal. Further subpopulation analysis was conducted to identify A549 cells (recovered mCTCs), which are CD45-/CD15-/CD41- and Phalloidin+, by setting the signal intensity threshold so as to discriminate the positive signal from the background one. Next, cell characteristic parameters were extracted, from the nucleus size and circularity (obtained from the primary mask) to the cytoskeleton size (secondary mask); and the nuclear-cytoplasmic ratio (N:C ratio) was calculated. This ratio is simply the ratio of the size of the nucleus of a cell to the size of the cytoplasm of that cell, the latter can be associated with the cytoskeleton size as the cytoskeleton crisscrosses the cytoplasm. Finally, these values were compared with the ones of A549 control which were not submitted to any purification step.

Besides, the enrichment efficacy of the magnetic purification step was quantified by fluorescence analysis. Similarly, a primary mask was applied (DAPI signal), followed by a subpopulation analysis to identify both WBCs (CD45+/CD15+/CD41+ and ALDH1-) and A549 cells (CD45-/CD15-/CD41- and ALDH1+) by setting a threshold value for both CY5 and GFP signals. Finally, the number of WBCs and A549 cells was based on the previous discrimination and the enrichment of A549 cells was determined.

Last but not least, heterogeneity of recovered mCTCs after purification could be visualized and even quantified by first applying DAPI primary mask and GFP secondary mask (targeting ALDH1+ cells). A549 cells were identified from the subpopulation analysis and cellular heterogeneity of ALDH1 expression level (based on GFP signal intensities) and cell size (from secondary mask size) was assessed.

A summary of fluorescent image analyses is reported in Table 2-1.

Table 2-1: Fluorescence imaging with Lionheart microscope and analysis with Gen5™ software.

Study of interest	First imaging channel	Second imaging channel	Primary mask	Secondary mask	Analysis metrics
A549 cell integrity	DAPI	GFP	DAPI	GFP*	Primary mask size, circularity, secondary mask size
WBC count	DAPI	CY5	DAPI	Not used	CY5+ cell count
A549 count	DAPI	GFP	DAPI	Not used	GFP+ cell count
A549 cell heterogeneity	DAPI	GFP	DAPI	GFP**	Secondary mask size, GFP intensity

*Expanded mask; **Ring mask. More information is given below.

It should be noted that secondary mask for Phalloidin and ALDH1 signals were obtained by two different tools from Gen5™ software. Indeed, since Phalloidin is present in cell cytoplasm, the fluorescent GFP signal is measured within the whole cell by expanding the primary mask (cell nucleus). The primary mask was expanding of a size of 15 μm (Figure 2.16-A). Regarding ALDH1, it is a surface marker, therefore the GFP signal was measured within a ring surrounding the cell nucleus. The ring width was set to 5 μm (Figure 2.16-B).

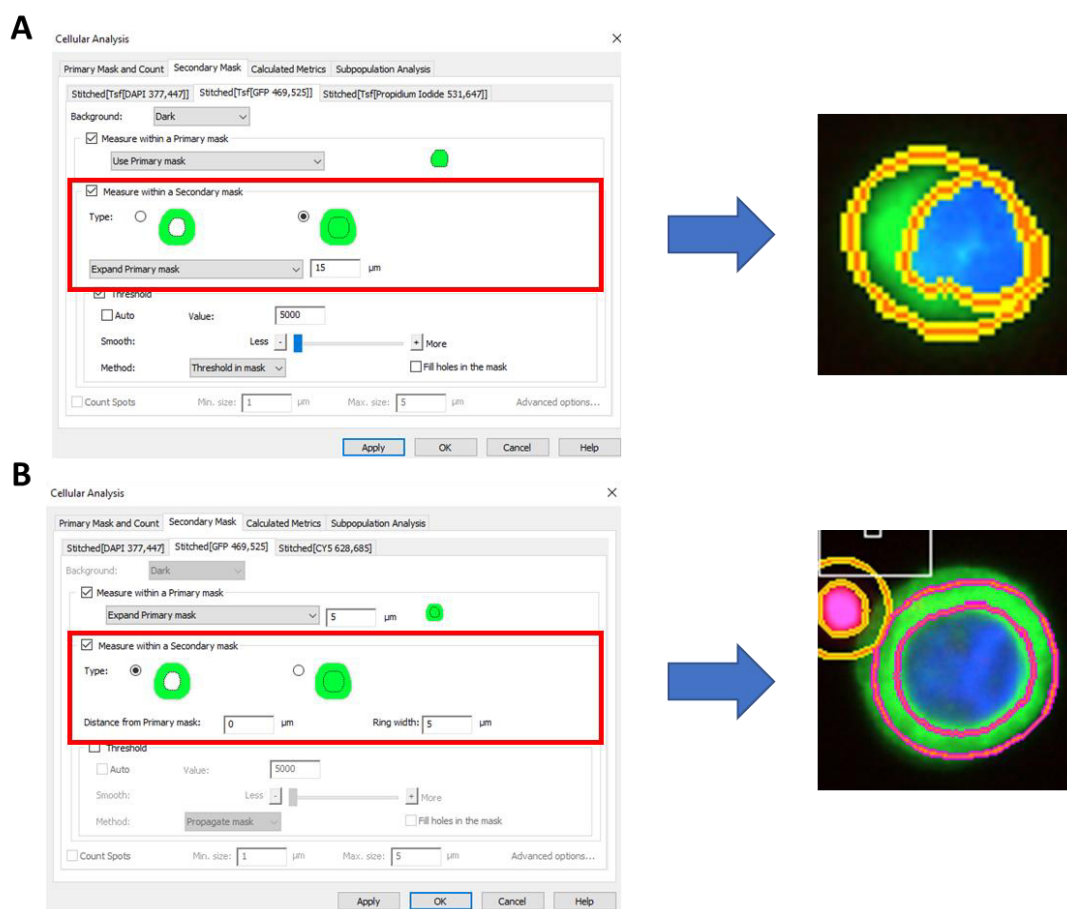


Figure 2.16: Phalloidin and ALDH1 fluorescent signal (GFP) measurements with a secondary mask. (A) Phalloidin was measured by expanding the primary mask (DAPI for nucleus staining) since the marker enters cell cytoplasm.

(B) ALDH1 was measured by defining a ring surrounding the primary mask since the marker is only present at the membrane surface.

4.5. Fluorescence In-Situ Hybridization

4.5.1. Principle and objective

Fluorescence in situ hybridization (FISH) is a powerful technique for probing the genetic content of individual cells at the molecular level. Cryptic genetic variations such as insertion, deletion, translocation, and rearrangement, can be easily recognized using FISH [15], which relies on the hybridization of DNA probes on entire chromosomes or single unique sequences. In many cancers, such chromosomal abnormalities often indicate lower survival rates and poor treatment efficacy [16]. In particular, the anaplastic lymphoma kinase (ALK) genetic abnormality, located on the short arm of chromosome 2, is a key oncogenic driver, especially in non-small cell lung cancer [17]. The EML4-ALK gene fusion caused by a chromosomal inversion (Figure 2.17) can produce a constitutively active ALK tyrosine kinase protein, which leads to enhanced cell survival and cell proliferation [18,19]. Detecting the EML4-ALK gene fusion within patients will enable targeted therapies based on ALK inhibitors and provide new clues for in anti-cancer drug discovery and development [20,21].

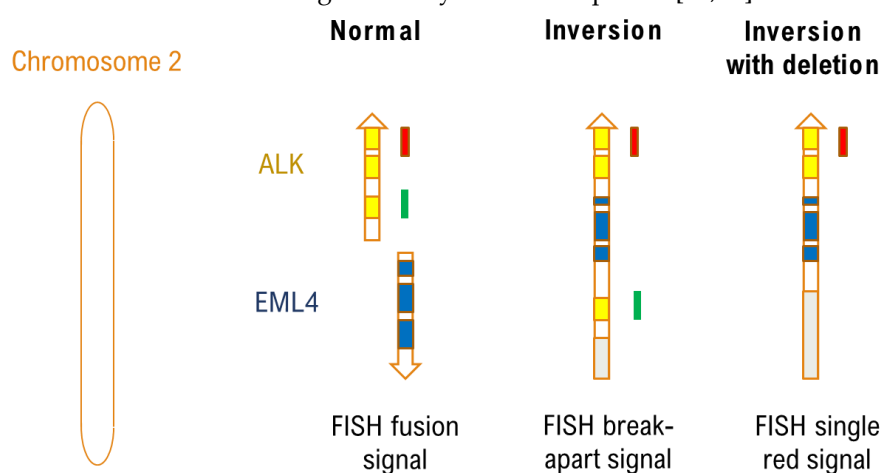


Figure 2.17 Detection of the EML4-ALK gene fusion with FISH technique using green and red probes.

4.5.2. Protocol

To study the EML4-ALK fusion, EML4-ALK fusion-A549 cell line was purchased from ATCC (CCL-185IG™). ATCC CCL-185IG can be a useful model to study tyrosine kinase signaling pathway, and to screen ALK inhibitors. There are multiple EML4-ALK fusion variants, ATCC CCL-185IG cell line contains the most prevalent one, the variant 1 (E13; A20), in which EML4 intron 13 is fused with ALK intron 20.

FISH experiments were performed using the Aquarius® kit (CytoCell, OGT) which contains a DAPI counterstain and the ALK Breakapart probe, consisting of a green 420kb probe, which spans the majority of the ALK gene and a red 486kb probe, which is telomeric to the ALK gene (i.e. occurring at the end of the chromosome). After magnetic purification, cell spots were prepared with Cytospin® 4 (400 rpm, 4 min) and fixed with a 3:1 methanol/acetic acid v/v solution for 20 min on ice. The spots were immersed in a 2X SSC solution (Formamide, Dextran Sulphate, CytoCell) at RT during 2 min, twice, and then dehydrated in 70%, 85%, and 100% ethanol (Merck) at RT for 2 min each. Next, 10 µL of the ALK Breakapart probe was spotted onto the sample slide (first prewarmed at 37 °C for 5 min), a cover slip was then mounted on top and sealed with a rubber solution glue (CytoCell). The sample and probe were simultaneously denatured by heating the slide on a hotplate at 75°C for 2 minutes. The slide was then placed in a humid, lightproof chamber at 37 °C overnight for hybridization. The day after, post-hybridization washes were done by immersing the slide (removed from the coverslip and glue), first in

a 0.4x SSC solution at 72°C (pH 7.0) for 2 min, and then in a 2x SSC, 0.05% Tween-20 solution at RT (pH 7.0) for 30 seconds after slide draining. Finally, 10 µL of DAPI was added to the sample, covered with a coverslip, and incubated for 10 min in dark at RT. Fluorescence images were taken with the PANNORAMIC Scan II (3DHISTECH Ltd), equipped with FITC, Texas Red, and DAPI filters.

5. Integrated workflow: size-based pre-enrichment separation followed by magnetic purification

5.1. Context: a need to take into account CTC heterogeneity and improve sample purity

Once the magnetic chip has been well characterized, from the calculation of capture and recovery efficiencies to the demonstration of the chip compatibility with downstream analysis, the magnetic-based separation was combined with a first size-based enrichment separation to improve purity. This pre-enrichment step is performed on ClearCell® FX1 instrument (Biolidics Ltd, Singapore, BIOSCIENCES®) since the Hospices Civils de Lyon (project partner laboratory) is equipped with this system, and widely used in their clinical studies [22]. The separation relies on the Dean Flow Fractionation (DFF) separation technology in a spiral chip. Two separation modes depending on CTC size cutoff were developed by Biolidics but no analysis of these two modes can be found in the literature. Based on different elements extracted from the literature, a CTC size cutoff of 14 µm was set (running program P1) but this value can be adjusted by altering the flow ratios at the output to enrich CTCs at a lower cell size [23], therefore increasing the recovery efficiency (running program P3). Inevitably, it will result in a larger background of WBCs, which can be a limitation for downstream processes. Thus, depending on the needed downstream analysis, ClearCell system offers P1 and P3 running programs. P1 yields recovery rates comprised between 40 and 60% [24,25] depending on cell type (and therefore on cell size), with a total WBC background of 16,666 WBCs (internal data, median obtained in 8 patient samples with head and neck cancer or NSCLC). P3 allows for recovery rates comprised between 60 and 80% [25,26], with 300,000 remaining WBCs (internal data, median obtained in 21 patient samples with head and neck cancer or NSCLC).

Since CTCs are highly heterogeneous in size (~8–22 µm), especially among different tumor origins [27], the program P3 is preferred to reach higher CTC recovery. There is therefore a high need to improve ClearCell P3 output purity, which can be achieved by conducting an immunomagnetic purification using the developed magnetic chip. The protocol of the integrated workflow will be described in this section.

5.2. ClearCell FX1 system instructions

The process protocol of the ClearCell instrument can be divided in three major steps: priming, processing, and cleaning. The priming step consists in injecting sterilized deionized water within a new CTChip® FR1 with the prime run (3 min). This first step should be repeated three times. Then, the next step consists in processing the CTC sample within the CTChip® by running either the program P3 or the program P1. Depending on the desired application, P3 provides a higher recovery (duration of 31 min) while P1 leads to higher purity (duration of 54 min). Finally, after sample processing, the system is cleaned by injecting FACS Clean Agent (BD Biosciences, 340345) for 25 min. The ClearCell FX instruction and maintenance steps were performed according to Garcia et al. protocol [26].

5.3. Workflow protocol

The whole workflow protocol is illustrated in Figure 2.18. Blood samples were obtained from healthy blood donors and collected in 10 mL K2 EDTA tubes (Tubes BD Vacutainer®). First, 20 000 A549 were spiked into 7.5 mL of whole blood and loaded into a new input tube (Corning® 50 mL centrifuge tube). Next, 22.5 mL of lysis buffer was added to the blood sample and RBC lysis steps were performed following the protocol described in section 3.2.1. After the centrifugation step and the removal of lysed RBCs, the cell pellet (composed of WBCs and A549 cells) is resuspended in 4 mL of resuspension buffer provided by Biolidics Ltd (ref CBB-F016003). Before proceeding to the size-based enrichment step, any bubbles present within the sample should be carefully removed without discarding the sample volume.

Then, the sample was processed on the ClearCell® FX-1 system and collected in an output tube (Falcon® 15 mL centrifuge tube). After the enrichment program, the mCTC-enriched sample was centrifuged at 500g for 10 min, and then resuspended in 300 μ L of 2 mM EDTA diluted in PBS-2% BSA. Afterwards, cell viability and enumeration were accessed by diluting 5 μ L of mCTC-enriched sample with 5 μ L of Trypan Blue solution (Gibco, 15250-061) and loaded in a KOVA slide. Trypan blue stains dead cells exclusively by penetrating the damaged cell membrane and entering the cytoplasm. Doing so, the number of total cells and alive cells was reported as a characteristic data of the ClearCell FX1 system separation. In particular, the number of WBCs was assessed to determine the corresponding volume of functionalized magnetic NP that should be added to respect the ratio of 400 NP/WBC and 100 NP/WBC for anti-CD45 and anti-CD15 antibodies, respectively.

After these pre-enrichment steps, the sample was loaded in a 24-well plate for WBC magnetic labeling following the protocol described in section 3.3.2. (30 min incubation at 37 °C under agitation). Next, the sample, containing magnetically labeled WBCs and A549 cells, was loaded into an eppendorf 1.5 mL tube and injected within the magnetic chip at 2 mL/h, which was priorly sterilized and Pluronic-coated (see section 4.1.1.). After purification, the number of total cells and alive cells was again determined with Trypan blue and reported as a characteristic data of the magnetic-based purification.

Finally, the output of the whole workflow was collected for subsequent analysis, either for 2D cell culture and cell proliferation study (the protocol can be found in section 3.1.), or for IF assay and ALDH1 surface marker expression study (protocol section 4.4.). It should be noted that, with the integrated workflow, blood samples were processed in less than 4 h (~3 h with ClearCell program P3, ~3h30 with program P1).

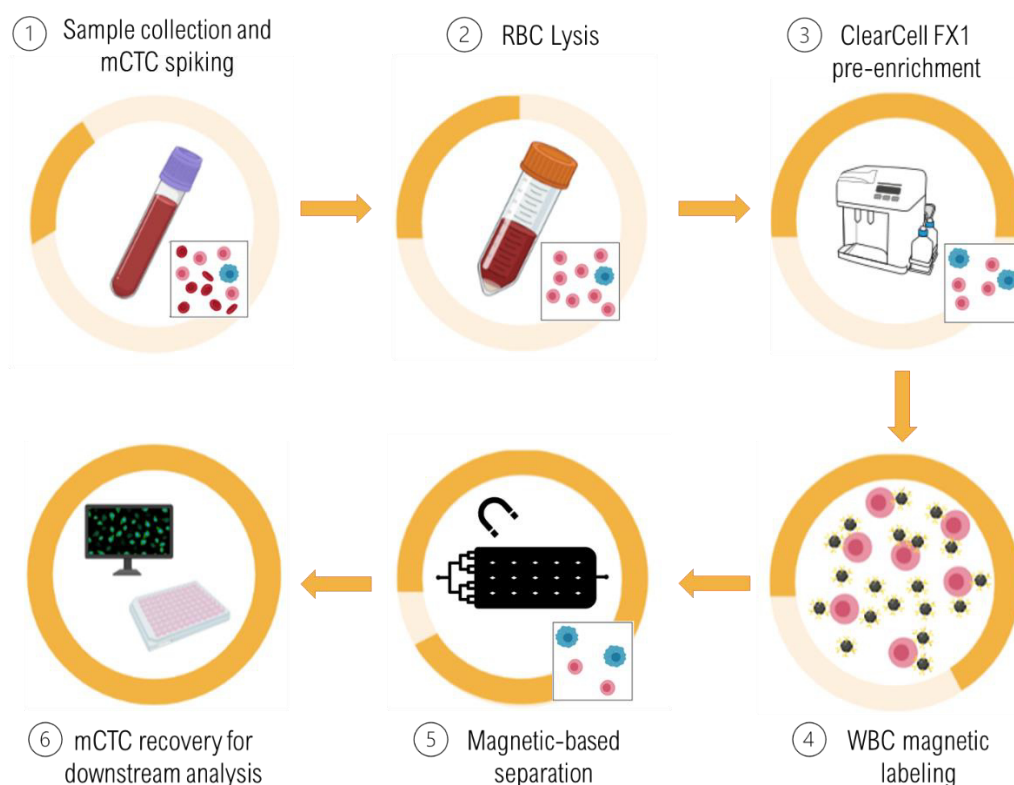


Figure 2.18: Integrated workflow for CTC isolation and downstream analysis. 1) Blood sample collection and mCTC spiking. 2) RBC lysis. Lysed RBCs and platelets are removed by discarding the supernatant and the cell pellet (mCTC and WBCs) is resuspended in ClearCell resuspension buffer. 3) Size-based enrichment step through ClearCell FX1 system. Tens to hundreds of thousands of WBCs remain after this step. 4) Magnetic labeling of WBCs with 500-nm magnetic nanoparticles functionalized with anti-CD45 and anti-CD15 antibodies (negative selection).

5) Magnetic-based purification step within the developed magnetic chip. This step allows for high sample purity, a major criterion for subsequent analysis. 6) mCTC are collected for downstream analysis (cell culture, phenotypic and genotypic studies). The whole workflow can be performed within 4h. An overview of the output sample is given after steps 1, 2, 3 and 5. Created with BioRender.com.

References

1. Chen, Z.; Miller, D.; Herchenroeder, J. High performance nanostructured Nd-Fe-B fine powder prepared by melt spinning and jet milling. *J. Appl. Phys.* **2010**, *107*, 1–3, doi:10.1063/1.3348544.
2. Renaud, L.; Selloum, D.; Tingry, S. Xurography for 2D and multi-level glucose/O₂ microfluidic biofuel cell. *Microfluid. Nanofluidics* **2015**, *18*, 1407–1416, doi:10.1007/s10404-014-1539-z.
3. Mekkaoui, S. Développement de polymères composites auto-organisés pour la mise en œuvre de fonctions magnétiques en microsystèmes fluidiques, Université Claude Bernard Lyon 1, 2019.
4. Baruchel, J.; Buffiere, J.Y.; Maire, E. *X-ray tomography in material science*; Hermes science publications: France, 2000; ISBN 2-7462-0115-1.
5. Fagaly, R.L. Superconducting quantum interference device instruments and applications. *Rev. Sci. Instrum.* **2006**, *77*, doi:10.1063/1.2354545.
6. Clarke, J. Principles and applications of SQUIDS. *Proc. IEEE* **1989**, *77*, 1208–1223, doi:10.1109/5.34120.
7. Ponomareva, S.; Dias, A.; Royer, B.; Marelli, H.; Motte, J.F.; Givord, D.; Dumas-Bouchiat, F.; Dempsey, N.M.; Marchi, F. A quantitative study of magnetic interactions between a micro-magnet array and individual magnetic micro-particles by scanning particle force microscopy. *J. Micromechanics Microengineering* **2019**, *29*, 015010, doi:10.1088/1361-6439/aaefd5.
8. AC/DC Module User's Guide. **1998**.
9. Sanders, E.R. Aseptic Laboratory Techniques: Plating Methods. *JoVE (Journal Vis. Exp.)* **2012**, e3064, doi:10.3791/3064.
10. Liu, V.A.; Jastromb, W.E.; Bhatia, S.N. Engineering protein and cell adhesivity using PEO-terminated triblock polymers. *J. Biomed. Mater. Res.* **2002**, *60*, 126–134, doi:10.1002/jbm.10005.
11. Kulasinghe, A.; Zhou, J.; Kenny, L.; Papautsky, I.; Punyadeera, C. Capture of circulating tumour cell clusters using straight microfluidic chips. *Cancers (Basel)*. **2019**, *11*, 1–11, doi:10.3390/cancers11010089.
12. Yao, J.; Jin, Q.; Wang, X.D.; Zhu, H.J.; Ni, Q.C.; Fan, H. Aldehyde dehydrogenase 1 expression is correlated with poor prognosis in breast cancer. *Med. (United States)* **2017**, *96*, 1–6, doi:10.1097/MD.00000000000007171.
13. Chen, M.F.; Chen, P.T.; Lu, M.S.; Chen, W.C. Role of ALDH1 in the prognosis of esophageal cancer and its relationship with tumor microenvironment. *Mol. Carcinog.* **2018**, *57*, 78–88, doi:10.1002/mc.22733.
14. Sirenko, O.; Hesley, J.; Rusyn, I.; Cromwell, E.F. High-content assays for hepatotoxicity using induced pluripotent stem cell-derived cells. *Assay Drug Dev. Technol.* **2014**, *12*, 43–54, doi:10.1089/adt.2013.520.
15. Takeuchi, K.; Togashi, Y.; Kamihara, Y.; Fukuyama, T.; Yoshioka, H.; Inoue, A.; Katsuki, H.; Kiura, K.; Nakagawa, K.; Seto, T.; et al. Prospective and clinical validation of ALK immunohistochemistry: Results from the phase I/II study of alectinib for ALK-positive lung cancer (AF-001JP study). *Ann. Oncol.* **2016**, *27*, 185–192, doi:10.1093/annonc/mdv501.
16. Gertz, M.A.; Lacy, M.Q.; Dispenzieri, A.; Greipp, P.R.; Litzow, M.R.; Henderson, K.J.; Van Wier, S.A.; Ahmann, G.J.; Fonseca, R. Clinical implications of t(11;14)(q13;q32), t(4;14)(p16.3;q32), and -17p13 in myeloma patients treated with high-dose therapy. *Blood* **2005**, *106*, 2837–2840, doi:10.1182/blood-2005-04-1411.
17. Soda, M.; Choi, Y.L.; Enomoto, M.; Takada, S.; Yamashita, Y.; Ishikawa, S.; Fujiwara, S.I.; Watanabe, H.; Kurashina, K.; Hatanaka, H.; et al. Identification of the transforming EML4-ALK fusion gene in non-small-cell lung cancer. *Nature* **2007**, *448*, 561–566, doi:10.1038/nature05945.
18. Qin, Z.; Sun, H.; Yue, M.; Pan, X.; Chen, L.; Feng, X.; Yan, X.; Zhu, X.; Ji, H. Phase separation of EML4–ALK in firing downstream signaling and promoting lung tumorigenesis. *Cell Discov.* **2021**, *7*, 33, doi:10.1038/s41421-021-00270-5.
19. Takeuchi, K.; Choi, Y.L.; Soda, M.; Inamura, K.; Togashi, Y.; Hatano, S.; Enomoto, M.; Takada, S.; Yamashita, Y.; Satoh, Y.; et al. Multiplex reverse transcription-PCR screening for EML4-ALK fusion transcripts. *Clin. Cancer Res.* **2008**, *14*, 6618–6624, doi:10.1158/1078-0432.CCR-08-1018.

20. Toyokawa, G.; Seto, T. Anaplastic lymphoma kinase rearrangement in lung cancer: its biological and clinical significance. *Respir. Investig.* **2014**, *52*, 330–338, doi:10.1016/j.resinv.2014.06.005.
21. Sánchez-Herrero, E.; Provencio, M.; Romero, A. Clinical utility of liquid biopsy for the diagnosis and monitoring of EML4-ALK NSCLC patients. *Adv. Lab. Med. / Av. en Med. Lab.* **2020**, *1*, doi:10.1515/almed-2019-0019.
22. Garcia, J. Évaluation du patrimoine tumoral circulant dans la prise en charge thérapeutique des patients atteints de cancer broncho-pulmonaire, 2019.
23. Lee, Y.; Guan, G.; Bhagat, A.A. ClearCell® FX, a label-free microfluidics technology for enrichment of viable circulating tumor cells. *Cytom. Part A* **2018**, *93*, 1251–1254, doi:10.1002/cyto.a.23507.
24. Takahashi, Y.; Shirai, K.; Ijiri, Y.; Morita, E.; Yoshida, T.; Iwanaga, S.; Yanagida, M. Integrated system for detection and molecular characterization of circulating tumor cells. *PLoS One* **2020**, *15*, 1–13, doi:10.1371/journal.pone.0237506.
25. Aya-Bonilla, C.A.; Morici, M.; Hong, X.; McEvoy, A.C.; Sullivan, R.J.; Freeman, J.; Calapre, L.; Khattak, M.A.; Meniawy, T.; Millward, M.; et al. Detection and prognostic role of heterogeneous populations of melanoma circulating tumour cells. *Br. J. Cancer* **2020**, *122*, 1059–1067, doi:10.1038/s41416-020-0750-9.
26. Garcia, J.; Barthelemy, D.; Geiguer, F.; Ballandier, J.; Li, K.W.; Aurel, J.P.; Breton, F. Le; Rodriguez-Lafresse, C.; Manship, B.; Couraud, S.; et al. Semi-automatic pd-l1 characterization and enumeration of circulating tumor cells from non-small cell lung cancer patients by immunofluorescence. *J. Vis. Exp.* **2019**, *2019*, doi:10.3791/59873.
27. Phillips, K.G.; Kuhn, P.; McCarty, O.J.T. Physical biology in cancer. 2. The physical biology of circulating tumor cells. *Am. J. Physiol. - Cell Physiol.* **2014**, *306*, 80–88, doi:10.1152/ajpcell.00294.2013.

Chapter III

PDMS membrane integrating self-organized micro-magnet arrays: Structure, magnetism, and magnetophoretic trapping in microfluidics

In this chapter, we will first place this thesis in the context of research on anisotropic composites within the laboratory. Then we will study the influence of the magnetic field during the fabrication of the composite on its microstructure and magnetic properties. Next, we will describe further characterization of the obtained micro-magnets, from their microstructure to magnetic properties. In particular, various characterization techniques were implemented, including numerical and experimental analyses, so as to provide a full study of the micro-magnets. In addition, we will present microfluidic experiments using superparamagnetic beads as target objects to demonstrate the magnetophoretic separation ability of the integrated micro-magnets, which act as micro-traps. Finally, we will look at all the obtained results against reported magnetic devices in the literature.

1. Previous work of the group on anisotropic magnetic composites

Magnetophoretic separation is particularly suited to microsystems as the downscaling of the magnetic source scales up the magnetic field gradients and therefore increases the magnetophoretic force [1]. The integration of micrometer-sized magnetic structures hence allows for the generated force increase, but also the manipulation of individual target objects. Furthermore, the integration of a high density of magnetic microstructures offers the possibility to sort and manipulate a large population of target entities in fluidic samples. The composite approach represents a powerful bottom-up method that could tackle, in a simple manner, the fabrication of magnetic sources with micrometric size and high density, as well as their integration in polymer-based microfluidic devices.

Among the many advantages of the composite approach, one can cite its versatility since the polymer matrix nature, the magnetic powder composition (size and morphology), the packing density and mixing uniformity, as well as the microfabrication technique, can be tailored [2]. In particular, the concentration of magnetic nano- or micro- particles can be varied. Highly concentrated magnetic composites can be seen as a fully dense material that exhibits relatively large magnetization, even comparable with pure metallic Ni-based alloys [3]. Such composite microstructures can be integrated either on the channel bottom or channel side to trap or deflect target objects, respectively. They usually present an isotropic dispersion of the magnetic particles within the polymer matrix and, if any, their magnetic anisotropy is governed by the overall shape of the pattern.

The induction of anisotropic magnetic properties has generated a great deal of interest, by controlling the dispersion of the magnetic particles. It can be achieved by submitting the composite mixture to a magnetic field during the polymer cross-linking step. In the non-reticulated polymer, the motion of the magnetic particles is essentially driven by magnetic dipolar interactions. Depending on the relative positions of two adjacent magnetized particles, the interaction can be repulsive or attractive (Figure 3.1), which leads to anisotropic mechanisms of field-induced structures such as agglomeration and self-organization [4–8].

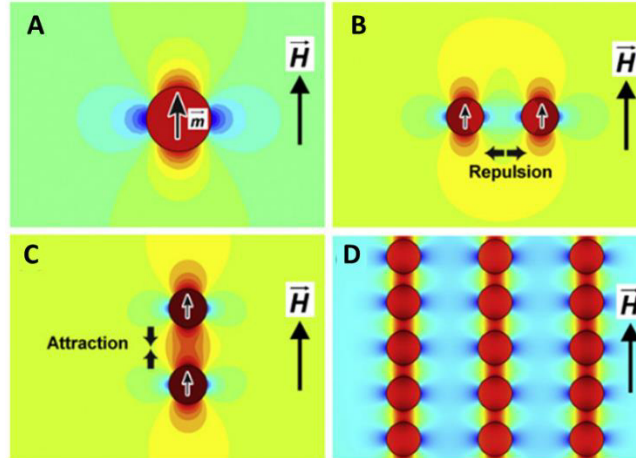


Figure 3.1: (A) Magnetic field distribution around a superparamagnetic particle with a dipole moment in the same direction as the external magnetic field. (B,C) Repulsive and attractive dipole–dipole interactions, respectively. (D) Anisotropic mechanisms drive the formation of chains along the magnetic field. Adapted from [7].

This self-assembly strategy has been studied by co-workers from INL and ILM over the last few years for the fabrication of 1D micro-concentrators dedicated to the manipulation of micro-objects in microfluidics [3,9–11]. Deman et al. self-organized an 83 wt% I-PDMS (iron carbonyl/PDMS) composite by applying a 130 mT magnetic field during the polymer cross-linking step. Despite a large number of iron particles limiting their motion, they aligned in chains along the field lines, leading to a uniaxial anisotropic microstructure [9]. In particular, they demonstrated the benefits of the anisotropic I-PDMS on magnetophoretic performances over the isotropic one. They measured a magnetic force twice bigger for anisotropic composites than for isotropic ones (at a distance of 150 μm from the micro-concentrator). This magnetophoretic force increase was not only attributed to the global susceptibility increase, but

also to the local magnetic field gradients originating from the fine alternation of magnetic and non-magnetic regions (periodic microstructure).

Besides, Le Roy et al. investigated the influence of the concentration of Fe-C magnetic micro-particles on the magnetic anisotropy [3]. They observed that, from a 10 wt% concentration, the magnetic anisotropy continuously decreases for increasing Fe-C concentrations, which was attributed to the combined effect of (i) increasing number of chain agglomerates with the particle concentration, which leads to an increase of agglomerate lateral size, therefore decreasing the shape anisotropy; and (ii) enhanced demagnetizing dipolar interactions as the density of agglomerates increases. The magnetic characterizations of this material [12] showed that the anisotropy was more pronounced for low composite concentrations, with a maximum when the volume fraction of Fe-C particles is around 1.5 vol% (10 wt%), at expense of the overall composite magnetization (Figure 3.2-A).

As described previously for high concentrated anisotropic composites, low concentrated anisotropic composites are obtained when submitted to a magnetic field during the polymer cross-linking step. Interestingly, this approach allows for the obtention of magnetic microstructures, diluted in the PDMS matrix, with aspect ratios that are hardly obtained with conventional microfabrication techniques (Figure 3.2-B). Mekkaoui et al. prepared 1 and 5 wt% anisotropic I-PDMS composites whose microstructures exhibit high aspect ratio (> 6) and high densities (1500 and 5000 traps/mm², respectively). These microstructures were magnetized with an external centimeter-sized magnet and were used as magnetic traps. The traps consist of chain-like agglomeration of Fe micro-particles, with a typical diameter inferior to 10 μm and an elongated shape, to efficiently concentrate an external magnetic flux (micro-concentrators). They implemented the traps in a microfluidic channel for magnetophoretic studies and demonstrated a trapping efficiency as high as 99.94% and probed the distribution of trapping forces, which reached up to 2 nN.

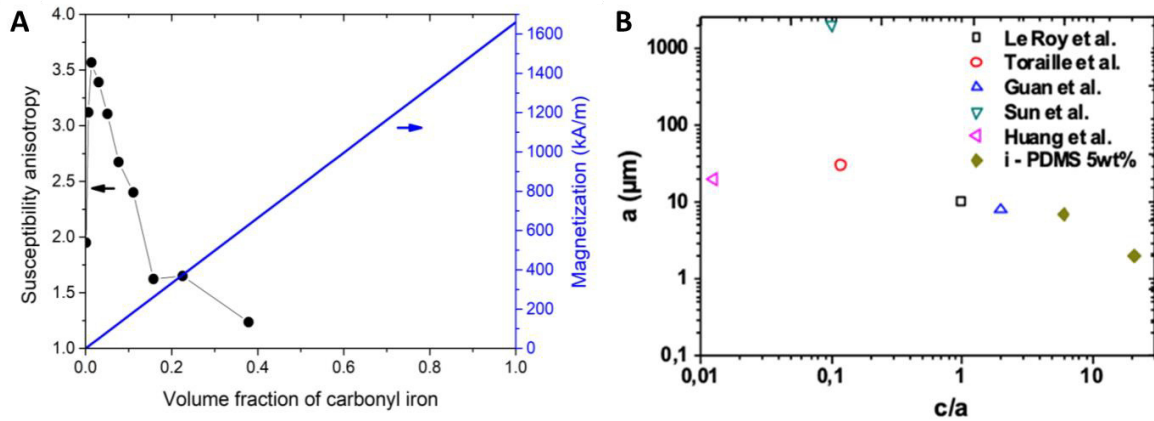


Figure 3.2: Anisotropic I-PDMS (A) Evolution of the anisotropy and the overall composite magnetization of the I-PDMS membranes. The susceptibility anisotropy is the ratio between the low field susceptibility in the direction of the applied field during the preparation and the in-plane perpendicular direction. Adapted from [3]. (B) Comparative study of various magnetic structures according to their diameter (ordinate a) and aspect ratio (long to short axis ratio, c/a). The microstructures were obtained either from conventional methods from literature or from the i-PDMS composite approach. Adapted from [11].

As reported above, the previous works within the team relied on soft magnetic composites (Fe-C particles), which do not lead to autonomous microsystems since they need an external magnet to operate. Within the framework of this thesis, we have developed a hard magnetic composite, NdFeB@PDMS, to allow devices to gain autonomy and portability. In particular, the work will focus on the preparation of anisotropic composites at low concentration to obtain an array of magnetic traps for magnetophoretic separation. Besides, the influence of NdFeB particle concentration, as well as the preparation under a non-uniform magnetic field, will be investigated.

2. Influence of the magnetic field on the micro-magnet array formation

As aforementioned, the magnetic composite can be organized under the application of a uniform magnetic field, which is relatively simple to implement and is well suited to obtain micro-traps for magnetic capture of individual entities, such as superparamagnetic beads or magnetically labeled cells that have typical sizes comparable with the trap sizes. In turn, it restricts the shape of agglomerates to 1D structures and does not allow for independent tuning of the lateral size, localization, and density of traps.

Other strategies implementing preparation under a non-uniform magnetic field, through the use of a magnetic template, were therefore investigated to form other geometries of micro-patterns. Dempsey et al. used a continuous magnetic film of NdFeB with written up and down domains (obtained by thermomagnetic patterning [13]) as a master to organize dispersed NdFeB particles within non-reticulated PDMS [14]. NdFeB particles concentrate in the regions of magnetic field maxima, typically at the frontier between adjacent up and down domains, broadening the range of pattern geometries. The fabricated NdFeB-PDMS membrane was permanently magnetized under a high field and used for the trapping of cells functionalized with superparamagnetic beads in open surface conditions. More recently, Bidan et al. applied a similar approach using a template made of topographically patterned NdFeB thick films, with an intercalated thin plastic foil, on which they poured a mixture of individual magnetic micro-pillars and liquid PDMS [15]. Doing so, the authors obtained lines of pillars regularly spaced within a PDMS matrix. It resulted in magneto-active substrates, with a rigidity in the range of cell matrices, which were used for cell growth monitoring under controlled mechanical stress. In this thesis, we studied the effect of a magnetic template on the microstructure and magnetic properties of the composite.

2.1. Study of two experimental set-ups

In this work, 100- μm high NdFeB@PDMS composites, whose concentration was varied between 1 and 2 wt%, were submitted to magnetic fields and magnetic field gradients generated by: either a single external magnet (60 \times 30 \times 15 mm³) positioned below the composite during the curing step (nearly uniform magnetic field), the composite being deposited on a glass slide substrate; or a combination of the external magnet with a magnetic template (non-uniform magnetic field), the template replacing the glass slide. The magnetic template consists of a Fe-C magnetic composite (I-PDMS) which contains chain-like agglomerates of Fe-C microparticles (97% Fe basis, nearly pure α -Fe), oriented in the direction perpendicular to the substrate's surface. The strategy of using this magnetic template, that allows the generation of numerous strong and localized magnetic field gradients, is multiple: (i) controlling the density of NdFeB micro-magnets within the composite as Fe-C particles represent patterns to position NdFeB particles; (ii) locating NdFeB particles on the surface of the composite membrane by attracting the particles towards the template; (iii) and compacting chains of NdFeB particles by lowering the interparticle distance.

The I-PDMS composite membrane was obtained following colleagues' protocol [10]: after pouring the mixture of Fe-C particles and liquid PDMS on a glass slide, the composite was submitted to a homogenous magnetic field of 150 mT (measured using a Keithley Teslameter), supplied by a pair of NdFeB permanent magnet of 10 \times 11 \times 2.5 cm³. The permanent magnets were facing each other in an attractive configuration and were separated by a gap of 6 cm. Fe-C particle concentration was varied from 5 to 10 wt%: at 10 wt%, the concentration of Fe-C particles was too high and resulted in particle chains with a length larger than the membrane thickness, the substrate was therefore not flat. At 5 wt%, Fe-C particle density and nearest neighbor distance were 1150 particles/mm² and 22 μm , respectively; while at 7.5 wt%, the density and nearest neighbor distance reached 1900 particles/mm² and 17 μm . Finally, 7.5 wt% I-PDMS composites were prepared in order to try to reach greater NdFeB micro-magnet densities.

The benefit of working under either a nearly uniform or non-uniform magnetic field during PDMS cross-linking was evaluated. In the configuration using a glass slide as a substrate during the curing step, the NdFeB@PDMS membrane is only submitted to the magnetic field gradient generated by the

external magnet, estimated at 20 T/m from numerical simulations (Comsol Multiphysics®). In the configuration using a magnetic template as a substrate, strong magnetic field gradients are generated locally, at the Fe-C chain positions, and were estimated within the scope of Mekkaoui thesis work [12] at 10^5 T/m at a distance of 1 μm from the template surface. The latter magnetic field gradient values being 5000 times larger, these two configurations will therefore be referred to as “low-gradient set-up” and “high-gradient set-up”, respectively. The influence of both set-ups on the structure of NdFeB micro-magnets, their magnetic properties, as well as on their trapping ability in microfluidics, will be studied.

2.2. Micro-magnet microstructure

The reconstructed 3D profile of the NdFeB@PDMS membrane from X-ray tomography observation is shown in Figure 3.3, for 1 and 2 wt% concentration, and for low-gradient (LG) and high-gradient (HG) set-up. In particular, section views of the composite membrane highlighted the chain-like organization of the NdFeB particles within the PDMS matrix.

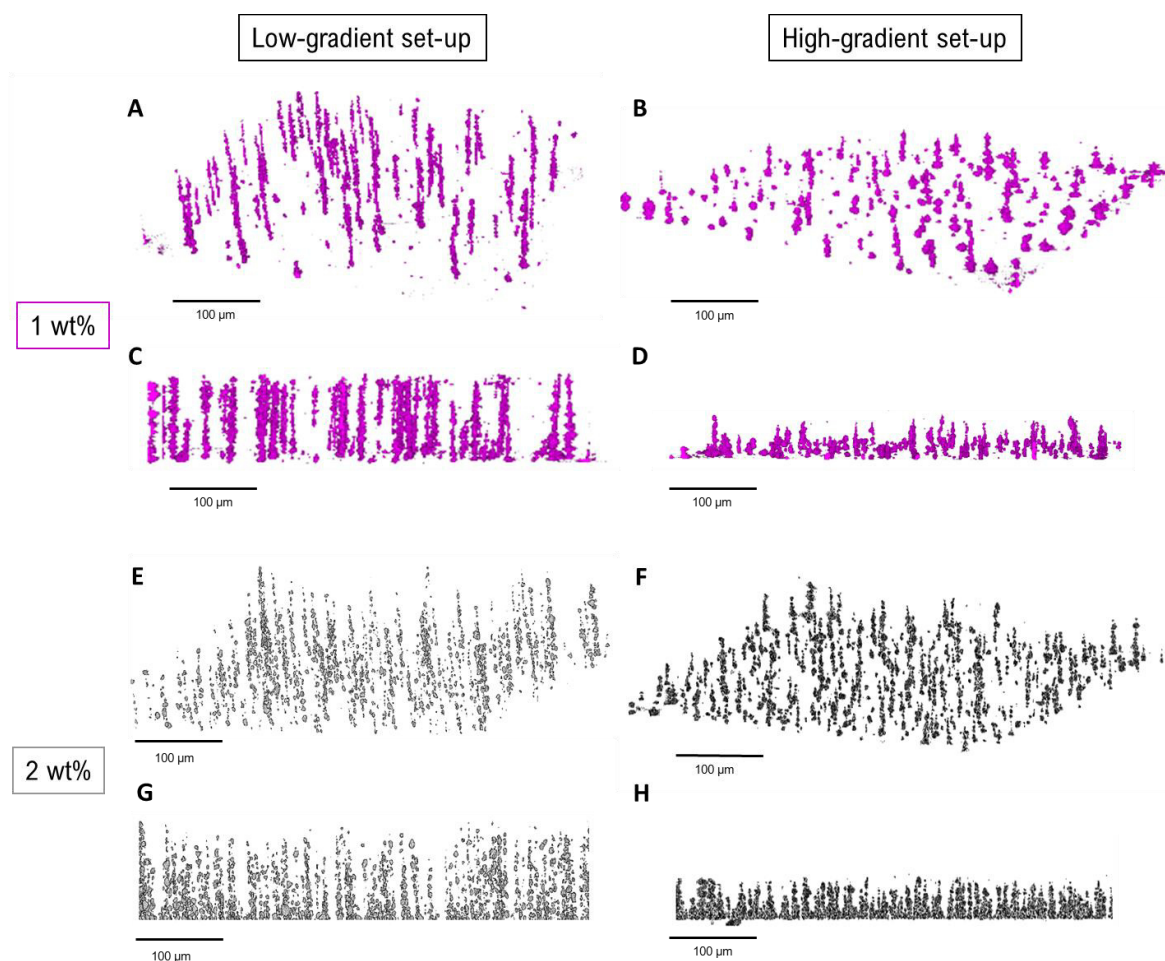


Figure 3.3: Reconstructed views from X-ray tomography performed on a volume of $510 \times 510 \times 120 \mu\text{m}^3$ of one representative membrane at (A-D) 1 wt% and (E-H) 2 wt%. (A,B) 3D views for LG and HG configurations at 1 wt%, respectively. (C,D) Projections on XZ plane revealing the chain-like organization of the 1% NdFeB particles for LG and HG set-up, respectively. (E,F) 3D views for LG and HG configurations at 2 wt%, respectively. (G,H) Projections on XZ plane of the chain-like organization of the 2% NdFeB particles for LG and HG set-up, respectively.

Several characteristic values of the micro-magnets were extracted from ImageJ analysis to study the effect of the concentration on the composite microstructure. 2D analyses in the XY plane allowed for the determination of micro-magnet density, diameter, and nearest neighbor distance (nnd); while 2D analyses in the XZ plane allowed for the characterization of chain-like agglomerates by measuring the chain length, the interparticle distance as well as the ratio of chain-like agglomerates/isotropic

agglomerates. Isotropic agglomerates referred to agglomerates of sizes inferior to 7 μm . They are mostly located at the bottom of the membrane. All these measurements are summarized in Table 3-1.

Effect of the low-gradient configuration

At low gradients and for both concentrations, NdFeB particles self-organized in chains along the membrane thickness, or in isolated agglomerates. The proportion of chain-like agglomerates and isotropic agglomerates is identical for both concentrations, with approximatively 3/4 of agglomerates being chain-like agglomerates (75% and 80% at 1 and 2 wt%, respectively). Chain-like agglomerates present a chain length of 84 and 75 μm for 1 and 2 wt%, respectively, with an interparticle distance of about 1.0 μm (\pm 0.3 μm). From these observations, it can be deduced that doubling the particle concentration did not modify the composite microstructure as chain-like agglomerates. Nevertheless, the particle concentration has an impact on the properties of the micro-magnet array: a concentration twice as large doubles micro-magnet density (from 600 micro-magnets/ m^2 at 1 wt% to 1465/ mm^2 at 2 wt%), therefore lowering nnd (from 24 to 15 μm). The micro-magnet diameter remains at a constant value of approximatively 5 μm .

Effect of the high-gradient configuration

On the contrary, cross-linking the composite under a high-gradient set-up (results in Table 3-2), through the use of a magnetic template, does have an impact on the chain particle organization when comparing with results in Table 3-1. Indeed, it leads to smaller chains, the chain length was divided by 4.7 (from 84 to 18 μm) and by 3 (from 75 to 25 μm) at 1 and 2 wt%, respectively. Not only the chains are shorter, but they also present a higher compacity. Indeed, at 1 wt%, the number of chains having an interparticle gap higher than 0.3 μm (X-ray tomography pixel resolution) is lower: it represents only 1/3 of agglomerates for the HG set-up, while there are 2/3 of them with the LG set-up. In addition, with the HG set-up, the agglomerates are located closer to the composite membrane surface: at 1 wt%, 90% of them are located at a depth inferior to 1 μm , against 30% with the LG set-up. Nevertheless, these observations on chain compacity and surface localization were not confirmed at 2 wt%. For both gradient set-ups, \sim 2/3 of chains present a visible interparticle gap and more than 95% of agglomerates are located at the composite surface (<1 μm deep).

Besides, the ratio of chain-like agglomerates and isotropic agglomerates was significantly modified with the HG set-up. Both agglomerate types are in similar proportions, of approximately 45-55% at both concentrations. The formation of twice as many IAs as with the LG set-up (20% of isotropic agglomerates) can be explained by the enhanced magnetic attraction force in the HG set-up. Isolated particles are rather attracted towards the substrate than forming chains. It should also be noticed that the chain-like agglomerates present a conical shape in comparison with the columnar shape in the LG set-up.

These differences in chain organization depending on the gradient set-up can be explained by the particle self-assembly mechanism during PDMS curing, in which two magnetic interactions come into play [3]: (i) the magnetic dipole-dipole interaction, that gathers the particles and tends to align their magnetic moments (m); (ii) the magnetic interaction between the dipole and the surrounding magnetic field gradient, that attracts the particle towards the region of maximum magnetic field. The magnitudes of the two corresponding forces are strongly affected by the substrate introduced between the external magnet and the uncured PDMS as it deeply modifies the external field distribution. As described in Figure 3.4, in the LG set-up, the substrate is a silanized glass slide, and the composite membrane is submitted to the magnetic vertical gradient of the bulk magnet (estimated at 20 T/m). In this case, the chain formation is mostly due to the dipole-dipole interaction [16,17], with a slight attraction towards the glass surface. Using the HG set-up, the substrate is an I-PDMS template, in which iron microstructures concentrate the magnetic flux lines and permit to achieve larger magnetic field gradients than that of the LG set-up. This time, the chain formation is due to both dipole-dipole and dipole-magnetic field interactions, the latter producing a strong attraction of the particles towards the template surface. The aforementioned forces are obviously in competition with the viscous force [18,19] that counteracts the NdFeB particles motion. As the crosslinking proceeds, the particles are less and less mobile until complete immobilization.

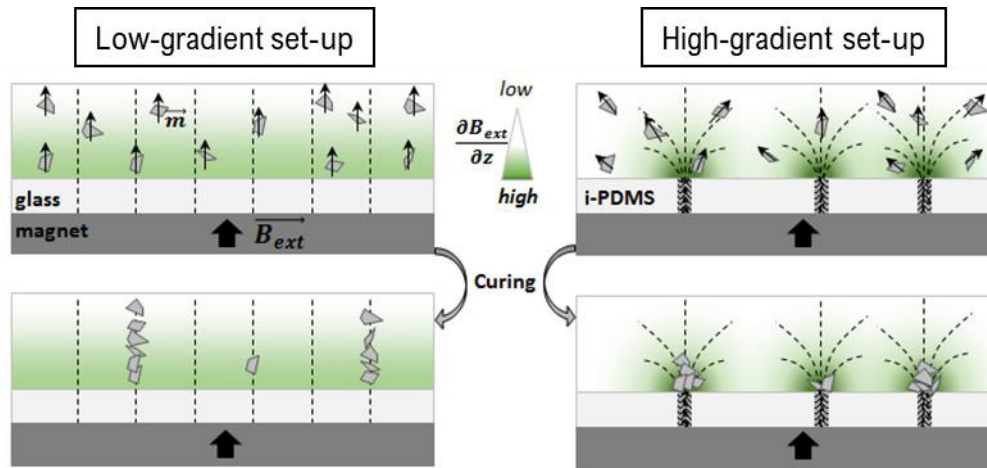


Figure 3.4: Sketch of the chain formation mechanism for both LG and HG set-up. While in the LG set-up the chain formation is mainly due to the dipole-dipole interaction, in the HG set-up the chain formation is due to both dipole-dipole and dipole-magnetic field interactions. It depends on the substrate which modifies the external magnetic field distribution.

Finally, the density of micro-magnets was increased with the HG set-up, to 1000/mm² and 1700/mm² at 1 and 2 wt%, respectively, while the diameter and nnd remain unchanged. The increase in micro-magnet density can be explained by the repartition of Fe-C particles within the magnetic template matrix (1900 Fe-C particles/mm², nnd of 17 μm), which can be seen as patterns to position NdFeB particles.

Table 3-1: Effect of the particle concentration on micro-magnet properties from X-ray tomography measurements.

Particle concentration	Density (mm ⁻²)	Diameter (μm)	Nnd (μm)	Chain length (μm)	Interparticle distance* (μm)	CA/IA ratio* (%)
1 wt%	600	6.1	24	84	0.7	75/25
2 wt%	1465	4.9	15	75	1.2	80/20

*Chain-like agglomerates/isotropic agglomerates ratio.

Table 3-2: Effect of the magnetic template on micro-magnet properties from X-ray tomography measurements.

Particle concentration	Density (mm ⁻²)	Diameter (μm)	Nnd (μm)	Chain length (μm)	Interparticle distance* (μm)	CA/IA ratio** (%)
1 wt% - HG set-up	1000	6.0	20	18	0.7	53/47
2 wt% - HG set-up	1700	4.8	15	25	0.95	56/44

*The interparticle distance is a mean value calculated for only chains showing an apparent interparticle gap, knowing that the resolution of X-ray tomography is 0.3 μm.

**Chain-like agglomerates/isotropic agglomerates ratio.

2.3. Micro-magnet organization within the array

Optical microscopy was used to characterize the properties of the magnetic network organization on its surface. The images were analyzed with ImageJ software. Figure 3.5 shows top view images of the micro-magnet arrays, obtained with a 10X objective, at 1 and 2 wt%, and for LG and HG set-ups. The magnetic array properties are summarized in Table 3-3. A dozen of samples were analyzed for each condition (with at least 4 pictures taken of each magnetic area) in order to study micro-magnet array heterogeneity.

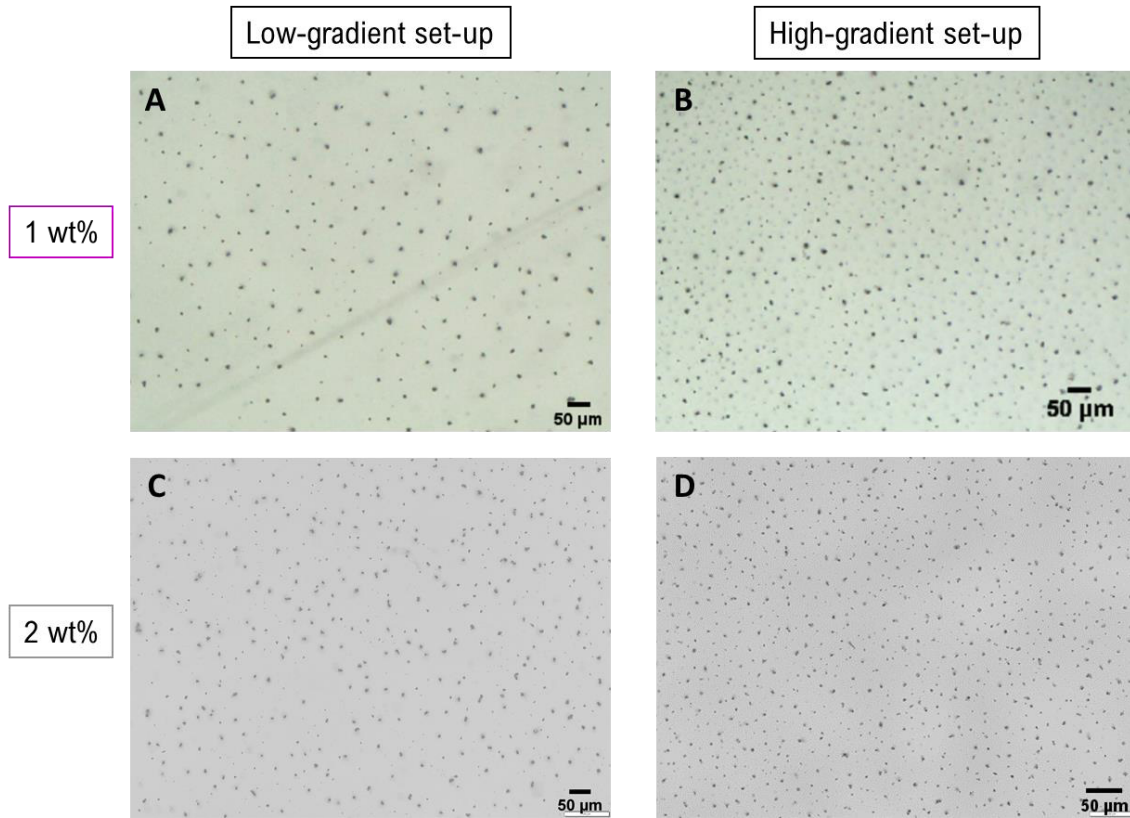


Figure 3.5: Brightfield microscopy images of an array of micro-magnets obtained at (A,B) 1 wt% with LG and HG set-up, respectively; and (C,D) 2 wt% with both LG and HG configurations, respectively.

Table 3-3: Micro-magnet array properties from optical microscopy observations (with 10X objective) depending on the concentration and gradient configuration.

Set-up	Density (mm ⁻²)	Diameter (μm)	Nnd (μm)
1 wt% - LG set-up	483 ± 146	7.4 ± 0.6	31 ± 7
1 wt% - HG set-up	741 ± 306	5.3 ± 0.6	26 ± 4
2 wt% - LG set-up	1121 ± 182	4.4 ± 0.6	16 ± 0.9
2 wt% - HG set-up	1349 ± 333	4.5 ± 0.7	15 ± 1.6

It is interesting to mention the complementarity of X-ray tomography and optical microscopy observations. Indeed, X-ray tomography provides a 3D observation of the composite microstructure, with a high resolution (300 nm). Nonetheless, it should be noted that when analyzing top view of the micro-magnet array, there is no distinction between NdFeB particles located on the composite surface, or within the composite thickness, since X-ray tomography returns a superposition of 2D slices. It is also worth mentioning that X-ray tomography is a quite expensive characterization method (performed as a service charged in an external laboratory). On the contrary, optical microscopy provides a 2D study of the micro-magnet array, and despite its lower resolution, it allows numerous samples to be analyzed, at low-cost, therefore providing statistical measurements. In addition, optical microscopy returns an image of the micro-magnet array with a focus on surface micro-magnets, which is of interest since they will represent the most effective micro-traps during microfluidic experiments.

Regarding optical microscopy measurements, micro-magnets have a diameter of approximatively 5 μm regardless of the concentration or gradient configuration, which is in accordance with X-ray tomography measurements. In particular, at 2 wt% and for the LG set-up, the micro-magnet diameter ranges from 0.5 to 20 μm , with 98% of the micro-magnets having a diameter inferior to 10 μm . The distribution of micro-magnet diameter can be found in Figure 3.6-A. Optical microscopy also enables the study of the control of micro-magnet distribution within the array, by comparing experimental nnd values with theoretical laws. Figure 3.6-B displays the experimental nnd distribution plot with Poisson and normal distribution fits. The experimental values were obtained from microscope images of 2 wt% samples with LG set-up (micro-magnet total density of $1250 \pm 130/\text{mm}^2$). In general, the Poisson law can describe independent events and has no adjustable parameters. Applied to a given number of particles on a known surface (2D images are therefore required), it allows the description of a random distribution. Here, it fails to describe the experimental nnd distribution. This distribution is better described by a normal distribution, demonstrating that the self-organization of micro-magnets, which relies on the composite approach, is not random.

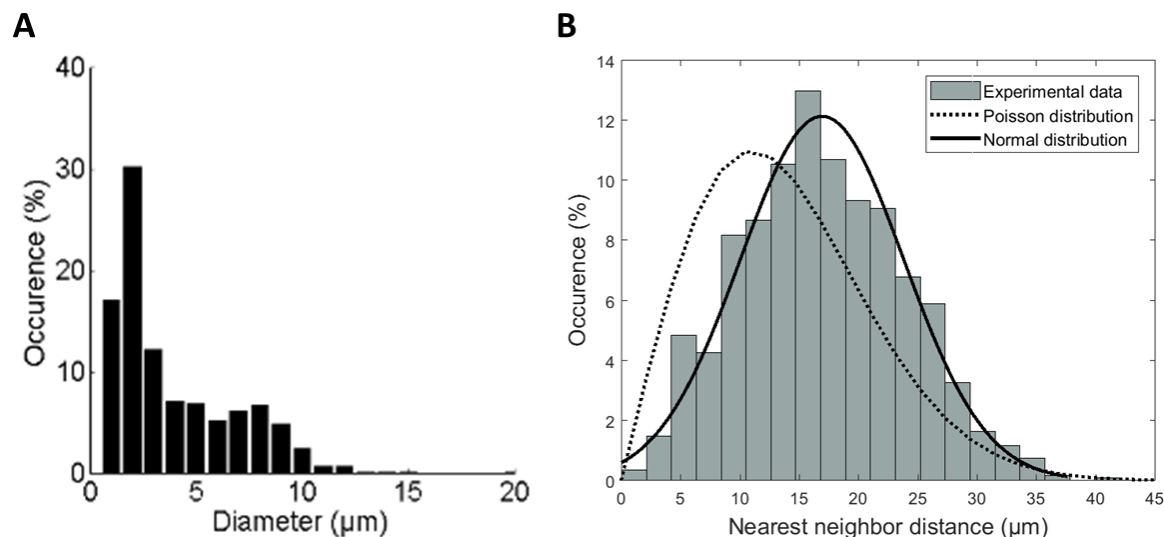


Figure 3.6: Optical microscopy study of some characteristics of 2 wt% composite prepared under a uniform magnetic field (LG set-up). **(A)** Micro-magnet diameter distribution. The diameter ranges from 0.5 to 20 μm , with a mean value of 5 μm . Interestingly, 98% of the micro-magnets have a diameter inferior to 10 μm . **(B)** Nearest neighbor distance distribution. The experimental distance, measured from brightfield microscopy observation (0.8 mm^2 images), follows a normal distribution and not a Poisson distribution (random distribution of $N = 1225$ particles in a 0.8 mm^2 frame), revealing that the self-organization of the micro-magnets is not random.

2.4. Magnetic properties of micro-magnets

Room temperature magnetization curves were measured by SQUID magnetometry. First, magnetization curves of micro-magnets prepared with either LG or HG set-ups were compared. They are reported in Figure 3.7-A. Both set-ups exhibit superimposed magnetization curves. Thus, the drastic difference in the agglomerates' shape obtained using the two set-ups and revealed by X-ray tomography does not influence the magnetization process. This can be expected considering the high magnetic hardness parameter ($\kappa = 1.54$) of the $\text{Nd}_2\text{Fe}_{14}\text{B}$ phase [20].

Magnetization curves measured either parallel or perpendicular to the long axis of the agglomerates referred to as out-of-plane (oop) and in-plane (ip), respectively, are shown in Figure 3.7-B. The oop curve shows a slightly larger squareness than the ip curve, revealing an easy direction for the magnetization along the agglomerates' orientation. This could then be attributed to a preferential alignment of the $\text{Nd}_2\text{Fe}_{14}\text{B}$ c-axes during the formation of the microparticle agglomerates along the applied field direction. This is however limited as the polycrystalline microparticles are poorly textured. The relatively small kink at low fields could be the sign of a secondary and magnetically soft phase, which might be due to surface oxidation.

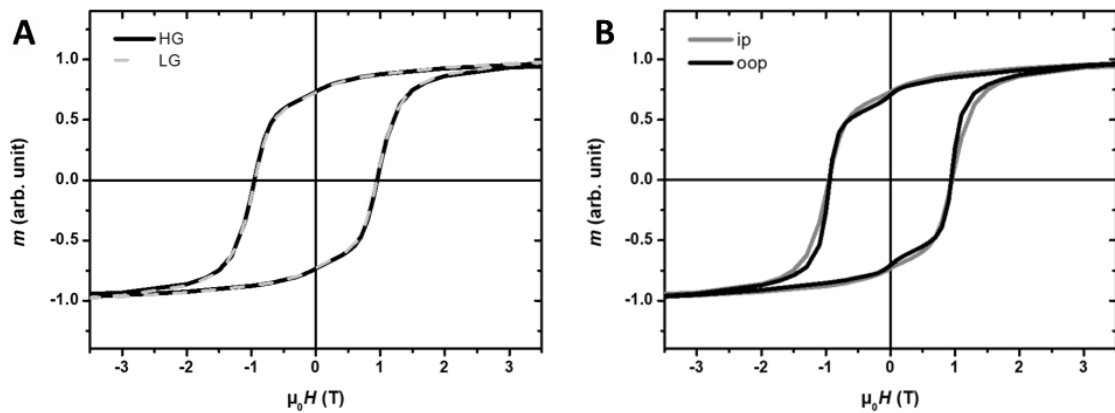


Figure 3.7: Room temperature magnetization curves of 1wt% NdFeB@PDMS membranes. (A) Comparison of the in-plane magnetization curves for membranes prepared with “high gradient set-up” (HG) and “low gradient set-up” (LG). (B) Comparison of the in-plane (ip) and out-of-plane (oop) magnetization for a HG-prepared membrane.

The magnetization of a 2wt% NdFeB@PDMS composite membrane, prepared with LG set-up, was measured in a SQUID magnetometer at room temperature. The out-of-plane magnetization loop is shown in Figure 3.8-A, specifically when the field is applied along the agglomerates' long axis. The remanent magnetization is an important parameter to determine, it gives the residual composite magnetization after the removal of the external magnetic field. For both concentrations, 1 and 2 wt%, the full remanent magnetization (M_{RF}) is 0.75 of the saturation magnetization (M_s), with $\mu_0 M_{\text{RF}} = 0.84$ T. This value was reached for applied field larger than 2.5 T.

Nevertheless, a parameter that does affect the remanent magnetization of the micro-magnets is the applied magnetic field at which the micro-magnets were magnetized in the latest part of the fabrication process. In order to determine this operating magnetization state, magnetization curves were measured with successive returns to the remanent state (Figure 3.8-B). The initial remanent magnetization (M_{RI}) indicates the remanent magnetization after the field reticulation process (field of 300 mT supplied by a bulk NdFeB magnet). The composite membrane is then submitted to a higher field, through the use of a homemade magnetizing system, resulting in an operating remanent magnetization (M_{RO}). M_{RO} reached 0.48 M_s when subjected to a magnetizing field of ~ 1 T, and the remanent magnetic field of the micro-magnets, $\mu_0 M_{\text{RO}}$, was estimated at 0.54 T. This remanent magnetic field was later enhanced by developing a new magnetizing system, which now generates a field of ~ 1.2 T. The new M_{RO} reached 0.62 M_s , with $\mu_0 M_{\text{RO}} = 0.7$ T. The magnetic field generated by both magnetizing systems were measured using a Magnetic Field Meter (PCE-MFM 3500).

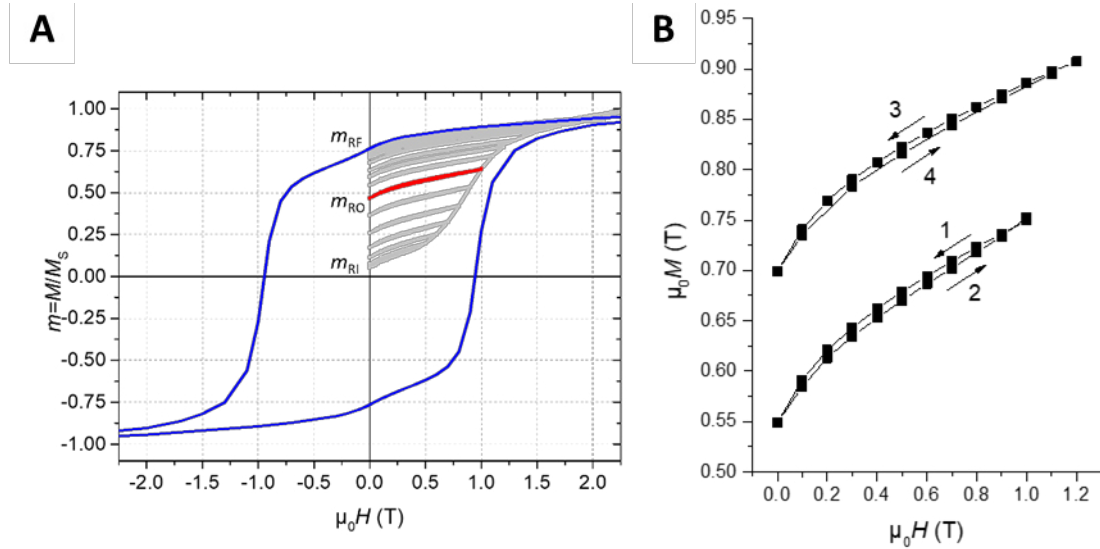


Figure 3.8: Room temperature magnetization curve of 2wt% NdFeB@PDMS membrane. **(A)** Out-of-plane magnetization curve. The light grey curve is the first magnetization curve with successive measurements of remanent magnetization. The thick red curve highlights the remanent magnetization at 1 T. The blue curve is the full magnetization loop. **(B)** Operating remanent magnetization depending on the applied magnetic field. The first developed magnetizing set-up generates a magnetic field of 1 T, which leads to micro-magnets with a remanent magnetization of 0.54 T. The improved magnetizing set-up, which generates a field of 1.2 T, resulted in a micro-magnet remanent magnetization of 0.7 T. The order in which magnetization curves were measured is annotated with a number from 1 to 4.

To sum up, the particle concentration and the gradient set-up don't modify the remanent magnetization of the micro-magnets, while the choice of the magnetizing system used in the latest step of the fabrication process could improve the operation remanent state of micro-magnets. In particular, superconducting coil magnetizing systems could generate magnetic field as high as 7 T and would enable to reach micro-magnet full remanent magnetization state.

2.5. Summary

The study of composite structure was enabled, either in 3D using X-ray tomography, or in 2D using optical microscopy observations. It revealed that the composite approach allows for the preparation of dense arrays of micro-magnets, of about 5 μm in diameter, with high aspect ratio and uniaxial anisotropy (X-ray tomography observations). In addition, the composite approach enables obtaining micro-magnet array with a controlled distribution (optical microscopy observations).

The effect of the concentration and gradient configuration was studied. As expected, higher densities are obtained when increasing the particle concentration. Regarding the influence of a high gradient magnetic field template, it also leads to higher micro-magnet densities, mainly located on the composite surface. These micro-magnets present a shorter chain length and a higher compacity, with a lower proportion of chain-like agglomerates.

Nevertheless, SQUID measurements revealed that particle concentration and gradient set-up didn't modify the magnetic properties of the micro-magnets, contrary to the magnetizing system used in the latest step of the fabrication process which could improve the operation remanent state of micro-magnets.

Finally, few drawbacks were highlighted using the non-uniform magnetic field preparation strategy, including a more complex fabrication process, a higher number of isolated agglomerates in the composite, as well as a heterogeneity between samples which results from the fabrication. This lack of reproducibility could be an issue for magnetophoretic experiments. Thus, 2wt% membranes prepared under low gradients will be further used as they lead to higher micro-magnet densities, with better reproducibility, and will be implemented for magnetophoretic trapping.

3. Micro-magnet finite element analysis

The magnetic properties of the organized 2wt% NdFeB micro-magnets in the PDMS matrix were modeled using a finite element approach (COMSOL, AC/DC module), based on SQUID measurements and X-ray tomography observations.

SQUID measurements enabled to determine the remanent field of the particles after the magnetizing step, which was set at 0.54 T. X-ray tomography revealed the 3D microstructure of the micro-magnets, with chain-like organization, and enabled the identification of geometrical parameters such as the chain length and the interparticle distance. It can therefore be interesting to study the effect of these microstructure parameters on the magnetic properties of a micro-magnet. Furthermore, the 2D surface arrangement of the micro-magnets in the matrix was simulated and the effect of neighboring chains (number of chains, distance to each other, etc.) on the generated magnetic field gradient in a dense array of micro-magnets was investigated.

Besides, the effect of adding an external millimeter-sized magnet, located below the composite, was studied. The goal of this external magnet is to attract flowing objects, located in the upper of the 100- μm high microchannel, towards the bottom where the micro-magnets are located. Other teams rather implemented specific microfluidic structuration, such as herringbone structures incorporated in the upper wall of the channel, to induce deflection of the target objects [21–24]. Their strategy is based on chaotic mixing, while this one relies on the generation of magnetic fields with high range.

Finally, the magnetic force generated by a micro-magnet on a model superparamagnetic bead was simulated so as to evaluate its magnetophoretic trapping ability.

3.1. Isolated microstructure

X-ray tomography revealed the chain-like microstructure of the micro-magnets, with varying chain length and interparticle distance depending on the gradient set-up. As a reminder, the chains length was found to be 3 times greater with the HG set-up than with the LG set-up at 2 wt% (25 μm against 75 μm), while the interparticle distance is slightly lower with the HG set-up ($0.95 \pm 0.4 \mu\text{m}$ against $1.2 \pm 0.8 \mu\text{m}$ with LG set-up). To study the effect of such structure changes, an individual chain-like structure was modeled in 2D axisymmetric. The chain is composed of NdFeB particles, which were modeled as a rectangle with a width of 4 μm and a height of 1.5 μm . The influence of the chain length (and thus the number of NdFeB particles within the chain) and the interparticle distance was studied by comparing the magnetic field gradient (depicted by a magnetic coefficient, C_m , see part 1.4 of chapter 2) for both gradient set-ups. To do so, a vertical cut line, centered in $r=0$ (center of the particle at the surface), and with a height z varying from 0 to 100 μm (microchannel height), was used. A schematic of the modeling is illustrated in Figure 3.9-A.

First, the chain length impact was simulated by setting the value at 25 μm for the HG set-up, or at 75 μm for the LG set-up. The interparticle distance was set at 1.5 μm . Figure 3.9-B shows the decreasing profile of the magnetic field gradient with the distance from the chain surface, for both chain lengths, but with a slightly faster decrease for the HG set-up. At the chain surface, the magnetic field gradient reaches 10^5 T/m for both set-ups, and then, at 100 μm from the chain surface, the value drops to a tenth of T/m , with a lower value by a factor of two for the HG set-up. From these observations, it can be deduced that the modification in chain length does not affect significantly the micro-magnets magnetic properties. Then, the impact of the interparticle distance on the magnetic field gradient was simulated by varying the value from 0 to 2 μm . The chain length was set at 25 μm . It can be seen in Figure 3.9-C that a compacter chain (lowest interparticle distance value) enhances the magnetic field gradient as the magnetic field gradient decreases faster with distance for chains with a higher interparticle distance. At distances of 0 and 20 μm from the chain surface, the magnetic gradient is 1.7 times greater for a chain with an interparticle distance of 0 μm than for a chain with 2- μm interparticle distance. Nevertheless, this difference becomes less significant at 100 μm from the chain surface, the magnetic field gradient is of 0.45 T/m for chains with an interparticle distance of 0 μm , and of 0.35 T/m for chains with an interparticle distance of 2 μm .

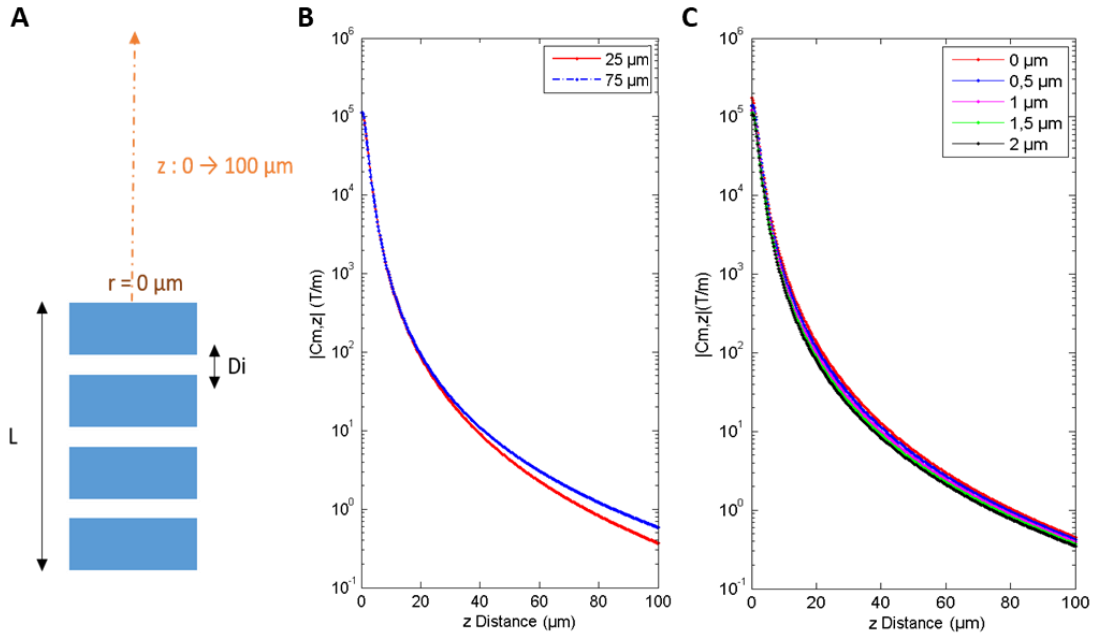


Figure 3.9: Simulation of the modifications in the microstructure (chain length L , interparticle distance D_i) and its impact on the magnetic field gradient (C_m, z). **(A)** Schematic of the chain-like organization of the micro-magnet, composed of NdFeB particles (remanent magnetization $B_r = 0.54 \text{ T}$) as a rectangle of width $4 \mu\text{m}$ and height $1.5 \mu\text{m}$, in 2D axisymmetric coordinates. The magnetic field gradient was calculated at $r = 0$ and for z height ranging from 0 to $100 \mu\text{m}$. **(B)** Effect of the chain length. Profile of the magnetic field gradient as a function of the distance from the chain surface, for a chain length of $75 \mu\text{m}$ (HG set-up) and $25 \mu\text{m}$ (LG set-up). **(C)** Effect of the interparticle distance. Profile of the magnetic field gradient as a function of the distance from the chain surface, for interparticle distance varying from 0 to $2 \mu\text{m}$.

3.2. Demagnetizing effect of the array

The 2D surface arrangement of the micro-magnets in an array was simulated to study the effect of neighboring chains on the generated magnetic field gradient. The network of chains was simulated in 2D coordinates, and the number of chains from which the network can be considered as an infinite number of chains was first determined. The nearest neighbor distance, nnd was set to $15 \mu\text{m}$ (X-ray tomography measurements). To do so, the magnetic coefficient was calculated along a horizontal cut line located at $6 \mu\text{m}$ (superparamagnetic bead radius) from the chains (Figure 3.10-A). Figure 3.10-B represents the magnitude of C_m generated by the central chain of the network as a function of an increasing number of neighboring chains. It can be observed that the magnetic field gradient decreases with increasing number of neighboring chains, until reaching a plateau (Figure 3.10-C). Above 7 chains, the magnetic field gradient remains nearly constant at 4300 T/m , suggesting that the network can be considered as “infinite” when composed of at least 9 chains.

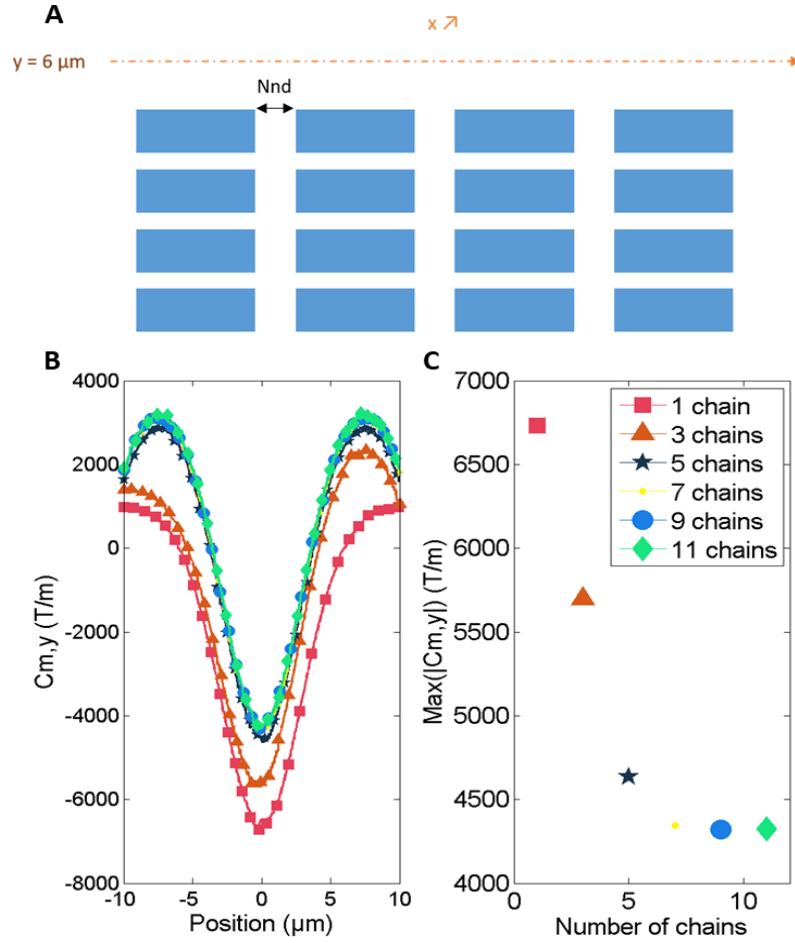


Figure 3.10: Simulations of the effect of a network of chains on the generated magnetic field gradient. **(A)** Schematic of the network of micro-magnet, composed of chain-like agglomerates of NdFeB particles (rectangle of width $4 \mu\text{m}$ and height $1.5 \mu\text{m}$), in 2D coordinates. The chain length and interparticle distance were set at 25 and $1.5 \mu\text{m}$, respectively, and the nnd was set at $15 \mu\text{m}$. **(B)** Simulations of the magnetic coefficient $C_{m,y}$ for an increasing number of chains in the array. $C_{m,y}$ was calculated above the central micro-magnet of the network. **(C)** Maximum value of $C_{m,y}$ as a function of the number of chains. The magnetic field gradient reaches a plateau for a number of chains above $7 \mu\text{m}$. The network can therefore be considered as infinite when composed of 9 chains.

Thus, 2D calculations allowed us to determine a corrective factor on the magnetic field gradient generated by a chain included in a network compared to that generated by an individual chain. As illustrated in Figure 3.11, a chain within a network produces a 34% lower C_m than an isolated chain. As for the broken symmetry at the edge of the network, its effect on C_m is significant over a distance of about $50 \mu\text{m}$ from the edge: the C_m produced by a chain on the side of the network is 15% greater than that of a chain included in the network. These observations show the demagnetizing interaction between neighboring chains which tends to decrease the generated magnetic force. This demagnetizing effect inevitably occurs in any dense micro-array of magnetic structures [25].

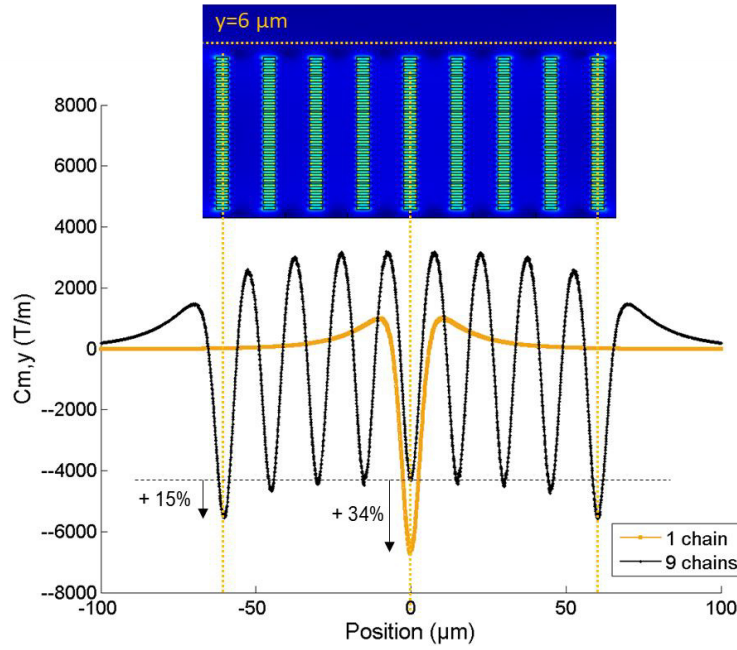


Figure 3.11: Simulations of $C_{m,y}$ generated above a network of 9 chains. $C_{m,y}$ is lower for a chain located in an array than for a unique chain. A chain located in the center of the network will also generate a smaller $C_{m,y}$ than a chain located at the edges of the network. This phenomenon can be explained by the demagnetizing field inevitably occurring in a dense array of micro-magnets.

Finally, as we observed from X-ray tomography measurements that, depending on the particle concentration and gradient set-up, nnd varies from 15 to 24 μm , we simulated a network of 9 chains whose nnd varies from 15 to 25 μm with a step of 5 μm . Figure 3.12 highlights the effect of nnd on the magnetic field gradient, which is the most visible at distance from the chains larger than 30 μm . At 100 μm above the central chain, the magnetic field gradient is of 31, 21, and 14 T/m, for a nnd of 15, 20, and 25 μm , respectively. The lower the nnd , the higher the number of particles within the same volume, resulting in a higher composite magnetization. We hypothesized that, although the demagnetizing field is increased for small nnd , the higher composite magnetization may contribute to the generation of a greater magnetic field gradient. Nevertheless, a difference of a maximum factor of two is observed and, at contact, similar values of the order of 10^5 T/m are obtained.

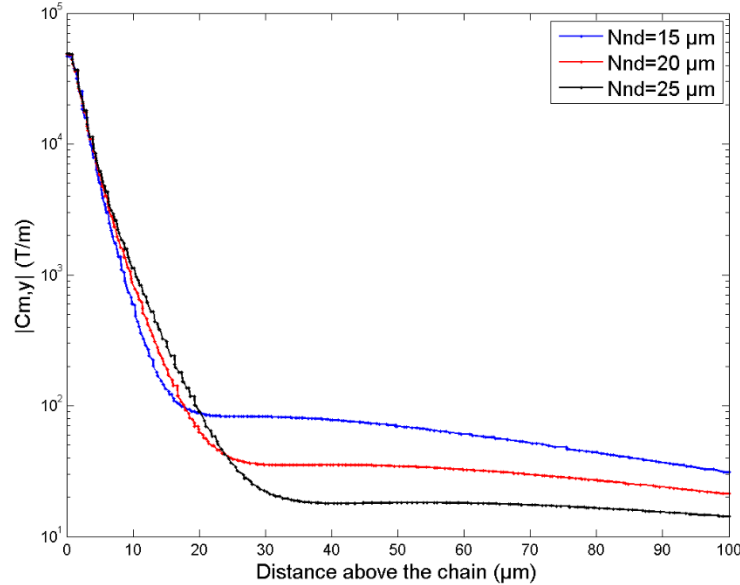


Figure 3.12: Simulation of $C_{m,y}$ for various nnd . The effect of nnd is mainly visible at distances from the chain larger than 30 μm . At the chain surface, $C_{m,y}$ is the order of 10^5 T/m regardless nnd , while at 100 μm from the chain, a difference of a maximum factor of two can be observed.

3.3. Effect of an external permanent magnet

Micro-magnets are known to produce high magnetic field gradients but also for their small interaction distance, as illustrated in Figure 3.13. The micro-magnet generates a magnetic field of 200 mT and a magnetic field gradient of 10^5 T/m at its surface, which are consistent with regard to numerical values found in the literature [26–28]. In turn, the magnetic field and the magnetic field gradient then decrease with the distance to the micro-magnet, down to 0.1 mT and 5 T/m, respectively, at a distance of 50 μm .

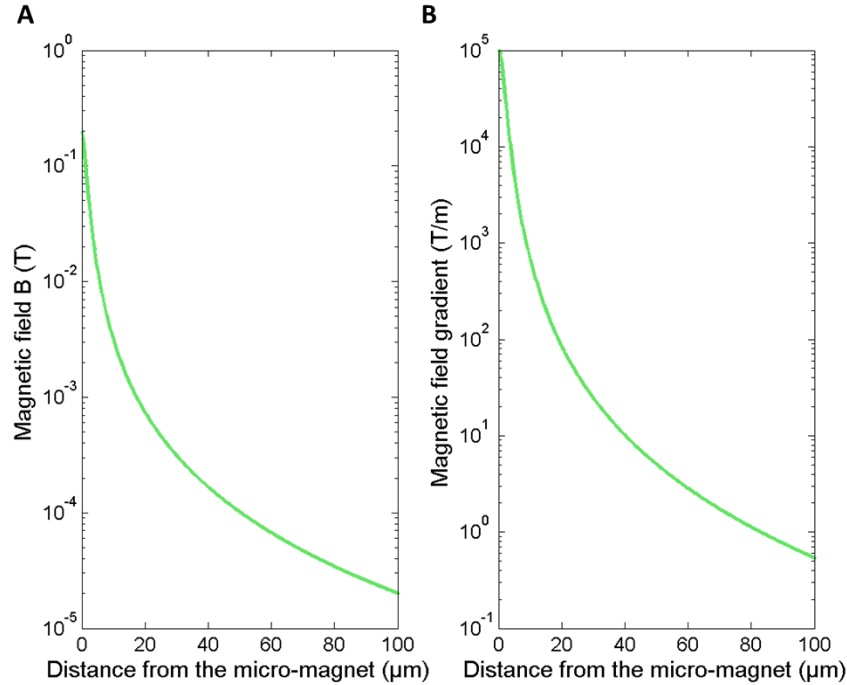


Figure 3.13: Numerical simulations of the (A) magnetic field and (B) magnetic field gradient generated by a chain-like micro-magnet. Chain length=25 μm . Interparticle distance=1.5 μm .

Magnetic objects initially flowing at the top of the channel may therefore not be subjected to the relatively short interaction range of the micro-magnets, limiting the trapping efficiency in a 100- μm -high channel. This can be a limitation for targets flowing far from the micromagnets within a microfluidic device. The deviation of the target objects towards the interaction reach of micro-magnets can be obtained either (i) using passive fluidics, for instance microstructures such as herringbone grooves located on the roof of the microchannel that will pull flowing objects down; or (ii) applying external fields as reported here, using external field gradients generated by an additional millimeter-scale permanent magnet to attract target objects towards the channel bottom. The advantage of this milli-magnet strategy is, firstly, to be able to keep monitoring particle trapping through optical microscopy, which is difficult to achieve with devices integrating vertical depth features, and, secondly, to avoid additional manufacturing steps related to the integration of passive fluidic functions [29]. The permanent magnet, of dimensions 25x8x2 mm³, and with a remanent magnetization of 1.17 T (manufacturer's datasheet), was put beneath the composite membrane, at a distance of 1-2 mm (composite thickness).

Because of the modeling of the micro-magnet in 2D axisymmetric, the simulated external permanent magnet will present a cylindrical geometry. Its magnetic properties should therefore be similar to the ones of a the regular rectangular magnet used for experiments. Thus, the permanent magnet was first modeled in 2D (longest dimension in the plane) to establish the generated magnetic field and magnetic field gradient. Next, the permanent magnet was modeled in 2D axisymmetric, and its dimensions (width and height) were varied so as to reach similar magnetic field and gradient values than those obtained in 2D. This was achieved with a permanent magnet with a width of 12 mm and a height of 2.1 mm. The magnetic field and magnetic field gradient generated by the permanent magnet, in 2D and 2D axisymmetric, can be found in Figure 3.14, for a vertical distance from the micro-magnet varying from 0 to 1 mm.

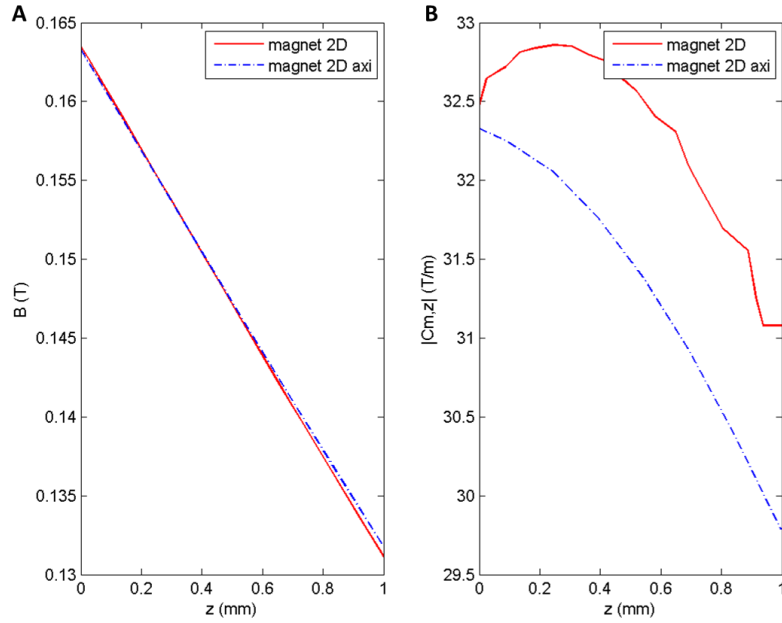


Figure 3.14: Numerical simulations of the (A) magnetic field and (B) magnetic field gradient generated by a millimeter-sized permanent magnet, either modeled in 2D or 2D axisymmetric. A magnet of 12 mm in width and 2.1 mm in height (2D axisymmetric modeling) allowed to reach similar values than the 2D magnet (8 mm wide and 2 mm high).

The effect of the external millimeter-sized permanent magnet under the composite membrane (at a distance of 1 mm from the micro-magnets) was then studied (Figure 3.15). The combined use of the micro-magnets and milli-magnets doubled the magnetic field value in contact, reaching 400 mT, and increased the minimum value inside the channel from 0.02 mT to 200 mT. The higher field value ensures a higher magnetic moment held by the target objects. Furthermore, the magnetic field gradient increased from 5 T/m to 40 T/m at a distance of 50 μm , therefore increasing the interaction distance. Indeed, from a certain distance to the micro-magnet, the magnetic performances of the milli-magnet dominate: this distance reaches 10 μm for the magnetic field and 60 μm for the magnetic field gradient. Thus, it not only has an effect on the attraction of target objects which could be far from the micro-traps, but also should enhance their trapping (higher magnetization and magnetic field gradient).

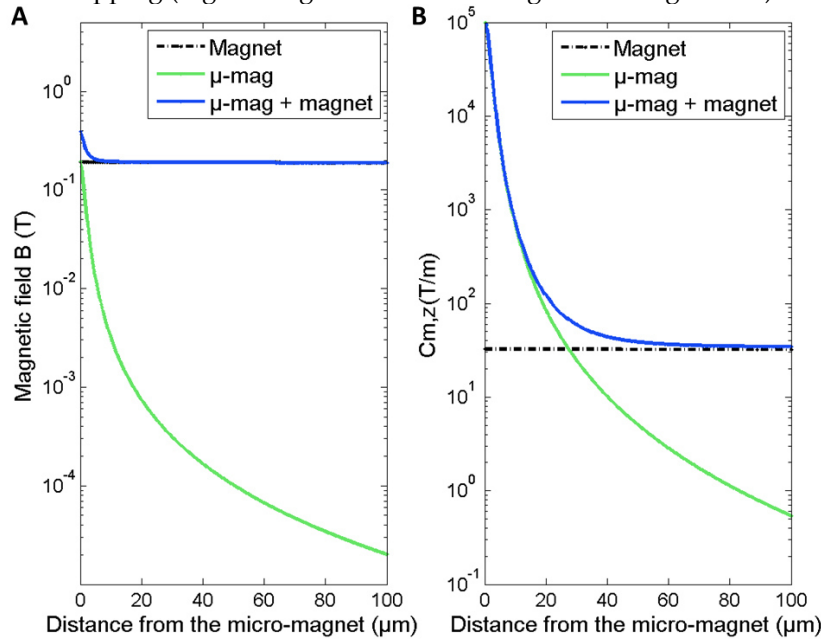


Figure 3.15: Numerical simulations of the (A) magnetic field and (B) magnetic field gradient (defined by $C_{m,z}$) generated by the micro-magnets ($\mu\text{-mag}$) as a function of the distance from the composite surface, with or without an external magnet below the composite surface.

To conclude, adding a millimeter-sized magnet sets a background field value of 200 mT over the whole section of the channel, which is four orders of magnitude greater at 100 μm with respect to the stray field of the micrometer-sized magnets alone. This is expected to significantly increase the magnetic moment held by the target object and so the magnetophoretic interaction, which will be the object of next sections.

3.4. Calculation of the magnetic force exerted on a model bead

The magnetic force generated by a chain of particles and acting on a magnetic bead was calculated in 2D axisymmetric with Comsol “domain probe” tool. The calculation will return an average of the field quantity over a domain. The domain aims to model a superparamagnetic bead. It was defined as a circular area, of diameter 12 μm , which corresponds to the average size in the superparamagnetic used in the experiments. The use of “domain probe” tool can therefore take into account the size of the target object. The domain is located above the chain of particles, and its height is varied from 0 to 50 μm , with 1- μm steps, to mimic the position of a bead along channel height (Figure 3.16).

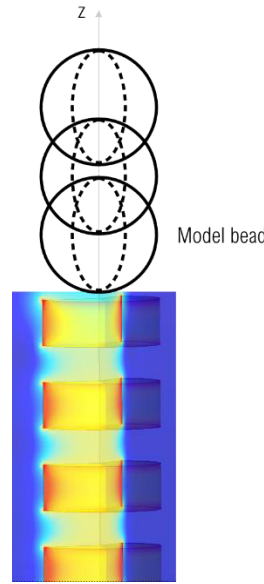


Figure 3.16: Schematic of a model bead (Comsol « domain probe » tool), centered above a chain of particles and with a varying height, which will calculate an average value of the field over its volume.

The magnetic coefficient $C_{m,z}$ is then calculated at each bead position, and will be used to determine the magnetic force, as follow:

$$\vec{F}_m = V_b (\vec{M}_b \cdot \vec{\nabla}) \vec{B} \quad (18)$$

With V_b the bead volume and M_b its magnetization. Here, the magnetic component is along z , the magnitude of the magnetic force can therefore be simplified and defined as the product of V_b , M_b , and the absolute value of the vertical magnetic coefficient $C_{m,z}$:

$$|F_{mag}| = V_b M_b |C_m| \quad (19)$$

Results of magnetic force calculations can be found in Figure 3.17-A. A micro-magnet can generate magnetic forces as high as 4.6 nN at its surface. This value decreases with the distance from its surface and equals to 1.7 pN at a distance of 50 μm . The addition of an external permanent magnet enabled to increase the interaction reach of the micro-magnet by a factor 10, the magnetic force reaches 19 pN at a distance of 50 μm . Besides, the benefit of downscaling the size of the magnet is underlined as the milli-magnet alone generates a constant magnetic force of 15 pN, which is 300 times lower than the force generated at the micro-magnet surface, and almost 10 times smaller at a distance of 10 μm . From these first results it can be deduced that the fabricated micro-magnets generate strong and localized magnetic forces and would participate in effective magnetophoretic trapping.

Furthermore, as mentioned in section 3.2, the magnetic field gradient generated by a chain located in a network is actually smaller than for a chain alone, due to the demagnetizing field occurring in an array of micro-magnets. This decreasing factor was estimated at 0.15 for a chain located at the edges of the network, or 0.34 for a chain at the center of the network. Figure 3.17-B shows the actual magnetic force when taking into the effect of the network. The magnetic force is slightly lower, reaching 3.1 nN or 3.9 nN, at the surface of a chain located either at the center of the network, or at its edges, respectively.

To conclude, Comsol simulations have allowed to deepen the study of the effects of the micro-magnet microstructure and network from what had been first observed with X-ray tomography and optical microscopy. Next, these calculated magnetic forces will be compared to experimental measurements.

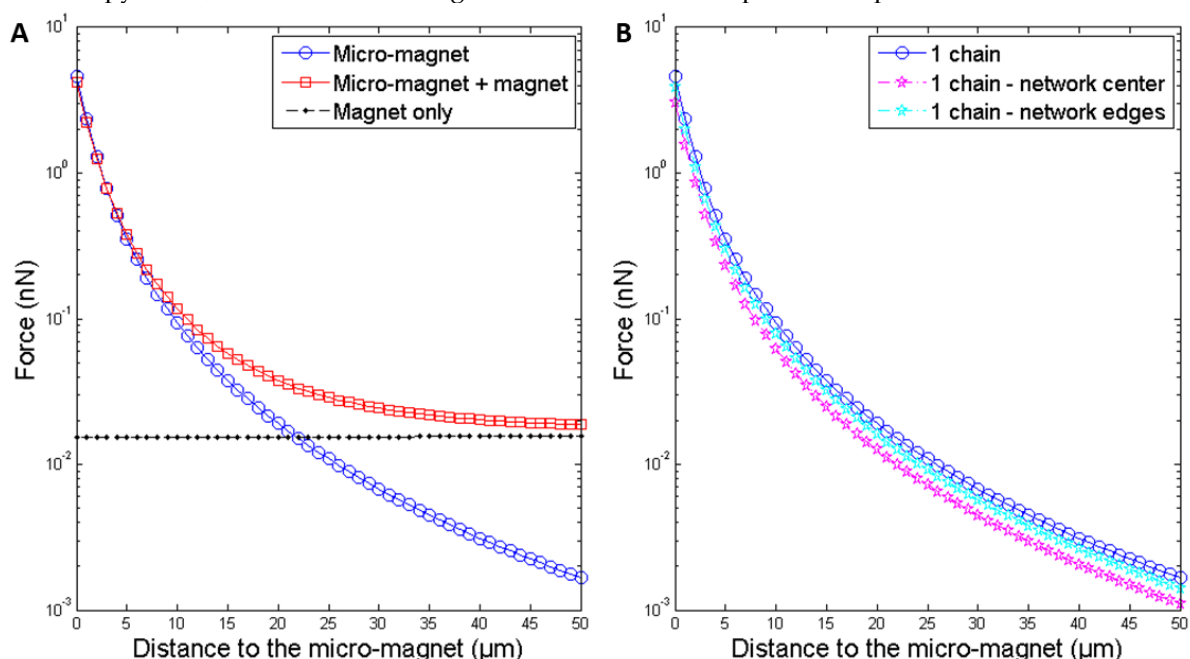


Figure 3.17: Numerical simulations of the magnetic forces generated by a micro-magnet and acting on a 12-μm superparamagnetic bead through the use of the “domain probe” Comsol tool. The distance to the micro-magnet surface was varied from 0 to 50 μm. **(A)** Comparison of the magnetic force generated by the micro-magnet alone, the combination of the micro-magnet with a milli-magnet, and the milli-magnet alone. Magnetic forces generated by the micro-magnet are 300 times greater than those produced by the milli-magnet alone. The combination of the two magnet scales allows for higher interaction reach. **(B)** Consideration of the effect of the network of chains on the generated magnetic force, for a chain located either at the center or at the edges of the network. The magnetic force is smaller due to the demagnetizing effect occurring in an array of micro-magnets. Simulations were conducted on a chain of NdFeB particles with a chain length of 75 μm and interparticle distance of 1.5 μm (X-ray tomography observations of a 2wt% composite membrane).

4. Magnetic force determination by colloidal probe AFM

Colloidal probe AFM allows for measurements of magnetic force produced by individual micro-magnets. Micro-magnets act as traps and give straight information about the capture performance. AFM force measurements were performed with a superparamagnetic bead (product average diameter: 12 μm, density: 1.1 g/cm³, magnetization: 0.66 kA/m, Kisker®), of diameter 12 or 15 μm depending on the one used, which was glued to a silicon nitride cantilever (stiffness 43 pN/nm). Measurements were performed in a PBS-BSA2% solution so as to prevent non-specific adsorption of the superparamagnetic bead (SPMB) to the sample surface. The SPMB will be submitted to an attractive force proportional to the magnetic field gradient. AFM approach and retract curves were performed on about 20 micro-magnets for each sample preparation. The effect of the micro-magnet microstructure, as well as the one of the external millimeter-scale permanent magnet, were studied on the generated magnetic force.

4.1. Effect of the micro-magnet microstructure

Magnetic force measurements were performed for individual micro-magnets as described in Figure 3.18. Micro-magnet location could first be visualized using optical images (Figure 3.18-A). Next, sample surface was scanned at contact using the colloidal probe to precisely spot the micro-magnet via topography measurement (Figure 3.18-B). Then, the height of the colloidal probe was shifted of hundreds of micrometers (ΔZ_{nap}) to record the cantilever's deflection and measure magnetic forces generated by the micro-magnets. The mapping of the magnetic attraction highlights that the maximum force is localized above the micro-magnet (Figure 3.18-C). Finally, the probe was positioned at the exact micro-magnet position where the magnetic force intensity is the highest and approach/retract curves towards the micro-magnet surface were measured. Figure 3.18-D represents force measurement above distinct micro-magnets. Thus, colloidal probe AFM enables single-micro-magnet measurements and, likewise X-ray tomography and optical microscopy observations, reveals the variability between micro-magnets in terms of produced magnetic forces. Indeed, two apparently identical micro-magnets (Figure 3.18-A) actually generated magnetic forces varying by a factor 5 (0.2 nN vs 1 nN, Figure 3.18-D).

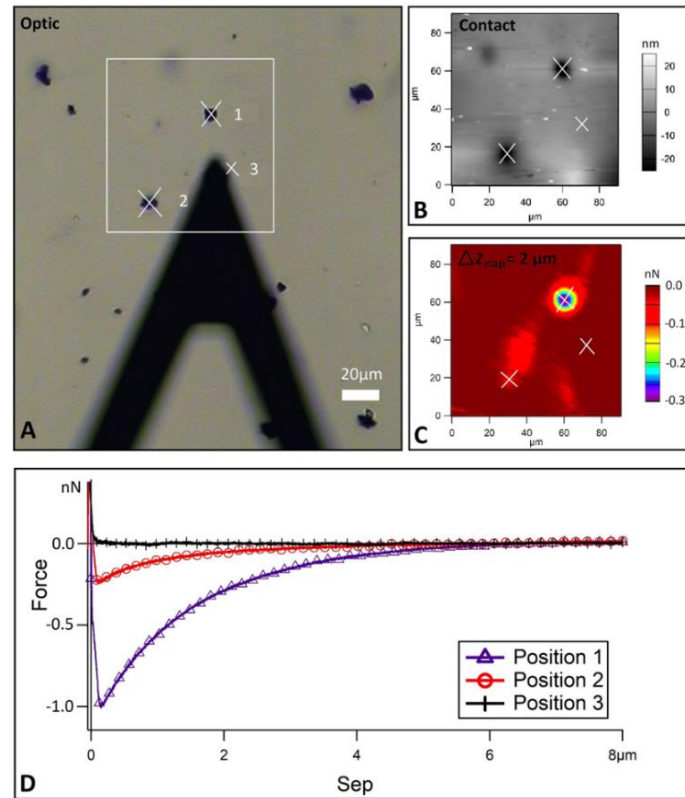


Figure 3.18: Magnetic force measurements steps for a 1wt% NdFeB@PDMS membrane prepared under a uniform magnetic field (LG set-up). **(A)** Optical image provides a first visualization of the micro-magnet location. In particular, three spots were probed: positions 1 and 2 at two distinct micro-magnets and position 3 on PDMS as a control. **(B)** Topography measurement of the sample surface to precisely determine the micro-magnet within the array. **(C)** Cartography of the magnetic force, performed at a distance of 2 μm from the surface, highlighting that the maximum force is localized above the micro-magnets. **(D)** Approach curves measured at exact micro-magnet positions revealing the variability of magnetic force measured for single micro-magnet (position 1 vs position 2).

Figure 3.19 represent magnetic force distribution for micro-magnets obtained with LG or HG set-ups (resulting in different micro-magnet microstructure), when the bead is either at contact with the sample surface (Figure 3.19-A) or at a distance of 3 μm from its surface (Figure 3.19-B). For the sample obtained with the LG set-up, the contact force ranges from 0.1 to 1.4 nN while for the HG sample, the maximum force reaches 4.1 nN. These values are in good agreement with the data found in the literature for microscale soft magnetic sources [30–32] and hard magnetic structures [33].

In addition, the average contact force for HG microstructures is almost three times larger than that of LG microstructures (1.7 nN against 0.6 nN). Regarding the magnetic force's range, AFM measurements reveal that a majority of the LG microstructures generates magnetic forces between 0.1 and 0.2 nN at a distance of 3 μm from their surface, while magnetic forces reach 0.3-0.5 nN for HG microstructures, which is twice as great as LG magnetic force range. Therefore, the use of an I-PDMS membrane during the NdFeB@PDMS composite curing has a substantial positive impact on the magnetic forces of the latter. This could be attributed to the combined effects of larger compactness, resulting in less magnetic flux loss, and a higher concentration of magnetic particles at the surface. Nevertheless, it should be noticed that the distribution of magnetic force values generated by micro-magnets obtained with the HG set-up is wider than that for LG micro-magnets. Further bead trapping experiments should enable the identification of the actual impact of the HG set-up on the magnetophoretic trapping performances.

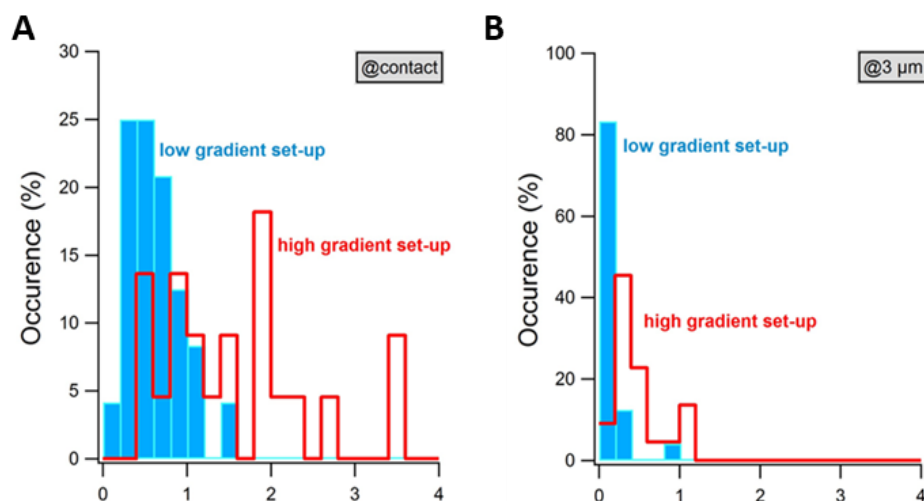


Figure 3.19: Measured magnetic forces by colloidal probe AFM in 1wt% composite membranes. **(A)** Force in contact with the composite surface for LG and HG set-ups. **(B)** Force at a 3- μm distance from the surface for LG and HG set-ups.

Besides, when looking at 2wt% composite membranes, prepared with either LG or HG configurations, it can be observed in Figure 3.20 that generated magnetic forces, measured at contact, are similar than those obtained for 1wt% composite membranes. This result was predictable from Comsol simulations as they showed that a nnd of 15 μm (2 wt%, higher micro-magnet density) or a nnd of 25 μm (1 wt%) led to similar contact magnetic field gradients (Figure 3.12).

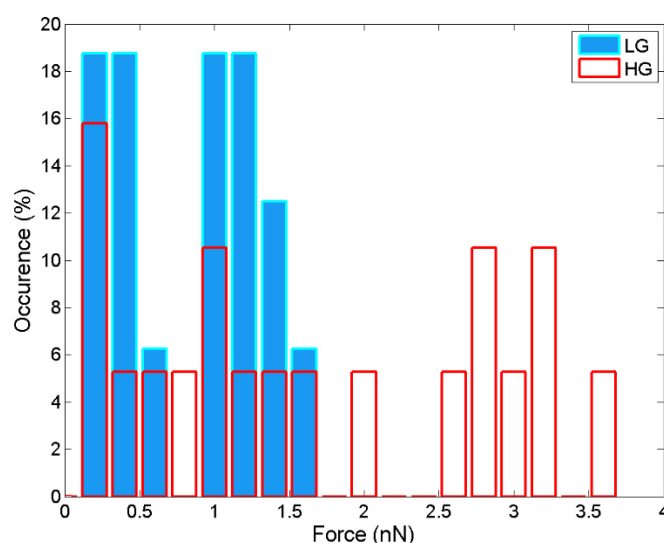


Figure 3.20: Colloidal probe AFM measurements of the magnetic force generated by 2wt% micro-magnets. Measurements were performed in contact with the micro-magnets, for both LG and HG set-ups. Similar values than those obtained with 1wt% micro-magnets were measured.

4.2. Effect of an external permanent magnet

Figure 3.21-A presents measured contact forces generated by the micro-magnets, as well as those generated in the presence of the external millimeter-sized permanent magnet. The magnetic force range was doubled in the presence of the external milli-magnet and reached 4 nN, against 2 nN for the micro-magnets alone. Indeed, the magnetic force acting on the superparamagnetic bead is defined by $\vec{F}_m = \mu_0 V_b (\vec{M}_b \cdot \vec{\nabla}) \vec{H}$, where H is the applied magnetic field. The magnetization of the SPMB (Figure 3.21-B), when positioned at the composite's surface, i.e., in a field of 200 mT (Comsol calculations), is not fully saturated, but the addition of the milli-magnet increases the magnetic field value, droving the bead magnetization up by 10% (from 570 to 620 A/m). Similarly, the magnetization of the micro-magnets was slightly raised by 5% in presence of the external magnet. Indeed, it can be observed on the magnetization curve of the NdFeB micro-magnets measured by SQUID magnetometry (Figure 3.8-B) that, when submitted to a magnetic field of 1 T, their remanence ($\mu_0 M$) in a field ($\mu_0 H$) of 200 mT (micro-magnets alone) is of 0.62 T, while it is of 0.67 T in a field of 400 mT (in the presence of the external magnet). It results in magnetizations of respectively 490 and 515 kA/m.

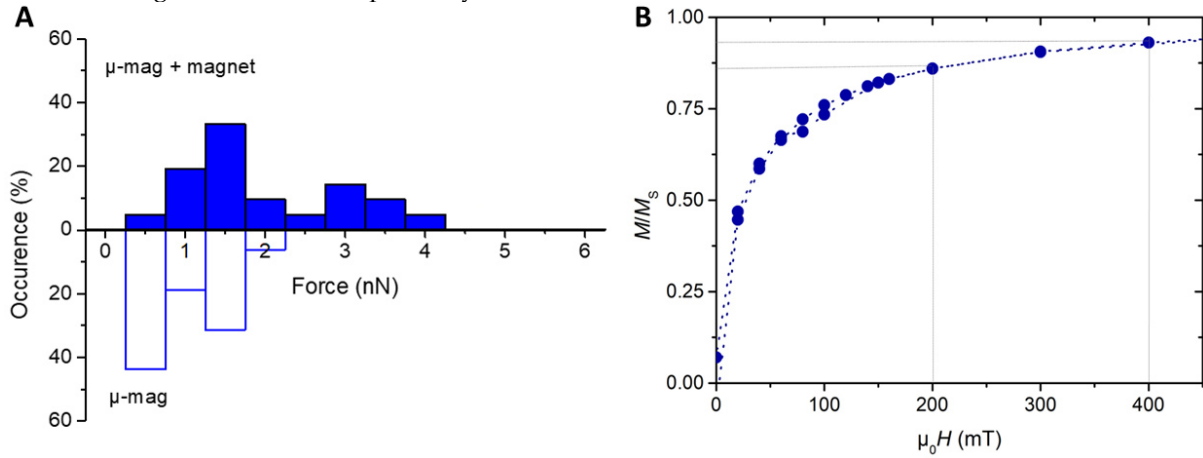


Figure 3.21: (A) Distribution of the contact magnetic force produced by the micro-magnets (μ -mag) from colloidal probe AFM measurements, with or without the external milli-magnet. The colloidal probe consists of a SPMB glued to the AFM cantilever. The inset shows an example of a second scan in two-pass mode, at 500 nm above a micro-magnet (no external magnet), in order to localize the force of maximum intensity. **(B)** Normalized magnetization curve at 300K of SPMB, obtained by SQUID magnetometry. $M_s = 660$ kA/m. Micro-magnets generate a field of 200 mT on their surface, this value is doubled in presence of the external permanent magnet.

These results highlight the high magnetic force generated by the micro-magnets at their surface, as high as several nN. Besides, measured magnetic forces are of the same order of magnitude as the calculated forces using Comsol, with slightly higher values for numerical values than experimental ones (~ 3 nN for Comsol calculations at contact against ~ 2 nN for AFM measurements). This difference can be explained by, on one hand, the homogenous modeled chain composed of regularly shaped and spaced magnetic particles, which was shown to be more variable in reality from X-ray tomography observations. On the other hand, the chain is actually buried in a PDMS membrane and can therefore present a thin PDMS layer at its surface. Nevertheless, Comsol calculations and AFM measurements are complementary since Comsol enabled studying the effect of the micro-magnet structure and provided an information on micro-magnet interaction reach while AFM enabled contact force measurements with an information on target object magnetization state.

To sum up, we demonstrated that the low interaction reach of micro-magnets was enhanced by adding an external millimeter-sized permanent magnet, which enabled the doubling of the magnetic force. The micrometer-scale magnets generate strong and localized magnetic field gradients, and their magnetization was enhanced in the presence of the milli-magnet. In particular, the millimeter-scale magnet has for aim not only to deflect flowing objects toward the channel bottom where the micro-magnets are located, but also to increase their magnetization. Although the use of the milli-magnet is at the expense of the compactness, implementing dual-scale magnets boost magnetophoretic performances.

5. Microfluidic experiments

Microfluidic experiments were conducted within microchannels integrating micro-magnets (2wt% composites), which act as micro-traps (Figure 3.22-A). Trapping efficiencies and magnetic forces were determined through the manipulation of SPMBs. Considering the low SPMB concentration, we used the single-particle-transport model to analyze the involved forces [34]. Moreover, given the low magnetic moment of the micro-beads, we neglected the dipole interactions and the contribution of their residual magnetization. Due to the micrometric size of the SPMBs, mass diffusion and magnetic diffusion based on Brownian motion can be ignored [35]. Finally, the buoyancy and gravity exerted on SPMBs are negligible, as compared with the magnetic and drag forces [36]. Thus, in the magnetic microfluidic system, the two main forces of importance to evaluate trapping efficiency are the magnetic force and Stokes' drag force (Figure 3.22-B). Reliable trapping is obtained when the magnetic force value exceeds that of the drag force.

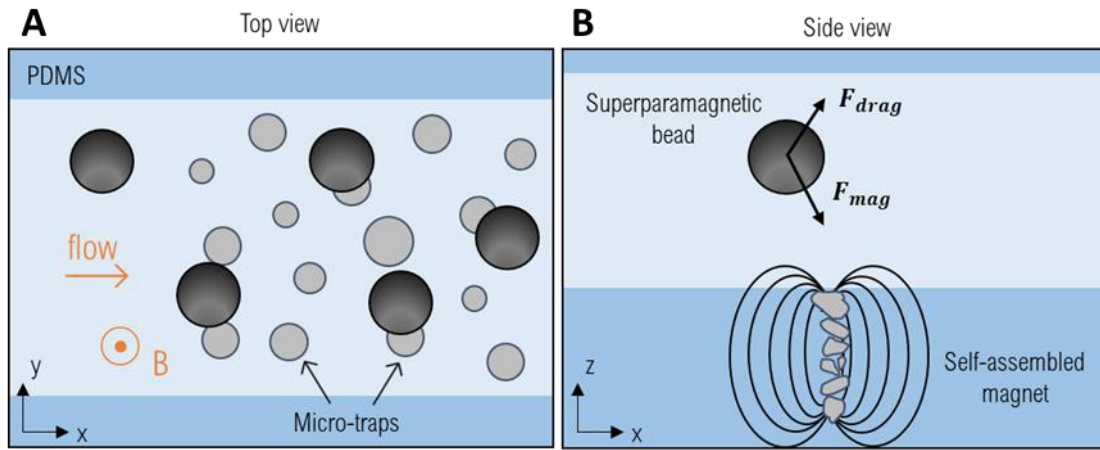


Figure 3.22: Schematics of the microfluidic channel integrating the self-assembled micro-magnets. **(A)** Top view. SPMBs (in black) are injected into the channel and get trapped on the micro-magnets. **(B)** Side view. The magnetic force (F_{mag}) and the fluidic drag force (F_{drag}) are the two forces coming into play in the microfluidic channel for magnetophoretic trapping.

5.1. Magnetic particle capture efficiency

An initial volume of SPMBs of 160 μL was prepared, with a concentration of 50 SPMBs/ μL , of which 30 μL were taken to assess the exact SPMB initial concentration by performing three counting in KOVA® slides (hemocytometer counting grid). Several counting is performed in order to depict the most precisely the SPMB content in the initial solution and therefore get the most accurate capture efficiency. This sample, containing a known number of SPMBs, was injected into the microsystem. The collected output was then centrifuged for 5 min at 1000 g in order to concentrate untrapped SPMBs. The supernatant was then removed carefully and a 30 μL volume was left for resuspension. Finally, the resuspended SPMB output was placed into KOVA® slides for counting. This way, the whole output sample was analyzed, and the final concentration was determined. This experiment was repeated at various flow rates in order to depict micro-magnet trapping performances.

Finally, the capture efficiency was calculated as follows:

$$\text{Capture efficiency (\%)} = \frac{C_{\text{initial}} - C_{\text{final}}}{C_{\text{initial}}} \times 100 \quad (20)$$

With C_{initial} and C_{final} the initial and final concentrations, respectively.

The magnetophoretic trapping efficiency of the micro-magnets integrated into the microfluidic system was determined at various flow rates. A representative picture of trapped SPMBs at 500 $\mu\text{L}/\text{h}$ is reported in Figure 3.23, SPMBs were trapped either individually or in clusters. At higher flow rates, less clusters

are obtained, as SPMBs are submitted to higher drag forces, therefore disrupting the cohesion of bead clusters, which is relatively low as expected from dipolar interactions between superparamagnetic beads.

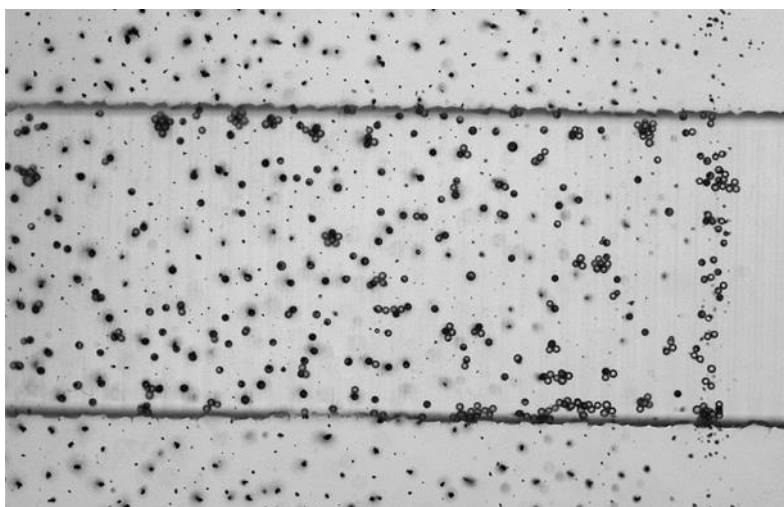


Figure 3.23: Microscope image showing trapped beads at 500 $\mu\text{L/h}$ within the microfluidic channel. Beads are trapped either individually or in clusters on micro-magnets which were prepared with the LG set-up.

We studied, the effect of micro-magnet microstructure (LG vs HG set-ups), as well as the influence of the external millimeter-sized permanent magnet, on trapping performances. The reproducibility was investigated by conducting each experiment at least three times. Results are summarized in Figure 3.24.

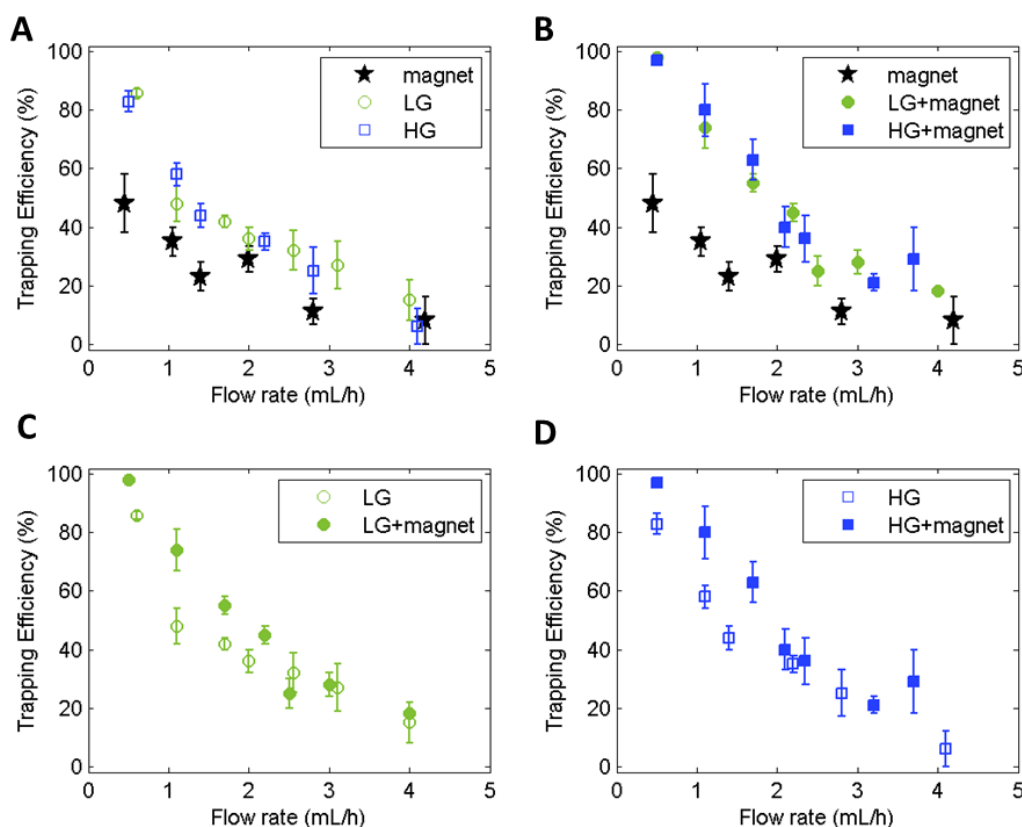


Figure 3.24: Magnetic trapping efficiencies of the micro-magnets at various flow rates. (A) Effect of the microstructure. Comparison of the trapping efficiencies for micro-magnets prepared with the LG set-up or HG set-up. Micro-magnets achieved higher trapping efficiencies than a millimeter-sized permanent magnet (star-shaped marker). (B,C,D) Influence of the external permanent magnet. The combination of the two magnet scales, micro- and milli-, leads to high trapping efficiencies.

First, as highlighted in Figure 3.24-A, micro-magnets obtained with LG set-up achieved 85% trapping efficiency at a flow rate of 500 $\mu\text{L/h}$ (corresponding speed of 2.8 mm/s). In other terms, since 6500 beads were injected, about 5500 beads were trapped, corresponding to a trapping throughput of 400 beads/min at this flow rate. The trapping area being 7.5 mm², the trapping density reaches 730 beads/mm². For increasing flow rate, the increasing drag force overcomes the magnetic force, resulting in decreasing trapping efficiencies. At 4 mL/h, 15% of trapping efficiency was achieved. Nevertheless, despite the lower number of trapped SPMBs, increasing flow rates allow for enhanced single-bead trapping. The trade-offs in trapping efficiency and single-object trapping highly depend on the desired application.

Besides, when comparing trapping performances between integrated micro-magnets and external milli-magnet, the efficiency is significantly higher with the micrometer-scaled magnet. For flow rates comprised between 0.5 and 1.5 mL/h, the trapping efficiency is almost twice greater with the micro-magnets: 85% and 45% at 0.5 and 1.5 mL/h, respectively; against 50% and 25% with the milli-magnet, respectively. These results illustrate the fact that reducing the size of the magnetic source allows for higher magnetic forces, and thus higher trapping efficiencies.

5.1.1. Effect of the micro-magnet microstructure

The effect of both LG and HG set-ups, which lead to either elongated chains or compact agglomerates, was studied on magnetophoretic trapping performances. It can be observed in Figure 3.24-A that both microstructures achieved similar trapping efficiencies. Micro-magnets obtained with the LG set-up reached 83%, 48%, and 36% trapping efficiencies at 0.5, 1, and 2 mL/h, respectively, while micro-magnets obtained with the HG set-up achieved 86%, 58%, and 35% trapping efficiencies, respectively. This small difference is in adequation with Comsol simulations, where the effect of chain length, interparticle distance, as well as nearest neighbor distance, had low impact on the generated magnetic field gradients. Although colloidal probe AFM experiments underlined a significant improvement of the magnetic force on the surface of the micro-magnets, at a distance of 3 μm from the surface, the enhancement was much smaller. In conducted microfluidic trapping experiments, SPMBs are flowing through the entire channel height and are thus subjected to similar forces for both configurations of micro-magnets. The HG set-up did not show to have an impact on micro-magnet interaction reach.

5.1.2. Influence of the external permanent magnet

As a reminder, the external permanent magnet has for aim to deflect flowing object towards the micro-magnet surface, similarly to strategies implementing chaotic mixing through the integration of microstructures on the channel roof [22]. Here, the strategy is to enhance the interaction reach of the micro-magnets within the whole channel height.

Figure 3.24-C and Figure 3.24-D show the impact of the external magnet for micro-magnets obtained with LG and HG set-ups, respectively. It can be observed that the combination of the two magnets, micro- and milli-meter scaled (Figure 3.24-B), enabled to achieve trapping efficiencies as high as 98 and 97% at 0.5 mL/h, for LG and HG set-ups, respectively. The efficiency was therefore increased by around 15% in the presence of the permanent milli-magnet. At a flow rate of 1 mL/h, this enhancement is even more pronounced: the efficiency reaches 74 and 80% in presence of the milli-magnet, for LG and HG set-ups, respectively, corresponding to an increase of 54 and 38%, respectively. Indeed, as shown previously by Comsol simulations, at a distance greater than 50 μm above micro-traps, the magnetic field gradient generated by the milli-magnet predominates (Figure 3.15), therefore significantly increasing the magnetization of flowing SPMBs throughout the channel and allowing for their downward deflection.

Thus, it is the combination of the two types of magnets that allows higher magnetic forces to be generated, which explains the higher trapping efficiencies (Figure 3.24-B). Only strong and localized magnetic field gradients generated by the micro-magnets efficiently retain the trapped targets. Beyond 2.5 mL/h (14 mm/s speed), the benefit of the external milli-magnet becomes negligible in comparison with the drag force. Thus, circulating micro-beads which are far from the traps are no longer attracted

to the latter with the external magnet. The trapping performances are therefore similar for both configurations, micro- and milli-magnets (Figure 3.24-A).

5.1.3. Summary

Finally, the final micro-magnet microstructure that will be used was determined from these trapping experiments. LG and HG set-ups lead to similar trapping efficiencies, but the HG set-up has less reproducibility in both fabrication and magnetic performances (error bars are particularly high in Figure 3.24-B). It should also be mentioned that fabrication method with the HG set-up required additional fabrication steps in comparison with the LG set-up, resulted in half a day longer processes. For all these reasons, the LG set-up has been chosen for the fabrication of micro-magnets dedicated to magnetophoretic-based microfluidic CTC isolation.

The performances of the magnet alone, of the micro-magnets alone (prepared with the LG set-up), and of the combination of the 2 are represented in the graph Figure 3.25.

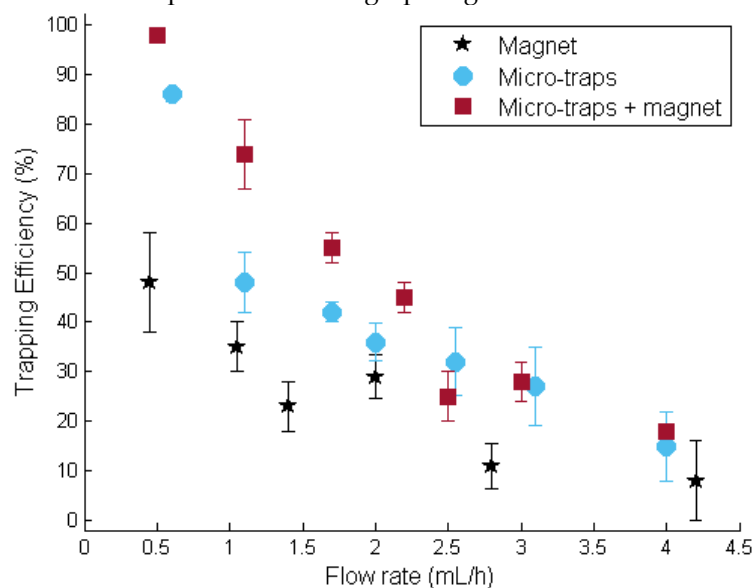


Figure 3.25: Benefit of combining micro- and milli-magnets to achieve high trapping performances. Micro-magnets were prepared with LG set-up. The strategy of the milli-magnet is to attract flowing object located in the upper part of the channel towards the channel bottom where the micro-magnets are located, therefore enhancing their interaction reach. The micro-magnets act as very effective micro-traps which can firmly retain trapped targets since they generate strong and localized magnetic field gradients.

5.2. Hydrodynamic determination of the holding magnetic force

The magnetic forces exerted by 2 wt% composite micro-magnets on SPMBs were estimated in operando, directly within a microfluidic channel. Hydrodynamic determination of the holding magnetic force consists in capturing SPMBs on the magnetic traps at a fixed flow rate and then measure the fluidic drag necessary to overcome the magnetic force.

SPMBs were first injected at an equivalent flow rate of 2 mL/h and trapped on micro-magnets. This first step is performed to get a homogenous SPMB trapping distribution, preferentially as single SPMB, in the microscope field of view ($1000 \times 750 \mu\text{m}^2$). For each experiment, a picture is taken to count the number of trapped beads initially. The injection is then interrupted to switch the SPMB reservoir input for a PBS solution. The second step consists in injecting PBS and gradually increasing the flow rate, from 4 mL/h to 12 mL/h by 2 mL/h increments, and then from 12 mL/h to 28 mL/h by 4 mL/h increments. The goal is to identify the flow velocity, and thus the shear stress, at which each trapped bead gets untrapped. For each flow rate, a picture of the same area is taken using the microscope to count the number of beads released by the fluidic force.

To determine the hydrodynamic drag force acting on the trapped SPMB which is immobilized on the channel floor, Stokes' Law is not appropriate [37]. For a particle positioned near a wall, the drag force should rather be calculated using the relationship determined by Goldman et al. in a uniform shear flow [38]:

$$F_d = 1.7005 \times 6\pi\eta r^2 G \quad (21)$$

Where η is the viscosity in Pa·s (10^{-3} Pa·s for a PBS solution), r the radius of the particle, and G the shear rate in s^{-1} . For laminar flows, the shear rate can be calculated under the condition of a uniform velocity gradient by using the velocity at the center of the particle:

$$G = \frac{v_{(z=r)}}{r} \quad (22)$$

With $v_{(z=r)}$ the fluid velocity at a height $z = r$, which corresponds to the distance from the surface to the center of the particle.

Finally, assuming that the SPMB essentially experiences the drag force and the magnetic force, the SPMB will be released from the trap when:

$$\|\vec{F}_d\| = \|\vec{F}_m\| \quad (23)$$

The magnetic force can therefore be calculated for each trapped bead by measuring the flow velocity at which the bead is freed.

Typical images obtained with this protocol are represented in Figure 3.26. At the initial flow rate of 2 mL/h, 170 beads were trapped in the field of view (Figure 3.26-A). After switching the input for PBS and increasing the flow rate successively at 4 and 6 mL/h, the number of trapped beads decreased at 69 (Figure 3.26-B) and 18, respectively. The experiment was stopped when there were no trapped SPMBs left, or when the pressure controller reached the pressure of 55 mbar. The range of applied pressure varied from 3 to 55 mBar, which corresponded to a flow rate in the channel ranging from 2 mL/h to 34 mL/h and a drag force exerted by the trapped beads ranging from 0.36 nN to 6.15 nN.

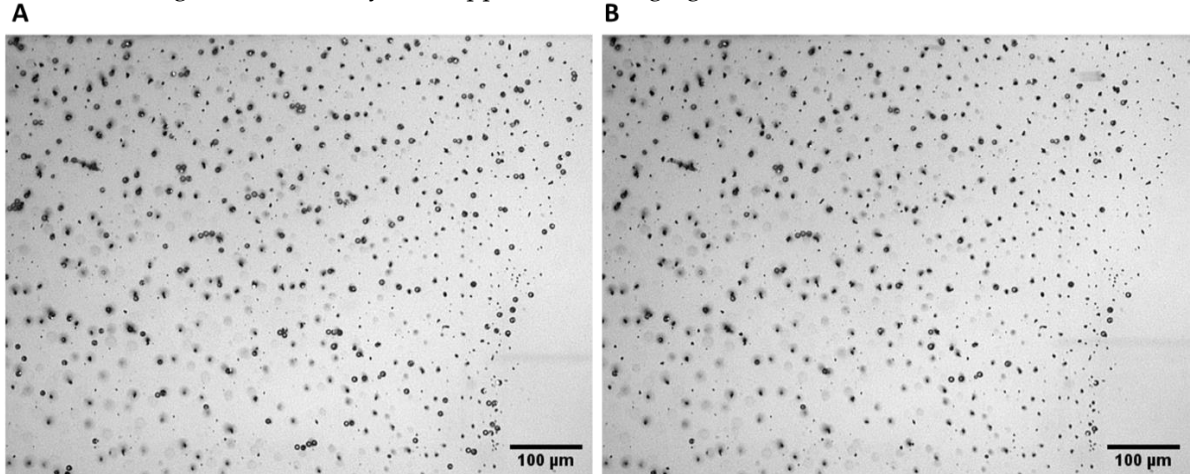


Figure 3.26: Microscope images of (A) the initial trapped bead configuration at 2 mL/h and (B) the releasing process at 4 mL/h. Initially, 170 beads were trapped in the field of view, while increasing the flow rate to 4 mL/h decreased this number to 69 beads.

The experiment was repeated three times and, for the micro-magnet-integrated device (no external magnet), an average magnetic force of 1.3 ± 0.3 nN was calculated on a total of 300 analyzed SPMBs. These results are in good agreement with measured forces by colloidal probe AFM since contact forces ranging from 0.5 to 2 nN were obtained. In particular, the magnetic force was determined collectively, on a population of trapped beads, therefore providing complementary results to AFM where the magnetic force is measured individually (single magnetic bead scanning micro-magnet surface). In operando measurements even showed that some micro-traps could generate magnetic forces superior to 6.15 nN since some beads remained trapped for an applied pressure of 55 mbar.

5.2.1. Effect of the micro-magnet network

The influence of the micro-traps position within the magnetic network on the magnetic force magnitude was studied. We observed that traps located at the beginning of the trapping area generated greater forces than those located in the middle of the trapping area. Figure 3.27 displays the relative force intensity as a function of the distance from the edge. It can be observed that traps located in the first 50 μm of the trapping zone generated forces on average 2.6 times greater than those produced overall in the trapping zone. This observation is consistent with finite element simulation calculations of the magnetic force generated by a chain located either in the center or at the edge of the network (Figure 3.17-B). This is a result of the demagnetizing field which inevitably occurs in any dense micro-array of magnetic structures. In these types of applications, there is always a tradeoff between the density of the micromagnets and their individual trapping efficacy.

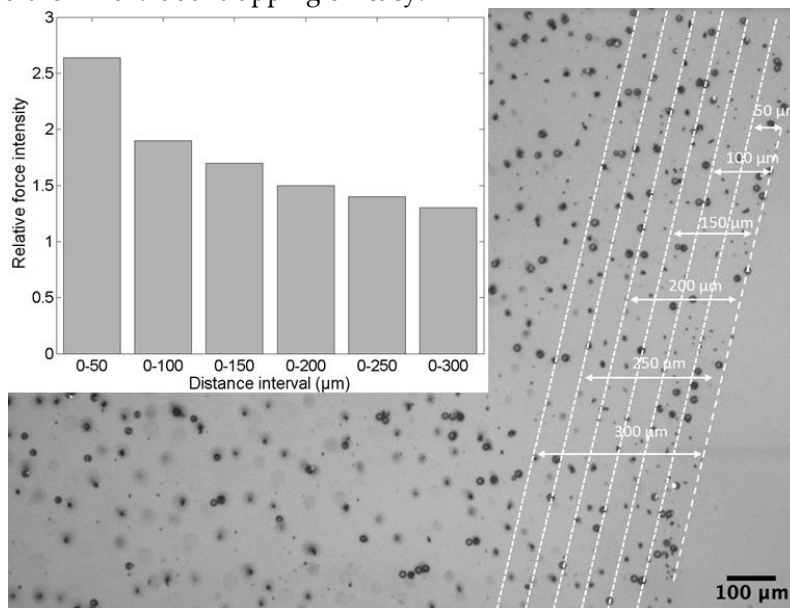


Figure 3.27: Influence of the micro-traps position within the trapping area on the magnetic force magnitude. The relative force intensity is the ratio of the average magnetic force within a given distance interval to the average magnetic force of 1.3 nN in the overall area.

5.2.2. Influence of the external permanent magnet

Finally, the effect of an external magnet was studied on the generated magnetic force. The same protocol as described above was used and an average magnetic force of 1.4 ± 0.6 calculated on a total amount of 750 analyzed SPMBs. In comparison with magnetic forces generated by the micro-traps only, the difference is not significant. Indeed, a drawback of these collective force measurements is the heterogeneity among SPMB/micro-trap pairs (in size, magnetic properties, etc.). This technique returns an order of magnitude rather than a precise discriminatory study. Nevertheless, it can be seen in Figure 3.28 that the magnetic force distribution in the presence of the magnet appears wider. For example, at a specific flow rate of 6 mL/h, which corresponds to a magnetic force of 1.1 nN, there were 11% of trapped beads left in the absence of the external magnet, while this value was doubled in the presence of the magnet (23% of trapped beads left).

The influence of the external magnet was further studied by determining forces generated by a same trap in the presence or absence of the external magnet. Although these measurements were performed with different trapped beads (SPMB diameter ranging from 8 to 20 μm), we observed, on 192 individual traps, that for 70% of them generated magnetic forces were greater or equal in the presence of the magnet. The external milli-magnet therefore increases contact magnetic forces, as priorly observed with AFM.

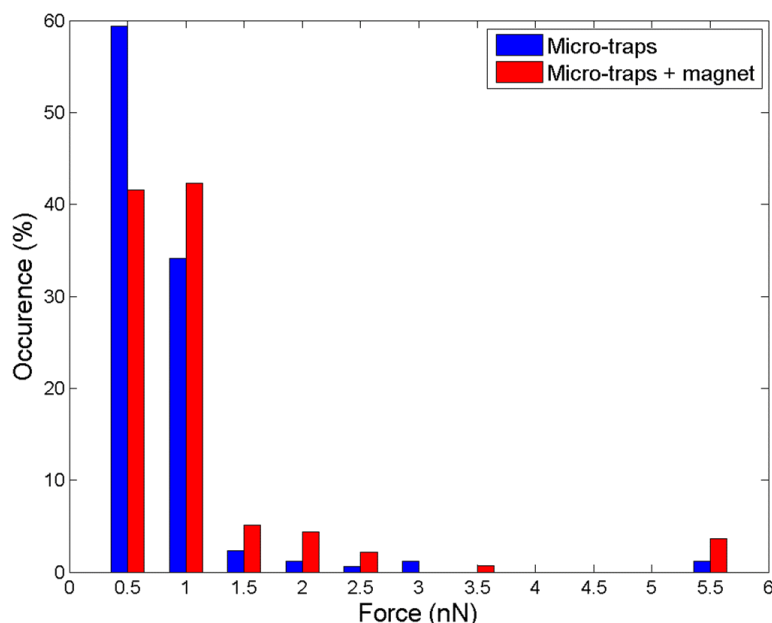


Figure 3.28: Magnetic force distribution exerted by the micro-traps on SPMBs, in the absence and in the presence of the external permanent magnet.

To put in a nutshell, microfluidic experiments on trapping efficiency and magnetic force measurements are consistent with theoretical calculations (Comsol) and experimental measurements (colloidal probe AFM). Micro-magnets, which generate strong magnetic field gradients on their surface leading to magnetic forces of several nN, enabled high magnetophoretic trapping efficiencies at relatively high flow rates (85% at 500 $\mu\text{L/h}$), as well as strong holding magnetic force (greater than 6.15 nN for a few SPMB/micro-magnet pairs). The strategy of adding an external milli-magnet was successful and resulted in multiple benefits: the attraction of distant flowing objects towards the micro-magnet surface as well as the increase of contact magnetic forces, leading to higher trapping efficiencies (up to a 50% increase at 1 mL/h).

6. Comparison with magnetic performances in the literature

As previously mentioned, numerous works have been reported on the implementation of magnetic micro-scale sources, fabricated using conventional fabrication methods in most cases, with the aim of manipulating target objects. In particular, deep investigations have been performed for the characterization of the magnetic performances of these magnetophoretic devices. To determine the magnetic forces generated by magnetic micro-scale sources, several approaches were described, the most encountered being numerical simulations, but also experimental studies by magnetic force microscopy (or colloidal probe AFM), and Stokes drag experiments.

Figure 3.29 displays the magnetic forces exerted on the center of a magnetic target as a function of the distance to the micro-source, for various studies. Typical forces in the fN-nN range were measured. The great disparity between studies can be attributed to the variability of the target object size (from 1 to 12 μm) and its magnetization, which are proportional to the magnetic force. A description of magnetic micro-sources fabricated using either conventional microfabrication processes or composite/ferrofluid approaches, as well as the magnetic force measurement method, can be found in Table 3-4 for plotted results.

A common point between studies, which is characteristic of micro-scale magnetic source, is the decay of the magnetic force on distances comparable to the size of the target object, of the order of the μm . When comparing the magnetic forces reported in the literature with the magnetic forces obtained by the developed NdFeB composite micro-magnets, comparable or greater force values were obtained, with the benefit of the composite approach which leads to cost-effective and easy-to-implement magnetophoretic devices.

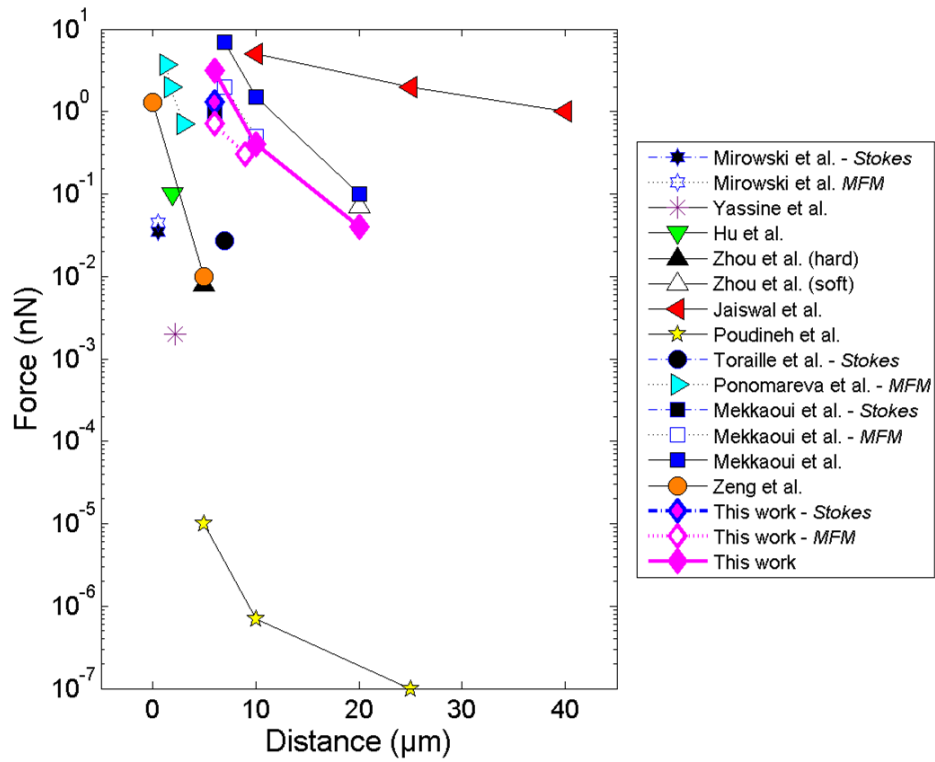


Figure 3.29: Forces exerted on the center of the magnetic target as a function of the distance to the micro-source. Results from other studies and comparison with this work. When not specified, the magnetic force was determined by numerical studies. A description of the magnetic micro-sources and magnetic force measurement methods can be found in Table 3-4.

Table 3-4: Reported magnetic forces generated by a wide range of magnetic micro-source types.

Researcher	Micro-source	Fabrication method	Force measurement method	Magnetic force	Ref
Mirowski et al.	Array of NiFe rectangles (1x3x0.03 μm^3)	N/A	Stokes drag force, Magnetic force microscopy (MFM)	35 pN (Stokes), 45 pN (MFM) @0.5 μm	[37]
Yassine et al.	NiFe disks (3 μm diameter, 30 nm thickness)	Electron beam physical vapor deposition	Finite element analysis (Comsol)	2.2 pN @2.2 μm	[39]
Hu et al.	NiFe disks (50 μm diameter, 100 nm thickness)	Sputtering	Finite element analysis (Maxwell 3D software)	0.1 nN @1.9 μm	[30]
Zhou et al.	NdFeB-PDMS-filled channel with rectangular structures (1000x500 μm^2)	Composite (NdFeB/PDMS = 2:1 w/w)	Finite element analysis (Comsol)	8 pN @5 μm	[27]
Zhou et al.	Fe-PDMS-filled channel with 60° isosceles triangle structures (1000 μm width)	Composite (Fe/PDMS = 2:1 w/w)	Finite element analysis (Comsol)	70 pN @20 μm	[40]
Jaiswal et al.	Array of diamond-shaped Ni structures (64 μm edge size, 200 nm height)	Thermal deposition	Finite element analysis (Comsol)	5 to 1 nN range @10-40 μm	[41]
Poudineh et al.	Array of circular-shaped Ni structures (272-470 μm diameter range, 1.5 μm thickness)	Sputtering	Finite element analysis (Comsol)	10 to 0.001 fN @5-25 μm	[42]
Toraille et al.	Array of NiFe rectangular cuboids (110x110 μm^2 , 4 μm thickness)	Electro-deposition	Stokes drag force	27 pN @7 μm	[43]
Ponomareva et al.	Stripped NdFeB 5- μm thick film with zones of reversed magnetization	Sputtering and thermo-magnetic patterning	MFM	3.75-0.7 nN range @1.35-2.95 μm	[33]
Mekkaoui et al.	Array of chain-like Fe microstructures	Composite (5wt% Fe-PDMS)	Stokes drag force, MFM, Finite element analysis (Comsol)	1 nN @6 μm , 2-0.5 nN @7-10 μm , 1.8-0.01 nN @6-20 μm	[12,44]
Zeng et al.	Fe ₃ O ₄ powder-filled channel (40- μm high) with a series of triangular structures (100 μm width, 50 μm height)	Ferrofluid (Fe ₃ O ₄ powder mixed with pure water = 1:500 m/v)	Finite element analysis (Comsol)	1.3-0.01 nN range @0-5 μm	[45]

7. Conclusion

The composite approach has shown to be a promising method for the fabrication of arrays of micrometer-sized permanent magnets and their direct integration into polymer-based microfluidic devices. This cost-effective and easy-to-handle fabrication process is based on hard magnetic powder and PDMS mixing, followed by NdFeB magnetic particle self-assembly in chains under the application of an external magnetic field during PDMS cross-linking. In particular, the structure of the micro-magnets could be tuned depending on the applied magnetic field during the cross-linking step. Two magnetic templates were used during the composite cross-linking: “low-gradient” and “high-gradient” set-ups. The use of a high-gradient set-up enabled the preparation of short and compact chain-like micro-magnets, while increasing NdFeB particle concentration allowed higher micro-magnet density to be achieved.

The fabricated micro-magnets aim to act as micro-traps for magnetophoretic trapping applications in microfluidics. Their magnetic performances were determined using a broad range of characterization methods. First, finite element simulations were conducted to calculate generated magnetic field gradients and magnetic forces and evaluate the demagnetizing effect within a network. In addition, colloidal probe AFM and Stokes drag force experiments led to complementary studies of the magnetic forces generated by the micro-magnets, through individual and collective measurements. Finally, microfluidic experiments were carried out to study trapping efficiencies using superparamagnetic beads as target objects.

Numerical and experimental approaches showed that magnetic forces as high as several nanoNewtons could be generated at contact. In particular, Comsol calculations, followed by hydrodynamic force experiments, underlined the magnetic behavior of a micro-magnet located within a magnetic network and revealed the demagnetizing effect inevitably occurring in a dense array of micro-magnets. Regarding the use of a high-gradient configuration, it led to increased contact magnetic forces, but similar trapping efficiencies compared to the low-gradient configuration. However, since its reproducibility was lower with respect to fabrication and magnetic performances, and its fabrication required additional steps, the high-gradient configuration was not chosen for the fabrication of micro-magnets for microfluidic isolation of CTCs by magnetophoresis (Chapter 4).

The strategy relying on the addition of an external millimeter-sized permanent magnet was successfully implemented to increase magnetic fields and magnetic field gradients in the whole channel height. The benefit of this external magnet was first demonstrated by Comsol simulations and colloidal probe AFM measurements and confirmed in microfluidics by improving SPMB trapping. It resulted in a deflection of flowing object trajectories towards the channel bottom where micro-magnets are located and magnetic field gradients the strongest, and a larger holding magnetic force.

To put in a nutshell, the composite approach leads to autonomous and compact systems which were successfully implemented for the manipulation of magnetic objects. The achieved magnetic performances of the micro-magnets, with contact forces up to several nN, are consistent with those produced by micro-scale magnetic sources obtained by more conventional microfabrication methods, which are more complex than the composite approach. In addition, the combination of micro- and millimeter scaled magnets represents an easy-to-implement strategy to attract distant beads within a microfluidic device, therefore offering promising perspectives for biomedical sorting applications, such as CTC isolation.

References

1. Cugat, O.; Delamare, J.; Reyne, G. Magnetic micro-actuators and systems (MAGMAS). *IEEE Trans. Magn.* **2003**, *39*, 3607–3612, doi:10.1109/TMAG.2003.816763.
2. Gray, B.L. A Review of Magnetic Composite Polymers Applied to Microfluidic Devices. *J. Electrochem. Soc.* **2014**, *161*, B3173–B3183, doi:10.1149/2.023402jes.
3. Le Roy, D.; Dhungana, D.; Ourry, L.; Faivre, M.; Ferrigno, R.; Tamion, A.; Dupuis, V.; Salles, V.; Deman, A. Anisotropic ferromagnetic polymer : A first step for their implementation in microfluidic systems. *AIP Adv.* **2016**, *6*, 056604.
4. Liu, J.; Lawrence, E.M.; Wu, A.; Ivey, M.L.; Flores, G.A.; Javier, K.; Bibette, J.; Richard, J. Field-induced structures in ferrofluid emulsions. *Phys. Rev. Lett.* **1995**, *74*, 2828–2831, doi:10.1103/PhysRevLett.74.2828.
5. Martin, J.E.; Venturini, E.; Odinek, J.; Anderson, R.A. Anisotropic magnetism in field-structured composites. *Phys. Rev. E - Stat. Physics, Plasmas, Fluids, Relat. Interdiscip. Top.* **2000**, *61*, 2818–2830, doi:10.1103/PhysRevE.61.2818.
6. Bertoni, G.; Torre, B.; Falqui, A.; Fragouli, D.; Athanassiou, A.; Cingolani, R. Nanochains formation of superparamagnetic nanoparticles. *J. Phys. Chem. C* **2011**, *115*, 7249–7254, doi:10.1021/jp111235n.
7. Wang, M.; He, L.; Yin, Y. Magnetic field guided colloidal assembly. *Mater. Today* **2013**, *16*, 110–116, doi:10.1016/j.mattod.2013.04.008.
8. Ghosh, S.; Puri, I.K. Changing the magnetic properties of microstructure by directing the self-assembly of superparamagnetic nanoparticles. *Faraday Discuss.* **2015**, *181*, 423–435, doi:10.1039/c4fd00245h.
9. Deman, A.L.; Mekkaoui, S.; Dhungana, D.; Chateaux, J.F.; Tamion, A.; Degouttes, J.; Dupuis, V.; Le Roy, D. Anisotropic composite polymer for high magnetic force in microfluidic systems. *Microfluid. Nanofluidics* **2017**, *21*, 1–8, doi:10.1007/s10404-017-2008-2.
10. Mekkaoui, S.; Le Roy, D.; Audry, M.C.; Lachambre, J.; Dupuis, V.; Desgouttes, J.; Deman, A.L. Arrays of high aspect ratio magnetic microstructures for large trapping throughput in lab-on-chip systems. *Microfluid. Nanofluidics* **2018**, *22*, 119, doi:10.1007/s10404-018-2141-6.
11. Mekkaoui, S.; Descamps, L.; Audry, M.; Deman, A.; Roy, D. Le Nanonewton Magnetophoretic Microtrap Array for Microsystems. *Langmuir* **2020**, doi:10.1021/acs.langmuir.0c02254.
12. Mekkaoui, S. Développement de polymères composites auto-organisés pour la mise en œuvre de fonctions magnétiques en microsystèmes fluidiques, Université Claude Bernard Lyon 1, 2019.
13. Dumas-Bouchiat, F.; Zanini, L.F.; Kustov, M.; Dempsey, N.M.; Grechishkin, R.; Hasselbach, K.; Orlianges, J.C.; Champeaux, C.; Catherinot, A.; Givord, D. Thermomagnetically patterned micromagnets. *Appl. Phys. Lett* **2010**, *96*, 102511, doi:10.1063/1.3341190.
14. Dempsey, N.M.; Le Roy, D.; Marelli-Mathevon, H.; Shaw, G.; Dias, A.; Kramer, R.B.G.; Viet Cuong, L.; Kustov, M.; Zanini, L.F.; Villard, C.; et al. Micro-magnetic imprinting of high field gradient magnetic flux sources. *Appl. Phys. Lett.* **2014**, *104*, 262401, doi:10.1063/1.4886375.
15. Bidan, C.M.; Fratzl, M.; Coullomb, A.; Moreau, P.; Lombard, A.H.; Wang, I.; Balland, M.; Boudou, T.; Dempsey, N.M.; Devillers, T.; et al. Magneto-active substrates for local mechanical stimulation of living cells. *Sci. Rep.* **2018**, *8*, 1–13, doi:10.1038/s41598-018-19804-1.
16. Fragouli, D.; Buonsanti, R.; Bertoni, G.; Sangregorio, C.; Innocenti, C.; Falqui, A.; Gatteschi, D.; Cozzoli, P.D.; Athanassiou, A.; Cingolani, R. Dynamical formation of spatially localized arrays of aligned nanowires in plastic films with magnetic anisotropy. *ACS Nano* **2010**, *4*, 1873–1878, doi:10.1021/nn901597a.
17. Tracy, J.B.; Crawford, T.M. Magnetic field-directed self-assembly of magnetic nanoparticles. *MRS Bull.* **2013**, *38*, 915–920, doi:10.1557/mrs.2013.233.
18. Ghosh, S.; Puri, I.K. Soft polymer magnetic nanocomposites: Microstructure patterning by magnetophoretic transport and self-assembly. *Soft Matter* **2013**, *9*, 2024–2029, doi:10.1039/c2sm27420e.
19. Marchi, S.; Casu, A.; Bertora, F.; Athanassiou, A.; Fragouli, D. Highly Magneto-Responsive Elastomeric Films Created by a Two-Step Fabrication Process. *ACS Appl. Mater. Interfaces* **2015**, *7*, 19112–19118,

doi:10.1021/acsami.5b04711.

20. Coey, J.M.D. Hard Magnetic Materials: A Perspective. *IEEE Trans. Magn.* **2011**, *47*, 4671–4681, doi:10.1109/TMAG.2011.2166975.
21. Stott, S.L.; Hsu, C.; Tsukrov, D.I.; Yu, M.; Miyamoto, D.T.; Waltman, B.A.; Rothenberg, S.M.; Shah, A.M.; Smas, M.E.; Korir, G.K.; et al. Isolation of circulating tumor cells using a microvortex-generating herringbone-chip. *Proc. Natl. Acad. Sci. U. S. A.* **2010**, doi:10.1073/pnas.1012539107/-/DCSupplemental.www.pnas.org/cgi/doi/10.1073/pnas.1012539107.
22. Chung, J.; Issadore, D.; Ullal, A.; Lee, K.; Weissleder, R.; Lee, H. Rare cell isolation and profiling on a hybrid magnetic/size-sorting chip. *Biomicrofluidics* **2013**, *7*, 1–9, doi:10.1063/1.4821923.
23. Jiang, X.; Wong, K.H.K.; Khankhel, A.H.; Zeinali, M.; Reategui, E.; Phillips, M.J.; Luo, X.; Aceto, N.; Fachin, F.; Hoang, A.N.; et al. Microfluidic isolation of platelet-covered circulating tumor cells. *Lab Chip* **2017**, *17*, 3498–3503, doi:10.1039/c7lc00654c.
24. Huang, X.; Tang, J.; Hu, L.; Bian, R.; Liu, M.; Cao, W.; Zhang, H. Arrayed microfluidic chip for detection of circulating tumor cells and evaluation of drug potency. *Anal. Biochem.* **2019**, *564–565*, 64–71, doi:10.1016/j.ab.2018.10.011.
25. Coey, J.M.D. Magnetostatics. In *Magnetism and Magnetic Materials*; Cambridge University Press, 2010; pp. 24–61.
26. Malic, L.; Zhang, X.; Brassard, D.; Clime, L.; Daoud, J.; Luebbert, C.; Barrere, V.; Boutin, A.; Bidawid, S.; Farber, J.; et al. Polymer-based microfluidic chip for rapid and efficient immunomagnetic capture and release of *Listeria monocytogenes*. *Lab Chip* **2015**, *15*, 3994–4007, doi:10.1039/C5LC00852B.
27. Zhou, R.; Yang, Q.; Bai, F.; Werner, J.A.; Shi, H.; Ma, Y.; Wang, C. Fabrication and integration of microscale permanent magnets for particle separation in microfluidics. *Microfluid. Nanofluidics* **2016**, *20*, 1–12, doi:10.1007/s10404-016-1774-6.
28. Royet, D.; Hériveaux, Y.; Marchalot, J.; Scorretti, R.; Dias, A.; Dempsey, N.M.; Bonfim, M.; Simonet, P.; Frénéa-Robin, M. Using injection molding and reversible bonding for easy fabrication of magnetic cell trapping and sorting devices. *J. Magn. Magn. Mater.* **2017**, *427*, 306–313, doi:10.1016/j.jmmm.2016.10.102.
29. Lin, M.; Chen, J.-F.; Lu, Y.-T.; Zhang, Y.; Song, J.; Hou, S.; Ke, Z.; Tseng, H.-R. Nanostructure embedded microchips for detection, isolation, and characterization of circulating tumor cells. *Acc. Chem. Res.* **2014**, *47*, 2941–2950, doi:10.1021/ar5001617.
30. Hu, X.; Goudou, S.R.; Torati, S.R.; Lim, B.; Kim, K.; Kim, C. An on-chip micromagnet frictionometer based on magnetically driven colloids for nano-bio interfaces. *Lab Chip* **2016**, *16*, 3485–3492, doi:10.1039/c6lc00666c.
31. Lin, S.; Zhi, X.; Chen, D.; Xia, F.; Shen, Y.; Niu, J.; Huang, S.; Song, J.; Miao, J.; Cui, D.; et al. A flyover style microfluidic chip for highly purified magnetic cell separation. *Biosens. Bioelectron.* **2019**, *129*, 175–181, doi:10.1016/j.bios.2018.12.058.
32. Bongaerts, M.; Aizel, K.; Secret, E.; Jan, A.; Nahar, T.; Raudzus, F.; Neumann, S.; Telling, N.; Heumann, R.; Siaugue, J.-M.; et al. Parallelized Manipulation of Adherent Living Cells by Magnetic Nanoparticles-Mediated Forces. *Int. J. Mol. Sci.* **2020**, *21*, 6560, doi:10.3390/ijms21186560.
33. Ponomareva, S.; Dias, A.; Royer, B.; Marelli, H.; Motte, J.F.; Givord, D.; Dumas-Bouchiat, F.; Dempsey, N.M.; Marchi, F. A quantitative study of magnetic interactions between a micro-magnet array and individual magnetic micro-particles by scanning particle force microscopy. *J. Micromechanics Microengineering* **2019**, *29*, 015010, doi:10.1088/1361-6439/aaefd5.
34. Furlani, E.P. Analysis of particle transport in a magnetophoretic microsystem. *J. Appl. Phys.* **2006**, *99*, 024912, doi:10.1063/1.2164531.
35. Gerber, R.; Takayasu, M.; Friedlaender, F. Generalization of HGMS theory: The capture of ultra-fine particles. *IEEE Trans. Magn.* **1983**, *19*, 2115–2117, doi:10.1109/TMAG.1983.1062795.
36. Deman, A.-L.; Le Roy, D. Magnetophoresis in Bio-Devices. In *Engineering of Micro/Nano Biosystems*; Springer, Singapore, 2020; pp. 309–361.

37. Mirowski, E.; Moreland, J.; Zhang, A.; Russek, S.E.; Donahue, M.J. Manipulation and sorting of magnetic particles by a magnetic force microscope on a microfluidic magnetic trap platform. *Appl. Phys. Lett.* **2005**, *86*, 1–3, doi:10.1063/1.1947368.
38. Goldman, A.J.; Cox, R.G.; Brenner, H. Slow viscous motion of a sphere parallel to a plane wall-II Couette flow. *Chem. Eng. Sci.* **1967**, *22*, 653–660, doi:10.1016/0009-2509(67)80048-4.
39. Yassine, O.; Gooneratne, C.P.; Smara, D.A.; Li, F.; Mohammed, H.; Merzaban, J.; Kosel, J. Isolation of cells for selective treatment and analysis using a magnetic microfluidic chip. *Biomicrofluidics* **2014**, *8*, doi:10.1063/1.4883855.
40. Zhou, R.; Wang, C. Microfluidic separation of magnetic particles with soft magnetic microstructures. *Microfluid. Nanofluidics* **2016**, *20*, 1–11, doi:10.1007/s10404-016-1714-5.
41. Jaiswal, D.; Rad, A.T.; Nieh, M.P.; Claffey, K.P.; Hoshino, K. Micromagnetic Cancer Cell Immobilization and Release for Real-Time Single Cell Analysis. *J. Magn. Magn. Mater.* **2017**, *427*, 7–13, doi:10.1016/j.jmmm.2016.11.002.
42. Poudineh, M.; Sargent, E.H.; Kelley, S.O. Amplified Micromagnetic Field Gradients Enable High-Resolution Profiling of Rare Cell Subpopulations. *ACS Appl. Mater. Interfaces* **2017**, *9*, 25683–25690, doi:10.1021/acsami.7b04677.
43. Toraille, L.; Aïzel, K.; Balloul, É.; Vicario, C.; Monzel, C.; Coppey, M.; Secret, E.; Siaugue, J.M.; Sampaio, J.; Rohart, S.; et al. Optical Magnetometry of Single Biocompatible Micromagnets for Quantitative Magnetogenetic and Magnetomechanical Assays. *Nano Lett.* **2018**, *18*, 7635–7641, doi:10.1021/acs.nanolett.8b03222.
44. Mekkaoui, S.; Descamps, L.; Audry, M.C.; Deman, A.L.; Le Roy, D. Nanonewton Magnetophoretic Microtrap Array for Microsystems. *Langmuir* **2020**, *36*, 14546–14553, doi:10.1021/acs.langmuir.0c02254.
45. Zeng, L.; Chen, X.; Du, J.; Yu, Z.; Zhang, R.; Zhang, Y.; Yang, H. Label-free separation of nanoscale particles by an ultrahigh gradient magnetic field in a microfluidic device. *Nanoscale* **2021**, *13*, 4029, doi:10.1039/d0nr08383f.

Chapter IV

Negative selection of cancer cells via white blood cell depletion for downstream analysis

In this chapter will be detailed the implementation strategy of the micro-magnet-integrated microfluidic device for CTC isolation. Cancer cell lines were used as CTC models. Several prior optimizations, conducted on the device features and operation procedure to ensure an optimal WBC depletion and CTC recovery, will be reported. Next, the compatibility of the device with routine biological studies (cell culture, phenotypic and genotypic analyses), after CTC recovery, will be investigated. Finally, as part of a collaboration with biologists from Hospices Civils de Lyon, the benefit of the magnetophoretic-based microfluidic chip after a pre-enrichment step through a size-based separation technology (ClearCell FX1®) will be determined. The aim of this two-step separation process is to meet the needs of physicians for highly purified samples, facilitating downstream analysis.

1. Introduction

In the past 15 years, the selection of CTCs directly from blood as a real-time liquid biopsy has received much attention, and further analysis of these cells may greatly aid in both research and clinical applications. CTC analysis could advance the understanding of the metastatic cascade [1], tumor evolution [2], patient heterogeneity [3], as well as drug resistance [4,5]. Among the broad range of CTC study applications, one can cite cancer diagnosis and prognosis, tumor marker identification and monitoring, as well as treatment tailoring through personalized therapy implementation and drug resistance monitoring.

First, cancer diagnosis and prognosis can be assessed by CTC enumeration, which offers insight on cancer progression and survival prognosis. The prognostic significance of CTCs has been demonstrated in numerous studies on patients at early disease stages without clinical and radiological signs of overt metastases, particularly in breast cancer [6–8], but also in other tumor entities [9,10]. Cristofanilli et al. showed in their landmark study that patients with over five CTCs per 7.5 ml of peripheral blood had poorer overall survival [6]. In addition, the clinical utility of CTC enumeration during chemotherapy and/or radiotherapy was demonstrated in gastrointestinal cancers (e.g. pancreatic, gastric, and colorectal cancers) since CTC counts are correlated with tumor staging and both progression-free survival and overall survival [11].

Furthermore, tumor marker identification and monitoring can be described by CTC phenotypic characterizations and may contribute to the analysis of therapeutically relevant proteins or genes, the identification of new therapeutic targets, and the discovery of mechanisms responsible for drug resistance. For example, Riethdorf et al. demonstrated the relevance of analyzing HER2 (epidermal growth factor receptor 2) protein expression for stratification of patients to anti-HER2 therapy [12]. More recently, immune checkpoint regulators such as programmed death–ligand 1 (PD-L1) have become exciting new therapeutic targets leading to long-lasting remissions in patients with advanced malignancies. Guibert et al. reported that PD-L1 is expressed on CTCs in nearly 70% of patients with non-small cell lung cancer (NSCLC), with an average of 4.5 PD-L1-positive CTCs/mL [13]. After initiation of radiotherapy, the proportion of PD-L1-positive CTCs increased significantly, indicating upregulation of PD-L1 expression in response to radiation [14]. PD-L1 expression analysis may therefore be used to monitor dynamic changes of the tumor in response to chemotherapy, radiotherapy, and likely immunotherapy. Additionally, CTCs can undergo epithelial–mesenchymal transition (EMT), thus downregulating epithelial marker expression, and may promote their motile/invasive properties [15], stemness properties [16], as well as resistance to apoptosis and anoikis (apoptosis resulting from loss of cell-matrix interactions) [17], all of which contribute to the survival and dissemination of CTCs [18]. Gradilone et al. observed that the presence of CTCs expressing mesenchymal-associated multidrug-resistance-related proteins and aldehyde dehydrogenase 1 (ALDH1) stem cell marker was predictive of response to chemotherapy and associated with shorter progression-free survival [19]. Thus, identifying CTC mesenchymal phenotype may help predicting treatment efficacy.

Tumor marker identification and monitoring can also be determined by cancer genome sequencing to tailor personalized therapies. Cancer genome sequencing has allowed for the identification of recurrent genes in different cancer types, named “oncdriver” genes, or oncogenes. Often mutated and overexpressed in cancers, oncogenes play an essential role in cancer progression since they promote cell proliferation and resistance to apoptosis. CTCs can therefore be screened for genetic mutations in known oncogenes, such as KRAS (Kirsten rat sarcoma), EGFR (epidermal growth factor receptor), HER2, ER (estrogen receptor), and AR (androgen receptor) genes [20], so as to facilitate identification of therapeutic targets and assessment of treatment efficacy. For example, recent studies performed on single CTCs obtained from patients with colorectal cancer revealed a high intra- and inter-patient heterogeneity of KRAS mutations [5,21]. Thus, early detection of mutated KRAS oncogene might help to guide therapy in individual patients.

In prostate cancer, the AR oncogene has great implications in cancer development, progression, and resistance. Many AR mutations have been shown to confer resistance to androgen deprivation therapies and lead to tumor proliferation in castration-resistant prostate cancer patients [22]. Secondary hormonal

therapy should therefore be considered to reduce drug resistance associated with suppression of AR reactivation [23].

In many patients with lung cancer, the fusion product of the anaplastic lymphoma kinase (ALK) and echinoderm microtubule-associated protein like-4 (EML4) genes is targeted to implement adapted treatment strategies. Indeed, patients with advanced NSCLC associated with ALK rearrangement showed a superior response to crizotinib, a small-molecule ALK inhibitor, in comparison with standard chemotherapy [24]. This ALK-gene rearrangement can be detected in single CTCs using fluorescence in situ hybridization (FISH) [25,26].

Thus, molecular analyses of CTCs, particularly those focused on mutations in oncogenes, facilitate the identification of therapeutic targets and may predict the efficacy of specific therapies.

Finally, therapy efficacy monitoring can be performed by in vitro culture of enriched CTCs since it has been extensively explored for drug susceptibility testing, particularly using (i) 3D models such as tumorspheres [27,28] or organoids [29,30] formed within microfluidic systems or (ii) in vivo animal models for xenograft studies [31,32]. For instance, expansion of CTCs from a patient with lung cancer presenting ALK rearrangement enabled the prediction of treatment response to specific ALK inhibitors [26]. A summary of reported research and clinical applications is given in Figure 4.1, revealing CTC clinical utility for personalized medicine.

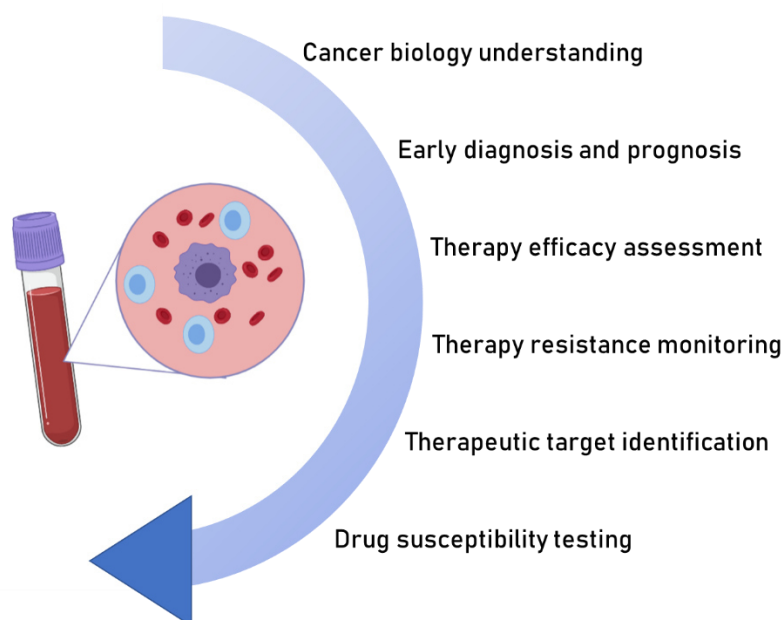


Figure 4.1: Clinical utility of CTCs as liquid biopsy for personalized medicine. Created with BioRender.com.

Hence, developing a CTC separation device for downstream analysis has emerged as a great challenge [33]. Key requirements of such device should include the following: (i) high recovery, (ii) high purity, (iii) high throughput, (iv) viability preservation, (v) versatility to adapt to different cell types, and (vi) compatibility with downstream analyses such as cell culture, phenotypic study (immunofluorescence assay), and molecular analyses (FISH, RT-PCR, RNA-sequencing, etc.).

Here, the adopted strategy relies on an immunomagnetic-based separation chip with three main features. First, the mode of CTC selection is tumor antigen- independent (negative selection). Second, the chip integrates a dense array of micro-traps (as high as 10^6) for WBC depletion. Third, the chip allows the collection of CTCs in suspension, facilitating immediate subsequent analysis.

This chip aims at providing highly pure enriched samples, enabling greater accuracy during genome sequencing and single-cell analysis. Indeed, usually 1-10 CTC in 10^7 WBC can be found in the peripheral blood of cancer patients, enrichment by a factor 10^3 - 10^4 would result in a concentration of 1 CTC in 10^3 WBC in enriched samples, which may be suitable for highly sensitive mutation analyses technologies such as digital PCR and next-generation sequencing [20].

An overview of the final implemented workflow during this thesis is illustrated in Figure 4.2. The developed immunomagnetic purification chip was combined with a prior size-based enrichment step (provided by ClearCell FX1 system, supplied by Hospices Civils de Lyon). Combined physical and biological-based enrichments therefore enable high throughput and high purity for downstream analysis in a clinical context.

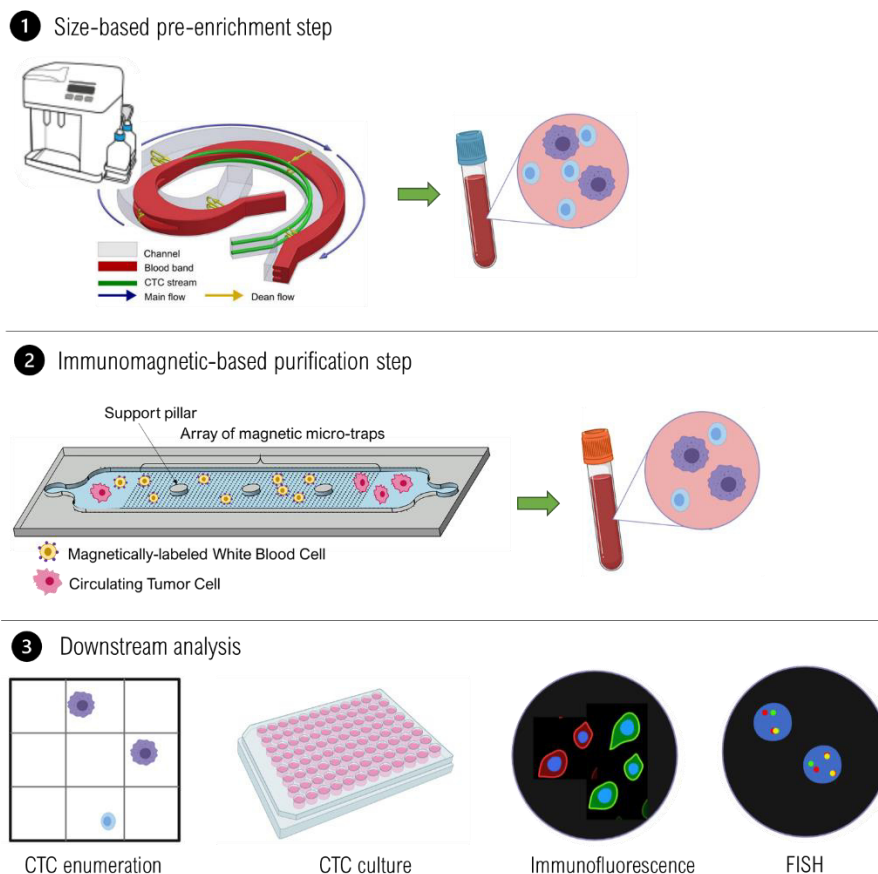


Figure 4.2: Total workflow for CTC isolation and characterization. Combination of (A) a size-based pre-enrichment step with (B) an immunomagnetic-based purification step for high purity. CTC isolation is followed by (C) immediate downstream analysis for a broad range of applications. Description images of the size-based separation step (ClearCell FX1 system) were adapted from [34]. Created with BioRender.com

2. Immuno-magneto-capture of white blood cells and cancer cell recovery

An immunomagnetophoresis-based separation device was developed for CTC enrichment through WBC capture (negative selection). The device integrates the micro-magnets whose fabrication and characterization were described in the previous chapter. In this part, the implementation of the magnetophoretic separation will be presented, particularly the conducted optimizations to enhance WBC depletion will be detailed. Next, the performances of the chip, i.e., WBC capture efficiency and CTC recovery efficiency, will be explored.

2.1. Optimization of the magnetic labeling

First, WBC depletion within the magnetophoretic device requires a prior magnetic labeling step to confer a significant magnetic moment to the WBCs. Both CD45 and CD15 WBC-specific antigens were targeted in order to consider a majority of WBCs. Indeed, since CD45 can be low or absent in some neutrophils or myeloid cells [35], CD15 was also targeted. CD15 is expressed preferentially in monocytes, mature neutrophils, and all myeloid cells.

Several parameters come into play during the labeling process: temperature, agitation, duration, nanoparticle (NP) concentration, as well as suspension medium. In the literature, various magnetic labeling conditions are reported, mostly partially, therefore careful optimization of these variables is necessary for the specific application described here. The optimized conditions were assessed from fluorescence measurements of the WBC (stained nucleus) functionalized with magnetic nanoparticles (conjugated to AlexaFluor-647 fluorophore). The labeling rate was determined on approximatively 100 WBCs for each condition. This study was performed in a staggered time frame with conducted experiments at both INL and HCL laboratories. Studied parameters are reported in Table 4-1.

A synthesis of impacting conditions on WBC labeling rate is presented below, with first the temperature, then the NP concentration, the duration and agitation, the WBC-to-NP ratio, and finally the medium.

Table 4-1: Studied parameters for WBC magnetic labeling.

Parameter	Temperature	Agitation	Duration	Nanoparticle concentration	Medium	Anti-bodies
Tested conditions	- TA - 37°C	- Without - With	- 2h - 30 min	- 100 NP/WBC - 200 NP/WBC - 500 NP/WBC	- PBS - EDTA	- Anti-CD45 - Anti-CD15

Temperature

First, the optimal temperature was determined by studying the viability after 1h incubation of WBCs with magnetic nanoparticles in a well plate put at either 37°C or room temperature (TA). A WBC viability 30% higher was obtained for the incubation at 37°C. The temperature was then fixed at 37°C for next experiments.

Nanoparticle concentration

The theoretical limit for a monolayer coating of particles around WBCs can be calculated as follows: since WBCs have a diameter size range of 8–12µm, their surface area, $4\pi r^2$ is comprised between 201-452 µm². Thus, the maximum number of 0.5-µm diameter particles that can be packed around a single WBC in a closest-packed lattice with an area per bead of $\sqrt{3}d^2/2$ [36] will range from 900 to 2000. Nevertheless, in the literature has been reported an actual ratio of 5-50 particles per WBC [37,38] for bigger particles of 1µm in diameter. Thus, initial nanoparticle concentrations of 100 NP/WBC and 200 NP/WBC were tested. Two separate batches of nanoparticles were prepared, either conjugated to anti-CD45 or anti-CD15 antibodies. WBCs with nanoparticles were incubated at 37°C for 2h. Results are summarized in Table 4-2, for nanoparticles conjugated to anti-CD45, anti-CD15 or both anti-CD45 and anti-CD15. The condition 200 NP/WBC with both anti-CD45 and anti-CD15 antibodies (400 NP/WBC in total) returns the highest labeling rate, of 87%. Nevertheless, an incubation time of 2 hours could be too long for CTCs and may degrade them, especially since this preparation time is added to the separation

time in both systems and recovered CTCs must be kept alive for further characterization. Thus, a lower duration was investigated, and agitation was added to enhance WBC and NP interactions.

Duration and agitation

WBCs and NP were incubated for 30 min on a microplate thermoshaker with heating at 37°C and agitation at 200 rpm. 100 NP/WBC and 500 NP/WBC were first tested but led to a low labeling rate or a high number of NP agglomerates, respectively. An intermediate ratio of 250 NP/WBC for both anti-CD45 and anti-CD15 antibodies (500 NP/WBC in total) was studied, and a labeling rate of 81% was obtained. Despite the slightly lower rate in comparison with the previous 87% labeling rate obtained with a 2h incubation time and a smaller number of NP/WBC, the priority is to preserve CTC viability. Reducing labeling time to 30 min was therefore a good compromise. Besides, adding an agitation enabled the enhancement of interactions between WBCs and nanoparticles and therefore participated in this achievement. These labeling rate results are summarized in Table 4-2.

Antibodies ratio

As aforementioned, in order to take into account the heterogeneity of CD45 expression among WBCs in circulation, CD15 marker was also targeted. For optimization experiments, anti-CD45 and anti-CD15 were set in the same proportions but CD45 is actually majorly expressed. Thus, a final NP-to-WBC ratio was fixed at 400 NP/WBC for anti-CD45 antibody and 100 NP/WBC for anti-CD15 antibody. A labeling rate as high as 85% could be reached with this ratio. Interestingly, using only anti-CD45-conjugated nanoparticles in a ratio of 400 NP/WBC resulted in a labeling rate of 63%, which confirms the importance of combining both anti-CD45 and anti-CD15 antibodies to target a maximum of WBC population. Results are summarized in Table 4-2 for a labeling duration of 30 min under agitation.

Table 4-2: Labeling rate for different NP-to-WBC ratio conditions at different incubation conditions, either 37°C, 2h, without agitation; or 37°C, 30min, with agitation. The additional agitation enabled the reduction of incubation time by increasing WBC and NP interactions.

NP-TO-WBC RATIO		LABELING RATE (%)
Anti-CD45	Anti-CD15	
Duration and agitation: 37°C – 2h – no agitation		
100 NP/WBC	–	70
–	100 NP/WBC	61
100 NP/WBC	100 NP/WBC	78
200 NP/WBC	–	77
–	200 NP/WBC	65
200 NP/WBC	200 NP/WBC	87
Duration and agitation: 37°C – 30min – 200 rpm agitation		
100 NP/WBC	100 NP/WBC	50
500 NP/WBC	500 NP/WBC	82
250 NP/WBC	250 NP/WBC	81
400 NP/WBC	100 NP/WBC	85

Medium

Finally, the medium had also to be optimized. Indeed, WBCs were initially labeled in a PBS solution, but it appeared that after a certain time of incubation WBCs would aggregate to each other resulting in channel clogging during injection (Figure 4.3-A). To prevent WBCs from aggregating, the PBS solution was supplemented with 2 mM ethylene diamine tetra-acetic acid (EDTA) and 2% bovine serum albumin (BSA) (Figure 4.3-B). EDTA is often encountered in cell preparation protocol to prevent cation-dependent cell-cell adhesion [39–41].

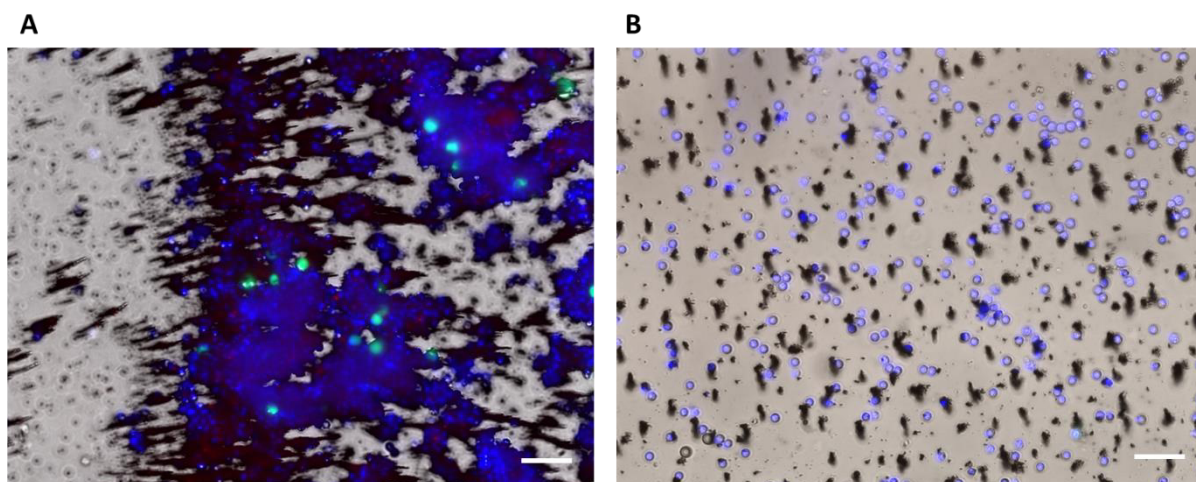


Figure 4.3: EDTA solution to prevent WBC from aggregating during magnetic labeling step. (A) Channel clogging due to WBC agglomerate (in blue) formation during incubation in a PBS solution. mCTC (in green) found themselves stuck in these agglomerates. (B) Dissociation of WBC clumps thanks to a PBS solution supplemented with EDTA. Scale bars are 50 μm .

Finally, a fluorescence picture of the characteristic magnetic labeling of WBCs is given in Figure 4.4, with the following final labeling conditions: 400 NP/WBC and 100 NP/WBC for anti-CD45- and anti-CD15-conjugated nanoparticles, respectively; 30 min incubation at 37°C under agitation in a PBS solution supplemented with 2mM EDTA and 2% BSA. Over the hundreds of observed WBCs, 85% of them were labeled.

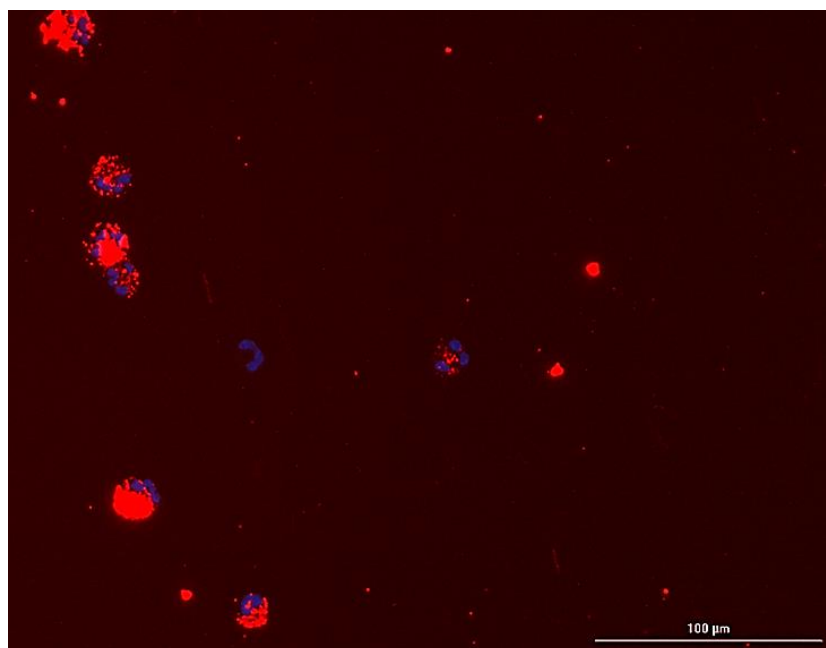


Figure 4.4: Fluorescence microscope image of labeled WBCs (nucleus stained in blue) whose surface is studded with magnetic nanoparticles (in red). Different level of labeling can be observed depending on surface marker expression. Excessed nanoparticles can also be found.

2.2. Optimization of the magnetic chip

Several avenues were investigated to optimize the magnetic chip and enhance WBC capture, from the increase of magnetic micro-trap density and magnetization to the design of a large microfluidic chamber and the determination of the operation flow rate to reach the highest capture efficiency.

2.2.1. Enhancement of micro-magnet properties

Two levers can be particularly easy to implement for micro-magnet trapping enhancement: (i) micro-magnet density and (ii) micro-magnet magnetization.

Micro-magnet density

Increasing NdFeB particle loading within the composite membrane enables to reach a higher density of micro-magnets, therefore improving trapping capacity of the magnetic chip. The initial concentration of 2 wt% of NdFeB magnetic powder was then increased to 3 wt% and 4 wt%. Optical microscopy study was conducted to determine micro-magnet 2D properties (density, diameter, and nearest neighbor distance) according to NdFeB particle concentration. The effect of the particle concentration can be found in Figure 4.5. Increasing the concentration resulted in a higher micro-magnet density and lower nearest neighbor distance (nnd), while micro-magnet diameter is kept constant at approximately 5 μm . A 4 wt% concentration enabled to reach a density as high as 1500 micro-magnets/ mm^2 and a nnd of 15 μm . This nnd value is compatible with the average sizes of WBC and CTC, of $\sim 8 \mu\text{m}$ and $\sim 14 \mu\text{m}$, respectively. Trapped WBCs on micro-magnet surface do not prevent other WBCs from being captured and CTCs from flowing by obstructing their path. Thus, particle concentration was set to 4 wt%.

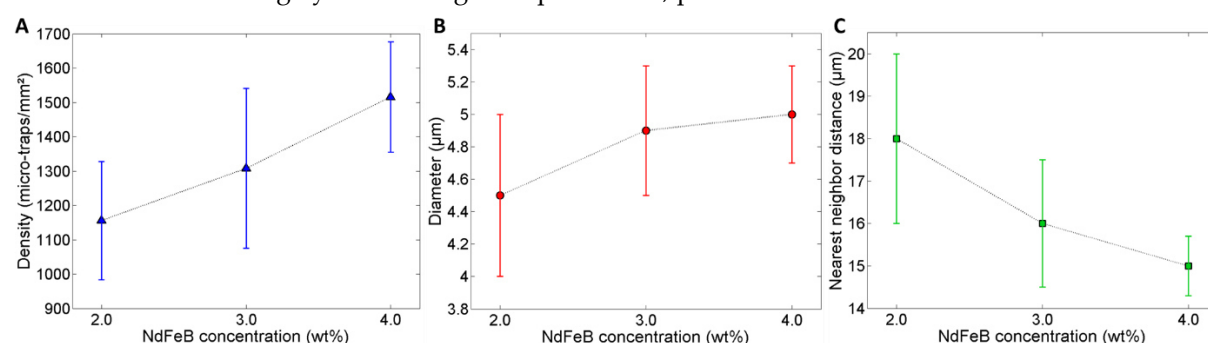


Figure 4.5: Micro-magnet characteristics as a function of NdFeB particle concentration. Impact on (A) Micro-magnet density, (B) micro-magnet diameter, (C) nearest neighbor distance.

Micro-magnet magnetization

As aforementioned, micro-magnet remanent magnetization was increased by designing a new magnetizing system which generates a magnetic field of 1.2 T. This new in-house magnetizing system allows for a 30% increase of micro-magnet remanent magnetization, reaching 0.7 T. Characteristics of both designed magnetizing systems and resulting magnetizations are summarized in Table 4-3. Detailed study was reported in Chapter 3 (part 2.4).

Table 4-3: In-house magnetizing system characteristics and effect on micro-magnet magnetization. The new designed system leads to a higher micro-magnet magnetization.

	Former magnetizing system	New magnetizing system
Dimensions (mm^3)	20 x 20 x 10	50.8 x 50.8 x 25.4
Generated magnetic field (T)	1	1.2
Micro-magnet remanent magnetization (T)	0.54	0.7

2.2.2. Conception of a microfluidic chamber with high trapping capacity

Large surface chamber had to be designed to allow for high trapping capacity of WBCs. The median number of WBCs remaining at the output of the size-based separation ClearCell FX1 system was estimated at 300,000 WBCs, and the maximum number could reach 1,000,000 for certain patients. The

trapping density should therefore be of at least 10^6 . Besides, the dimensions of the chamber should be compatible with the current glass slide format ($25 \times 75 \text{ mm}^2$). Finally, the chamber dimensions were fixed at $40 \times 20 \text{ mm}^2$, providing a trapping density as high as 1.2×10^6 traps.

Chamber mold was obtained by UV lithography (UV-KUB 2, Kloe) using plastic masks. This approach allowed several chamber geometries to be tested since about designs could be loaded on the A4 plastic sheet in a fast and cost-effective way. Several requirements had to be considered:

- Develop a large surface chamber as high as 800 mm^2 to integrate a high micro-trap density ($>10^6$ traps).
- Optimize the liquid filling within the chamber and limit air bubble formation through the use of parallel input microchannels.
- Integrate support pillars to avoid the collapse of the chamber roof due to the large ratio (>10) between the chamber width and height ($100 \mu\text{m}$).

Chamber designs were rendered in KLayout (v. 0.25.5). In particular, several chamber parameters were varied to fulfill these requirements, including (i) the number of input and output channels in a series, (ii) their bent geometries, as well as (iii) support pillar shape. The number of channel input in a series was varied between 2 and 3 to ensure an optimized liquid filling within the chamber. The number of channel output in a series was varied between 1 and 2 to ensure an optimized sample collection. Furthermore, two channel bent geometries were tested, showing either a 90° or a 120° orientation. Finally, support pillar with either circular or diamond-like shapes were tested. Examples of tested chamber designs are reported in Figure 4.6. It is interesting to note that the chamber was designed with round corners to reduce bubble formation.

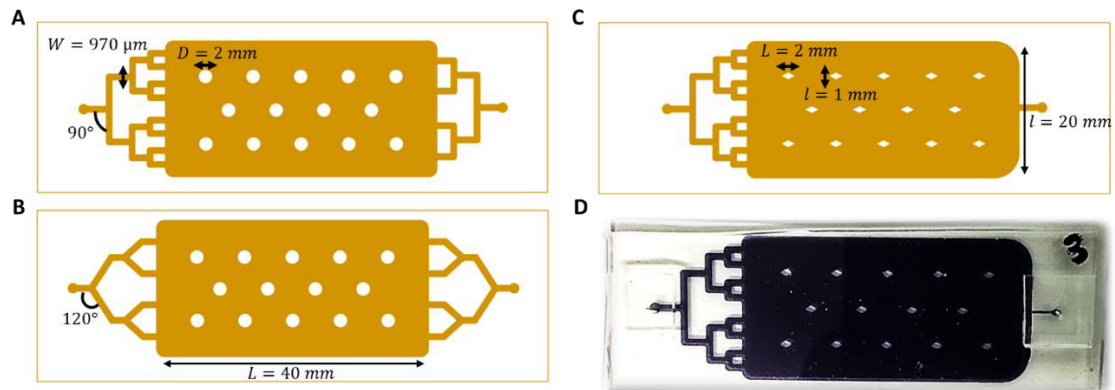


Figure 4.6: Examples of tested chamber designs. **(A)** Three input channel levels and two output channel levels in a series with a 90° bent. Support pillars are circular with a diameter of 2 mm. **(B)** Two channel levels in a series for both input and output with a 120° bent. **(C)** Three input channel levels in a series and one single straight output channel. Support pillars have a diamond shape with a size of $2 \times 1 \text{ mm}^2$. All channels are $970 \mu\text{m}$ wide. The trapping chamber is 20 mm wide and 40 mm long. **(D)** Chosen design with ink-filled chamber.

The different channel designs were tested by first injecting colored ink to check for the chamber sealing and liquid filling, and then by injecting beads to study their circulation within the chamber. Finally, the chosen design is the one represented in Figure 4.6-C and Figure 4.6-D for the following reasons. First, the three-channel input stages allow for a simultaneous chamber filling with a good repartition of the liquid and no bubble formation, regardless of the angle geometry. The 90° bent geometry was later favored since it offers a more compact size. Second, diamond support pillars were selected since they lead to a smaller bead path deviation in comparison with circular ones. Third, the single straight output channel ensures the collection of the whole sample in a simple way. Nevertheless, despite all these microfluidic design optimizations, a certain expertise is still needed to handle the chip and anticipate potential injection issues specific to microfluidic (such as air bubble formation).

This design was further used for chamber mold fabrication and WBC trapping experiments. After selecting the optimal chip design, next step was to assess the operating flow rate to ensure efficient WBC trapping and cancer cell recovery.

2.2.3. Determination of the operating flow rate

To determine the experimental conditions of the magnetic chip, the flow rate for sample injection was optimized. The influence of the flow rate on trapping efficiency was studied since the drag force is the main force opposing the magnetic force. The injection was controlled in pressure and the exact flow rate was determined after each experiment from the collected volume and injection duration. Pressure ranged between 4 and 9 mbar for corresponding flow rates comprised between 1.5 and 5.5 mL/h (0.21-0.76 mm/s speed range). Each experiment at a fixed flow rate was repeated at least five times for reproducibility study. Cell samples consisted of 300,000 magnetically labeled WBCs and 20,000 A549 cancer cells (referred to as mCTCs for mimicking CTCs), suspended in a volume of 300 μ L. Details on the experiment protocol can be found in chapter two (part 4.1).

After injection, WBC capture and mCTC recovery efficiencies were determined as follows:

$$\text{Capture efficiency (\%)} = \frac{N_i(\text{WBCs}) - N_f(\text{WBCs})}{N_i(\text{WBCs})} \times 100$$

$$\text{Recovery efficiency (\%)} = \frac{N_f(\text{mCTCs})}{N_i(\text{mCTCs})} \times 100$$

With N_i and N_f the initial number and final number of targeted cells, respectively. WBCs and mCTCs were discriminated by their emitted fluorescence, blue for WBCs (Hoechst staining) and green for mCTCs (CellTracker™ green staining).

The cell sample injection protocol was improved to ensure the injection of all cells which can be hindered by cell sedimentation in the input reservoir, especially for mCTC which are bigger. This phenomenon was limited by reducing the injected sample volume to 300 μ L and injecting pluronic (300 μ L) when the majority of the sample was injected into the chip and only a few microliters remained in the input reservoir. This step enabled the resuspension of sedimented cells at the bottom of the reservoir which were not injected for subsequent processing within the magnetic chip. In addition, the shape of the input reservoir turned out to have an influence on cell injection. A conical shape (1.5 mL Eppendorf tube) was preferred to a round shape (2 mL Eppendorf tube) since cells were all located at the very tube bottom where the inlet tubing is positioned.

Besides, the cell counting technique was also much discussed as we did not have the equipment to count all cells in this volume and at such low concentration for A549 cells, especially since cells should be collected for downstream analysis. We finally opted for KOVA slide counting, a standard procedure which consists in withdrawing 10 μ L from the sample for enumeration within a 10-chambered slide with counting grids. Due to this small volume in comparison with the output volume (600 μ L), two to three counts were performed so as to get an overall view of cell concentration. Another counting strategy was investigated using ULA 96-well plates. The collected volume was dispatched in three wells (150 μ L/well) and the plate was centrifuged at 500g for 5min to concentrate the cells at the well bottom. The three wells were then scanned using LionHeart Biotek automated microscope and cells were discriminated based on their fluorescence (blue: WBC, green: A549). Due to the low adherence nature of the well plate, cells could then be retrieved for downstream analysis. Nevertheless, this strategy was more time-consuming and required more attention regarding the counting accuracy (difference in cell focus and in sedimentation time between A549 cells and WBCs, etc). KOVA slide counting was therefore identified as the most reliable technique at our disposal.

The WBC capture efficiency and the mCTC recovery efficiency at different flow rates are shown in Figure 4.7. WBC capture efficiencies reached 88, 84, 72, and 53% at 1.5, 2.0, 2.5, and 5.5 mL/h, respectively; while mCTC recovery efficiencies reached 66, 79, 80, and 83%, respectively. It can be observed that increasing the flow rate diminishes capture efficiency but improves mCTC recovery. Indeed, capture efficiency decrease can be explained by the higher drag force competing with the magnetic force. Regarding recovery increase, faster injection time prevents cell sedimentation in the input reservoir prior to injection. Injection time of approximatively 15-20 min for flow rates comprised

between 2 and 2.5 mL/h was achieved. Cell sedimentation phenomenon could be even more reduced by providing a smooth agitation to the input reservoir containing the cell sample to inject.

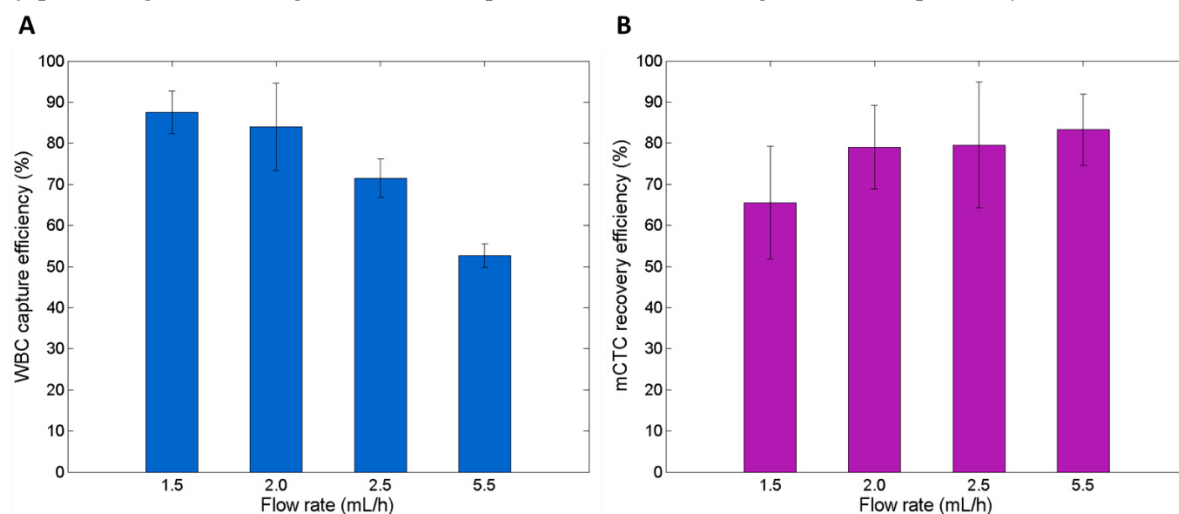


Figure 4.7: Performances of the magnetic chip. (A) WBC capture efficiency and (B) mCTC recovery efficiency as a function of the flow rate.

Finally, the size-independence of the magnetic chip separation was demonstrated by studying the recovery efficiency of MCF-7 cancer cells which present a slightly larger cell diameter than A549 cells (average diameter 19 μm against 16 μm) [42]. Experiments were performed at 2 mL/h. Comparison with A549 results are shown in Figure 4.8. Similar recovery efficiencies were achieved by the magnetic chip, reaching $82 \pm 8\%$ and $79 \pm 10\%$ for MCF-7 and A549 cells, respectively. Besides, WBC capture efficiencies were also consistent: $88 \pm 9\%$ and $84 \pm 11\%$ for spiked MCF-7 and A549 cells, respectively. Thus, the magnetic chip enables size-independent sorting, in combination with tumor marker-independent separation, therefore showing the versatility of the magnetic chip.

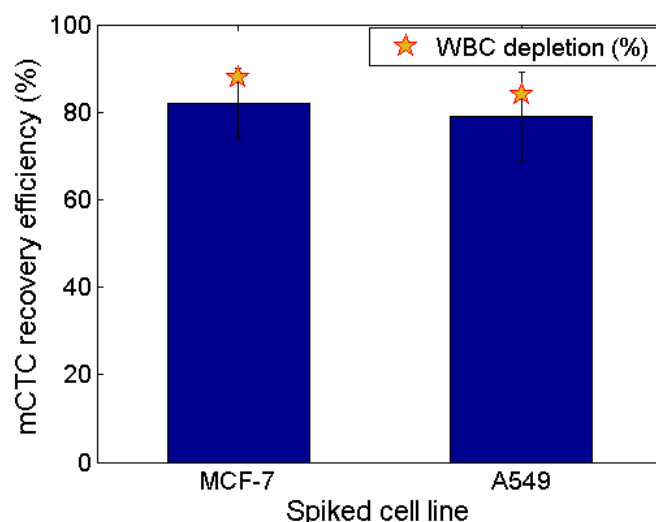


Figure 4.8: Recovery efficiency for two different spiked cell lines, MCF-7 and A549 cancer cells at a flow rate of 2 mL/h. Consistent recoveries were obtained regardless of cancer cell sizes. Similar WBC capture efficiencies were also achieved.

To put in a nutshell, at a processing flow rate of 2 mL/h (corresponding speed of 0.28 mm/s), WBC depletion efficiency of $\sim 86 \pm 10\%$ was achieved. From an initial number of 300,000 WBCs (median ClearCell FX1 system output), 15,000 to 80,000 WBCs remains after the magnetic purification, leading to high mCTC-to-WBC ratio, comprised between 1:1 and 1:5 for A549 cells. Indeed, from an initial 1:15 ratio (mCTC:WBC), the magnetic purification step within the microfluidic chip increased this ratio by a

factor 5 or 8 for A549 or MCF-7 experiments, respectively. Performances of the magnetic chip are summarized in Table 4-4.

Table 4-4: Performances of the magnetic chip for mCTC isolation. 20,000 mCTCs and 300,000 WBCs were processed at a flow rate of 2 mL/h.

Spiked cell line	Final WBC number (x10 ³)	Capture efficiency (%)	Recovery efficiency (%)	Average mCTC:WBC ratio ¹
A549	48 ± 33	84 ± 11	79 ± 10	1:3
MCF-7	36 ± 27	88 ± 9	82 ± 8	1:2

¹Initial ratio of 1:15. Final ratio calculated from the mean of mCTC and WBC final numbers.

We have determined the operating flow rate and optimized procedure providing the greater WBC capture and mCTC recovery. The magnetic chip enabled the isolation of mCTC and hence could be used as a diagnostic/prognostic tool by detecting CTC counts. Nevertheless, it is also of first interest to ensure that recovered mCTC are viable so as to conduct subsequent characterization analyses.

3. Downstream analysis after magnetic-based separation

The compatibility of the magnetophoretic separation device with subsequent analyses were investigated. Cell samples (300,000 WBCs and 20,000 spiked A549) were processed at a flow rate of 2 mL/h and A549 cancer cells were further collected to perform routine biological studies. The compatibility of the magnetic chip with these studies was evaluated by looking at cancer cell viability, integrity, their spheroid formation ability, as well as their genotype signature preservation.

3.1. Study of cancer cell viability

The viability of collected A549 cancer cells was investigated after the magnetophoretic separation using a Live/Dead assay. The device-operating parameters were chosen to be the same as those used in the aforementioned experiments. After processing the cell sample through the magnetic chip at a flow rate of 2 mL/h, cancer cells were collected and cultured in a 96 well-plate in culture medium for 48h until reaching pre-confluence. Control A549 cells, i.e., which were not run through the chip, were also seeded in the same conditions (live control cells).

For the Live/Dead assay, cancer cells were stained with 2 µM calcein-AM and 4 µM EthD-1 for 30 min in the incubator. Death control cells were then exposed to 10% Triton-PBS solution for 10 min. Next, cell fluorescent signal was measured: cancer cells with a calcein-AM+/EthD-1- staining pattern were counted as live cells, whereas cells with calcein-AM-/ EthD-1+ staining patterns were counted as dead cells. The discrimination of the two populations was assessed thanks to fluorescent signal measurement within live and death control A549 wells. Representative fluorescence images of collected cancer cells and control A549 cells are shown in Figure 4.9. The magnetic chip enabled reaching an 81% cell viability (~1000 analyzed fluorescence cancer cells) after 48h of cell culture, which is consistent in comparison with the 91% viability of control cells which were not run through the chip. The 10% decrease in cell viability can have various sources. Contrary to control A549 cells which were kept in the incubator at 37°C and without any WBC, processed A549 cells at room temperature were subjected to prolonged interactions with WBCs. Spiked A549 cancer cells represent foreign cells to WBCs (obtained from healthy donors), thus, secreted proteins could harm A549 cell line. In addition, cell circulation within the magnetophoretic microsystem and injection tubing can represent a source of stress for A549 cancer

cells. Nevertheless, despite all these potential harmful sources for A549 cells, they were collected with a good viability.

Capacity of recovered A549 cancer cells to grow for several days in either 2D or 3D culture, in the presence of untrapped WBCs, will be explored later.

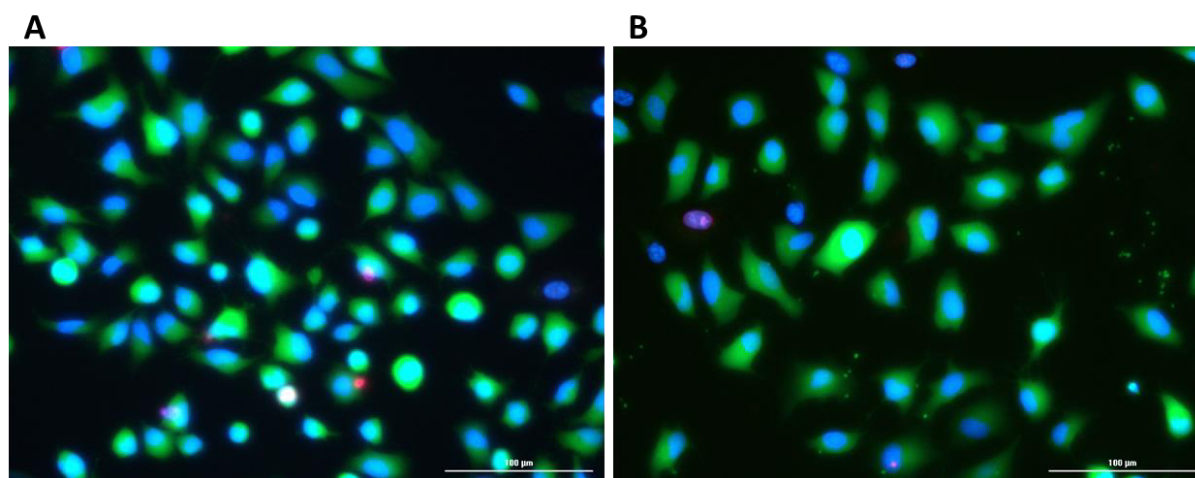


Figure 4.9: Representative fluorescence images of Live/Dead cell staining after 48h culture for (A) control A549 group and (B) recovered A549 cancer cells after magnetic chip processing. Cell viabilities of the control group and recovered cancer cells were determined to be 91% and 81%, respectively. Scale bar is 100 μm .

3.2. Study of cancer cell integrity

Not only cancer cell viability was studied but also cancer cell integrity was determined using immunofluorescence assay. Cell samples were processed through the magnetic chip at a flow rate of 2 mL/h and collected cells were stained with DAPI for nucleus staining, anti-CD45/anti-CD15/anti-CD41 antibodies for WBC targeting, and Phalloidin for F-actin cytoskeleton staining. Recovered A549 cancer cells could be differentiated from WBCs based on Phalloidin-positive (Phalloidin+), CD45/CD15/CD41-negative (CD45-/CD15-/CD41-) and DAPI positive (DAPI+). Interestingly, WBCs showed a lower expression of Phalloidin since Phalloidin binds preferentially with F-actin and both F-actin and G-actin are present within WBC. G-actin (or globular actin) is a monomeric actin which polymerizes into actin filaments (F-actin). Unpolymerized G-actin is highly expressed within WBCs and diffuses within WBCs, as well as in many other nonmuscle cells, in order to ensure the availability of actin subunits for subsequent polymerization into F-actin at specific sites when the conditions are met [43]. Depolymerization of F-actin later occurs at sites where they are no longer required. Dynamic polymerization and depolymerization processes account for WBC actin cytoskeleton plasticity, and therefore WBC motility [44], which is crucial to their role in defensive mechanisms of the body. These processes are therefore responsible for the observed lower F-actin expression within WBC cytoskeleton.

Several morphological characteristics of recovered cancer cells were established from DAPI and Phalloidin fluorescence signal measurements, these being cell nucleus and cytoplasm sizes, nuclear-cytoplasmic ratio (N:C ratio), and circularity. Nucleus size was determined from DAPI measurement while cytoplasm size was calculated from Phalloidin measurements. Measured morphological characteristics were compared to the ones obtained from control A549 cells (no processing within the magnetic chip). Fluorescence images of control cells and collected cells are reported in Figure 4.10. It is worth mentioning the highly purified samples obtained after the magnetic chip (Figure 4.10-B) in comparison with spiked control A549 cells in unpurified WBC sample (Figure 4.10-A). Indeed, both samples had same WBC concentrations (1,000 WBCs/ μL) but the one processed within the magnetic chip enabled WBC depletion (180 WBCs/ μL). On the contrary, unprocessed sample shows a high number of background cells. These prior observations testify the need to achieve high purity for separation devices so as to facilitate subsequent analysis and enable CTC characterizations.

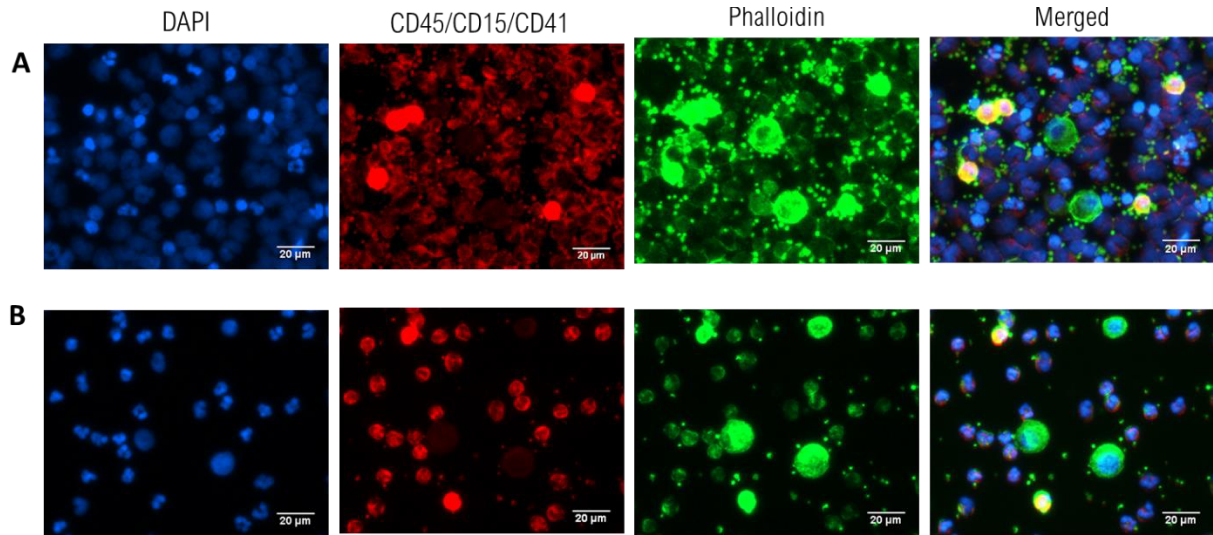


Figure 4.10: Immunofluorescence staining for (A) control group (no purification step) and (B) recovered cells after magnetic separation. A549 cancer cells are determined according to DAPI+/CD45-CD15-CD41-/Phalloidin+. Benefit of the magnetic purification can be seen on the removal of excess background cells. On the control image (A), 2 A549 cells surrounded by ~100 background cells can be visualized (2% of cancer cells). On the collected sample post magnetic purification (B), 3 A549 cells and ~30 background can be observed (10% of cancer cells).

Regarding cancer cell integrity preservation, morphological characteristics on 1,500 and 1,000 control and chip output cells, respectively, were measured. Results are reported in Figure 4.11. It can be observed that for cytoplasm size and circularity, similar values were obtained for isolated cancer cells and control group. One can notice that the nucleus size for output cells appears slightly smaller than that of control cells. However, these values remain consistent with reported values for A549 nucleus size. In particular, the N:C ratio of recovered cancer cells determined using an immunofluorescence staining (0.61 ± 0.11 for A549) is consistent with values obtained using imaging flow cytometry (0.67 ± 0.07 for PC-3 [45]). N:C ratio has become a commonly accepted parameter in tumor staging and grading since CTCs generally exhibit a high N:C ratio.

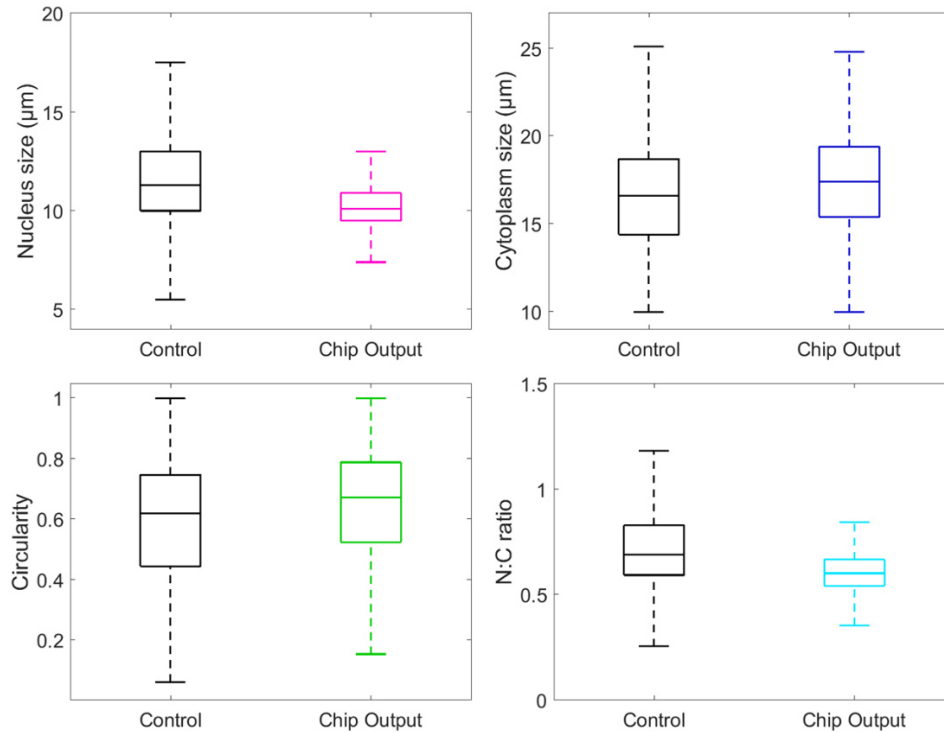


Figure 4.11: Morphological characteristics obtained from immunofluorescence staining. Nucleus and cytoplasm sizes were determined by DAPI and Phalloidin fluorescent signals, respectively. 1,500 and 1,000 A549 cells were analyzed for control and chip output conditions, respectively.

To put in a nutshell, this immunofluorescence assay enabled to assess the preservation of isolated cancer cell integrity after processing through the magnetic chip. In particular, the study demonstrated the benefit of the purification step to remove excess background cells, therefore facilitating CTC detection. In addition, the commonly employed N:C ratio criteria for CTC identification could be calculated. All these elements assess the compatibility of the magnetic chip with routine biological analyses.

3.3. Long-term 2D cell culturing

Long-term cell culturing and viability were investigated after magnetic purification. The device-operating parameters were the same as those used in previous experiments. Recovered cells were centrifuged and resuspended in culture medium at a concentration of 50 A549 cells/ μL . This value was chosen so as to be compatible with 96-well plate format requiring an initial seeding density of $\sim 10^4$ cells and growth medium volume of approximately 100-200 μL . A549 control cells (no magnetic purification, incubated at 37°C without WBCs) were also seeded in similar conditions. Cell medium renewal was performed every two days, removing by the same way remaining non-adherent WBCs. Cell growth was followed by taking optical images every day for 10 days using the automated BioTek Lionheart FX imaging system. As reported in Figure 4.12, recovered cancer cells succeeded in re-adhering and proliferating after the purification step within the magnetic chip, likewise control cells. In particular, it can be seen in Figure 4.12-D the presence of both adherent cells (elongated shape) and dividing cells (round shape) which accounts for cell good viability and favorable culture conditions for cell proliferation. The presence of cellular clusters also assesses ongoing cell division.

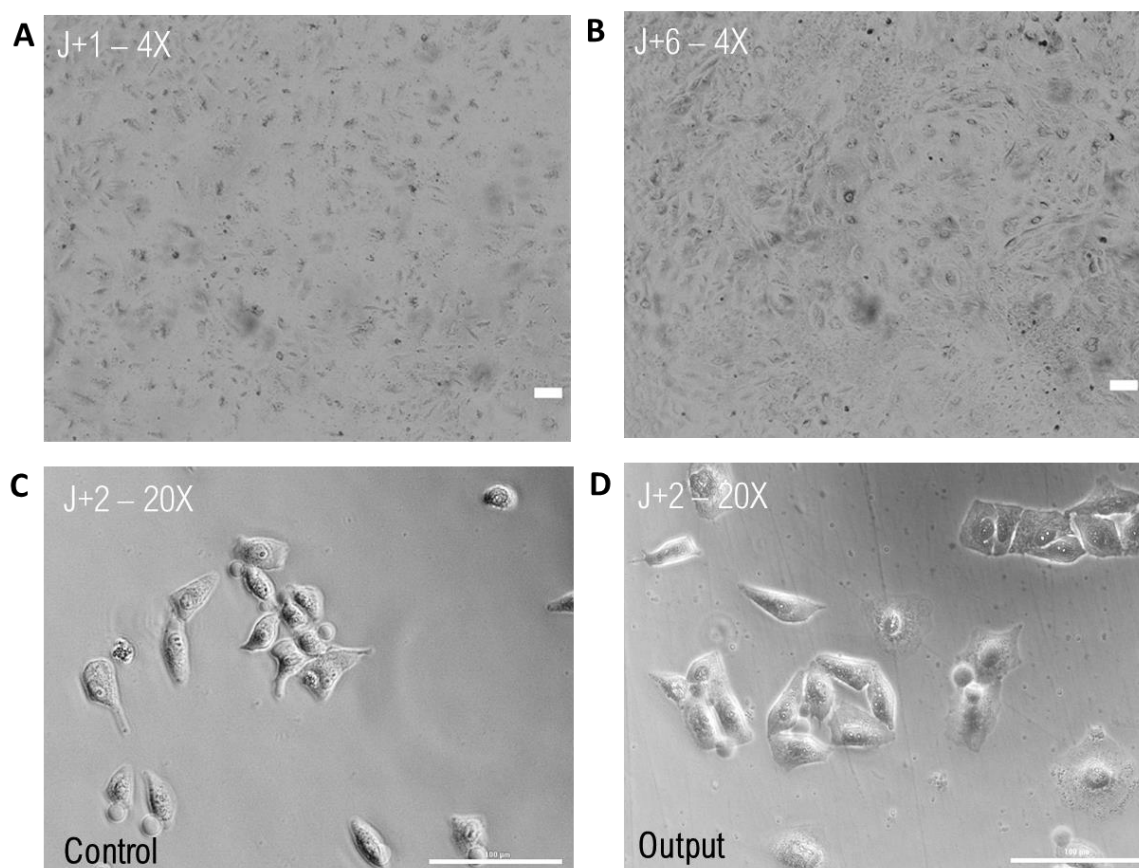


Figure 4.12: Cell culturing of recovered cells in 96-well plate format. (A), (B) Phase contrast images (4X objective) after (A) one day and (B) six days of cell culture. Processed cells within the magnetic chip managed to re-adhere and proliferate. (C), (D) Phase contrast images (20X objective) after two days of cell culture for (C) control group and (D) purified sample. Recovered cancer cells show identical morphology to the one of control cancer cells. Scale bars are 100 μm .

Furthermore, the long-term cell viability was studied using Live/Dead assay. Cell sample was processed within the magnetic chip and put in culture for a week. Live/Dead assay was then performed, and viability rate was compared to control group. Viabilities of 93% and 94% were observed for control A549 and recovered A549 after magnetic chip purification, respectively. Labeled cells using the Live/Dead kit are represented in Figure 4.13.

To conclude, successful 2D cell culture was achieved after the purification step through the magnetic chip. Recovered cancer cells were able to re-adhere and proliferate for 10 days, with 94% of viability at day 6. The magnetic chip is therefore harmless for cells and compatible for subsequent cell culturing.

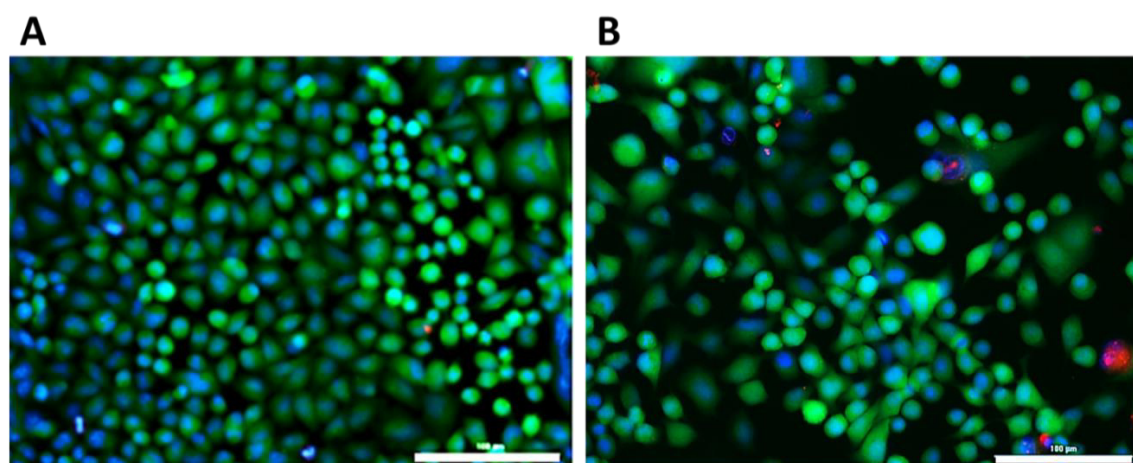


Figure 4.13: Representative fluorescence images of Live/Dead cell staining after 6 days of cell culture for (A) control A549 group and (B) recovered A549 cancer cells after magnetic chip processing. Scale bars are 100 μm .

3.4. Spheroid formation

In addition to 2D cell culturing, recovered cancer cells were cultured in 3D using ultra-low attachment (ULA) round bottom 96-well plate and cancer cell spheroid formation was investigated. Spheroids, which refer to three-dimensional aggregates of cells, have emerged as better models to mimic the 3D conformation of the tumor structure [46]. Indeed, spheroids have a characteristic layer-like structure consisting of a necrotic core, an inner layer of quiescent cells, and a layer of proliferating cells. As a result, a spheroid has gradients in nutrients, secretions, and oxygen along the spheroid radius. In this regard, spheroid cultures more accurately recapitulate *in vivo* physiological situation than standard 2D cultures. Previous works reported the resistance of spheroids to chemotherapy [47–49] and photodynamic therapy [50,51]; as well as the differential expression of several genes (associated with cell survival, proliferation, differentiation, and resistance to therapy) in cells grown as spheroids as compared to 2D monolayers [52–54]. Thus, spheroid formation is highly relevant for the establishment of drug resistance and testing of novel therapeutic targets.

The compatibility of the magnetic chip with subsequent 3D cell culture was studied and A549 cancer cell line was used for cancer cell spheroid formation. After processing through the magnetic chip, recovered cells were centrifugated and resuspended in filtered culture medium at a concentration of 50 A549/ μL . Three replicates were performed for reproducibility. Protocol for cell culturing in ULA 96-well plate is reported in Chapter 2, part 4.2. Control A549 cells were also prepared (37°C incubation without WBCs). Each well contained an initial number of 5000 A549 cancer cells. Spheroid growth was monitored for 7 days and imaged with BioTek Lionheart FX system. Representative images of formed spheroids over days are reported in Figure 4.14. Recovered A549 cancer cells self-agglomerated to form compact spheroids. In particular, the evolution of spheroid growth over days was studied by calculating spheroid area. Spheroid area was determined using ImageJ software for image processing. Comparison of spheroid area values obtained from recovered cells after magnetic purification through the chip and control values can be found in Figure 4.14-C.

It can be observed that formed spheroids present a similar growth pattern as the control group, with a growth reduction between 4 and 5 days of culture. It demonstrates spheroid compaction, a cellular arrangement naturally occurring during spheroid formation. Indeed, at first cells form loose aggregates, but direct cell-cell contact results in upregulated cadherin expression, which promotes strong adhesion of initial cell aggregates. After this delay phase during which homophilic binding occurs between cadherins of peripheral cells, cells are compacted into solid aggregates to form spheroids due to this homophilic cadherin-cadherin binding [55,56]. Finally, at day 7, a 20% spheroid area increase was observed, therefore demonstrating spheroid growth. Thus, spheroid formation can be described as a three-step process: (i) initial cell aggregation, followed by (ii) spheroid compaction and, finally, (iii) spheroid growth [57]. The lower measured spheroid area for the chip output compared to the control group could be explained by the variability in cell counting and spiking (few microliters compared to milliliter volume).

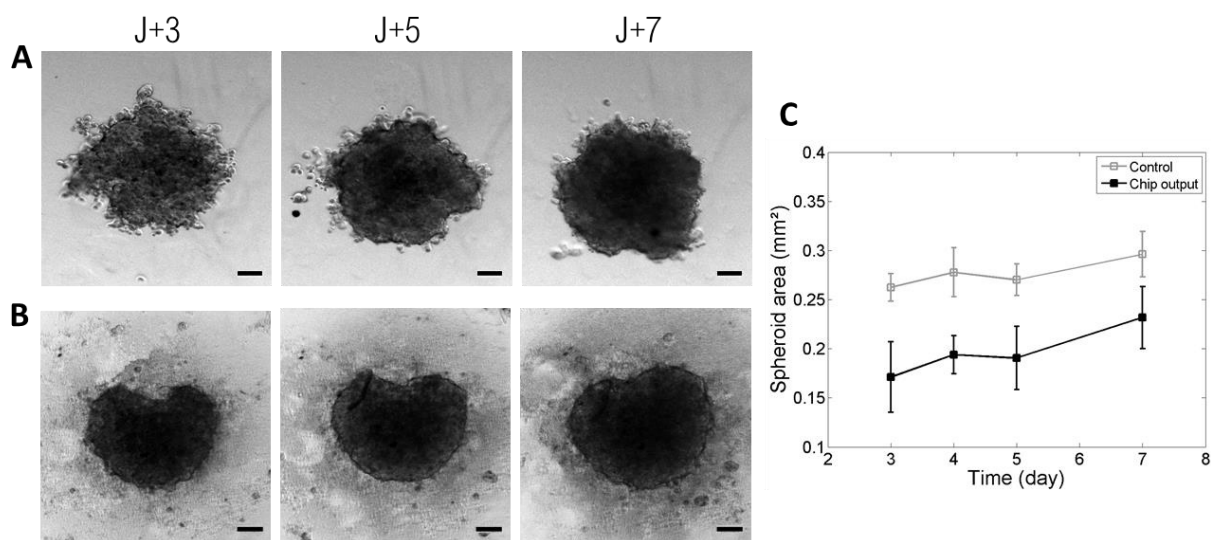


Figure 4.14: A549 cancer cell spheroid culture for 7 days. Similarly to (A) the control group, (B) recovered cells could be cultured as spheroids during 7 days (in grey background, the excess of magnetic nanoparticles). Scale bars are 100 μ m. (C) Evolution of spheroid area over 7 days. Spheroids obtained from recovered A549 cells show similar growth pattern as control spheroids.

Furthermore, the self-agglomeration phenomena of recovered cancer cells was more deeply studied by labeling A549 cells with CellTracker™ green before being processed through the magnetic chip and imaging spheroid formation in fluorescence. Merged phase contrast and fluorescence images are shown in Figure 4.15. The agglomeration phenomena of A549 cancer cells between the day of processing within the magnetic chip (day 0) and the next day (day 1) appears clearly. In addition, spheroid compaction can be observed from day 3, revealing cell-cell adhesion and intact actin cytoskeleton [57]. Thus, even in the presence of remaining WBCs that were not trapped in the magnetic chip, as well as excess magnetic nanoparticles (dark background visible behind spheroid), collected A549 cells were able to form spheroids and proliferate. Besides, it should be mentioned that careful manipulation is required when renewing culture medium (half of it is replaced by fresh medium). This step, conducted every two days, may result in cellular detachment from the spheroid as occurred at day 6 in Figure 4.15.

It is worth mentioning that spheroid formation has been challenging since many parameters could influence their proper culture. Among them were identified the number of A549 cell passages, the choice of fetal bovine serum, as well as the medium renewal step as previously mentioned. Successful spheroid formation rate reached 70% of 7 trials.

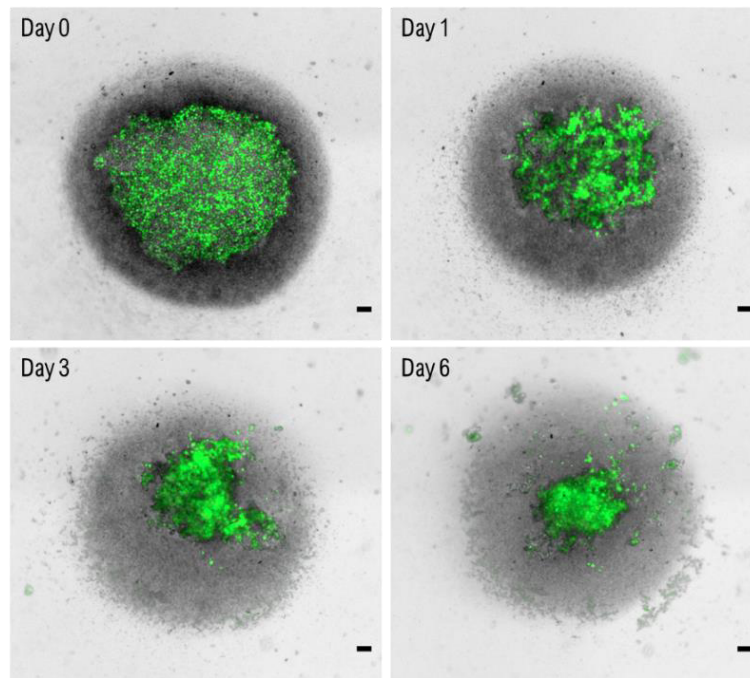


Figure 4.15: Monitoring of recovered A549 cells (CellTracked in green) agglomerating to form spheroid (initial concentration: 5000 A549/well). The day after the magnetic purification, cancer cells form a compact spheroid. Spheroid shrinkage is observed from day 3 revealing cell viability. Cellular detachment can be observed in day 6 which results from tricky manipulation during medium renewal. Scale bars: 100 μm .

Finally, long-term culture of spheroids was investigated. Recovered A549 cells were cultured for 20 days, and evolution of the spheroid area was monitored (Figure 4.16). Spheroid area reached 0.7 mm^2 after two weeks before decreasing. Indeed, from a certain point, the necrotic core starts sending extracellular signals stopping cell proliferation and leading to apoptosis. Thus, the purification step performed by the magnetic chip enabled successful spheroid formation and monitoring for several weeks. Drug sensitivity testing could therefore be considered as another downstream application on recovered cancer cells.

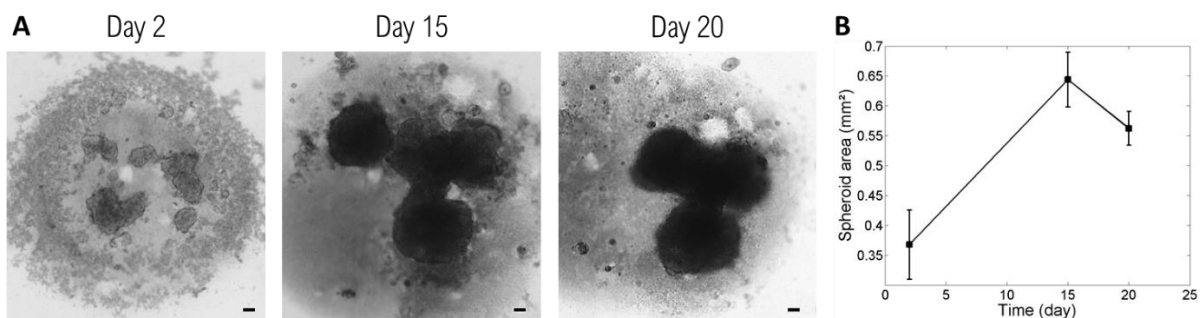


Figure 4.16: Long-term spheroid culture. (A) Spheroid growth imaging and (B) spheroid area monitoring over 20 days. After two weeks of spheroid culture, spheroid area starts to decrease. Scale bars 100 μm .

3.5. Analysis of cancer cell genotype

Fluorescence in situ hybridization (FISH) is a gold standard technique for probing genetic aberrations such as gene rearrangements (translocations, inversions) and changes in gene copy number associated with cancer [25]. For example, FISH is routinely performed on lung cancer tissues to detect EML4 and ALK gene fusion which occurs in 3–7% of NSCLC patients [58]. This detection is crucial since crizotinib is recommended as the first-line standard therapy for these patients (according to the US FDA), improving both the patient's quality of life and overall survival compared to traditional chemotherapy [59,60].

To demonstrate that the magnetic chip provides retrievable CTCs for molecular profiling of individual cells at the chromosomal scale, EML4-ALK Fusion-A549 (A549 EML4-ALK) cell line was employed for the detection of this intrachromosomal translocation by FISH. A549 EML4-ALK cells and WBCs were first processed through the magnetic chip for purification and FISH was subsequently performed recovered cells using CytoCell AKL Breakapart probe kit (for the preparation protocol, see Chapter 2, part 4.5.). The 5' ALK probe was labeled with a red fluorophore and the 3' ALK probe with a green one (Figure 4.17-A). ALK-negative cells (i.e. control WBCs) show an overlapping of 5' (g) and 3' (green) signals, producing a fused 5'3' (yellow signal). ALK-positive cells (spiked A549 EML4-ALK cells) can be identified by a split of the 5' (red) and 3' (green) signal. Cells were scanned on the PANNORAMIC Scan II (3DHISTECH™). Representative images showing molecular FISH analysis in both WBCs and recovered A549 EML4-ALK cells and comparison with unprocessed cells can be found in Figure 4.17-B.

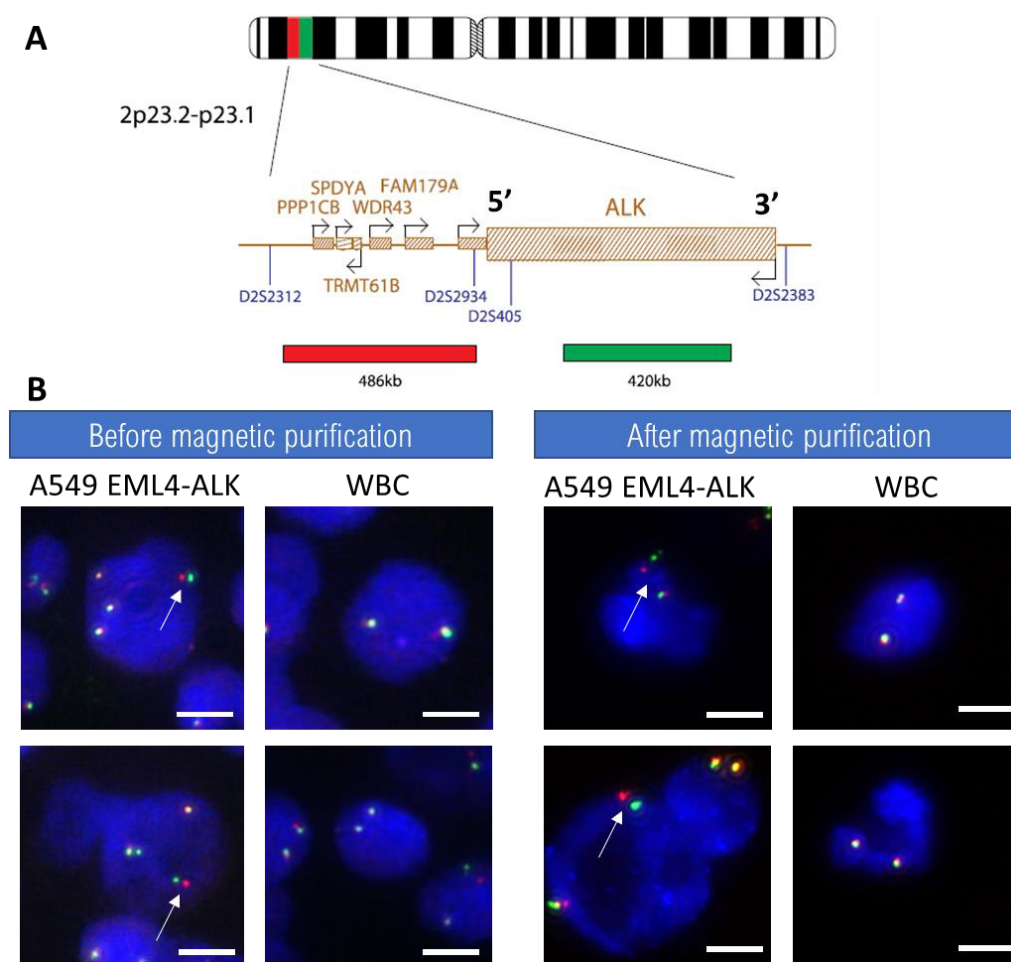


Figure 4.17: Molecular FISH analysis on enriched mCTCs. **(A)** Schematic of CytoCell ALK Breakapart FISH probe (www.ogt.com). **(B)** Images of ALK-positive cells (A549 EML4-ALK) and ALK-negative cells (WBC) before (left) and after (right) magnetic purification step. Cells were stained using CytoCell ALK Breakapart FISH probe and counterstained with DAPI. The distinct separation of red and green signals (arrows) indicates a rearrangement in the 2p23 ALK-gene region in A549 EML4-ALK cells. Scale bar: 10 μm.

Molecular analysis by FISH performed before and after the purification step within the magnetic chip enabled to demonstrate the preservation of EML4-ALK gene fusion in recovered A549 EML4-ALK cells. From this result can be deduced that (i) recovered cancer cells were viable and structurally intact, and (ii) remaining WBCs did not affect the analysis of recovered cancer cells. Thus, the magnetic chip provides purified samples that can be readily investigated via standard genetic analysis, which is usually very difficult to conduct due to the rarity of CTCs and large number of contaminated WBCs. The compatibility of the magnetic chip technology with FISH assay has therefore been assessed for the detection of ALK gene arrangement in mCTCs.

3.6. Summary

In this initial proof-of-concept study, the compatibility of the magnetic chip with a large panel of standard biological studies has been demonstrated. Viability/cytotoxicity assay and phenotypic study revealed that the magnetic purification step allows for the recovery of viable mCTCs with preserved cell membrane integrity. In particular, the achieved WBC depletion facilitates downstream analysis of recovered mCTCs, from long-term 2D cell culturing to spheroid formation and genotype analysis. Based on these results, the developed magnetic chip technology could not only provide rapid diagnosis via CTC detection and enumeration but also represent an efficient tool for the identification of targeted therapies via drug susceptibility testing in spheroid cultures and genotypic aberrations detection.

4. Test of the complete workflow for blood sample processing

The magnetic-based purification device developed here is intended to be the last block of a complete workflow that processes raw blood samples. This part will deal with preliminary tests of the complete workflow, combining size- and magnetic-based separation steps, and the investigation of its performances. The aim of this two-step workflow is to improve CTC/WBC ratio, hence enabling further phenotypic characterizations of recovered CTCs.

4.1. Sample purification

Briefly, the whole workflow (detailed in Chapter 2, part 5) can be divided in the following steps: (i) A549 spiking into whole blood (20 000 mCTCs), (ii) RBC lysis, (iii) size-based enrichment step through ClearCell FX1 system, (iv) magnetic-based purification step through the magnetic chip, and (v) mCTC recovery for downstream analysis. In particular, as aforementioned in Chapter 2, ClearCell FX1 system provides two specific running programs, referred to as P3 and P1, whose enrichment performances will be further detailed.

The number of WBC and A549 was assessed during the process. The initial number of WBC was determined by carrying out an automated blood count from a small volume of the blood sample. For the other steps, WBC and A549 counts were determined using hemocytometer-type grids (KOVA® slides). The whole workflow was performed three times with ClearCell program P3 and twice with program P1. It should be mentioned that each experiment had to be judiciously conducted since one ClearCell cassette costs 200€. The cell viability was ensured during the workflow with Trypan blue staining which determines the number of dead cells. Cell viabilities after the first size-based enrichment step and the second magnetic-based purification step are reported in Figure 4.18. As previously observed, the viability of the cells is little affected by the passage in the chip

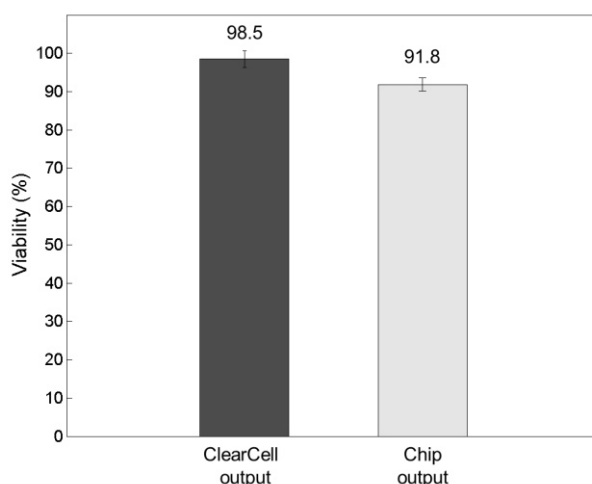


Figure 4.18: Cell viabilities after size-based enrichment step (ClearCell output) and magnetic-based purification step (Chip output). The number of dead cells was assessed by Trypan blue staining.

Output performances of the two-step workflow are reported in Figure 4.19. The number of cells after each separation step was determined by performing one KOVA slide counting. CTC/WBC ratio was then calculated for each step in order to underline the benefit of the two-step separation process.

First, ClearCell program P3 (Figure 4.19-A) enabled to reduce WBC number by a factor 300, from an initial number of $4.6 \cdot 10^7$ WBCs to a remaining number of $1.4 \cdot 10^5$. The mCTC recovery rate of the size-based enrichment step using P3 program reached 55%, leading to a CTC/WBC ratio of 8%. Adding the magnetic chip for further purification resulted in a 3 times higher CTC/WBC ratio, which reached 25%. The mCTC recovery rate of the magnetic-based purification reached 70% (7,900 collected mCTCs out of 11,000) and the depletion efficiency reached 78%. The combination of the two separation methods led to a total depletion rate of 99.93%, with a final number of $\sim 30,000$ WBCs. Subsequent phenotypic and genotypic studies can therefore be performed with low contaminating background WBCs.

Regarding ClearCell program P1 (Figure 4.19-B), it achieved a greater WBC depletion, with $\sim 50,000$ remaining WBCs (against 140,000 with P3), resulting in a CTC/WBC ratio of 40%. This value is particularly high and accounts for the higher recovery achieved with program P1, reaching 95%, in comparison with program P3 (55%). These results are not consistent with tests performed in other studies using ClearCell (chapter 2, part 5.1), where the recovery with the P1 program was about 60% in average [61,62]. It is worth noting that spiking experiments with program P1 were performed only twice and may lack reproducibility. In addition, KOVA® slide counting is not always reliable since one of the two counting for the ClearCell output returned 20,200 A549 (20,000 supposed spiked number). Finally, the subsequent processing through the magnetic chip enabled to reach a 2 times higher number of mCTC than WBC, with 14,000 A549 cells against 7,100 WBCs (74% recovery efficiency and 87% depletion efficiency). The combination of the two sorting methods resulted in a depletion rate as high as 99.99%.

Although CTC counts in patient samples usually ranges between 1-1000/mL of blood, the outstanding CTC/WBC ratio obtained after the magnetic chip paves the way for downstream transcriptomic single-cell studies, such as single-cell RNA-sequencing. Single-cell RNA sequencing, which presents significant challenges including preservation of RNA quality and single-cell mRNA amplification [63], can explore drug resistance mechanisms and elucidate inter- and intra- patient heterogeneity, therefore filling the gap in personalized medicine approach.

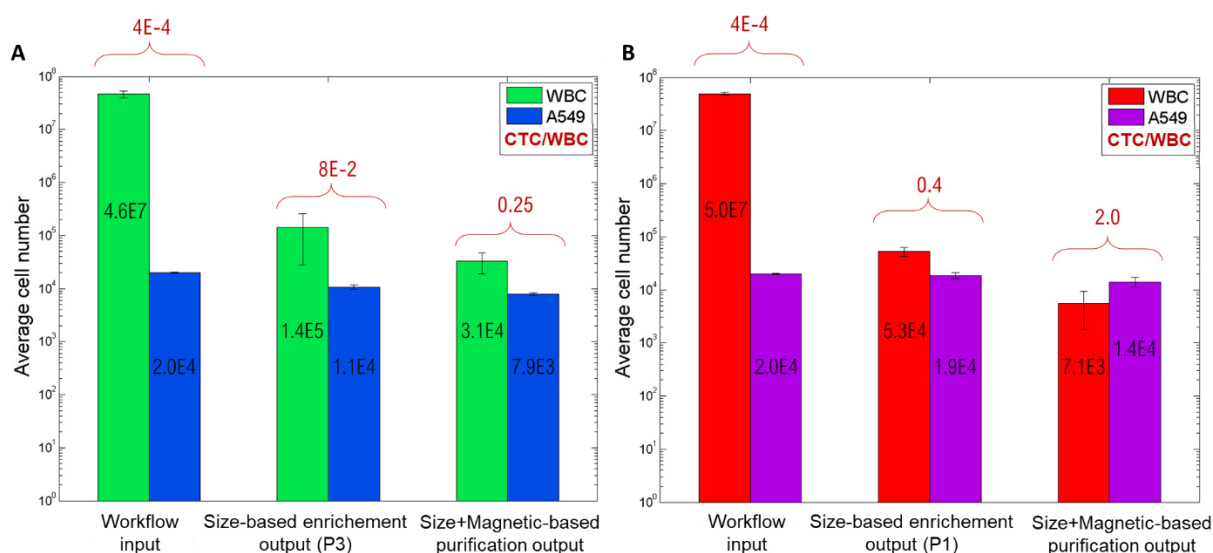


Figure 4.19: Output performances of the two-step workflow. First enrichment step was performed with (A) ClearCell program P3 or (B) ClearCell program P1. Second step consists of purification through the magnetic chip via WBC depletion. CTC/WBC ratio highlights the benefit of the magnetic chip for improved purity.

Furthermore, benefit of the additional magnetic purification step is further highlighted in Table 4-5, where performances of the ClearCell and ClearCell+Magnetic Chip are provided. In particular, purity, WBC log depletion, and enrichment factor were calculated as follows:

$$\text{Purity (\%)} = \frac{N(\text{A549 cells})_{\text{output}}}{N(\text{A549 cells} + \text{WBCs})_{\text{output}}}$$

$$\text{WBC log depletion} = \log \left(\frac{N(\text{WBCs})_{\text{input}}}{N(\text{WBCs})_{\text{output}}} \right)$$

$$\text{Enrichment factor} = \frac{N(\text{A549 cells})_{\text{output}} / N(\text{WBCs})_{\text{output}}}{N(\text{A549 cells})_{\text{input}} / N(\text{WBCs})_{\text{input}}}$$

Interestingly, the additional magnetic purification step enabled improving purity by a factor 1.4 (P3) to 2.5 (P1) and increasing the enrichment factor by 145% and up to 486%, respectively. The whole workflow could be conducted in less than 3 hours, ensuring cell viability preservation for subsequent analysis and culture.

Table 4-5: Benefit of the two-step workflow on separation performances.

	ClearCell P3	ClearCell P3 + Magnetic Chip	ClearCell P1	ClearCell P1 + Magnetic Chip
Separation method	DFF	DFF + Magnetophoresis	DFF	DFF + Magnetophoresis
Selection criteria	Size	Size + CD45, CD15	Size (14 µm)	Size (14 µm) + CD45, CD15
Throughput	8 mL/h	5.75 mL/h*	4 mL/h	3.5 mL/h*
Sample composition	20,000 A549 in 7.5 mL lysed blood			
Recovery	53.4 ± 5.4%	39.3 ± 3.5%	92.8 ± 11.7%	71.0 ± 15.6%
Viability	99.8 ± 0.35% (Trypan)	91.8 ± 2.5% (Trypan) 90% (Live/Dead)	96% (Trypan)	92% (Trypan)
Purity	14.9 ± 10.1%	21.3 ± 18.7%	26.4 ± 6.4%	66.5 ± 10.4%
WBC Depletion	99.69 ± 0.25% 2.63 ± 0.42 log	99.93 ± 0.04% 3.24 ± 0.31 log	99.89 ± 0.02% 2.98 ± 0.09 log	99.986 ± 0.004% 3.85 ± 0.11 log
Enrichment factor	428	1047	902	5288

*The throughput is given as the injection time within the two separation devices. For the whole workflow, including RBC lysis step (30 min) and WBC labeling step (30 min), the total duration is 2h (P3+Chip) and 2h30 (P1+Chip), leading to a throughput for a 7.5 mL blood sample of 3.75 mL/h and 3 mL/h, respectively.

These achieved performances are competing with CTC isolation devices reported in the literature, which are based on either passive or active sorting methods (see Chapter 1). In particular, the performances were compared to immunomagnetic-based sorting mechanisms (positive or negative selection) and the importance of combining size- and magnetic-based separation to deplete a maximum number of WBCs to improve purity was highlighted. Results are summarized in Table 4-6.

Despite the lower measured recovery efficiency, a similar number of remaining WBCs and a great enrichment factor were reported using the two-step workflow. Regarding the other implemented magnetic-based separation methods, the magnetic source was either an external magnet (μ -MixMACS Chip, CTC-iChip, Integrated spiral/magnetic modules) or integrated magnetic structures (MagRC). The former strategy leads to limited magnetic forces, while the latter requires a complex and expensive fabrication method (thermal deposition). On the contrary, the reported fabrication technique based on the composite approach for the integration of permanent micro-magnets within the microchannel is a promising strategy. After further optimization of the recovery efficiency, the two-step workflow could open new perspectives in CTC isolation study.

Table 4-6: Comparison of the two-step workflow performances with those of other reported CTC sorting devices.

	ClearCell	MagRC	μ -MixMACS Chip	CTC-iChip	Integrated spiral/magnetic modules	This work
Inertial separation	Yes	No	No	Yes	Yes	Yes
Magnetic separation	No	Yes	Yes	Yes	Yes	Yes
EpCAM-dependant	No	Yes	No	No	Yes	No
Throughput (mL/h)	12	0.5	24	9.6	3	3.5
Recovery	80%	93%	91%	98%	90%	67% (74%)*
Remaining WBCs/mL	3,109	2000	--	445	42.4	947
Enrichment factor	--	--	763	--	--	5288
Ref	[64]	[65]	[66]	[67]	[68]	-

*The recovery efficiency of the magnetic chip itself is given in parenthesis.

Finally, after processing through the two-step workflow, cells were collected for downstream analysis which will be detailed in the next section.

4.2. Study of long-term cell viability

First, long-term cell viability was assessed by collecting cells for subsequent 2D cell culture. After processing through the whole workflow (size-based enrichment using program P3 followed by further purification with the magnetic chip), collected cells were seeded in 96-well plate. Medium renewal was performed every two days, removing at the same time remaining non-adherent WBCs.

Long-term cell viability was determined by a Live/Dead assay (same as detailed above in part 3.1.) after 4-days of cell culture and compared with control A549 cells. Phase contrast and fluorescence images are represented in Figure 4.20. The viability rate, which was determined by analyzing 2,000 cells, reached 90% and 89% for recovered cells and control A549 cells (incubated without WBCs), respectively. Phase contrast image shows good re-adherence of recovered cells, whose viability was further established with the Live/Dead assay.

These results highlight the preservation of long-term cell viability after the two-step separation process, which is crucial since intact cells are required for subsequent downstream analysis. Further phenotypic, genotypic, and transcriptomic studies could therefore be carried out, as well as cell culturing for drug susceptibility testing. Here, we will focus on the phenotypic study of recovered cells, which will be the object of the last subsection.

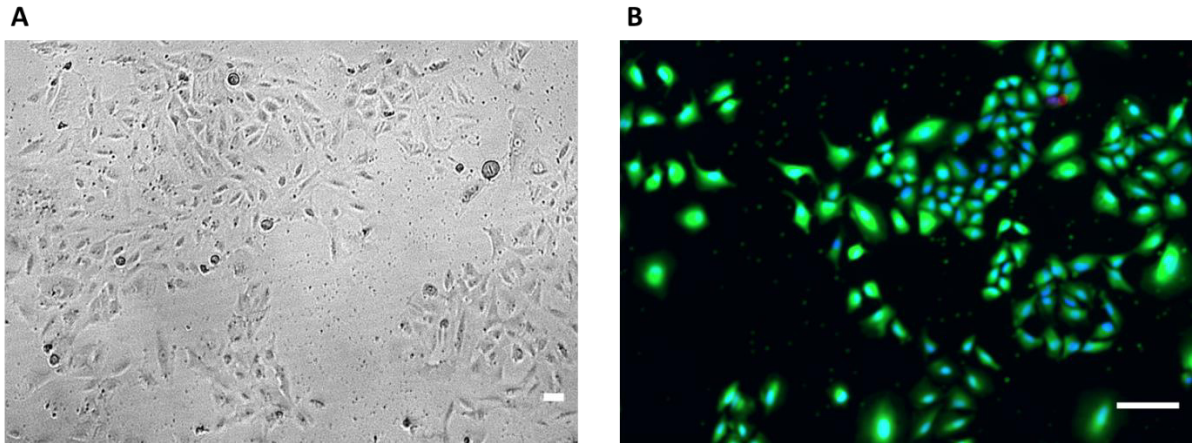


Figure 4.20: Recovered cells after the whole workflow were cultured for 4 days before determining cell viability. **(A)** Phase contrast images showing cell re-adherence. **(B)** Fluorescence images obtained during Live/Dead assay. Scale bars: 100 μm .

4.3. Analysis of cancer cell phenotype

After processing through the two-step workflow, cells were recovered for phenotypic study. A549 cancer cells were targeted by anti-ALDH1 antibody and AlexaFluor-488 fluorophore (green) while WBCs were labeled with anti-CD45, anti-CD15, and anti-CD41 antibodies conjugated to AlexaFluor-647 (red). For both, cell nucleus was stained using DAPI (blue). To assess the benefit of the additional magnetic-based purification step, output of the first size-based enrichment step through ClearCell was divided in two: one half for direct subsequent immunofluorescence assay, the other for processing through the magnetic chip and then immunofluorescence assay (Figure 4.21). This way, outputs of ClearCell and the magnetic chip can be directly compared.

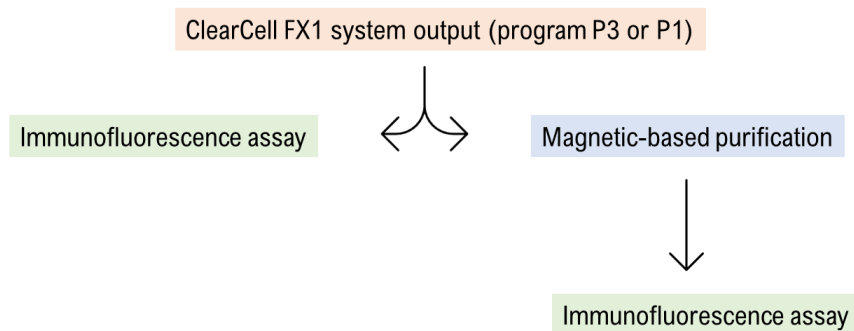


Figure 4.21: Split of ClearCell output for representative comparison of the benefit of the additional magnetic purification step.

First, an overview of the immunolabeled cell spots at various stages of the workflow is depicted in Figure 4.22. Cell nuclei of WBCs and A549 cells appear in blue (DAPI channel) and more specifically, WBC surface markers are in red (CY5 channel) while A549 surface marker (ALDH1) appears in green (GFP channel). The size-based enrichment step enables a first WBC depletion in comparison with the input, but the benefit of the additional magnetic-based purification step appears even more clearly since mainly green dots (A549 cells) are present in the spot, excess background WBCs were for the most part removed. The purity was determined according to the number of A549 cancer cells (CY5-/GFP+), after ClearCell enrichment, a purity of 41% was found and this value reached 84% after the magnetic chip.

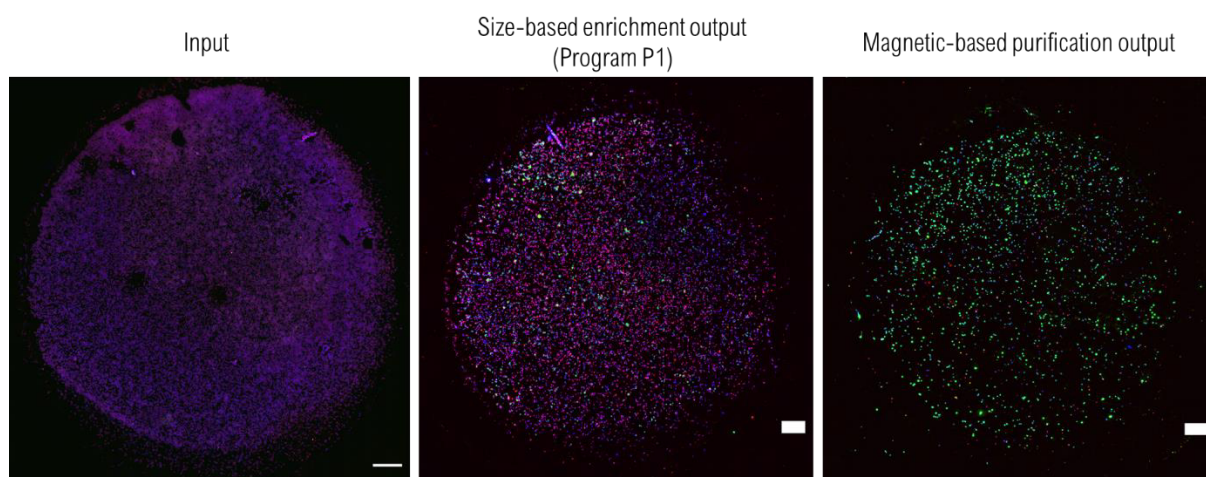


Figure 4.22: Cytospin spots with immunolabeled cells at various stages of the workflow. The input is to represent a typical WBC concentration when no enrichment is conducted. The size-based enrichment step (program P1) followed by the second magnetic purification allows for great background cell reduction by removing WBCs (in red). After ClearCell enrichment, 41% of analyzed cells were A549 cancer cells (CY5-/FITC+). This value reached 84% after the magnetic chip. Scale bars: 2000 μm .

Furthermore, zoomed fluorescence images of immunolabeled cells at various stages of the workflow are presented in Figure 4.23. The size-based enrichment step enabled a first WBC removal (which is higher using ClearCell program P1) and the second magnetic-based purification step enabled reaching almost WBC-free A549 cell visualization, therefore favoring phenotypic study of rare cells.

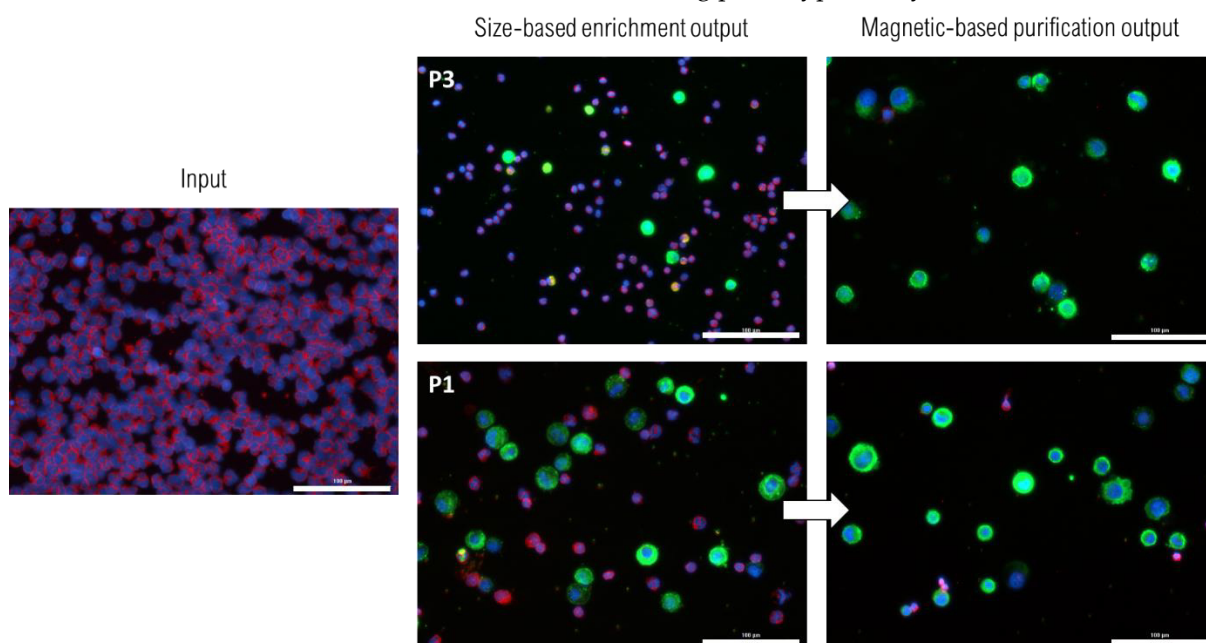


Figure 4.23: Fluorescence images of immunolabeled cells at various stages of the workflow. A typical WBC concentration is given by the input. Pre-enrichment step using either program P3 or P1 allows for a better visualization of A549 cancer cells. The second purification step enables an excellent WBC removal with mainly A549 cells remaining. Scale bars: 100 μm .

Finally, since a highly purified sample was obtained after processing through the magnetic chip, further heterogeneity studies on recovered cancer cells were accessible. Indeed, as illustrated in Figure 4.24-A, recovered cancer cells are heterogeneous in both size and ALDH1 expression level. In particular, cell size and ALDH1 surface marker expression heterogeneities were studied. Cell diameter and ALDH1 expression measurements are reported in Figure 4.24-B. Cell diameter and ALDH1 expression were established from DAPI and GFP signals, respectively. Recovered A549 cancer cell diameter ranges from

5.4 to 28 μm and ALDH1 expression varies between 3,000 and 50,000 a.u. Cancer cells presenting a high level of ALDH1 expression, a marker of cancer stem-like cells, is evidence of an aggressive phenotype and can be associated with poor prognosis [69]. Thus, being able to quantify ALDH1 expression level could help determining patient prognosis.

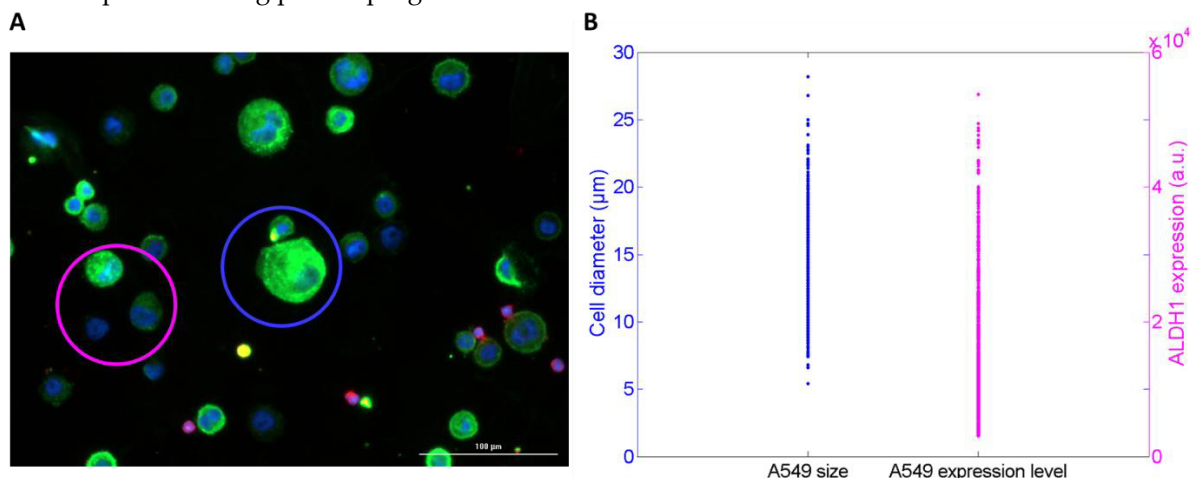


Figure 4.24: Highlights on cancer cell heterogeneity in both size and marker surface expression. **(A)** Fluorescence image showing heterogeneous cancer cell size (blue circle example) and ALDH1 expression level (pink circle example) Scale bar is 100 μm . **(B)** Measurement of cancer cell size and ALDH1 expression level revealing heterogeneities among cells. Cell diameter and ALDH1 expression were established from DAPI and GFP signals, respectively. Cells were processed with ClearCell program P1 as the first size-based separation step.

Besides, challenges of the size-based sorting method were underlined after comparing the size of collected mCTCs with that of remaining WBCs (Figure 4.25). Some of recovered A549 present a diameter comprised between 5 and 15 μm , like WBC diameter. This size overlap reveals the challenges in size-based sorting methods. Median diameter values are 13.9 μm and 10.3 μm , for A549 cells and WBCs, respectively. These values are consistent with ClearCell program P1 cut-off size (14 μm according to manufacturer's information) through which cells were first processed as the first size-based separation step. Thus, in theory, cells smaller than 14 μm are removed, but few cells escaped to this sorting parameter, including A549 cells. The additional immunomagnetophoretic-based purification step allowed for further WBC depletion, reducing their number by ~ 7.5 (from average 53,000 WBCs after P1 to 7,100 after the magnetic chip). This study highlights that, in addition to providing purified and viable cell samples, the magnetic chip enables the recovery of CTCs independent of their size or marker expression, which is highly requested given the reported heterogeneity of CTCs [65,67,70].

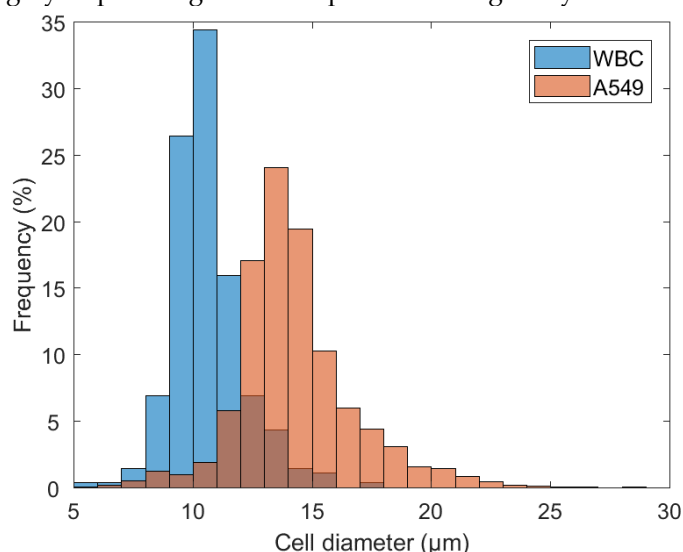


Figure 4.25: Comparison of A549 cell diameter with WBC diameter. A549 diameter can be comprised between 5 and 15 μm , like WBC size, underlining the challenges in CTC isolation by size-based sorting methods. Cells were first processed with ClearCell program P1, followed by the magnetic purification step.

5. Conclusion

In summary, we have developed a magnetophoretic-based microfluidic chip for tumor marker- and size-independent isolation of CTCs via negative depletion of WBCs. This study first dealt with the optimization of the magnetophoretic trapping performances of the chip, through enhancement of the WBC magnetic labeling, improvement of the microfluidic chamber integrating permanent micro-magnets, and determination of the operation fluidic conditions. The developed magnetophoretic chip achieved an average WBC depletion efficiency of 87% and an average mCTC recovery rate of 81%.

Furthermore, the magnetic chip compatibility with conventional biological studies, including 2D and 3D cell culture, as well as genotypic analysis, by preserving recovered cancer cell viability and integrity, was demonstrated. After conducting these studies on model blood samples with spiked cancer cell lines, the magnetic chip was combined with a size-based separation system to benefit from both technologies' advantages. The two-step designed workflow led to high-throughput and high purity, with a final mCTC recovery efficiency of 70% and WBC depletion rate of 99.99%, and an average contaminating number of WBCs of 7,100 after P1 enrichment program and magnetic purification. The highly purified sample thus obtained enabled downstream analysis such as long-term cell culture and phenotypic analysis. Such subsequent studies are crucial to relate to clinical decisions and personalized medicine strategies. These results could help guiding the design of future CTC isolation devices based on negative depletion of WBCs.

Future work will consist in assessing the two-step workflow performances in a clinical context by isolation CTCs from patient samples. Indeed, the magnetic chip has for aim to help biologists with their clinical studies and should therefore present the following characteristics: "plug and play" function, easy handling, robustness, and finally versatility. Several improvements could be imagined to achieve this objective and they will be further detailed in the conclusion.

To put in a nutshell, there is an urgent need to provide ready-to-use and reliable devices for clinical applications. The conducted research in this thesis helps to demonstrate the value of emerging microfluidic and magnetophoretic technologies for characterizing liquid biopsy samples, an important research topic that will lead to changes in the paradigm of cancer diagnosis and management.

References

1. Wan, L.; Pantel, K.; Kang, Y. Tumor metastasis: Moving new biological insights into the clinic. *Nat. Med.* **2013**, *19*, 1450–1464, doi:10.1038/nm.3391.
2. Cristofanilli, M. Circulating Tumor Cells, Disease Progression, and Survival in Metastatic Breast Cancer. *Semin. Oncol.* **2006**, *33*, 9–14, doi:10.1053/j.seminoncol.2006.03.016.
3. Sachs, N.; Clevers, H. Organoid cultures for the analysis of cancer phenotypes. *Curr. Opin. Genet. Dev.* **2014**, *24*, 68–73, doi:10.1016/j.gde.2013.11.012.
4. Maheswaran, S.; Sequist, L. V.; Nagrath, S.; Ulkus, L.; Brannigan, B.; Collura, C. V.; Inserra, E.; Diederichs, S.; Iafrate, A.J.; Bell, D.W.; et al. Detection of mutations in EGFR in circulating lung-cancer cells. *N. Engl. J. Med.* **2008**, *359*, 366–377, doi:10.1056/NEJMOA0800668.
5. Gasch, C.; Bauernhofer, T.; Pichler, M.; Langer-Freitag, S.; Reeh, M.; Seifert, A.M.; Mauermann, O.; Izbicki, J.R.; Pantel, K.; Riethdorf, S. Heterogeneity of epidermal growth factor receptor status and mutations of KRAS/PIK3CA in circulating tumor cells of patients with colorectal cancer. *Clin. Chem.* **2013**, *59*, 252–260, doi:10.1373/CLINCHEM.2012.188557.
6. Cristofanilli, M.; Hayes, D.F.; Budd, G.T.; Ellis, M.J.; Stopeck, A.; Reuben, J.M.; Doyle, G. V.; Matera, J.; Allard, W.J.; Miller, M.C.; et al. Circulating tumor cells: A novel prognostic factor for newly diagnosed metastatic breast cancer. *J. Clin. Oncol.* **2005**, *23*, 1420–1430, doi:10.1200/JCO.2005.08.140.
7. Zhang, L.; Riethdorf, S.; Wu, G.; Wang, T.; Yang, K.; Peng, G.; Liu, J.; Pantel, K. Meta-analysis of the prognostic value of circulating tumor cells in breast cancer. *Clin. Cancer Res.* **2012**, *18*, 5701–5710, doi:10.1158/1078-0432.CCR-12-1587.
8. Rack, B.; Schindlbeck, C.; Jückstock, J.; Andergassen, U.; Hepp, P.; Zwingers, T.; Friedl, T.W.P.; Lorenz, R.; Tesch, H.; Fasching, P.A.; et al. Circulating tumor cells predict survival in early average-to-high risk breast cancer patients. *J. Natl. Cancer Inst.* **2014**, *106*, doi:10.1093/JNCI/DJU066.
9. Pantel, K.; Alix-Panabières, C. The potential of circulating tumor cells as a liquid biopsy to guide therapy in prostate cancer. *Cancer Discov.* **2012**, *2*, 974–975, doi:10.1158/2159-8290.CD-12-0432.
10. Samandari, M.; Julia, M.G.; Rice, A.; Chronopoulos, A.; del Rio Hernandez, A.E. Liquid biopsies for management of pancreatic cancer. *Transl. Res.* **2018**, doi:10.1016/j.trsl.2018.07.008.
11. Hiraiwa, K.; Takeuchi, H.; Hasegawa, H.; Saikawa, Y.; Suda, K.; Ando, T.; Kumagai, K.; Irino, T.; Yoshikawa, T.; Matsuda, S.; et al. Clinical significance of circulating tumor cells in blood from patients with gastrointestinal cancers. *Ann. Surg. Oncol.* **2008**, *15*, 3092–3100, doi:10.1245/S10434-008-0122-9.
12. Riethdorf, S.; Müller, V.; Zhang, L.; Rau, T.; Loibl, S.; Komor, M.; Roller, M.; Huober, J.; Fehm, T.; Schrader, I.; et al. Detection and HER2 expression of circulating tumor cells: prospective monitoring in breast cancer patients treated in the neoadjuvant GeparQuattro trial. *Clin. Cancer Res.* **2010**, *16*, 2634–2645, doi:10.1158/1078-0432.CCR-09-2042.
13. Guibert, N.; Delaunay, M.; Lusque, A.; Boubekour, N.; Rouquette, I.; Clermont, E.; Mourlanette, J.; Gouin, S.; Dormoy, I.; Favre, G.; et al. PD-L1 expression in circulating tumor cells of advanced non-small cell lung cancer patients treated with nivolumab. *Lung Cancer* **2018**, *120*, 108–112, doi:10.1016/j.lungcan.2018.04.001.
14. Wang, Y.; Kim, T.H.; Fouladdel, S.; Zhang, Z.; Soni, P.; Qin, A.; Zhao, L.; Azizi, E.; Lawrence, T.S.; Ramnath, N.; et al. PD-L1 Expression in Circulating Tumor Cells Increases during Radio(chemo)therapy and Indicates Poor Prognosis in Non-small Cell Lung Cancer. *Sci. Rep.* **2019**, *9*, doi:10.1038/S41598-018-36096-7.
15. Francart, M.E.; Lambert, J.; Vanwynsberghe, A.M.; Thompson, E.W.; Bourcy, M.; Polette, M.; Gilles, C. Epithelial–mesenchymal plasticity and circulating tumor cells: Travel companions to metastases. *Dev. Dyn.* **2018**, *247*, 432–450, doi:10.1002/dvdy.24506.
16. Mani, S.A.; Guo, W.; Liao, M.-J.; Eaton, E.N.; Ayyanan, A.; Zhou, A.Y.; Brooks, M.; Reinhard, F.; Zhang, C.C.; Shipitsin, M.; et al. The epithelial–mesenchymal transition generates cells with properties of stem cells. *Cell* **2008**, *133*, 704–715, doi:10.1016/j.cell.2008.03.027.
17. Cao, Z.; Livas, T.; Kyprianou, N. Anoikis and EMT: Lethal “Liaisons” during Cancer Progression. *Crit. Rev. Oncog.* **2016**, *21*, 155–168, doi:10.1615/CritRevOncog.2016016955.

18. Chemi, F.; Mohan, S.; Guevara, T.; Clipson, A.; Rothwell, D.G.; Dive, C. Early Dissemination of Circulating Tumor Cells: Biological and Clinical Insights. *Front. Oncol.* **2021**, *11*.
19. Gradilone, A.; Naso, G.; Raimondi, C.; Cortesi, E.; Gandini, O.; Vincenzi, B.; Saltarelli, R.; Chiapparino, E.; Spremberg, F.; Cristofanilli, M.; et al. Circulating tumor cells (CTCs) in metastatic breast cancer (MBC): Prognosis, drug resistance and phenotypic characterization. *Ann. Oncol.* **2011**, *22*, 86–92, doi:10.1093/annonc/mdq323.
20. Alix-Panabières, C.; Pantel, K. *Challenges in circulating tumour cell research*; 2014;
21. Mostert, B.; Jiang, Y.; Sieuwerts, A.M.; Wang, H.; Bolt-de Vries, J.; Biermann, K.; Kraan, J.; Lalmahomed, Z.; van Galen, A.; de Weerd, V.; et al. KRAS and BRAF mutation status in circulating colorectal tumor cells and their correlation with primary and metastatic tumor tissue. *Int. J. cancer* **2013**, *133*, 130–141, doi:10.1002/ijc.27987.
22. Jiang, Y.; Palma, J.F.; Agus, D.B.; Wang, Y.; Gross, M.E. Detection of androgen receptor mutations in circulating tumor cells in castration-resistant prostate cancer. *Clin. Chem.* **2010**, *56*, 1492–1495, doi:10.1373/clinchem.2010.143297.
23. Miyamoto, D.T.; Lee, R.J.; Stott, S.L.; Ting, D.T.; Wittner, B.S.; Ulman, M.; Smas, M.E.; Lord, J.B.; Brannigan, B.W.; Trautwein, J.; et al. Androgen receptor signaling in circulating tumor cells as a marker of hormonally responsive prostate cancer. *Cancer Discov.* **2012**, *2*, 995–1003, doi:10.1158/2159-8290.CD-12-0222.
24. Shaw, A.T.; Kim, D.-W.; Nakagawa, K.; Seto, T.; Crinó, L.; Ahn, M.-J.; De Pas, T.; Besse, B.; Solomon, B.J.; Blackhall, F.; et al. Crizotinib versus chemotherapy in advanced ALK-positive lung cancer. *N. Engl. J. Med.* **2013**, *368*, 2385–2394, doi:10.1056/NEJMoa1214886.
25. Ilie, M.; Long, E.; Butori, C.; Hofman, V.; Coelle, C.; Mauro, V.; Zahaf, K.; Marquette, C.H.; Mouroux, J.; Paterlini-Bréchet, P.; et al. ALK-gene rearrangement: a comparative analysis on circulating tumour cells and tumour tissue from patients with lung adenocarcinoma. *Ann. Oncol. Off. J. Eur. Soc. Med. Oncol.* **2012**, *23*, 2907–2913, doi:10.1093/annonc/mds137.
26. Zhang, Z.; Shiratsuchi, H.; Palanisamy, N.; Negrath, S.; Ramnath, N. Expanded Circulating Tumor Cells from a Patient with ALK-Positive Lung Cancer Present with EML4-ALK Rearrangement Along with Resistance Mutation and Enable Drug Sensitivity Testing: A Case Study. *J. Thorac. Oncol.* **2017**, *12*, 397–402, doi:10.1016/j.jtho.2016.07.027.
27. Khoo, B.L.; Greci, G.; Lim, Y.B.; Lee, S.C.; Han, J.; Lim, C.T. Expansion of patient-derived circulating tumor cells from liquid biopsies using a CTC microfluidic culture device. *Nat. Protoc.* **2017**, *13*, 34–58, doi:10.1038/nprot.2017.125.
28. Zhang, Z.; Shiratsuchi, H.; Lin, J.; Chen, G.; Reddy, R.M.; Azizi, E.; Fouladdel, S.; Chang, A.C.; Lin, L.; Jiang, H.; et al. Expansion of CTCs from early stage lung cancer patients using a microfluidic co-culture model. *Oncotarget* **2014**, *5*, doi:10.18632/oncotarget.2592.
29. Weeber, F.; Ooft, S.N.; Dijkstra, K.K.; Voest, E.E. Tumor Organoids as a Pre-clinical Cancer Model for Drug Discovery. *Cell Chem. Biol.* **2017**, *24*, 1092–1100, doi:10.1016/j.chembiol.2017.06.012.
30. Jung, D.J.; Shin, T.H.; Kim, M.; Sung, C.O.; Jang, S.J.; Jeong, G.S. A one-stop microfluidic-based lung cancer organoid culture platform for testing drug sensitivity. *Lab Chip* **2019**, *19*, 2854–2865, doi:10.1039/c9lc00496c.
31. Yu, M.; Bardia, A.; Aceto, N.; Bersani, F.; Madden, M.W.; Donaldson, M.C.; Desai, R.; Zhu, H.; Comaills, V.; Zheng, Z.; et al. Ex vivo culture of circulating breast tumor cells for individualized testing of drug susceptibility. *Science (80-.).* **2014**, *345*, 216–220, doi:10.1126/science.1253533.Ex.
32. Nagle, P.W.; Plukker, J.T.M.; Muijs, C.T.; van Luijk, P.; Coppes, R.P. Patient-derived tumor organoids for prediction of cancer treatment response. *Semin. Cancer Biol.* **2018**, *53*, 258–264, doi:10.1016/j.semcancer.2018.06.005.
33. Den Toonder, J. Circulating tumor cells: The Grand Challenge. *Lab Chip* **2011**, *11*, 375–377, doi:10.1039/c0lc90100h.
34. Lee, Y.; Guan, G.; Bhagat, A.A. ClearCell® FX, a label-free microfluidics technology for enrichment of viable circulating tumor cells. *Cytom. Part A* **2018**, *93*, 1251–1254, doi:10.1002/cyto.a.23507.

35. Schehr, J.L.; Schultz, Z.D.; Warrick, J.W.; Guckenberger, D.J.; Pezzi, H.M.; Sperger, J.M.; Heninger, E.; Saeed, A.; Leal, T.; Mattox, K.; et al. High specificity in circulating tumor cell identification is required for accurate evaluation of programmed death-ligand 1. *PLoS One* **2016**, *11*, 1–15, doi:10.1371/journal.pone.0159397.
36. Matijevic, E. *Medical Applications of Colloids*; 2008; ISBN 9780387769202.
37. Ozkumur, E.; Shah, A.M.; Ciciliano, J.C.; Emmink, B.L.; David, T.; Brachtel, E.; Yu, M.; Chen, P.; Morgan, B.; Trautwein, J.; et al. Inertial Focusing for Tumor Antigen-Dependent and -Independent Sorting of Rare Circulating Tumor Cells. *Sci. Transl. Med.* **2013**, *5*, 1–20, doi:10.1126/scitranslmed.3005616.Inertial.
38. Zhao, W.; Liu, Y.; Jenkins, B.D.; Cheng, R.; Harris, B.N.; Zhang, W.; Xie, J.; Murrow, J.R.; Hodgson, J.; Egan, M.; et al. Tumor antigen-independent and cell size variation-inclusive enrichment of viable circulating tumor cells. *Lab Chip* **2019**, *19*, 1860–1876, doi:10.1039/c9lc00210c.
39. Chen, C.L.; Chen, K.C.; Pan, Y.C.; Lee, T.P.; Hsiung, L.C.; Lin, C.M.; Chen, C.Y.; Lin, C.H.; Chiang, B.L.; Wo, A.M. Separation and detection of rare cells in a microfluidic disk via negative selection. *Lab Chip* **2011**, *11*, 474–483, doi:10.1039/c0lc00332h.
40. Lee, T.Y.; Hyun, K.A.; Kim, S. II; Jung, H. II An integrated microfluidic chip for one-step isolation of circulating tumor cells. *Sensors Actuators, B Chem.* **2017**, *238*, 1144–1150, doi:10.1016/j.snb.2016.05.163.
41. Aldridge, P.M.; Mukhopadhyay, M.; Ahmed, S.U.; Zhou, W.; Christinck, E.; Makonnen, R.; Sargent, E.H.; Kelley, S.O. Prismatic Deflection of Live Tumor Cells and Cell Clusters. *ACS Nano* **2018**, *12*, 12692–12700, doi:10.1021/acsnano.8b07616.
42. Zhao, W.; Cheng, R.; Jenkins, B.D.; Zhu, T.; Okonkwo, N.E.; Jones, C.E.; Davis, M.B.; Kavuri, S.K.; Hao, Z.; Schroeder, C.; et al. Label-free ferrohydrodynamic cell separation of circulating tumor cells. *Lab Chip* **2017**, *17*, 3097–3111, doi:10.1039/c7lc00680b.
43. Zhu, C.; Skalak, R. A continuum model of protrusion of pseudopod in leukocytes. *Biophys. J.* **1988**, *54*, 1115–1137, doi:https://doi.org/10.1016/S0006-3495(88)83047-9.
44. Samstag, Y. Actin cytoskeletal dynamics in T lymphocyte activation and migration. *J. Leukoc. Biol.* **2003**, *73*, 30–48, doi:10.1189/jlb.0602272.
45. Moore, M.J.; Sebastian, J.A.; Kolios, M.C. Determination of cell nucleus-to-cytoplasmic ratio using imaging flow cytometry and a combined ultrasound and photoacoustic technique: a comparison study. *J. Biomed. Opt.* **2019**, *24*, 1, doi:10.1117/1.jbo.24.10.106502.
46. Moshksayan, K.; Kashaninejad, N.; Warkiani, M.E.; Lock, J.G.; Moghadas, H.; Firoozabadi, B.; Saidi, M.S.; Nguyen, N.T. Spheroids-on-a-chip: Recent advances and design considerations in microfluidic platforms for spheroid formation and culture. *Sensors Actuators, B Chem.* **2018**, *263*, 151–176, doi:10.1016/j.snb.2018.01.223.
47. Wen, Z.; Liao, Q.; Hu, Y.; You, L.; Zhou, L.; Zhao, Y. A spheroid-based 3-D culture model for pancreatic cancer drug testing, using the acid phosphatase assay. *Brazilian J. Med. Biol. Res.* **2013**, *46*, 634–642, doi:10.1590/1414-431X20132647.
48. Zuchowska, A.; Kwapiszewska, K.; Chudy, M.; Dybko, A.; Brzozka, Z. Studies of anticancer drug cytotoxicity based on long-term HepG2 spheroid culture in a microfluidic system. *Electrophoresis* **2017**, *38*, 1206–1216, doi:10.1002/elps.201600417.
49. Liu, X.; Lin, H.; Song, J.; Zhang, T.; Wang, X.; Huang, X.; Zheng, C. A novel simple drop chip for 3d spheroid formation and anti-cancer drug assay. *Micromachines* **2021**, *12*, doi:10.3390/mi12060681.
50. Chen, Y.C.; Lou, X.; Zhang, Z.; Ingram, P.; Yoon, E. High-Throughput Cancer Cell Sphere Formation for Characterizing the Efficacy of Photo Dynamic Therapy in 3D Cell Cultures. *Sci. Rep.* **2015**, *5*, 1–12, doi:10.1038/srep12175.
51. Wu, R.W.K.; Chu, E.S.M.; Yuen, J.W.M.; Huang, Z. Comparative study of FosPeg® photodynamic effect on nasopharyngeal carcinoma cells in 2D and 3D models. *J. Photochem. Photobiol. B.* **2020**, *210*, 111987, doi:10.1016/j.jphotobiol.2020.111987.
52. Longati, P.; Jia, X.; Eimer, J.; Wagman, A.; Witt, M.-R.; Rehnmark, S.; Verbeke, C.; Toftgård, R.; Löhr, M.; Heuchel, R.L. 3D pancreatic carcinoma spheroids induce a matrix-rich, chemoresistant phenotype offering a better model for drug testing. *BMC Cancer* **2013**, *13*, 95, doi:10.1186/1471-2407-13-95.

53. Chandrasekaran, S.; Marshall, J.R.; Messing, J.A.; Hsu, J.-W.; King, M.R. TRAIL-Mediated Apoptosis in Breast Cancer Cells Cultured as 3D Spheroids. *PLoS One* **2014**, *9*, 1–12, doi:10.1371/journal.pone.0111487.
54. Shichi, Y.; Sasaki, N.; Michishita, M.; Hasegawa, F.; Matsuda, Y.; Arai, T.; Gomi, F.; Aida, J.; Takubo, K.; Toyoda, M.; et al. Enhanced morphological and functional differences of pancreatic cancer with epithelial or mesenchymal characteristics in 3D culture. *Sci. Rep.* **2019**, *9*, 1–10, doi:10.1038/s41598-019-47416-w.
55. Lin, R.Z.; Chang, H.Y. Recent advances in three-dimensional multicellular spheroid culture for biomedical research. *Biotechnol. J.* **2008**, *3*, 1172–1184, doi:10.1002/biot.200700228.
56. Cui, X.; Hartanto, Y.; Zhang, H. Advances in multicellular spheroids formation. *J. R. Soc. Interface* **2017**, *14*, doi:10.1098/rsif.2016.0877.
57. Smyrek, I.; Mathew, B.; Fischer, S.C.; Lissek, S.M.; Becker, S.; Stelzer, E.H.K. E-cadherin, actin, microtubules and FAK dominate different spheroid formation phases and important elements of tissue integrity. *Biol. Open* **2019**, *8*, doi:10.1242/bio.037051.
58. Sánchez-Herrero, E.; Provencio, M.; Romero, A. Clinical utility of liquid biopsy for the diagnosis and monitoring of EML4-ALK NSCLC patients. *Adv. Lab. Med. / Av. en Med. Lab.* **2020**, *1*, doi:10.1515/almed-2019-0019.
59. Solomon, B.J.; Kim, D.-W.; Wu, Y.-L.; Nakagawa, K.; Mekhail, T.; Felip, E.; Cappuzzo, F.; Paolini, J.; Usari, T.; Tang, Y.; et al. Final Overall Survival Analysis From a Study Comparing First-Line Crizotinib Versus Chemotherapy in ALK-Mutation-Positive Non-Small-Cell Lung Cancer. *J. Clin. Oncol.* **2018**, *36*, 2251–2258, doi:10.1200/JCO.2017.77.4794.
60. Zhou, J.; Zheng, J.; Zhang, X.; Zhao, J.; Zhu, Y.; Shen, Q.; Wang, Y.; Sun, K.; Zhang, Z.; Pan, Z.; et al. Crizotinib in patients with anaplastic lymphoma kinase-positive advanced non-small cell lung cancer versus chemotherapy as a first-line treatment. *BMC Cancer* **2018**, *18*, 10, doi:10.1186/s12885-017-3720-8.
61. Takahashi, Y.; Shirai, K.; Ijiri, Y.; Morita, E.; Yoshida, T.; Iwanaga, S.; Yanagida, M. Integrated system for detection and molecular characterization of circulating tumor cells. *PLoS One* **2020**, *15*, 1–13, doi:10.1371/journal.pone.0237506.
62. Aya-Bonilla, C.A.; Morici, M.; Hong, X.; McEvoy, A.C.; Sullivan, R.J.; Freeman, J.; Calapre, L.; Khattak, M.A.; Meniawy, T.; Millward, M.; et al. Detection and prognostic role of heterogeneous populations of melanoma circulating tumour cells. *Br. J. Cancer* **2020**, *122*, 1059–1067, doi:10.1038/s41416-020-0750-9.
63. Li, Y.; Wu, S.; Bai, F. Molecular characterization of circulating tumor cells—from bench to bedside. *Semin. Cell Dev. Biol.* **2018**.
64. Warkiani, M.E. brahim.; Khoo, B.L. ua.; Wu, L.; Tay, A.K. a. P.; Bhagat, A.A. sga. S.; Han, J.; Lim, C.T. ec. Ultra-fast, label-free isolation of circulating tumor cells from blood using spiral microfluidics. *Nat. Protoc.* **2016**, *11*, 134–148, doi:10.1038/nprot.2016.003.
65. Poudineh, M.; Aldridge, P.M.; Ahmed, S.; Green, B.J.; Kermanshah, L.; Nguyen, V.; Tu, C.; Mohamadi, R.M.; Nam, R.K.; Hansen, A.; et al. Tracking the dynamics of circulating tumour cell phenotypes using nanoparticle-mediated magnetic ranking. *Nat. Nanotechnol.* **2017**, *12*, 274–281, doi:10.1038/nnano.2016.239.
66. Lee, T.Y.; Hyun, K.A.; Kim, S. Il; Jung, H. Il An integrated microfluidic chip for one-step isolation of circulating tumor cells. *Sensors Actuators, B Chem.* **2017**, *238*, 1144–1150, doi:10.1016/j.snb.2016.05.163.
67. Fachin, F.; Spuhler, P.; Martel-Foley, J.M.; Edd, J.F.; Barber, T.A.; Walsh, J.; Karabacak, M.; Pai, V.; Yu, M.; Smith, K.; et al. Monolithic Chip for High-throughput Blood Cell Depletion to Sort Rare Circulating Tumor Cells. *Sci. Rep.* **2017**, *7*, 1–11, doi:10.1038/s41598-017-11119-x.
68. Jack, R.M.; Grafton, M.M.G.; Rodrigues, D.; Giraldez, M.D.; Griffith, C.; Cieslak, R.; Zeinali, M.; Kumar Sinha, C.; Azizi, E.; Wicha, M.; et al. Ultra-Specific Isolation of Circulating Tumor Cells Enables Rare-Cell RNA Profiling. *Adv. Sci.* **2016**, *3*, 1–8, doi:10.1002/advs.201600063.
69. Yao, J.; Jin, Q.; Wang, X.D.; Zhu, H.J.; Ni, Q.C.; Fan, H. Aldehyde dehydrogenase 1 expression is correlated with poor prognosis in breast cancer. *Med. (United States)* **2017**, *96*, 1–6, doi:10.1097/MD.000000000000171.
70. Renier, C.; Pao, E.; Che, J.; Liu, H.E.; Lemaire, C.A.; Matsumoto, M.; Triboulet, M.; Srivinas, S.; Jeffrey, S.S.; Rettig, M.; et al. Label-free isolation of prostate circulating tumor cells using Vortex microfluidic technology. *npj Precis. Oncol.* **2017**, *1*, 15, doi:10.1038/s41698-017-0015-0.

Conclusion and future outlook

1. Summary

In the context of liquid biopsy and personalized cancer medicine, researchers have shed light on CTCs as biomarkers for cancer diagnosis, prognosis, and monitoring. Nevertheless, there is still a lot of ongoing work to tackle the challenges raised by their isolation, being their rarity among other blood cells, their phenotypic and size heterogeneities, as well as the need to preserve their viability for downstream analysis. Over the past decade, microfluidic devices have shown promising features to address these challenges and studies are still widely conducted to keep providing the best performances for CTC isolation, including high throughput, purity, recovery, and clinical relevance.

In this study, we have presented a magnetophoretic-based microfluidic chip for negative selection of CTCs through depletion of magnetically labeled WBCs. In particular, we have reported an original approach, based on magnetic polymer composites, to integrate large density arrays of permanent micro-magnets into a microfluidic system, which act as micro-traps. This approach consists in mixing hard NdFeB magnetic particles with a PDMS matrix and relies on the self-organization of the magnetic particles due to dipole-dipole interactions in a designed magnetic field pattern. These self-assembled micrometric-sized magnets were then integrated into a microfluidic device, leading to autonomous and compact systems. We have conducted the research with the objective of achieving a final operational device, as summarized below.

First, the work has been focused on the fabrication of the micro-magnets, and particularly on the determination of the optimal fabrication conditions. Several aspects of the process were investigated, such as the concentration of hard magnetic particles within the PDMS matrix, as well as the influence of the magnetic field gradient applied during PDMS cross-linking. Furthermore, this study highlighted the self-organization of the magnetic particles as chain-like agglomerates with high aspect ratio, whose structural characteristics were determined using complementary methods. X-ray tomography enabled the characterization of the magnetic composite membrane 3D microstructure while optical microscopy explored the particle arrangement within the 2D surface. Interestingly, we have demonstrated the non-randomness of the magnetic particle self-organization within the PDMS matrix. In the end, some characteristics of the micro-magnets prepared at a final concentration of 4 wt% under a low gradient magnetic field include a diameter of 5 μm , a density of 1500 micro-magnets/ mm^2 , and a nearest neighbor distance of 15 μm .

Second, micro-magnet magnetic properties were determined using a broad range of methods. Micro-magnet remanent magnetization was analyzed by SQUID magnetometry and the importance of enhancing the magnetization field was underlined. A final remanent magnetization of 0.7 T (0.62 Ms) was finally achieved. Furthermore, generated magnetic forces by the micro-magnets were both numerically and experimentally determined. Numerical calculations using Comsol finite element modeling first enabled estimating magnetic field and magnetic field gradient as a function of the distance to the micro-magnets. Magnetic field gradients as high as 10^5 T/m were calculated at the surface of the micro-magnets, in an ambient magnetic field of 200 mT. Besides, Comsol simulations allowed for neighboring effect study and revealed the demagnetizing field occurring in a dense array of permanent micro-magnets. Comsol modeling was completed with magnetic force measurement on a model

superparamagnetic bead and forces of the order of several nN were calculated (3 nN at the micro-magnet surface). Besides, experimental measurements of the generated magnetic force were also performed by colloidal probe AFM and hydrodynamic determination in microsystem. Both experimental methods show consistent values, with an average magnetic force of 1.3 nN. These experimental measurements take micro-magnet structure complexity into account, with its variety between micro-magnets, but still showed good agreement with Comsol calculations.

These magnetic characterizations revealed the behavior of micrometric-sized magnets, which generate high magnetic field gradients at their surface, but with limited interaction reach. The third step has therefore consisted in improving micro-magnet interaction distance to attract target objects flowing in the upper part of the microchannel. Some researchers reported the use of passive fluidics, such as herringbone grooves located on the roof of the microchannel to pull flowing objects down. Here, the implemented strategy relied on the application of external fields generated by an additional millimeter-scale permanent magnet to attract target objects towards the channel bottom. By doubling the ambient magnetic field, hence increasing micro-magnet and target object magnetizations, it resulted in higher magnetic forces. The ability of micro-magnets to trap a larger number of target objects in the presence of an external milli-magnet was demonstrated through superparamagnetic bead trapping experiments. With an increase in micro-magnet trapping efficiency of around 15% in the presence of the permanent milli-magnet, an efficiency as high as 98% was achieved at a flow rate of 0.5 mL/h.

Finally, once well characterized, the magnetophoretic-based chip was implemented for CTC isolation (or mCTC since spiked cancer cell lines were used) via WBC depletion. A prior step required the optimization of WBC magnetic labeling by assessing temperature, agitation, duration, nanoparticle concentration, and medium conditions. In addition, the design of the chip was revised to provide a large surface chamber for dense micro-magnet array integration. Next, the operating procedure, including the flow rate leading to maximized WBC capture and CTC recovery, was determined. This value was found to be 2 mL/h, providing 85% WBC capture efficiency and 80% mCTC recovery from a sample of 300,000 WBCs and 20,000 mCTCs. After performing these optimizations, the compatibility of the chip with routine biological studies was demonstrated. A crucial requirement was to preserve cancer cell viability and integrity during the magnetophoretic isolation, which was achieved according to long-term cell culture, viability/cytotoxicity assay, as well as phenotypic study. Downstream analysis was extended to the formation of spheroids, which were maintained in culture during few weeks, and the detection of EML4-ALK gene fusion, a rearrangement often screened to tailor treatments. To our knowledge, this is the first reported device integrating permanent micro-meter sized magnets for CTC isolation. The adopted strategy, i.e., negative selection and immunomagnetic sorting, benefits from the high specificity of antigen-antibody interaction, as well as the high selectivity due to the magnetic contrast of magnetically labeled WBCs, therefore offering tumor marker- and size-independent separation so as to collect heterogeneous cancer cells.

Last but not least, the magnetophoretic-based microfluidic chip was combined to a size-based separation technology, leading to a two-step workflow process for enhanced purity. The first step consists of a pre-enrichment step through ClearCell FX1, a system used by biologists at Hospices Civils de Lyon for clinical studies. The separation relies on the size difference between CTCs and WBCs (cut-off size of 14 μm) and allows for a WBC depletion by a factor 300 (program P3) and 1000 (program P1), with a mCTC recovery comprised between 60-80%. Since thousands to hundred of thousands of WBCs remain after this first size-based enrichment, representing contaminating cells, the developed magnetophoretic-based chip was added to the workflow so as to increase purity. This second purification step resulted in an average number of contaminating WBCs comprised between 7,000 and 30,000 (depending on ClearCell running program). This low amount of background cells facilitates subsequent analyses and phenotypic study of ALDH1-positive cancer cells enabled quantifying cancer cell heterogeneity in both size and marker expression level. This study could be used in a clinical context to assess phenotype aggressiveness and prognosis rate.

In the following sections, features of the developed device will be detailed, and future outlook of the project will be presented.

2. Assets and limitations of the developed device

As aforementioned, we have reported the first magnetophoretic device integrating permanent micro-scale magnets acting as micro-traps for CTC isolation. This could be achieved thanks to the selected fabrication approach using magnetic composites. Magnetic composite approach is breaking with conventional microfabrication techniques since it allows reaching high aspect ratio microstructures (chain-like agglomerates) which are buried and localized in the polymer matrix. These microstructures can then be directly integrated into the microchannels in a one-step soft-lithography process. Thus, no tedious alignment procedures are involved, and since the polymer matrix (PDMS) is the same for the whole system, the magnetic structures are tightly integrated and do not raise heterogeneous integration issues. This strategy therefore enabled the integration of micrometer-scale permanent magnets, leading to an autonomous and compact device since no external bulky source is needed. In particular, dense arrays of micro-traps were obtained, with micrometric features comparable to the size of a cell, allowing for single-cell trapping.

The assets of the developed device not only rely on the fabrication process, but also on the implemented immunomagnetophoretic separation strategy. Magnetophoresis has shown several advantages, such as easy operation, low cost, and simple design, with features particularly suitable with the manipulation of biological samples. Indeed, magnetophoresis offers (i) contactless manipulation, hence preserving cell viability and integrity; (ii) robustness, since medium properties such as surface charges, ionic concentration, pH, and temperature do not affect this technique; as well as (iii) tunability, as the magnetic force could be enhanced by improving generated magnetic fields and magnetic field gradients, with the aid of an external milli-magnet. Besides, the preferred negative selection approach, which consisted in functionalizing magnetic nanoparticles with antibodies targeting WBCs to perform negative depletion, was favorable for successful recovery of CTCs. This way, all CTCs could be collected regardless of their size or surface marker expression, which are known for being heterogeneous.

To sum up, the presented device features make it compatible for successful implementation in a biological context. Nevertheless, certain limitations represent an obstacle to widespread mass production and “plug-and-play” use. First, PDMS material, which is well characterized and readily available for microfluidics research, is not the most suitable polymer from a mass production perspective. Other polymer materials, such as polymethylmethacrylate (PMMA), polycarbonate (PC), and cyclic olefin copolymer (COC), are commonly employed by the lab-on-a-chip (LOC) industries. Besides, the observed micro-magnet structural heterogeneity, associated with magnetic force variability, can be attributed to certain fabrication steps which are operator-dependent (composite mixing, pouring, etc.). Further work would require automating some of these critical steps.

In addition to improving the fabrication process and fulfilling mass production perspectives, there are still several hurdles to overcome to move from a proof-of-concept study to practical application. At the moment, handling the developed device requires a certain microfluidic expertise to be able to install the set-up (tubing, connectors, pressure controller, etc.) and anticipate potential issues which can occur during the injection, such as bubble formation. Thus, the final microfluidic platform should be user-friendly and avoid too many operational steps for the end-users, hence enabling biologists to easily perform the microfluidic sorting and collect CTCs for subsequent analysis.

In the next section, we will review possible improvements to the device and elaborate on downstream applications in a clinical context.

3. Future outlook

3.1. Improvements to the device

On one hand, from a technical point of view, several improvements could be achieved.

First, magnetophoretic performances could be enhanced by reaching micro-magnet magnetization saturation, which can be achieved by applying a magnetic field superior to 2.5 T, which cannot be achieved with permanent magnets, but could be with superconducting magnets.

Second, during the sample injection step, cell sedimentation occurs within the input reservoir, which could lead to target cell loss. To prevent from this phenomenon, small agitation can be added in parallel to the injection to maintain the cells in suspension. Since the sample suspension is composed of cancer cells, magnetically labeled white blood cells, and free magnetic nanoparticles, a pulsed magnetic field could be applied regularly by a coil surrounding the input reservoir. This way, it would cause the liquid to agitate and avoid cells to sediment at the reservoir bottom.

Third, another improvement would consist in removing excess nanoparticles that did not bound to white blood cells during the labeling step. Although it did not appear like their presence affected trapping performance and subsequent analysis, they could be easily removed by adding a size-based hydrodynamic step given the size of the magnetic nanoparticles (500 nm) compared to the cells. The size-based separation of particles is an established field of research in microfluidics and a variety of techniques could be implemented for this purpose (DLD, micro-vortices, inertial focusing, etc.). This additional microfluidic feature could be performed before the entrance within the magnetic-based trapping chamber.

On the other hand, from an end-user perspective, we could imagine developing a fully integrated microfluidic platform with the following stages: magnetic purification (presented in this study), 3D cell culturing, and secretion detection. This could be achieved thanks to the multi-disciplinary collaboration between three institutes, involving several research fields: microfluidics (Institut des Nanotechnologies de Lyon, INL), magnetism (Institut Lumière Matière, ILM), biosensing (INL), and CTC-related biological analyses (Hospices Civils de Lyon, HCL). It is envisioned to integrate into this future platform three modules: (i) sorting and purification of CTCs by specific magnetic capture of WBCs; (ii) 3D culture of collected CTCs in microfluidic cell culture microreactors for spheroid formation and injection of different treatments; (iii) label-free detection of characteristic biomarkers secreted by CTCs using a nanoplasmonic biosensor for treatment response study. This microfluidic platform should be compatible with routine use and enable the deciphering of anticancer drug efficacy and resistance mechanisms from secreted biomarker monitoring.

3.2. Clinical applications

The added value of the developed magnetophoretic-based microfluidic device has been validated on cell lines and must now be tested in a clinical context with patient blood samples. The clinical study has for aim to isolate CTCs from blood samples of patients with metastatic non-small-cell lung cancer (NSCLC) and ensure that the magnetic purification step preserves CTC viability and characteristics for subsequent *in vitro* and *in ovo* cultures. After CTC enrichment and purification through the two-step workflow presented earlier, recovered CTCs would be cultured for three days in 3D (cellular growth) before proceeding to *in ovo* culture for tumor growth. Tumor cell transcriptomics would then be determined by RNA-sequencing. In parallel, if the number of patient blood samples allows it, recovered CTCs would be cultured in 3D and drug susceptibility testing would be monitored. CTC viability after drug exposure would be determined by Live/Dead assay. In addition, CTC counts could be determined after the two-step separation as a prognosis value. All these steps are summarized in Figure 5.1.

The study should gather the expertise of three teams: INL (magnetic purification step), HCL (clinical sample processing and *in vitro* culture), and the company Inovotion (*in ovo* culture).

The group plans to conduct *in ovo* cultures following Inovotion's experimental model, the chick embryo chorioallantoic membrane (CAM), which has proven to be highly suitable for tumor engraftment due to the membrane vascularization and absence of a fully developed immune system until day 18 of embryo development.

Finally, this study aims to develop a tool for tumor molecular characterization (*in ovo* culture and RNA-seq study) and treatment efficacy prediction (*in vitro* 3D culture and Live/Dead assay).

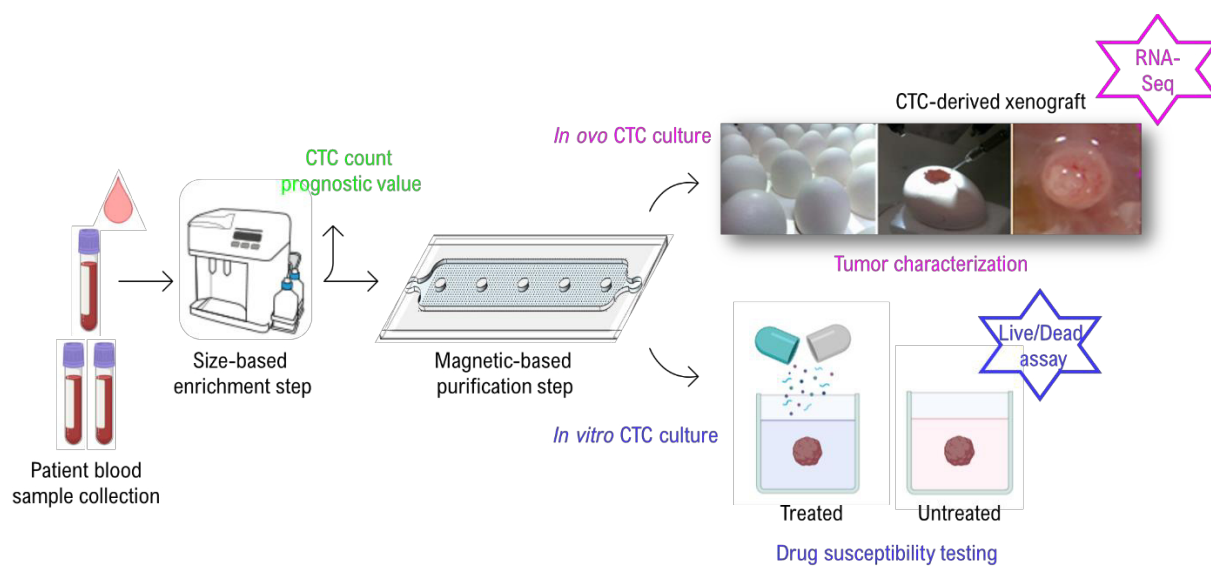


Figure 5.1: Workflow clinical application. Recovered CTCs from patient blood samples are collected for subsequent *in ovo* culture and, if the number of blood sample allows it, *in vitro* culture, aiming at determining tumor molecular characteristics and predicting response to treatment, respectively.

List of publications

1. **Descamps, L.**, Howard, J., Garcia, J., Mekkaoui, S., Audry, M-C., Laurenceau, E., Payen, L., Le Roy, D., Deman, A-L. Self-Assembled Permanent Micro-Magnets in a Polymer-Based Microfluidic Device for Magnetic Cell Sorting. *Cells* 10(7), 1734 (2021).
2. **Descamps, L.**, Le Roy, D., Tomba, C., Deman, A-L. Magnetic Polymers for Magnetophoretic Separation in Microfluidic Devices. *Magnetochemistry* 7(7), 100 (2021).
3. Mekkaoui, S., **Descamps, L.**, Audry, M-C., Deman, A-L., Le Roy, D. Nanonewton magnetophoretic micro-trap array for microsystems. *Langmuir* 36(48), 14546–14553 (2020).
4. **Descamps, L.**, Mekkaoui, S., Audry, M-C., Deman, A-L., Le Roy, D. Optimized process for the fabrication of PDMS membranes integrating permanent micro-magnet arrays. *AIP Advances* 10, 015215 (2020).

List of communications

Oral presentations

1. IEEE International Magnetism virtual conference (Intermag 2021). *Online*.
2. The 36th International Symposium on Microscale Separations and Bioanalysis (MSB 2020). *Online*. **Rewarded with a Young Scientist Award.**
3. The 2nd Workshop on Cancer Cell-On-Chip, 2019. *Lyon, France*.

Posters

1. Oncology Research in Auvergne-Rhône-Alpes Workshop (CLARA 2021). *Online*. “My poster in 300 seconds”.
2. The 24th International Conference on Miniaturized Systems for Chemistry and Life Sciences (μ TAS 2020). *Online*.
3. The 64th Annual Conference on Magnetism and Magnetic Materials (MMM 2019). *Las Vegas, USA*.
4. The 23rd International Conference on Miniaturized Systems for Chemistry and Life Sciences (μ TAS 2019). *Basel, Switzerland*.
5. The Joint European Magnetic Symposia (JEMS), 2019. *Uppsala, Sweden*.
6. Microfluidics Summer School, 2019. *Sète, France*.

Résumé en français

1. Introduction

1. Contexte : étude des CTCs

Le diagnostic précoce et le développement d'une médecine personnalisée constituent les principaux objectifs des travaux de recherche menés sur le cancer. Identifié tôt, le cancer a plus de chances de répondre à la thérapie, améliorant donc les chances de survie. Toutefois, au stade précoce de la maladie, la petite taille de la tumeur primaire, ainsi que l'absence de symptômes, rendent son dépistage difficile. Par ailleurs, l'efficacité des thérapies varie d'un patient à l'autre et il devient nécessaire de suivre la réponse aux traitements afin de les personnaliser. À ce jour, les biopsies de tissus sont utilisées pour la prise en charge des patients atteints de cancer pour diagnostiquer, évaluer le stade de la maladie et prescrire des régimes thérapeutiques appropriés. Cependant, les biopsies tissulaires sont non seulement invasives et risquées, mais elles peinent aussi à refléter l'hétérogénéité intra-tumorale [1]. Pour toutes ces raisons, les biopsies tissulaires solides ne permettent pas d'obtenir un suivi régulier de l'évolution de la tumeur.

L'étude des cellules tumorales circulantes (CTC), complémentaire des biopsies tissulaires, peut surmonter ces limites [2]. Les CTCs sont libérées dans la circulation sanguine par les tumeurs primaires et métastatiques, et sont impliquées dans le développement de métastases (Figure 1) [3]. Elles offrent un potentiel clinique prometteur pour le diagnostic et le pronostic du cancer [4]. L'isolation des CTCs directement à partir d'une analyse de sang, appelée "biopsie liquide", a donc suscité un vif intérêt ces dernières années. Ces échantillons peuvent être collectés de manière non invasive et fréquente, ce qui permet de suivre en temps réel l'évolution de la tumeur et la réponse au traitement. La biopsie liquide peut conduire à des changements de paradigme du diagnostic et de la gestion du cancer en permettant un diagnostic plus précoce et de meilleurs traitements personnalisés.

Néanmoins, jusqu'à présent, l'isolation des CTCs a été un défi technique limitant leur utilisation plus répandue dans la recherche et les études cliniques. Le premier défi est la rareté des CTCs (1-1000 CTCs par mL) parmi de nombreuses cellules du sang (10^9 globules rouges et 10^7 globules blancs par mL). L'autre défi est leur hétérogénéité phénotypique, car les CTCs peuvent subir une transition épithéliale-mésenchymateuse (TEM) [5], se traduisant par une diminution de l'expression des marqueurs épithéliaux et une plasticité phénotypique accrue. Enfin, la méthode d'isolation des CTCs doit permettre la préservation de leur viabilité et intégrité afin de pouvoir conduire des études ultérieures (culture cellulaire, caractérisation moléculaire, etc.).

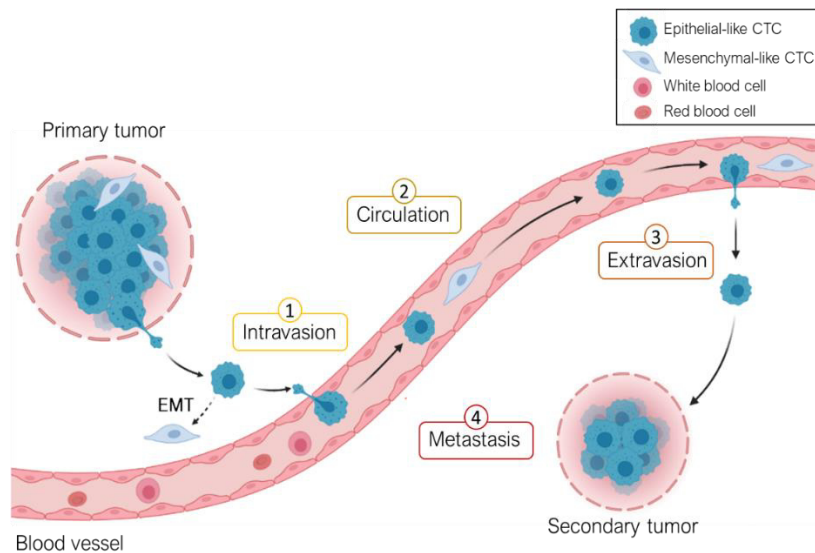


Figure 1 : Rôle des CTCs dans la formation de métastases. Détachement des CTCs de la tumeur primaire et leur (1) invasion dans la circulation sanguine, (2) survie dans la circulation, (3) extravasation, et (4) colonisation de sites distants (tumeur secondaire). Les CTCs peuvent subir une transition épithéliale-mésenchymateuse (EMT) leur octroyant une plus grande plasticité et capacité d'invasion.

Le système CellSearch™ (Veridex, États-Unis) a été le premier instrument disponible pour l'isolation des CTCs et reste le seul test approuvé par la Food and Drug Administration (FDA) pour l'énumération des CTCs dans le but de prédire l'issue de la maladie. La méthode repose sur l'enrichissement des CTCs exprimant des marqueurs de surface épithéliaux (EpCAM) via l'utilisation de particules immunomagnétiques. Bien que ce système soit la référence pour la détection des CTCs, la sensibilité de la détection dépend fortement des marqueurs épithéliaux, et par conséquent les cellules dépourvues de ces marqueurs ne sont pas détectées [6]. En plus d'une récupération relativement faible, une faible pureté a été observée, car les CTCs sont enrichies avec un nombre élevé de globules blancs contaminants, ce qui limite le panel de caractérisations possibles.

2. Isolation des CTCs en microfluidique

Au cours de la dernière décennie, les dispositifs microfluidiques sont apparus comme des outils prometteurs pour remédier à ces limitations. Ils sont rentables et polyvalents (possibilité d'intégration de plusieurs fonctions sur une puce) et, en raison de leurs dimensions micrométriques et des flux laminaires associés, il est possible de réaliser une manipulation précise des cellules et une étude à l'échelle de la cellule unique. La manipulation de petites quantités de volume facilite également l'analyse de ces échantillons rares et accélère les processus. Plusieurs technologies microfluidiques, en attente d'autorisation par la FDA, ont été commercialisées pour l'isolation des CTCs, comme Parsortix™ (ANGLE plc, UK) [7], ClearCell® FX1 (Biolidics, Singapour) [8] et VTX-1 (Vortex Biosciences, USA) [9]. Ces technologies sont basées sur la différence de taille et de déformabilité des CTCs par rapport aux cellules du sang. D'autres propriétés physiques telles que la densité et les charges électriques, peuvent être exploitées [10]. Les principales méthodes de séparation physique reposent sur la microfiltration (structures micrométriques intégrées), l'hydrodynamique (forces d'inertie en microfluidique) et la diélectrophorèse (application de champs électriques). Un résumé des avantages et inconvénients de chacune des techniques est donné Tableau 1. Les méthodes de séparation physiques ont l'avantage de ne pas nécessiter de marquage et d'offrir un débit élevé, mais leur faible pureté limite les analyses.

Les propriétés biologiques, essentiellement l'expression de marqueurs de surface, peuvent également être exploitées pour le développement de dispositifs microfluidiques de séparation des CTCs. Ces méthodes reposent sur la grande spécificité de la liaison anticorps-antigènes des cellules cibles. L'isolation des CTCs peut être réalisée soit par sélection positive, les CTCs étant la population ciblée, soit par sélection négative, les globules blancs (GBs) étant les cellules cibles. Les méthodes de séparation biologiques peuvent être classées en deux catégories : l'approche par affinité de surface par fonctionnalisation des canaux microfluidiques et l'approche immunomagnétique utilisant des

particules magnétiques fonctionnalisées. Les avantages et limitations de chacune de ces techniques sont résumés dans le Tableau 2. Les méthodes de séparation biologiques (affinité de surface et séparation immunomagnétique) permettent d'obtenir une sensibilité et une spécificité élevées, et donc une plus grande pureté, par rapport aux méthodes de séparation physiques.

Tableau 1 : Avantages et limitations des principales méthodes de séparation basées sur les propriétés physiques des CTCs.

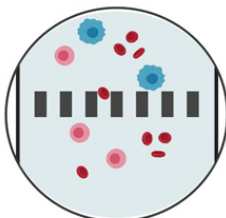

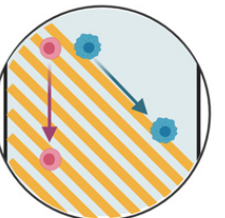
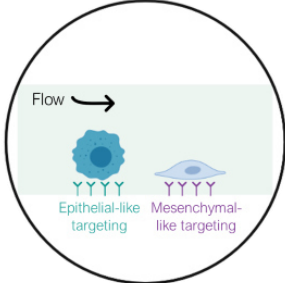
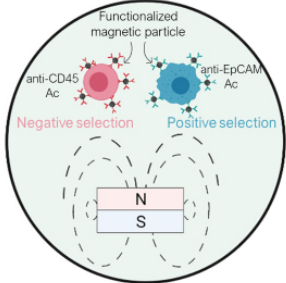
Méthode de séparation			
	Microfiltration	Hydrodynamics	Dielectrophoresis
Critère de séparation	Taille, déformabilité	Taille, déformabilité	Taille et propriétés diélectriques
Avantages	Débit élevé, pas de marquage	Débit élevé, pas de marquage, récupération aisée des CTCs	Sans marquage, récupération des CTCs
Inconvénients	Risque de colmatage, pureté faible, récupération des CTCs limitée	Pureté limitée	Débit faible, separation limitée dans le temps, mise en oeuvre difficile

Tableau 2 : Avantages et limitations des principales méthodes de séparation basées sur les propriétés biologiques des CTCs.

Méthode de séparation		
	Surface affinity	Immunomagnetic
Critère de séparation	Marqueurs de surface des cellules	Propriétés magnétiques des particules et expression des marqueurs de surface des cellules
Avantages	Sensibilité, spécificité et pureté élevée	Sensibilité, spécificité et pureté élevée, débit élevé, récupération des CTCs
Inconvénients	Débit faible, récupération des CTCs difficile, dépend de l'expression des marqueurs	Etape de marquage magnétique

Malgré l'ensemble des recherches menées dans les dispositifs d'isolation des CTCs, il reste des défis spécifiques aux CTCs qui doivent être relevés. En effet, l'hétérogénéité de la taille des CTCs et des marqueurs tumoraux expliquent la difficulté d'atteindre une grande pureté et de réaliser des analyses ultérieures. Toutefois, l'approche par séparation immunomagnétique est particulièrement prometteuse car elle représente un bon compromis entre le débit, la pureté, la sensibilité et l'analyse en aval (récupération des CTCs). La séparation immunomagnétique repose sur la magnétophorèse, qui désigne le mouvement de particules magnétiques ou de cellules marquées magnétiquement lorsqu'elles sont soumises à un champ magnétique non uniforme. Cette thèse s'inscrit dans le cadre de la séparation par magnétophorèse, cette stratégie sera donc décrite plus en détail dans la partie suivante.

3. Enjeu de la séparation magnétophorétique

La magnétophorèse a démontré être une méthode efficace de tri d'entités biologiques, aussi bien pour la manipulation d'ADN [11], de protéines [12] et de cellules [13], notamment de globules rouges désoxygénés [14]. Cette stratégie bénéficie de plusieurs avantages : (i) la manipulation sans contact, qui rend cette technique non destructive pour les échantillons biologiques et préserve la viabilité des cellules ; (ii) la spécificité, puisque les champs magnétiques augmentent le contraste magnétique des objets non magnétiques, soit en utilisant des marqueurs magnétiques, soit à l'aide de fluides magnétiques [15], (iii) la faible sensibilité aux paramètres du milieu, tels que les charges de surface, la concentration ionique, le pH et la température ; et (iv) le contrôle fin de la force magnétique, puisque cette dernière dépend de la taille des particules, des propriétés magnétiques de l'objet cible et du milieu, ainsi que du gradient du champ magnétique. L'expression de la force magnétique (\vec{F}_{mag}) est donnée Equation 1, où V_p est le volume de la particule cible, M_p son aimantation et B le champ magnétique appliqué.

$$\vec{F}_{mag} = V_p(\vec{M}_p \cdot \vec{\nabla})\vec{B} \quad (1)$$

En particulier, lorsque la magnétophorèse est mise en œuvre en microfluidique, la force magnétique est en compétition avec plusieurs autres forces (Figure 2), celles-ci étant la force de trainée du fluide (\vec{F}_{drag}), la force gravitationnelle (\vec{F}_{grav}) et la force de flottaison (\vec{F}_{buo}).

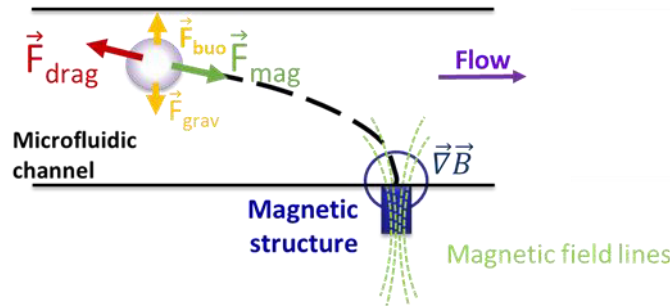


Figure 2 : Forces en compétition dans un système microfluidique intégrant des structures magnétiques.

Les forces de gravitation et de flottaison sont négligées pour des particules submicrométriques ou nanométriques. La force de trainée est donc la principale force opposant la force magnétique. Elle dépend de la viscosité du milieu (η), du rayon de la particule (R_p), de la vitesse relative de la particule (v_p) dans la direction de la force magnétique et celle du fluide porteur (v_f). Son expression est donnée Equation 2.

$$\vec{F}_{drag} = -6\pi\eta R_p(\vec{v}_p - \vec{v}_f) \quad (2)$$

Finalement, la deuxième loi de Newton, pour une particule submicrométrique (masse négligeable), permet d'obtenir l'expression de l'équilibre des forces (Equation 3).

$$V_p(\vec{M}_p \cdot \vec{\nabla})\vec{B} = 6\pi\eta R_p(\vec{v}_p - \vec{v}_f) \quad (3)$$

Ainsi, les performances de la séparation magnétophorétique peuvent être optimisées par un choix judicieux des propriétés de la particule (R_p, M_p), des caractéristiques du fluide (η, χ_f), et du débit du flux (v_f). En particulier, la génération de forts gradients de champ magnétique ($\vec{\nabla}B$) peut permettre de surmonter la force de traînée. De nombreux travaux ont été menés pour atteindre des forces magnétiques élevées et réaliser ainsi une séparation efficace [16]. L'intégration de sources magnétiques micrométriques dans des dispositifs microfluidiques s'est avérée être la stratégie la plus appropriée, car les sources magnétiques à l'échelle micrométrique génèrent de forts gradients de champ magnétique à leur surface [17].

4. *Intégration de micro-sources magnétiques et enjeux de l'approche polymères composites*

Trois approches principales sont utilisées pour générer des micro-sources de gradients de champ magnétique localisées : les micro-bobines conduisant le courant, les micro-concentrateurs constitués de ferromagnétiques doux (principalement Ni et alliages Fe-Ni) aimantés dans un champ magnétique externe, et les micro-aimants à aimantation permanente, constitués de matériaux ferromagnétiques durs (généralement NdFeB). Malgré la flexibilité de contrôle de l'intensité du champ magnétique lors de l'utilisation de micro-bobines, l'échauffement par effet Joule limite le champ magnétique à quelques dizaines de mT lorsqu'il fonctionne dans des conditions statiques [18]. En revanche, les micro-concentrateurs et les micro-aimants peuvent produire des champs magnétiques relativement puissants (d'une fraction de Tesla) et sont donc particulièrement adaptés aux applications de séparation en microfluidique. Néanmoins, des défis subsistent en ce qui concerne la complexité de la microfabrication des micro-sources magnétiques et leur intégration dans des systèmes microfluidiques fabriqués à base de polymères. Les méthodes de microfabrication basées sur les films, dans lesquelles les éléments magnétiques sont intégrés par des techniques telles que la pulvérisation [19], l'électrodéposition [20], l'évaporation [21] ou le modelage thermo-magnétique [22], ont permis un contrôle inégalé de la reproductibilité, de la forme et de la microstructuration. Cependant, ces approches souffrent d'une mauvaise adhésion avec les substrats polymères, de la difficulté d'obtenir des microstructures de grand aspect de forme, et nécessitent des processus de fabrication coûteux et fastidieux.

Les polymères composites sont apparus récemment comme une solution idéale pour l'intégration compatible et peu coûteuse de matériaux magnétiques dans les dispositifs microfluidiques à base de polymères [23]. Les polymères composites magnétiques sont obtenus en dopant une matrice polymère avec des particules magnétiques. Cette approche permet de personnaliser la fonction magnétique en jouant sur la nature, la taille, la concentration et la morphologie de la particule magnétique, sur la nature de la matrice polymère et sur la méthode de microstructuration. En particulier, le composite à base de polydiméthylsiloxane (PDMS) est le plus couramment rencontré en raison des propriétés de microfabrication du PDMS par lithographie douce et de l'utilisation massive de ce dernier pour la réalisation de systèmes microfluidiques.

L'approche des composites PDMS magnétiques a été développée au sein du laboratoire depuis une dizaine d'années pour la manipulation d'objets en microfluidique [24–26]. Cette thèse s'inscrit dans la continuité de ces travaux et explorera son application pour l'isolation des CTCs.

5. *Objectifs de la thèse*

La thèse a pour objectif de développer un dispositif microfluidique pour l'isolation des CTC par déplétion des GBs (sélection négative) par magnétophorèse. L'avantage de la sélection négative par rapport à la sélection positive est la possibilité de collecter tous les CTC indépendamment de l'expression de leur marqueur de surface. Le dispositif microfluidique intégrera des réseaux de micro-aimants, agissant comme des micro-pièges, obtenus par l'approche composite. Ce projet résulte d'une collaboration pluridisciplinaire, avec des acteurs des domaines de la microfluidique (INL-Lyon 1), du magnétisme (Institut Lumière Matière, ILM), de la chimie (INL-Centrale), et de la biologie (Hospices Civils de Lyon, HCL). Etant donné la forte concentration de GBs dans le sang, la puce magnétique développée sera combinée à une étape de pré-enrichissement dans le ClearCell FX1® (Biolidics), un système utilisé aux HCL pour des études cliniques. La séparation immunomagnétique aura pour but d'améliorer la pureté de cette première étape de séparation par la taille et ainsi faciliter les

caractérisations ultérieures. Les GBs restants seront capturés au sein de la puce et les CTCs seront récupérées en sortie. Le dispositif devra donc montrer une bonne déplétion des GBs et récupération des CTCs, un débit de travail élevé, ainsi qu'une compatibilité avec des caractérisations biologiques de routine. Son principe est illustré dans la Figure 3.

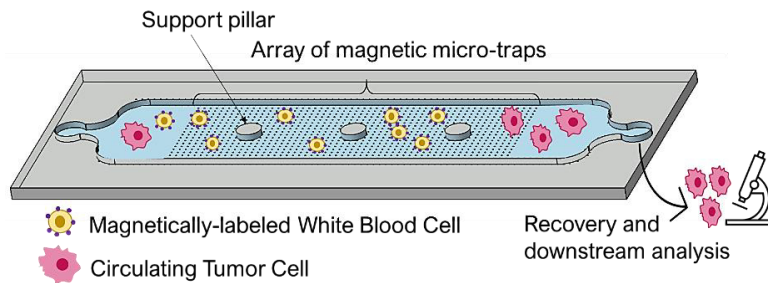


Figure 3 : Isolation des CTCs après piégeage de GBs marqués magnétiquement dans le dispositif microfluidique intégrant des micro-aimants obtenus par l'approche composite.

Le travail de thèse a pu être divisé en plusieurs étapes :

- Fabrication des micro-aimants par l'approche composite et caractérisation de leurs performances magnétiques.
- Intégration dans un dispositif microfluidique et optimisation des performances de piégeage.
- Etude de la compatibilité de la puce magnétique avec les analyses biologiques de routine
- Application à l'isolation des CTCs à partir de sang total après un premier système d'enrichissement par la taille.

2. Fabrication et caractérisation de micro-aimants auto-organisés et intégrés dans un dispositif microfluidique

Dans cette partie sera détaillé le procédé de fabrication des membranes composites de NdFeB@PDMS (particules de NdFeB dans une matrice de PDMS). En particulier, l'influence de la nature du champ magnétique appliqué lors de la fabrication du composite de NdFeB@PDMS sur sa microstructure et ses propriétés magnétiques a été étudiée et sera présentée. Pour ce faire, diverses méthodes de caractérisation ont été mises en œuvre afin de proposer une étude complète des micro-aimants fabriqués. Des calculs numériques utilisant la modélisation par éléments finis (Comsol Multiphysics®) ont été réalisés pour estimer les champs magnétiques et les gradients de champ magnétique en jeu, ainsi que des mesures expérimentales basées sur la microscopie à force atomique (AFM) à sonde colloïdale et sur des expériences hydrodynamiques en microsystème pour déterminer les forces magnétiques générées. En outre, des expériences microfluidiques mettant en œuvre des billes superparamagnétiques comme objets cibles ont été conduites pour démontrer la capacité de séparation magnétophorétique des micro-aimants intégrés, agissant comme des micro-pièges.

1. Fabrication et structuration

La fabrication de micro-aimants est basée sur l'approche composite qui consiste à mélanger une poudre magnétique dure avec un matériau polymère. Des membranes composites NdFeB@PDMS ont été fabriquées avec des concentrations variant de 1 à 4 w% de NdFeB (fraction massique). Les étapes de fabrication des micro-aimants sont présentées dans la Figure 4. Brièvement, le composite est préparé à partir d'un mélange contenant des microparticules de NdFeB (0.5-7 μm , Magnequench) et du PDMS non polymérisé (Sylgard™, Samaro). Le composite est ensuite versé dans un moule en Kapton (100 μm d'épaisseur) collé à un substrat (étape 1, Figure 4). Après avoir retiré le moule, laissant une couche de composite de 100 μm d'épaisseur, le composite est cuit pendant 2h à 70°C en présence d'un champ magnétique de 300 mT généré par un aimant de NdFeB (60 x 30 x 15 mm³) (étape 2, Figure 4). Pendant l'étape de réticulation du PDMS, les particules de NdFeB sont libres de se déplacer dans le polymère liquide et de s'auto-organiser sous l'effet des interactions dipolaires magnétiques. Après le durcissement, les particules de NdFeB sont immobilisées dans la matrice polymère. L'épaisseur de la

membrane composite est ensuite augmentée jusqu'à 2 mm en versant du PDMS liquide sur celle-ci (étape 3, Figure 4). La membrane est polymérisée à 70°C pendant 2 heures et décollée du substrat (étape 4, Figure 4). Enfin, les microstructures de NdFeB@PDMS sont aimantées sous un champ magnétique d'environ 1 T généré par un système d'aimantation fait maison (étape 5, Figure 4).

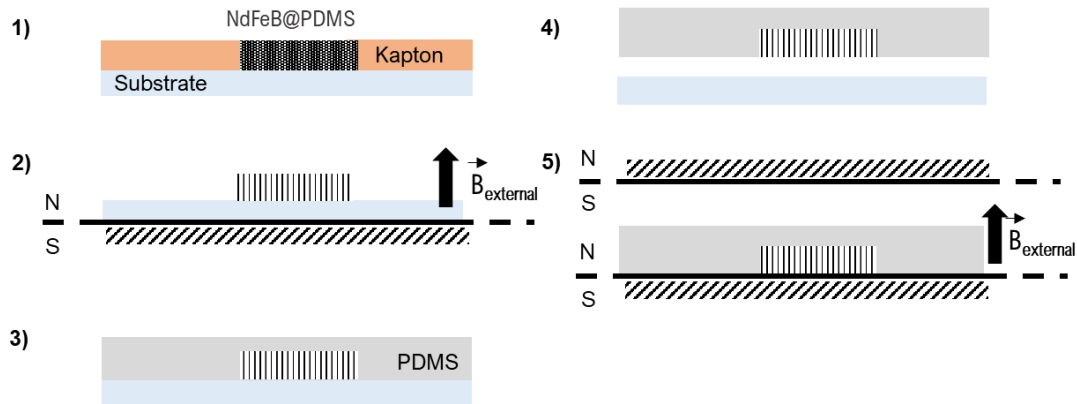


Figure 4 : Etapes de fabrication des micro-aimants par l'approche composite.

Nous avons utilisé deux substrats différents pour préparer le composite, soit (i) une lame de verre silanisée, soit (ii) un motif magnétique en FeC@PDMS, et avons étudié leur impact sur la microstructure du composite NdFeB. Le motif magnétique FeC@PDMS consiste en une membrane composite ferromagnétique douce composée de microparticules de carbonyle de fer auto-organisées (poudre à base de 97% de Fe, 0,5-7 μm de diamètre, Sigma-Aldrich) dans du PDMS (fraction massique de 7,5%). En utilisant la lame de verre, la membrane composite est uniquement soumise au gradient de champ magnétique généré par l'aimant massif externe pendant l'étape de réticulation, estimé à 20 T/m à partir de simulations numériques (Comsol Multiphysics®). En présence de la membrane magnétique douce, qui contient des agglomérats en chaîne de microparticules de Fe orientées dans la direction perpendiculaire à la surface du substrat, de forts gradients de champ magnétique sont générés localement, d'environ 10^5 T/m aux positions des chaînes selon les résultats des simulations Comsol® [27]. Ces deux configurations seront donc dénommées respectivement comme étant à gradients faibles ou gradients élevés.

2. Caractérisation de la microstructure des micro-aimants

La caractérisation de la microstructure des micro-aimants a été réalisée dans le volume du composite par tomographie à rayons X et en surface par microscopie optique. L'influence des deux configurations de préparation (gradients faibles et gradients élevés) sur celle-ci a notamment été étudiée. Il est intéressant de mentionner la complémentarité des observations par tomographie à rayons X et par microscopie optique. En effet, la tomographie à rayons X permet une observation 3D de la microstructure du composite, avec une haute résolution (300 nm). Au contraire, la microscopie optique fournit une étude 2D du réseau de micro-aimants, et malgré sa résolution plus faible, elle permet d'analyser de nombreux échantillons, à faible coût, fournissant ainsi des mesures statistiques. En outre, la microscopie optique renvoie une image du réseau de micro-aimants en se concentrant sur les micro-aimants de surface, ce qui est intéressant car ils représentent les micro-pièges les plus efficaces lors des expériences microfluidiques. Les images obtenues en tomographie à rayons X et microscopie optique ont été analysées avec le logiciel ImageJ.

L'étude de la structure des composites a révélé que l'approche composite conduit à la formation d'agglomérats de particules de NdFeB en forme de chaîne (anisotropie uniaxiale). Elle permet la préparation de réseaux denses de micro-aimants (>1000 micro-aimants/ mm^2), d'environ 5 μm de diamètre, avec un rapport d'aspect élevé. En particulier, la caractérisation de la microstructure des micro-aimants par tomographie, représentée Figure 5, a mis en exergue les différences dans le processus d'auto-organisation des particules selon la nature du champ appliqué (gradients faibles ou élevés) lors de la fabrication des micro-aimants.

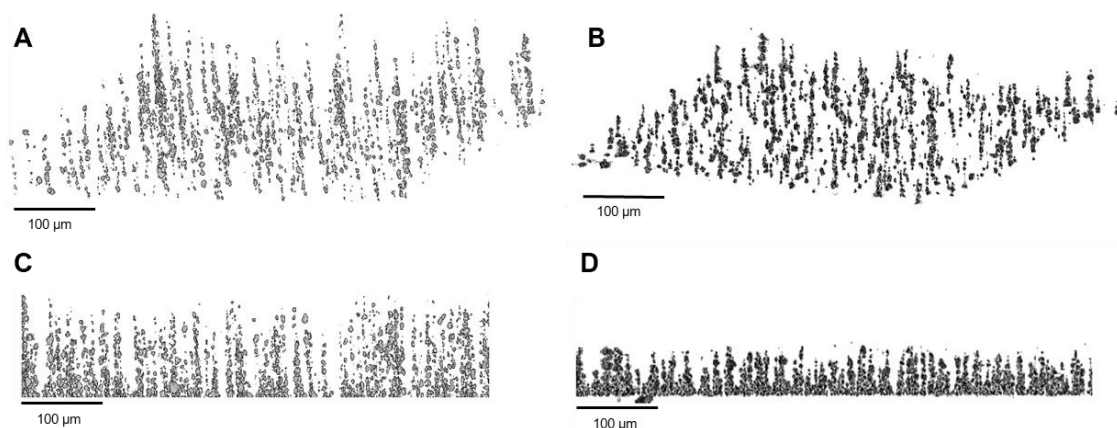


Figure 5 : Vues reconstruites à partir de la tomographie à rayons X d'une membrane ($510 \times 510 \times 120 \mu\text{m}^3$) à 2 w% de NdFeB. (A,B) Vues 3D pour respectivement les configurations à gradients faibles et élevés. (C,D) Projections sur le plan XZ pour respectivement les configurations à gradients faibles et élevés.

Plusieurs valeurs caractéristiques des micro-aimants ont été extraites de l'analyse ImageJ. Les analyses 2D dans le plan XY ont permis de déterminer la densité, le diamètre et la distance du plus proche voisin (nnd) des micro-aimants, tandis que les analyses 2D dans le plan XZ ont permis de caractériser les agglomérats en chaîne en mesurant la longueur de la chaîne, la distance inter-particule ainsi que le rapport agglomérats en chaîne (CA)/agglomérats isotropes (IA). Les agglomérats isotropes sont des agglomérats de taille inférieure à $7 \mu\text{m}$. Ils sont principalement situés au fond de la membrane. Les mesures obtenues pour des composites à 2 w% en NdFeB sont résumées dans le Tableau 3.

Tableau 3 : Influence de la configuration magnétique sur les caractéristiques des micro-aimants (2w% NdFeB) d'après les observations en tomographie à rayons X de la structure 3D.

Configuration	Densité (mm^{-2})	Diamètre (μm)	Nnd (μm)	Longueur chaîne (μm)	Distance inter- particule (μm)	Rapport CA/IA (%)
Gradients faibles	1465	4.9	15	75	1.2	80/20
Gradients élevés	1700	4.8	15	25	0.95	56/54

L'application de gradients élevés conduit à la formation de chaînes plus courtes et compactes, et localisées plus en surface de la membrane. Elle conduit également à une densité de micro-aimants plus élevée, avec un nombre plus important d'agglomérats isotropes.

Par ailleurs, la microscopie optique a mis en évidence la distribution ordonnée des micro-aimants en surface de la membrane composite. En effet, la distribution expérimentale de la distance au premier voisin est mieux décrite par une distribution normale que par une distribution de Poisson (Figure 6), cette dernière décrivant des événements indépendants (distribution aléatoire). Cette étude a donc montré que la fabrication par approche composite conduit à une auto-organisation des micro-aimants non aléatoire.

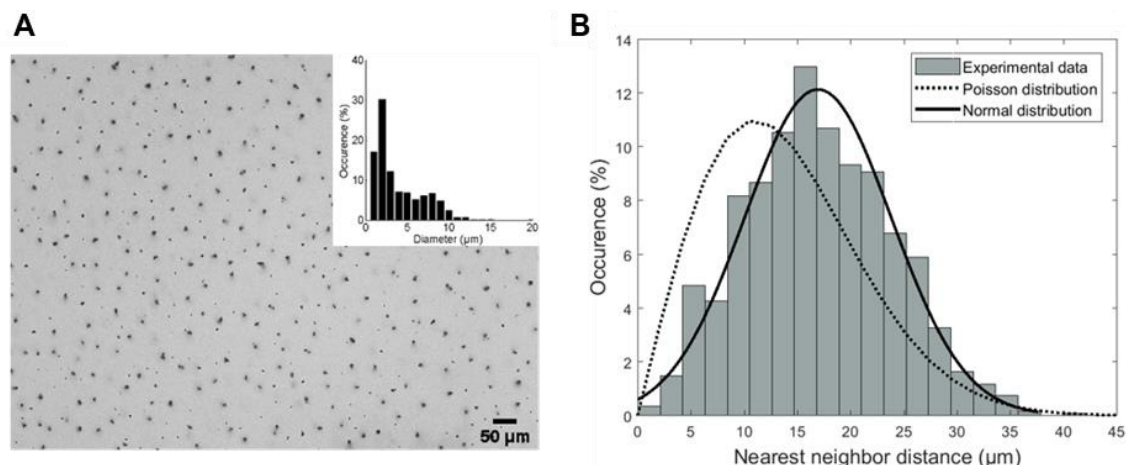


Figure 6 : Caractérisation de l’auto-organisation des micro-aimants (2w% NdFeB) à la surface du composite par microscopie optique. **(A)** Image optique du réseau de micro-aimants et inset de la distribution du diamètre mesuré. **(B)** Distribution expérimentale de la distance au premier voisin et comparaison avec des lois théoriques.

Il est intéressant de mentionner que l'utilisation d'un motif magnétique (Fe-C@PDMS) pendant la préparation du composite conduit à un réseau de micro-aimants plus hétérogène et moins reproductible d'un échantillon à l'autre d'après les caractéristiques mesurées. Ce manque de reproductibilité peut s'expliquer par la nature plus douce du substrat magnétique par rapport à une lame de verre, dont la surface dure rend l'étape de coulée du composite plus facile et plus répétable. En outre, l'hétérogénéité de la structure du composite pourrait également entraîner une hétérogénéité des performances magnétiques.

3. Intégration dans un dispositif microfluidique

Le réseau de micro-aimants a été intégré dans un système microfluidique pour évaluer ses performances de séparation magnétophorétique d'objets magnétiques (billes magnétiques ou globules blancs marqués magnétiquement). Les membranes de NdFeB@PDMS ont été collées de manière irréversible à des canaux microfluidiques en PDMS par collage plasma. Les moules des micro-canaux ont été obtenues par lithographie douce. Deux modèles ont été fabriqués en fonction de l'application souhaitée : un premier canal droit pour les expériences de caractérisation des performances des micro-pièges en utilisant des billes superparamagnétiques comme cibles (Figure -A) et un second modèle plus complexe pour les expériences finales sur les cellules (Figure 7-B). Pour cette deuxième conception, plusieurs exigences ont dû être satisfaites : (i) développer une grande chambre de piégeage pour intégrer un grand nombre de micro-pièges ; (ii) optimiser le remplissage du liquide dans la chambre et empêcher la formation de bulles d'air ; et (iii) intégrer des piliers de support pour éviter l'effondrement du toit de la chambre en raison du rapport important entre la largeur (20 mm) et la hauteur (100 μm) de la chambre.

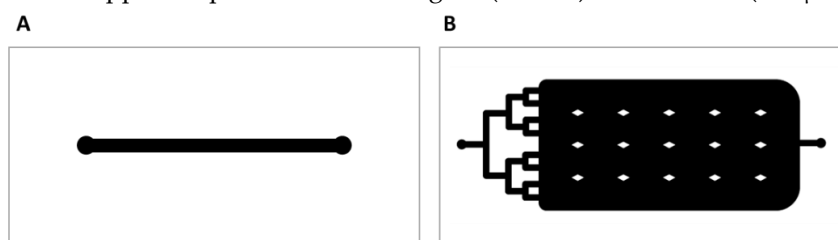


Figure 7 : Designs des moules de canaux. **(A)** Canal droit (45x0,5x0,1 mm³) pour les expériences de piégeage de billes superparamagnétiques. **(B)** Chambre de capture (45x20x0,1 mm³) pour la sélection négative des CTC. Les canaux d'entrée et de sortie ont une largeur de 970 μm. Les piliers de support en forme de diamant ont une largeur de 1 mm (petite diagonale) et une hauteur de 2 mm (grande diagonale).

Les performances magnétophorétiques des micro-aimants ont été étudiées, d'abord numériquement, puis expérimentalement.

4. Simulation des micro-aimants par éléments finis

Les propriétés magnétiques des micro-aimants organisés à 2w% de NdFeB dans la matrice PDMS ont été modélisées à l'aide d'une approche par éléments finis (COMSOL, module AC/DC), sur la base de mesures SQUID et d'observations par tomographie à rayons X. Un schéma de la configuration modélisée est donné dans la Figure 8-A.

Les mesures SQUID ont permis de déterminer que le champ rémanent des particules, après l'étape d'aimantation, est de 0,54 T. La tomographie à rayons X a révélé que la microstructure 3D des micro-aimants présente une organisation en chaîne, et a permis d'identifier des paramètres géométriques tels que la longueur de la chaîne et la distance inter-particule. Il a donc été intéressant d'étudier l'effet de ces paramètres de microstructure sur les propriétés magnétiques d'un micro-aimant. Des gradients magnétiques s'élevant à 10^5 T/m ont pu être calculés à la surface d'un micro-aimant. L'effet de la microstructure a par ailleurs montré une influence négligeable sur la portée de l'interaction. De plus, l'arrangement des micro-aimants en réseau dense et donc l'effet des chaînes voisines (nombre de chaînes, distance entre elles, etc.) a été étudié. Il a été montré que le gradient de champ magnétique généré par une chaîne située dans un réseau est plus faible que pour une chaîne isolée ou pour une chaîne en bord de réseau, qui sont des manifestations du champ démagnétisant du réseau [28].

Afin d'attirer vers les micro-aimants les cibles circulant dans la partie haute du canal microfluidique, l'effet de l'ajout d'un aimant externe de taille millimétrique, situé sous le composite, a été étudié. D'autres équipes ont plutôt mis en place une structuration des canaux microfluidiques en ajoutant des structures en chevrons sur la paroi supérieure du canal, pour induire une déviation des objets cibles vers les structures magnétiques [29,30]. Leur stratégie est basée sur le mélange chaotique, alors que celle-ci repose sur la génération de champs magnétiques de grande portée. Elle a permis d'augmenter la distance d'interaction des micro-aimants. En effet, le micro-aimant seul génère à sa surface un champ de 200 mT et de forts gradients de champ, estimés à 10^5 T/m d'après les simulations Comsol (Figure 8-B). En revanche, le champ magnétique et le gradient de champ magnétique diminuent ensuite avec la distance au micro-aimant, jusqu'à 0,1 mT et 5 T/m, respectivement, à une distance de 50 μ m. L'utilisation combinée des micro-aimants et des milli-aimants a permis de doubler la valeur du champ magnétique en contact, atteignant 400 mT, et a augmenté sa valeur minimale à l'intérieur du canal, de 0,02 mT à 200 mT. Le champ plus élevé permet d'augmenter le moment magnétique des objets cibles. De plus, à partir d'une certaine distance du micro-aimant, les performances magnétiques du milli-aimant dominent : cette distance atteint 10 μ m pour le champ magnétique et 60 μ m pour le gradient de champ magnétique. Ainsi, il favorise non seulement l'attraction d'objets cibles plus éloignés de la surface mais renforce aussi la force de piégeage (aimantation et gradient de champ magnétique plus élevés).

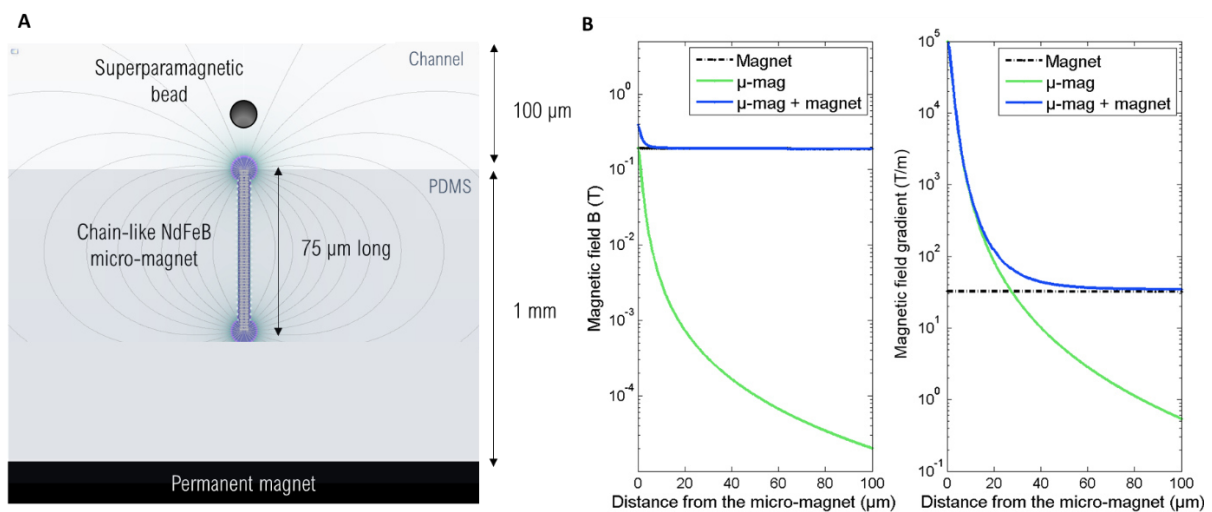


Figure 8 : (A) Modélisation d'une chaîne magnétique sur Comsol d'après les observations en tomographie à rayon X de la structure des micro-aimants. (B) Apport de l'aimant externe millimétrique sur le champ magnétique et le gradient magnétique générés.

Enfin, la force magnétique générée par un micro-aimant sur une bille superparamagnétique modèle a été simulée en utilisant l'outil Comsol « sonde sur domaine » (Figure 9-A). La distance de la bille au micro-aimant a été variée de 0 à 50 μm afin d'évaluer la capacité de piégeage magnétophorétique en microsystème. La simulation, dont les résultats sont représentés Figure 9-B, a permis de montrer que le micro-aimant peut générer des forces magnétiques aussi élevées que 4,6 nN à sa surface. Cette valeur diminue avec la distance à sa surface et s'élève à 1,7 pN à une distance de 50 μm . L'ajout d'un aimant permanent externe a permis d'augmenter la portée d'interaction du micro-aimant d'un facteur 10, la force magnétique atteignant alors 19 pN à une distance de 50 μm .

La force magnétique a été corrigée en prenant en compte le champ démagnétisant, dont le facteur correctif a été estimé à 0,15 pour une chaîne située aux bords du réseau, et à 0,34 pour une chaîne au centre du réseau (Figure 9-C). Celle-ci est légèrement inférieure en tenant compte de l'effet du réseau, atteignant 3,1 nN et 3,9 nN, à la surface d'une chaîne située respectivement au centre du réseau, ou sur ses bords. Ces calculs numériques de la force magnétique ont par la suite été comparés à des mesures expérimentales.

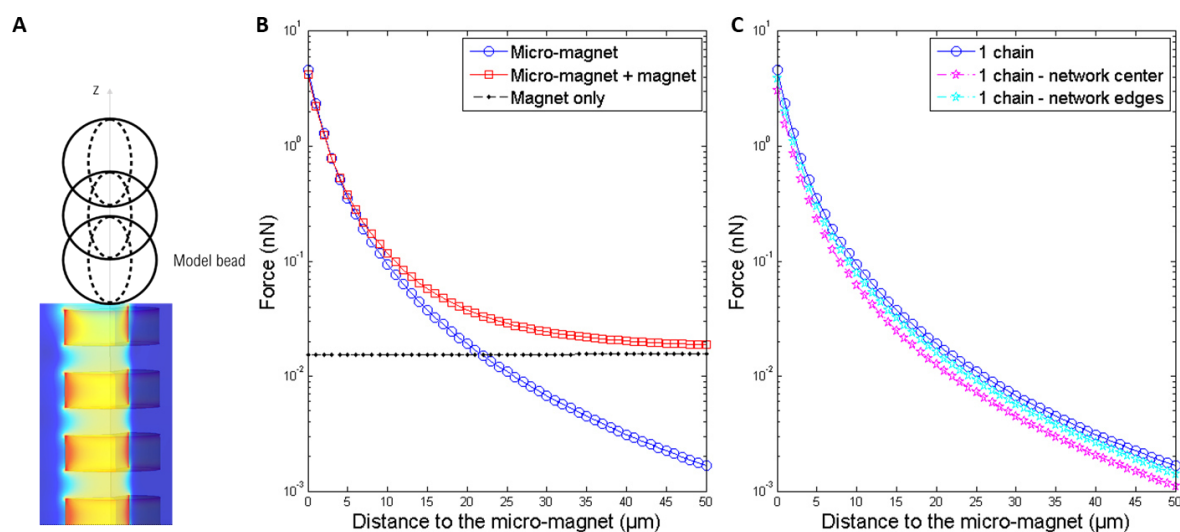


Figure 9 : Calcul de la force magnétique générée par un micro-aimant sur une bille modèle. (A) Schéma de la modélisation sur Comsol. (B) Force magnétique en fonction de la distance à l'aimant et intérêt de l'aimant extérieur sur la portée de la force. (C) Force magnétique calculée en tenant compte de l'effet démagnétisant du réseau de chaînes magnétiques.

5. Mesures expérimentales des forces magnétiques générées

Les forces magnétiques générées par le réseau de micro-aimants ont été déterminées expérimentalement par microscopie à force magnétique à sonde colloïdale (AFM) et par mesure en microfluidique via la force de trainée. L'AFM à sonde colloïdale est une technique de microscopie en champ proche permettant la mesure des forces d'interaction entre la surface de l'échantillon et la pointe d'un levier, sur laquelle a été fixée une bille superparamagnétique (12 μm , Kisker®). Le levier balaye la surface de l'échantillon et la présence de gradients de champ magnétique provoque sa déflexion. En particulier, le balayage magnétique sur la surface du composite a été effectué avec un mode appelé « two-pass » ou « nap ». Finalement, les différentes étapes de mesures par AFM sont résumées par la Figure 10. Le micro-aimant a d'abord été localisé à l'aide d'images optiques (Figure 10-A). La position du micro-aimant a ensuite été déterminée précisément en balayant la surface au contact et mesurant la topographie (Figure 10-B). Puis, la hauteur de la sonde colloïdale a été décalée de plusieurs centaines de nanomètres (ΔZ_{nap}) pour enregistrer la déflexion du levier et cartographier les forces magnétiques générées par les micro-aimants (Figure 10-C). Cette cartographie de l'attraction magnétique met en évidence que la force maximale est localisée au-dessus du micro-aimant (Figure 10-C). Enfin, la sonde a été positionnée à l'endroit exact où l'intensité de la force magnétique au-dessus du micro-aimant est la plus élevée. Des courbes d'approche/retrait de la sonde vers la surface du micro-aimant ont été mesurées (Figure 10-D). Les mesures de force sont effectuées pour des micro-aimants individuels.

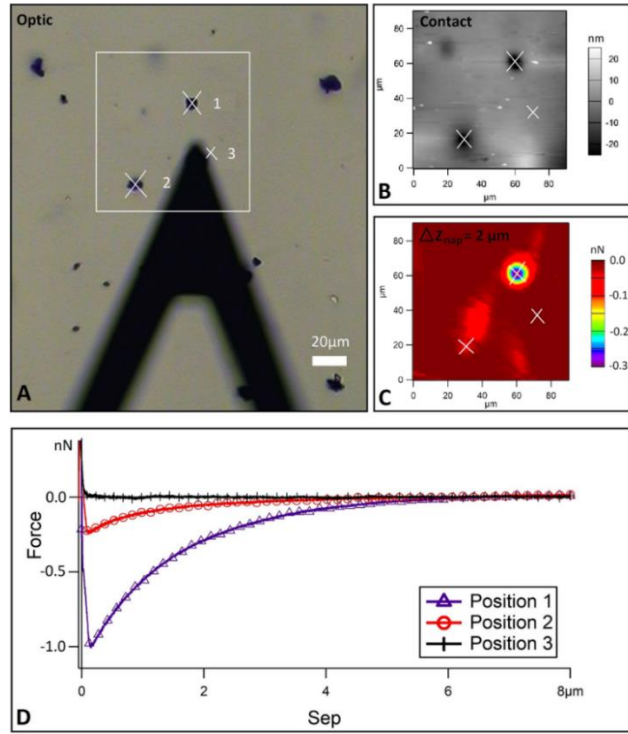


Figure 10 : Etapes de l’AFM à sonde colloïdale pour la mesure de forces magnétiques. (A) Visualisation des micro-aimants à l’optique. (B) Cartographie de la topographie de la surface. (C) Cartographie de l’attraction magnétique. (D) Courbes d’approche/retrait de la sonde vers la surface de l’aimant.

Les mesures par AFM ont notamment permis d’étudier l’impact de la microstructure sur les forces générées. La préparation des micro-aimants sous gradients de champ élevés conduit à des forces magnétiques générées au contact des micro-aimants jusqu’à trois fois plus élevées que lorsque ces derniers ont été préparés sous gradients faibles (Figure 11). La force moyenne au contact est de 1.7 nN contre 0.6 nN. En revanche, cette différence est moins significative pour des mesures effectuées à 3 μm de la surface. Cette augmentation de la force magnétique générée au contact peut être attribuée aux effets combinés d’une plus grande compacité des chaînes de particules, entraînant une moindre perte de flux magnétique, et d’une plus grande concentration de particules magnétiques localisées à la surface du composite. Néanmoins, il convient de noter que la distribution des valeurs de force magnétique générées par les micro-aimants obtenus avec la configuration à gradients élevés est plus grande que celle des micro-aimants obtenus à gradients faibles.

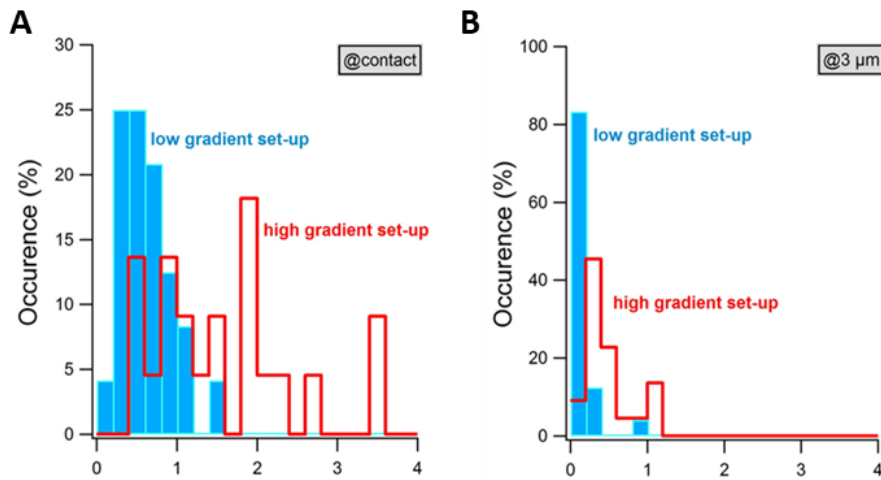


Figure 11 : Mesure de la force magnétiques par AFM à sonde colloïdale (A) au contact ou (B) à 3 μm de la surface des micro-aimants (NdFeB 1w%). Comparaison des configurations de préparation sous gradient faible (« low gradient set-up ») ou gradient élevé (« high gradient set-up »).

Par ailleurs, les mesures par AFM ont démontré l'intérêt de combiner des micro-aimants avec un milli-aimant car des forces deux fois plus grandes ont été observées, pouvant atteindre jusqu'à 4 nN au contact. Le champ magnétique plus élevé en présence de l'aimant extérieur (simulations Comsol) entraîne une augmentation de l'aimantation de la sonde magnétique, mais également des pièges magnétiques, et donc de la force magnétique ($\vec{F}_{mag} = V_p(\vec{M}_p \cdot \vec{\nabla})\vec{B}$).

Ces mesures de force obtenues par AFM ont été comparées à une autre méthode expérimentale basée sur des mesures en microfluidique. Les forces magnétiques exercées par les micro-aimants composites sur des billes superparamagnétiques (diamètre moyen 12 μm , Kisker) ont été estimées *in operando*, directement dans un canal microfluidique. La détermination hydrodynamique de la force magnétique de piégeage consiste à capturer des billes sur les pièges magnétiques à un débit fixe, puis à mesurer la force de traînée fluïdique nécessaire pour surmonter la force magnétique et entraîner le dépiégeage de la bille [26,31]. Avec cette méthode, des forces moyennes de $1,3 \pm 0,3$ nN ont été mesurées, ce qui concorde avec les mesures par AFM. Notons que ces deux méthodes sont complémentaires car l'AFM permet des mesures individuelles (piège par piège) tandis que la mesure en microfluidique permet de déterminer collectivement les forces générées sur une population de billes par un réseau de pièges.

En résumé, ces résultats mettent en évidence que les forces magnétiques générées par les micro-aimants à leur surface sont importantes, pouvant atteindre plusieurs nN. De plus, les forces magnétiques mesurées sont du même ordre de grandeur que celles calculées à l'aide de Comsol, les valeurs numériques étant légèrement supérieures aux valeurs expérimentales (~3 nN pour les calculs Comsol au contact contre ~2 nN pour les mesures expérimentales). Cette différence peut s'expliquer par la modélisation d'une chaîne idéale, les particules magnétiques la constituant étant de forme et d'espacement réguliers. En réalité, la microstructure des chaînes est inhomogène (tomographie aux rayons X) et celle-ci est enfouie dans une membrane de PDMS et peut donc présenter une fine couche de PDMS à sa surface.

Ces forces ont été comparées à celles rapportées dans la littérature (Figure 12) et montrent des résultats comparables ou meilleurs, révélant la pertinence de l'approche magnétique pour fabriquer des micro-aimants performants.

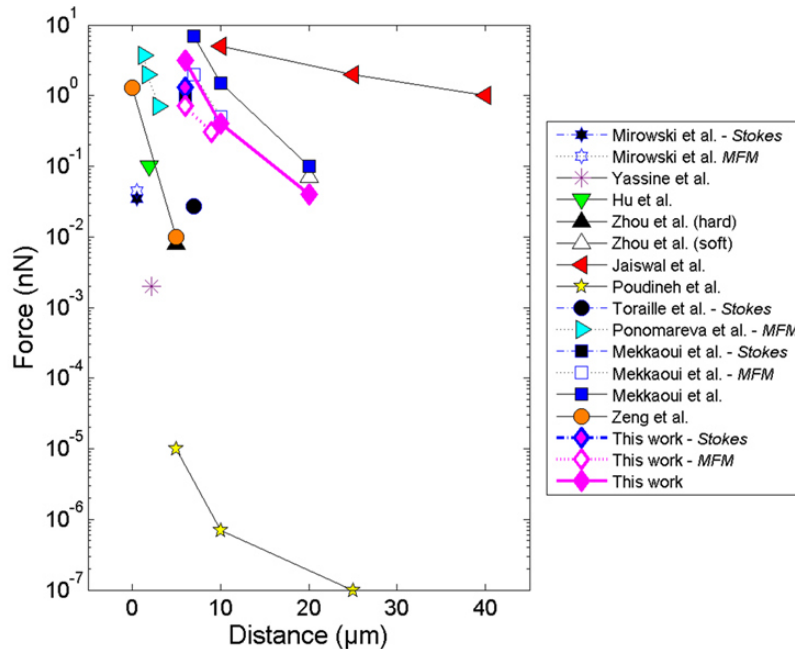


Figure 12 : Comparaison des forces magnétiques avec la littérature. Les forces ont été déterminées par différentes méthodes, lorsque non précisée, la simulation a été utilisée.

Pour conclure sur la caractérisation des micro-aimants, Comsol a permis d'étudier l'effet de la structure du micro-aimant et a fourni une information sur la portée de l'interaction des micro-aimants, tandis que l'AFM a permis de mesurer la force au contact, donnant une information sur l'état d'aimantation de l'objet cible. La faible portée d'interaction des micro-aimants a été améliorée par l'ajout d'un aimant permanent externe de taille millimétrique. Ce dernier a également permis d'augmenter l'aimantation des cibles et de doubler les forces magnétiques. Bien que l'utilisation du milli-aimant se fasse au détriment de la compacité, la mise en œuvre d'aimants à double échelle améliore les performances magnétophorétiques. A un débit de 500 $\mu\text{L/h}$, l'efficacité de piégeage de billes superparamagnétique circulant dans un canal microfluidique intégrant des micro-aimants a été augmentée de 15% en présence du milli-aimant, conduisant à une efficacité de piégeage de 98%.

3. Application à l'isolation des CTCs dans un dispositif microfluidique magnétophorétique

Comme évoqué dans l'introduction, l'isolation des CTCs pourrait répondre à de nombreux enjeux aussi bien pour la recherche sur le cancer, notamment pour la compréhension des mécanismes de résistance aux médicaments, l'identification de nouvelles cibles thérapeutiques, que pour les applications cliniques (diagnostic et pronostic de la maladie, mise au point de traitements personnalisés) [32]. Ainsi, de nombreux travaux ont porté sur le développement de dispositifs microfluidiques de séparation des CTCs pour répondre à ces enjeux. Les exigences clés de ce type de dispositif doivent inclure les éléments suivants : (i) récupération élevée, (ii) pureté élevée, (iii) débit élevé, (iv) préservation de la viabilité et (v) compatibilité avec les analyses en aval (culture cellulaire, études phénotypique et génotypique). Ici, la stratégie adoptée repose sur un dispositif de séparation magnétophorétique, présentant trois caractéristiques principales. Premièrement, le mode de sélection des CTCs est indépendant de marqueurs tumoraux (sélection négative). Deuxièmement, la puce intègre un réseau dense de micro-pièges (jusqu'à 10^6) pour la déplétion des WBC. Enfin, la puce permet de collecter les CTCs en suspension, ce qui facilite leur analyse ultérieure immédiate. Afin de répondre aux exigences décrites précédemment, notamment de pureté, la séparation est réalisée en deux étapes [33,34]. La séparation immunomagnétique intervient après une première étape de séparation par la taille (ClearCell FX1) afin de fournir des échantillons enrichis d'une meilleure pureté, facilitant ainsi les études après la collection des CTCs.

1. Optimisation du dispositif pour la capture des globules blancs

Avant de mettre en œuvre la séparation magnétophorétique des CTCs, plusieurs paramètres ont dû être optimisés afin d'obtenir les meilleures performances de déplétion des globules blancs (GB). Tout d'abord, l'étape de marquage magnétique des globules blancs avec des nanoparticules magnétiques (fonctionnalisées avec les anticorps anti-CD45 et anti-CD15) a été optimisée. Plusieurs conditions ont été étudiées, telles que la température, la durée, l'agitation, le ratio nanoparticules/GB et le milieu. Finalement le meilleur marquage a été obtenu pour les conditions suivantes : 37°C, 30 min, agitation 200 rpm, 400 NP-antiCD45/GB, 100 NP-antiCD15/GB et milieu PBS supplémenté avec 2% BSA (albumine de sérum bovin) et 2 mM EDTA.

Certaines caractéristiques de la puce ont également été optimisées, comme la densité des pièges magnétiques, et la surface de la chambre de piégeage. Finalement jusqu'à 10^6 pièges ont pu être intégrés dans une chambre de dimensions 20x40 mm². Pour obtenir une chambre de piégeage d'une telle surface, un design spécial a dû être conçu avec des canaux d'entrée en parallèle pour un remplissage simultané de la chambre, ou encore des piliers de support pour éviter l'effondrement du plafond de la chambre. Enfin, le protocole d'injection des cellules a également dû être optimisé afin de limiter la perte de cellules dans les différents systèmes d'injection.

Finalement, après toutes ces optimisations, les performances de la puce ont été étudiées sur des lignées cellulaires cancéreuses (A549, MCF-7) comme modèles des CTCs (mCTCs). Un échantillon modèle de 20 000 mCTCs et 300 000 GBs a été utilisé pour ces études. Le nombre de CTCs a été choisi de sorte à obtenir un nombre suffisant de mCTC pour étudier la compatibilité avec des analyses ultérieures, tout en prenant en compte leur rareté. Le nombre de GBs a été défini en concordance des échantillons types obtenus en sortie du système ClearCell FX1, ce dernier étant utilisé par les biologistes aux Hospices Civils de Lyon (laboratoire partenaire) dans leurs études cliniques. En particulier, l'influence du débit

sur les performances de piégeage des GBs et de récupération des mCTCs a été examinée. Les expériences ont été menées au minimum 4 fois pour évaluer la reproductibilité. Les résultats présentés Figure 13 démontrent que lorsque le débit augmente, l'efficacité de piégeage diminue, en raison de la force de trainée du fluide plus importante concurrençant la force magnétique, tandis que l'efficacité de récupération de mCTCs augmente. Cette augmentation peut s'expliquer par la réduction du temps d'injection, limitant la sédimentation, mais également les interactions potentiellement indésirables entre les GBs et les mCTCs (cellules étrangères). Finalement, le débit optimal d'injection a été fixé à 2 mL/h, conduisant à une efficacité de piégeage de $\sim 84 \pm 11\%$ et une efficacité de récupération des cellules cancéreuses A549 de $79 \pm 10\%$. Des résultats similaires ont été obtenus sur la lignée cellulaire MCF-7 de taille plus petite.

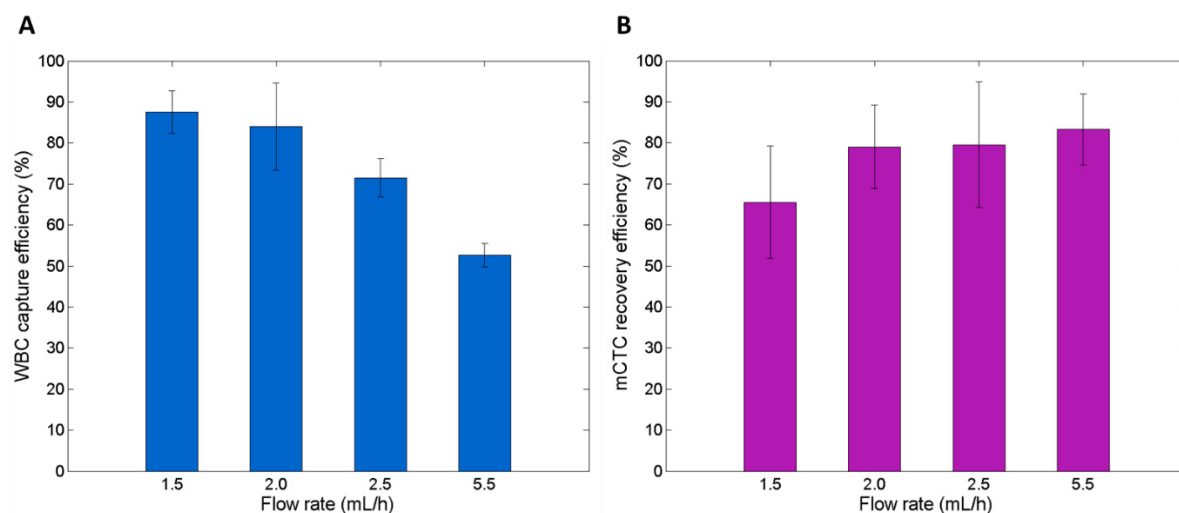


Figure 13 : Etude de l'influence du débit sur les efficacités de (A) piégeage des GBs et (B) récupération des mCTCs.

Après avoir fixé les paramètres de fonctionnement de la puce, la compatibilité du dispositif de séparation magnétique avec des analyses biologiques a été déterminée.

2. Compatibilité du dispositif de séparation avec des analyses biologiques de routine

Un besoin majeur est la récupération de mCTCs viables et intactes en sortie de la puce microfluidique pour pouvoir mener des caractérisations à la suite de leur isolation. Dans un premier temps, la viabilité des mCTCs récupérées a été déterminée par un test de viabilité/cytotoxicité (Live/Dead™ kit, Invitrogen). Les cellules ont été récupérées en sortie de la puce et mises en culture dans des plaques 96 puits. Le milieu de culture a été changé tous les deux jours. Des cellules A549 contrôles (pas de GB, pas d'étape de séparation subie) ont également été mises en culture en parallèle pour comparaison. Après 48h de culture, 81% de cellules vivantes ont été observées (Figure 14-A), contre 91% pour les cellules contrôles. Cette différence peut s'expliquer par les conditions optimales de conservation des cellules contrôles : pas d'interaction avec les GBs et conservation à l'incubateur pendant toute la durée, ce qui n'a pas été le cas pour les cellules injectées dans la puce. Une autre expérience a également permis d'étudier la viabilité des mCTCs récupérées après 6 jours de culture et une viabilité de 94% a été observée (93% pour les cellules contrôles), démontrant la capacité des cellules à continuer de croître même après l'étape de séparation magnétophorétique.

Par ailleurs, l'intégrité des cellules a été étudiée par immunofluorescence en ciblant la phalloïdine au sein des cellules. La phalloïdine marque l'actine filamenteuse, un composant majeur du cytosquelette impliqué dans des processus cellulaires fondamentaux, tels que la division cellulaire, la morphogenèse et la migration [35]. Le noyau des cellules a également été marqué par le DAPI. Ces marquages ont permis de mesurer par la suite la taille du noyau, la taille du cytoplasme, la circularité et le rapport nucléocytoplasmique. Ces mesures ont été comparées avec celles obtenues pour des cellules contrôles (Figure 14-B). Ce test d'immunofluorescence a montré que l'intégrité des cellules est préservée après leur passage dans la puce. L'ensemble de ces résultats préliminaires démontrent que les cellules ne sont pas dégradées lors de leur passage dans la puce.

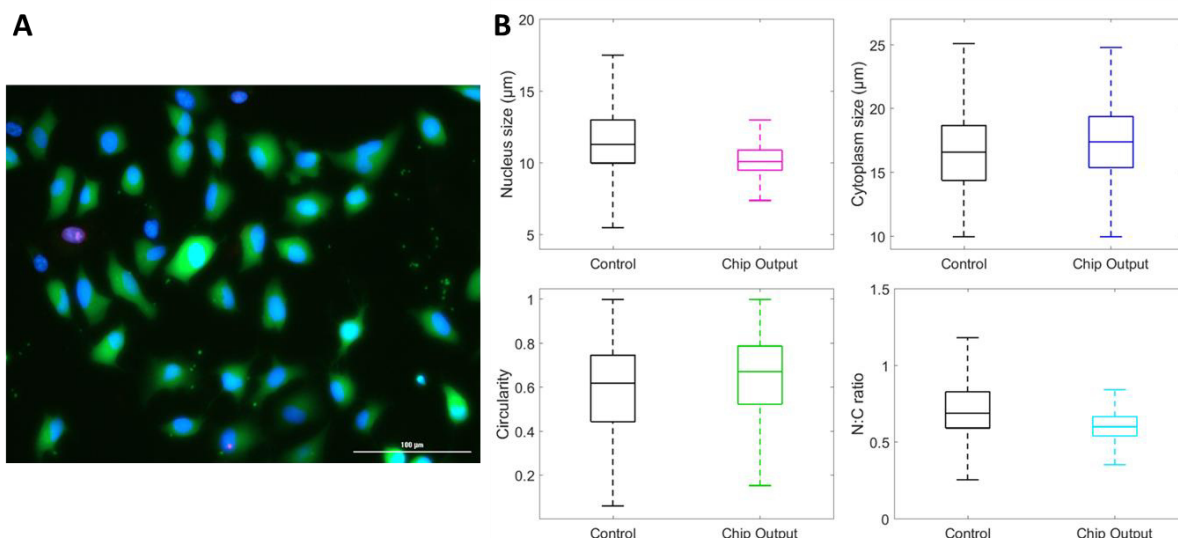


Figure 14 : Etude de la viabilité et de l'intégrité des mCTCs en sortie de la puce microfluidique. **(A)** Image fluorescente des cellules après 48h de remise en culture. Les cellules vertes sont des cellules vivantes (Calceine AM) tandis que les cellules rouges sont mortes (EthD-1). Leur noyau a été marqué au DAPI. **(B)** Mesures des caractéristiques morphologiques des cellules après un test d'immunofluorescence. Les marqueurs DAPI et Phalloïdine ont été utilisés respectivement pour marquer le noyau et le cytosquelette des cellules.

Par la suite, une étude plus poussée des caractérisations possibles en sortie de la puce a été effectuée. La compatibilité de la séparation magnétique avec de la culture cellulaire sur des dizaines de jours, aussi bien en 2D qu'en 3D (formation de sphéroïdes), mais également avec des analyses génotypiques (hybridation in situ fluorescente, FISH) a été démontrée.

Tout d'abord, les mCTCs récupérées en sortie de la puce ont pu être cultivées en 2D dans des plaques 96 puits pendant une dizaine de jours. En particulier, les cellules ont montré une bonne ré-adhérence et prolifération d'après les observations au microscope (objectif 20X) retrouvées Figure 15-A. En effet, on peut retrouver à la fois des cellules adhérentes (forme allongée) et des cellules en division (forme ronde), ce qui témoigne de la bonne viabilité des cellules et de conditions de culture favorables à leur prolifération. La présence d'amas cellulaires témoigne également de la division cellulaire en cours.

Par ailleurs, les mCTCs récupérées ont également pu être cultivées en 3D dans des plaques 96 puits à fond rond (Round Bottom Ultra-Low Attachment Microplate, Corning®) afin de former des sphéroïdes. Les sphéroïdes, qui désignent des agrégats tridimensionnels de cellules, sont apparus comme de meilleurs modèles pour reproduire l'environnement tumoral in vivo [36]. La croissance des sphéroïdes a pu être suivie pendant 20 jours en mesurant la surface de ces derniers (Figure 15-B). La surface des sphéroïdes a atteint 0,7 mm² après deux semaines avant de diminuer. En effet, à partir d'un certain point, le noyau nécrotique commence à envoyer des signaux extracellulaires stoppant la prolifération des cellules et conduisant à l'apoptose. Le suivi de la culture des sphéroïdes pendant plusieurs semaines après que les cellules sont passées dans la puce ouvre la voie aux tests de sensibilité des médicaments comme une autre application sur les cellules cancéreuses isolées.

Enfin, la compatibilité de la puce avec des études génotypiques a été étudiée sur des cellules cancéreuses A549 présentant une fusion des gènes EML4 et ALK (A549 EML4-ALK). La fusion EML4-ALK est présente dans environ 5% des adénocarcinomes pulmonaires [37] et sa détection est cruciale pour pouvoir mettre en place des thérapeutiques adaptées [38]. L'hybridation in situ fluorescente (FISH) est une technique de référence pour détecter de telles aberrations génétiques. En sortie de la puce microfluidique, l'analyse FISH des cellules A549 EML4-ALK a permis d'identifier ce réarrangement génétique comme illustré Figure 15-C.

Pour conclure, ces résultats démontrent le panel d'applications possibles en sortie du dispositif. Comme évoqué plus haut, cette thèse s'inscrit dans le cadre d'une collaboration avec les HCL, et a pour but de proposer aux biologistes une meilleure purification des échantillons en sortie de leur système ClearCell.

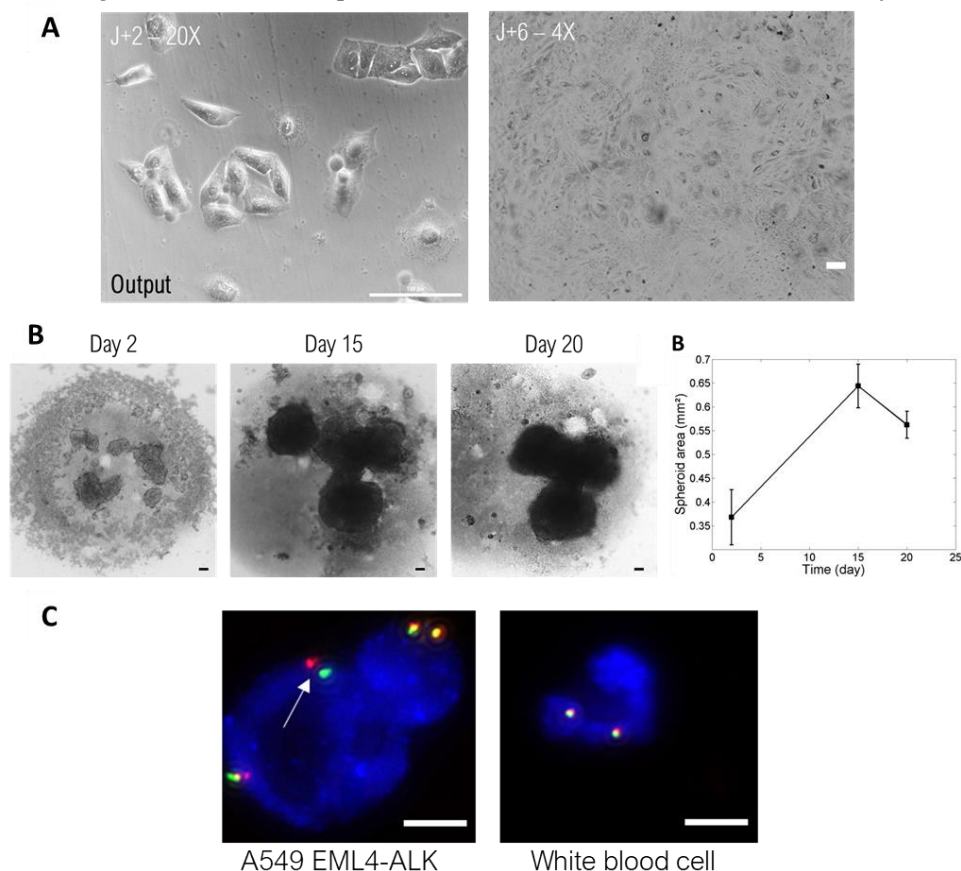


Figure 15 : Compatibilité du dispositif de séparation magnétique avec **(A)** la culture cellulaire en 2D (barre d'échelle 100 μm), **(B)** la culture en 3D sur plusieurs semaines pour la croissance de sphéroïdes (barre d'échelle 100 μm), **(C)** l'analyse FISH pour la détection de la fusion des gènes EML4-ALK (barre d'échelle 10 μm).

3. Workflow total : combinaison avec une méthode de séparation par la taille

Le dispositif de purification par magnétophorèse développé ici est destiné à être le dernier bloc d'un workflow complet qui manipule des échantillons de sang total. Un premier enrichissement par la taille est effectué dans le système ClearCell FX1, suivi d'une purification magnétique au sein de la puce développée. L'objectif de ce workflow en deux étapes est d'améliorer le rapport mCTC/GB, permettant ainsi des caractérisations phénotypiques sur les mCTC récupérées. La lignée cellulaire cancéreuse A549 a été utilisée comme modèle des CTCs et ajoutée dans les échantillons de sang totaux prélevés chez des individus sains à une concentration de 20 000 cellules.

La première étape de séparation au sein du ClearCell repose sur la différence de taille entre les CTCs et les GBs. En effet, les CTCs présentent une taille plus grande (12-25 μm) que les GBs (5-20 μm) [10]. Le système ClearCell FX1 propose deux modes de séparation, P1 et P3, avec des seuils différents pour la séparation par la taille. Avec le mode P1, la taille limite pour la séparation est de 14 μm . Les cellules dont la taille est au-delà de ce seuil sont récupérées, tandis que celles dont la taille est inférieure à cette valeur sont éliminées. Cette valeur limite peut être ajustée en modifiant les rapports de débit à la sortie afin d'enrichir les CTCs à une taille de cellule inférieure [8]. C'est ce que propose le mode P3, prenant ainsi en compte l'hétérogénéité de la taille des CTCs, et conduisant à de meilleures efficacités de récupération, mais aussi à une moins bonne pureté. Selon l'application souhaitée en sortie, les programmes P1 et P3 peuvent être sélectionnés.

La puce microfluidique magnétophorétique intervient à la suite de cette première étape de séparation par la taille afin d'améliorer la pureté. Le protocole total, de la collecte de l'échantillon à la récupération des cellules en sortie du workflow, peut être menée dans une durée inférieure à 3h. Les différentes étapes de ce workflow sont résumées Figure 16.

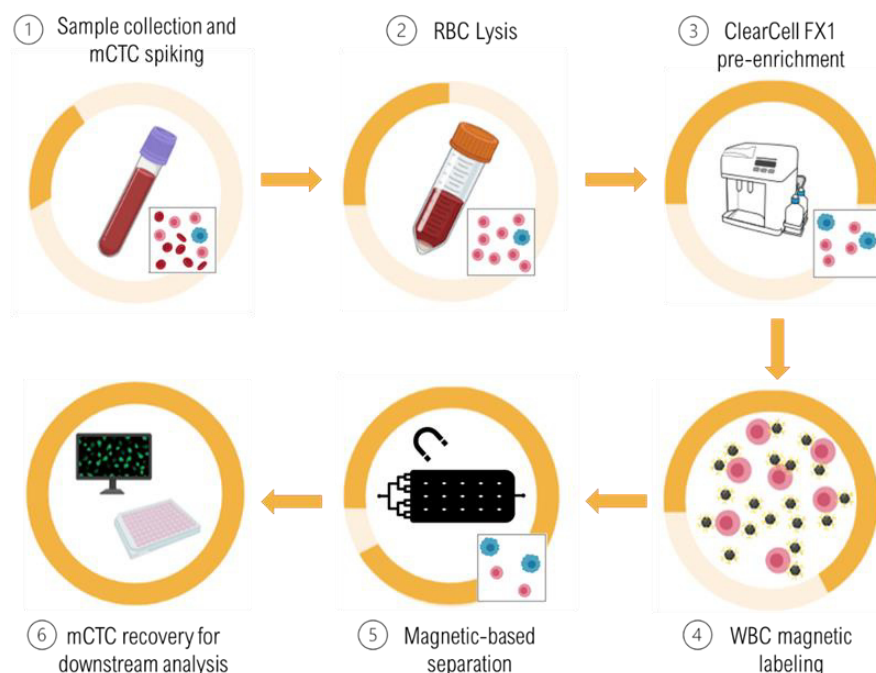


Figure 16 : Workflow complet pour l'isolation des CTCs et leur caractérisation. 1) Collecte de l'échantillon de sang et ajout des mCTCs (A549). 2) Lyse de globules rouges (GR). 3) Pré-enrichissement dans le ClearCell par la taille des cellules. Une bonne partie des GB est éliminée. 4) Marquage magnétique des GB restants. 5) Purification magnétique dans la puce microfluidique. 6) Récupération des mCTCs pour leur caractérisation. Un aperçu de l'échantillon de sortie est donné après les étapes 1, 2, 3 et 5. Les mCTCs apparaissent en bleu, les GB en rose et les GR en rouge.

Les performances des différentes étapes du workflow (pré-enrichissement dans le ClearCell, suivi de la purification magnétique) sont représentées dans le graphe Figure 17, avec le nombre de mCTC, de GB, et le rapport des deux. Brièvement, avec le mode P3 du ClearCell (Figure 17-A), le nombre de GB a pu être réduit d'un facteur 300 (de $4.6.10^7$ à $1.4.10^5$ GBs). Suite à l'étape de purification magnétique au sein de la puce microfluidique, le rapport mCTC/GB est trois fois plus grand, et atteint 25%. La combinaison des deux méthodes de séparation a permis d'obtenir un taux de déplétion total de 99,93 %, avec un nombre final de ~30 000 GBs.

Avec le mode P1 du ClearCell (Figure 17-B), la déplétion après la première étape est meilleure qu'en sortie de P3, comme attendu (taille limite plus grande), avec ~50,000 GBs restants (contre 140 000 GBs avec P3). Suite à la deuxième étape de séparation dans la puce magnétique, le nombre de mCTC est 2 fois plus élevé que celui de GB, avec 14 000 cellules A549 contre 7 100 GBs. Finalement, la combinaison des deux méthodes de tri a permis d'atteindre un taux de déplétion des GBs de 99,99%.

Il est intéressant de souligner que l'étape supplémentaire de purification magnétique a amélioré la pureté d'un facteur 1,4 (P3) à 2,5 (P1). L'ensemble du workflow a pu être réalisé en moins de 3 heures, garantissant la préservation de la viabilité cellulaire pour les analyses et les cultures ultérieures. Les mCTCs récupérées en sortie du workflow total ont pu être remises en culture avec une viabilité de 90% (test de viabilité/cytotoxicité) observée après 4 jours (89% pour le contrôle).

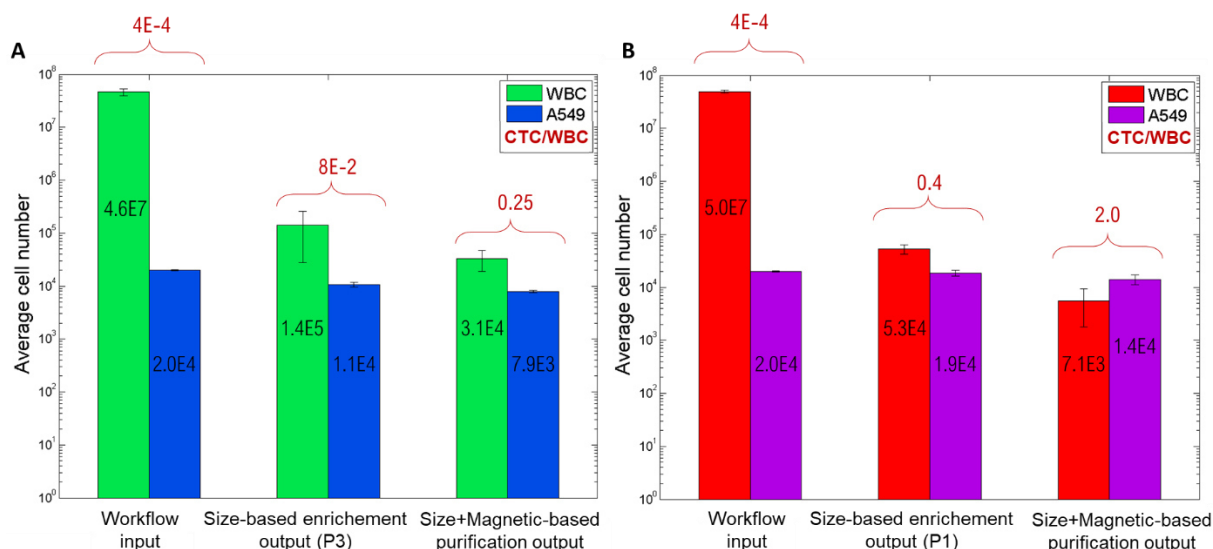


Figure 17 : Performances du workflow avec en première étape un enrichissement par la taille avec ClearCell (A) mode P3 ou (B) mode P1, suivi d'une deuxième étape de purification magnétique dans la puce.

Par ailleurs, une analyse en immunofluorescence (IF) des cellules collectées a également été menée, en ciblant le marqueur tumoral ALDH1 (aldéhyde déshydrogénase 1), exprimé dans les cellules souches cancéreuses et associé à un phénotype agressif [39]. Afin d'évaluer le bénéfice de la purification magnétique, la sortie du ClearCell a été divisée en deux : une moitié pour une lame d'IF, l'autre pour passage dans la puce magnétique suivi d'une deuxième lame d'IF. La Figure 18-A présente les différentes images en fluorescence obtenues. L'image d'une concentration typique de GB dans un tube de sang est donnée pour l'entrée. L'étape de pré-enrichissement utilisant le programme P3 ou P1 permet une meilleure visualisation des mCTCs. Enfin, la deuxième étape de purification permet une excellente/conséquente élimination des GBs avec principalement des cellules cancéreuses restantes.

En particulier, cette deuxième étape de purification a permis de mettre en avant l'hétérogénéité des mCTCs (A549) à la fois sur leur taille et leur niveau d'expression d'ALDH1. A partir des signaux de fluorescence de DAPI et GFP, respectivement, les mesures du diamètre cellulaire et de l'expression de l'ALDH1 ont pu être déterminées, rapportées dans la Figure 18-B. Le diamètre des cellules cancéreuses A549 récupérées est compris entre 5,4 et 28 μm et l'expression de l'ALDH1 varie entre 3 000 et 50 000 u.a. Les cellules cancéreuses présentant un niveau élevé d'expression de l'ALDH1 sont la preuve d'un phénotype agressif et peuvent être associées à un mauvais pronostic [40]. Ainsi, être capable de quantifier le niveau d'expression d'ALDH1 pourrait aider à déterminer le pronostic des patients. Cette étude souligne qu'en plus de fournir des échantillons de cellules purifiées et viables, la puce magnétique permet de récupérer les CTC indépendamment de leur taille ou de l'expression de leurs marqueurs, ce qui est un atout étant donné l'hétérogénéité signalée des CTC.

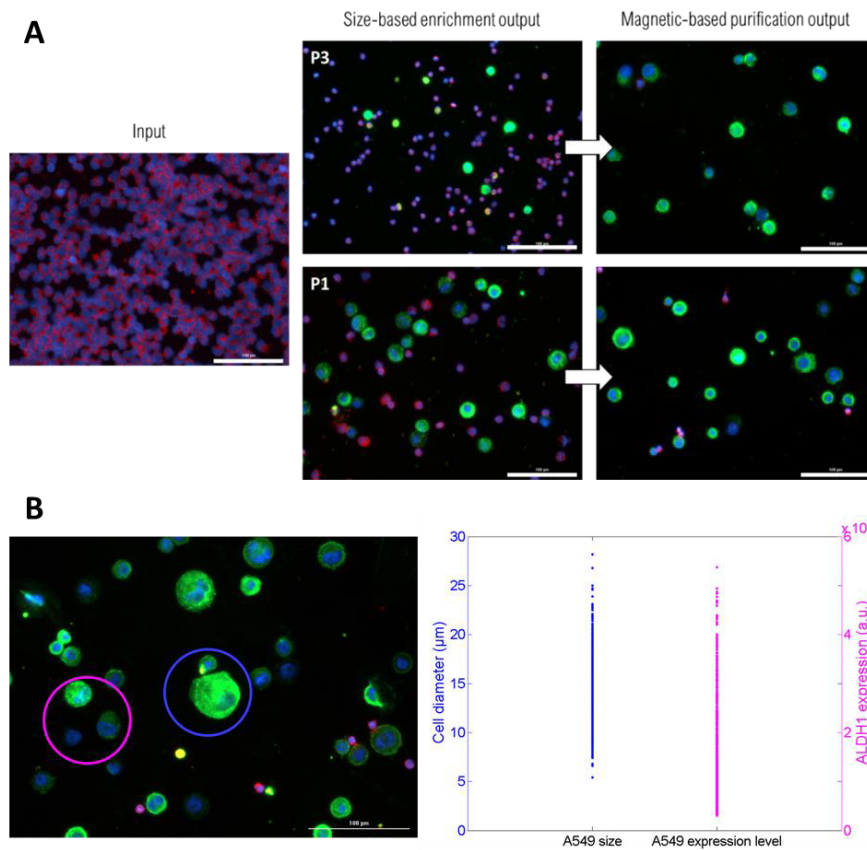


Figure 18 : Analyse en immunofluorescence post-séparation. **(A)** Images de fluorescence de cellules immunomarquées à différentes étapes du workflow (échelle 100 μm). Les mCTCs (cellules A549) fluorescent dans le vert (GFP) tandis que les GBs fluorescent dans le rouge (CY5). Leurs noyaux sont marqués en bleu (DAPI). **(B)** Mise en évidence de l'hétérogénéité des mCTCs en termes de taille (cercle bleu sur l'image en fluorescence) et d'expression des marqueurs de surface (cercle rose) par mesure de la taille (signal DAPI) et du niveau d'expression d'ALDH1 (signal GFP) sur l'ensemble des mCTCs récupérées après le mode P1 de ClearCell et la puce magnétique.

4. Conclusion et perspectives

En résumé, nous avons développé une puce microfluidique basée sur la magnétophorèse pour l'isolation des CTCs indépendamment de leur taille et des marqueurs à leur surface, via une déplétion des GBs (sélection négative). Cette étude a d'abord porté sur la fabrication et la caractérisation de micro-aimants permanents obtenus par l'approche composite. Ces micro-aimants sont formés à partir de l'auto-organisation de particules magnétiques de NdFeB dans une membrane PDMS, via l'application d'un champ magnétique extérieur pendant la réticulation du composite. Les micro-aimants obtenus génèrent de très forts gradients de champ magnétique à leur surface, de l'ordre de 10^5 T/m, et des forces magnétiques de plusieurs nN. En particulier, la distance d'interaction des micro-aimants a été améliorée en la présence d'un milli-aimant, favorisant la déflexion des objets magnétiques circulant dans le canal microfluidique.

Ces micro-aimants permanents intégrés en microfluidique ont été mis en œuvre pour l'isolation de cellules cancéreuses par piégeage des GBs. La puce magnétophorétique développée a atteint une efficacité moyenne de déplétion des GB de 87% et un taux moyen de récupération des CTCs de 81%. Lorsque combinée avec une étape de séparation par la taille (ClearCell), la purification magnétique conduit à des échantillons d'une excellente pureté, facilitant les études phénotypiques.

La puce magnétophorétique a démontré son efficacité sur des lignées cellulaires cancéreuses, les futurs travaux consisteront donc à évaluer les performances du workflow dans un contexte clinique en isolant les CTCs à partir d'échantillons de patients. Par ailleurs, plusieurs améliorations peuvent être imaginées afin d'obtenir un produit final facile d'utilisation, robuste, polyvalent, et fabriquable en masse.

Il existe toujours un besoin de fournir des dispositifs prêts à l'emploi et fiables pour les applications cliniques. Les recherches menées dans le cadre de cette thèse contribuent à démontrer la plus-value des technologies émergentes telles que la microfluidique et la magnétophorèse pour la caractérisation des échantillons issus de biopsie liquide, représentant un changement de paradigme dans le diagnostic et de la gestion du cancer.

Références

1. Jackson, J.M.; Witek, M.A.; Kamande, J.W.; Soper, S.A. Materials and Microfluidics: Enabling the Efficient Isolation and Analysis of Circulating Tumour Cells. *Chem. Soc. Rev.* **2017**, *46*, 4245–4280, doi:10.1039/c7cs00016b.
2. Thiele, J.A.; Bethel, K.; Králíčková, M.; Kuhn, P. Circulating Tumor Cells: Fluid Surrogates of Solid Tumors. *Annu. Rev. Pathol. Mech. Dis.* **2017**, *12*, 419–447.
3. Wan, L.; Pantel, K.; Kang, Y. Tumor metastasis: Moving new biological insights into the clinic. *Nat. Med.* **2013**, *19*, 1450–1464, doi:10.1038/nm.3391.
4. Chemi, F.; Mohan, S.; Guevara, T.; Clipson, A.; Rothwell, D.G.; Dive, C. Early Dissemination of Circulating Tumor Cells: Biological and Clinical Insights. *Front. Oncol.* **2021**, *11*.
5. Kalluri, R.; Weinberg, R.A. The basics of epithelial-mesenchymal transition. *J. Clin. Invest.* **2009**, *119*, 1420–1428, doi:10.1172/JCI39104.
6. Mostert, B.; Kraan, J.; Bolt-de Vries, J.; van der Spoel, P.; Sieuwerts, A.M.; Schutte, M.; Timmermans, A.M.; Foekens, R.; Martens, J.W.M.; Gratama, J.-W.; et al. Detection of circulating tumor cells in breast cancer may improve through enrichment with anti-CD146. *Breast Cancer Res. Treat.* **2011**, *127*, 33–41, doi:10.1007/s10549-010-0879-y.
7. Miller, M.C.; Robinson, P.S.; Wagner, C.; O'Shannessy, D.J. The Parsortix™ Cell Separation System – A versatile liquid biopsy platform. *Cytom. Part A* **2018**, *93*, 1234–1239, doi:10.1002/cyto.a.23571.
8. Lee, Y.; Guan, G.; Bhagat, A.A. ClearCell® FX, a label-free microfluidics technology for enrichment of viable circulating tumor cells. *Cytom. Part A* **2018**, *93*, 1251–1254, doi:10.1002/cyto.a.23507.
9. Sollier-Christen, E.; Renier, C.; Kaplan, T.; Kfir, E.; Crouse, S.C. VTX-1 Liquid Biopsy System for Fully-Automated and Label-Free Isolation of Circulating Tumor Cells with Automated Enumeration by BioView Platform. *Cytom. Part A* **2018**, *93*, 1240–1245, doi:10.1002/cyto.a.23592.
10. Hao, S.-J.; Wan, Y.; Xia, Y.-Q.; Zou, X.; Zheng, S.-Y. Size-based separation methods of circulating tumor cells. *Adv. Drug Deliv. Rev.* **2018**, *125*, 3–20, doi:10.1016/j.addr.2018.01.002.
11. Garbarino, F.; Minero, G.A.S.; Rizzi, G.; Fock, J.; Hansen, M.F. Integration of rolling circle amplification and optomagnetic detection on a polymer chip. *Biosens. Bioelectron.* **2019**, *142*, 111485, doi:10.1016/j.bios.2019.111485.
12. Gao, Y.; Huo, W.; Zhang, L.; Lian, J.; Tao, W.; Song, C.; Tang, J.; Shi, S.; Gao, Y. Multiplex measurement of twelve tumor markers using a GMR multi-biomarker immunoassay biosensor. *Biosens. Bioelectron.* **2019**, *123*, 204–210, doi:10.1016/j.bios.2018.08.060.
13. Luo, L.; He, Y. Magnetically driven microfluidics for isolation of circulating tumor cells. *Cancer Med.* **2020**, *9*, 4207–4231, doi:10.1002/cam4.3077.
14. Moore, L.R.; Mizutani, D.; Tanaka, T.; Buck, A.; Yazer, M.; Zborowski, M.; Chalmers, J.J. Continuous, intrinsic magnetic depletion of erythrocytes from whole blood with a quadrupole magnet and annular flow channel; pilot scale study. *Biotechnol. Bioeng.* **2018**, *115*, 1521–1530, doi:10.1002/bit.26581.
15. Xuan, X. Recent advances in continuous-flow particle manipulations using magnetic fluids. *Micromachines* **2019**, *10*, doi:10.3390/mi10110744.
16. Alnaimat, F.; Karam, S.; Mathew, B.; Mathew, B. Magnetophoresis and Microfluidics: A Great Union. *IEEE Nanotechnol. Mag.* **2020**, *14*, 24–41, doi:10.1109/MNANO.2020.2966029.
17. Cugat, O.; Delamare, J.; Reyne, G. Magnetic micro-actuators and systems (MAGMAS). *IEEE Trans. Magn.* **2003**, *39*, 3607–3612, doi:10.1109/TMAG.2003.816763.
18. Dempsey, N.M.; Le Roy, D.; Marelli-Mathevon, H.; Shaw, G.; Dias, A.; Kramer, R.B.G.; Viet Cuong, L.; Kustov, M.; Zanini, L.F.; Villard, C.; et al. Micro-magnetic imprinting of high field gradient magnetic flux sources. *Appl. Phys. Lett.* **2014**, *104*, 262401, doi:10.1063/1.4886375.
19. Castillo-Torres, K.Y.; Arnold, D.P.; McLamore, E.S. Rapid isolation of Escherichia coli from water samples using magnetic microdiscs. *Sensors Actuators, B Chem.* **2019**, *291*, 58–66, doi:10.1016/j.snb.2019.04.043.
20. Zhi, S.; Sun, X.; Feng, Z.; Lei, C.; Zhou, Y. An innovative micro magnetic separator based on 3D micro-copper-coil exciting soft magnetic tips and FeNi wires for bio-target sorting. *Microfluid. Nanofluidics* **2019**, *23*, 0, doi:10.1007/s10404-019-2215-0.
21. De Los Santos Valladares, L.; Ionescu, A.; Holmes, S.; Barnes, C.H.W.; Bustamante Domínguez, A.; Avalos Quispe, O.; González, J.C.; Milana, S.; Barbone, M.; Ferrari, A.C.; et al. Characterization of Ni thin films following thermal oxidation in air. *J. Vac. Sci. Technol. B, Nanotechnol. Microelectron. Mater. Process. Meas. Phenom.* **2014**, *32*, 051808, doi:10.1116/1.4895846.

22. Dumas-Bouchiat, F.; Zanini, L.F.; Kustov, M.; Dempsey, N.M.; Grechishkin, R.; Hasselbach, K.; Orlianges, J.C.; Champeaux, C.; Catherinot, A.; Givord, D. Thermomagnetically patterned micromagnets. *Appl. Phys. Lett* **2010**, *96*, 102511, doi:10.1063/1.3341190.
23. Descamps, L.; Roy, D. Le; Tomba, C. Magnetic Polymers for Magnetophoretic Separation in Microfluidic Devices. **2021**.
24. Faivre, M.; Gelszinnis, R.; Degouttes, J.; Terrier, N.; Rivière, C.; Ferrigno, R.; Deman, A.-L. Magnetophoretic manipulation in microsystem using carbonyl iron-polydimethylsiloxane microstructures. *Biomicrofluidics* **2014**, *8*, 054103, doi:10.1063/1.4894497.
25. Deman, A.-L.; Mekkaoui, S.; Dhungana, D.; Chateaux, J.-F.; Tamion, A.; Degouttes, J.; Dupuis, V.; Le Roy, D. Anisotropic composite polymer for high magnetic force in microfluidic systems. *Microfluid. Nanofluidics* **2017**, *21*, 170, doi:10.1007/s10404-017-2008-2.
26. Mekkaoui, S.; Descamps, L.; Audry, M.C.; Deman, A.L.; Le Roy, D. Nanonewton Magnetophoretic Microtrap Array for Microsystems. *Langmuir* **2020**, *36*, 14546–14553, doi:10.1021/acs.langmuir.0c02254.
27. Mekkaoui, S. Développement de polymères composites auto-organisés pour la mise en œuvre de fonctions magnétiques en microsystèmes fluidiques, Université Claude Bernard Lyon 1, 2019.
28. Coey, J.M.D. Magnetostatics. In *Magnetism and Magnetic Materials*; Cambridge University Press, 2010; pp. 24–61.
29. Stott, S.L.; Hsu, C.; Tsukrov, D.I.; Yu, M.; Miyamoto, D.T.; Waltman, B.A.; Rothenberg, S.M.; Shah, A.M.; Smas, M.E.; Korir, G.K.; et al. Isolation of circulating tumor cells using a microvortex-generating herringbone-chip. *Proc. Natl. Acad. Sci. U. S. A.* **2010**, doi:10.1073/pnas.1012539107/-/DCSupplemental.www.pnas.org/cgi/doi/10.1073/pnas.1012539107.
30. Jiang, X.; Wong, K.H.K.; Khankhel, A.H.; Zeinali, M.; Reategui, E.; Phillips, M.J.; Luo, X.; Aceto, N.; Fachin, F.; Hoang, A.N.; et al. Microfluidic isolation of platelet-covered circulating tumor cells. *Lab Chip* **2017**, *17*, 3498–3503, doi:10.1039/c7lc00654c.
31. Mirowski, E.; Moreland, J.; Zhang, A.; Russek, S.E.; Donahue, M.J. Manipulation and sorting of magnetic particles by a magnetic force microscope on a microfluidic magnetic trap platform. *Appl. Phys. Lett.* **2005**, *86*, 1–3, doi:10.1063/1.1947368.
32. Alix-Panabières, C.; Pantel, K. Clinical applications of circulating tumor cells and circulating tumor DNA as liquid biopsy. *Cancer Discov.* **2016**, *6*, 479–491, doi:10.1158/2159-8290.CD-15-1483.
33. Fachin, F.; Spuhler, P.; Martel-Foley, J.M.; Edd, J.F.; Barber, T.A.; Walsh, J.; Karabacak, M.; Pai, V.; Yu, M.; Smith, K.; et al. Monolithic Chip for High-throughput Blood Cell Depletion to Sort Rare Circulating Tumor Cells. *Sci. Rep.* **2017**, *7*, 1–11, doi:10.1038/s41598-017-11119-x.
34. Jack, R.; Hussain, K.; Rodrigues, D.; Zeinali, M.; Azizi, E.; Wicha, M.; Simeone, D.M.; Nagrath, S. Microfluidic continuum sorting of sub-populations of tumor cells via surface antibody expression levels. *Lab Chip* **2017**, *17*, 1349–1358, doi:10.1039/C6LC01496H.
35. Sirenko, O.; Hesley, J.; Rusyn, I.; Cromwell, E.F. High-content assays for hepatotoxicity using induced pluripotent stem cell-derived cells. *Assay Drug Dev. Technol.* **2014**, *12*, 43–54, doi:10.1089/adt.2013.520.
36. Moshksayan, K.; Kashaninejad, N.; Warkiani, M.E.; Lock, J.G.; Moghadas, H.; Firoozabadi, B.; Saidi, M.S.; Nguyen, N.T. Spheroids-on-a-chip: Recent advances and design considerations in microfluidic platforms for spheroid formation and culture. *Sensors Actuators, B Chem.* **2018**, *263*, 151–176, doi:10.1016/j.snb.2018.01.223.
37. Sánchez-Herrero, E.; Provencio, M.; Romero, A. Clinical utility of liquid biopsy for the diagnosis and monitoring of EML4-ALK NSCLC patients. *Adv. Lab. Med. / Av. en Med. Lab.* **2020**, *1*, doi:10.1515/almed-2019-0019.
38. Toyokawa, G.; Seto, T. Anaplastic lymphoma kinase rearrangement in lung cancer: its biological and clinical significance. *Respir. Investig.* **2014**, *52*, 330–338, doi:10.1016/j.resinv.2014.06.005.
39. Yao, J.; Jin, Q.; Wang, X.D.; Zhu, H.J.; Ni, Q.C.; Fan, H. Aldehyde dehydrogenase 1 expression is correlated with poor prognosis in breast cancer. *Med. (United States)* **2017**, *96*, 1–6, doi:10.1097/MD.000000000000171.
40. Chen, M.F.; Chen, P.T.; Lu, M.S.; Chen, W.C. Role of ALDH1 in the prognosis of esophageal cancer and its relationship with tumor microenvironment. *Mol. Carcinog.* **2018**, *57*, 78–88, doi:10.1002/mc.22733.

Abstracts

Self-assembled permanent micro-magnets for the isolation of Circulating Tumor Cells in a microfluidic device

Circulating tumor cells (CTCs) have received significant attention over years for their potential clinical significance. The isolation of CTCs directly from blood, as a liquid biopsy, could be used for early cancer diagnosis, patient outcome prognosis, and treatment efficacy monitoring, paving the way for personalized cancer medicine. Microfluidic devices have emerged as promising tools to isolate CTCs since they offer precise cell manipulation, versatile functions, and cost-effective fabrication. In this thesis, we developed a microfluidic device integrating dense arrays of permanent micro-magnets that can isolate viable and pure CTCs from whole blood for downstream characterization. We reported an original fabrication approach, based on magnetic polymer composites, breaking with standard microfabrication techniques. Micro-magnets were obtained by microstructuring a mixture of NdFeB microparticles and PDMS, which leads to the self-organization of magnetic particles due to dipole-dipole interactions. We further characterized the micro-magnets, which revealed a high aspect ratio structure and generated magnetic forces up to several nanoNewtons at their surface. The micro-magnets, acting like micro-traps, were implemented for CTC isolation by performing white blood cell depletion. We used cancer cell lines (A549, MCF-7) as CTC models and demonstrated their successful recovery, while preserving their viability for subsequent analyses, including cell culture, phenotypic and genotypic studies. Finally, the magnetophoretic device was combined with a size-based separation technology to achieve high purity, therefore meeting the needs of clinicians.

Micro-aimants permanents auto-organisés pour l'isolation de Cellules Tumorales Circulantes dans un dispositif microfluidique

Les cellules tumorales circulantes (CTCs) ont suscité une attention particulière au fil des années en raison du potentiel de leur utilité clinique. L'isolation des CTCs directement à partir du sang (biopsie liquide) s'inscrit dans le développement d'une médecine personnalisée du cancer. Les dispositifs microfluidiques sont apparus comme des outils prometteurs pour isoler les CTCs car ils permettent entre autres une manipulation précise des cellules. Dans cette thèse, nous avons développé un dispositif microfluidique intégrant des réseaux denses de micro-aimants permanents dans le but d'isoler des CTCs viables à partir de sang total et permettre ainsi leur caractérisation ultérieure. Nous avons présenté une approche de fabrication originale, basée sur les composites polymères magnétiques, rompant avec les techniques de microfabrication standards. Les micro-aimants ont été obtenus en mélangeant des particules magnétiques de NdFeB avec une matrice PDMS, ces dernières s'auto-organisant sous l'action des interactions dipolaires. Leur caractérisation a permis de mettre en avant leur microstructure allongée et la génération de forces magnétiques allant jusqu'à plusieurs nanoNewtons à leur surface. Les micro-aimants, agissant comme des micro-pièges, ont été mis en œuvre pour l'isolation des CTCs (modélisées par des lignées cellulaires) en effectuant une déplétion des globules blancs. Nous avons étudié les performances de piégeage et de récupération du dispositif, et démontré sa compatibilité avec des analyses biologiques de routine. Enfin, le dispositif magnétophorétique a été combiné à une technologie de séparation basée sur la taille pour obtenir des échantillons d'une grande pureté, répondant ainsi aux besoins des praticiens.